ParisTech
INSTITUT DES SCIENCES ET TECHNOLOGIES
PARIS INSTITUTE OF TECHNOLOGY

Fraunhofer
ITWM

TECHNISCHE UNIVERSITÄT
KAISERSLAUTERN

MINES
ParisTech

PhD Thesis

to achieve the doctor's degree delivered by

l'École nationale supérieure des mines de Paris
École doctorale n^{o}432: Sciences des Métiers de l'Ingénieur
Doctorat européen ParisTech – Spécialité « Morphologie Mathématique »

and

Technische Universität Kaiserslautern – Fachbereich Mathematik
Vom Fachbereich Mathematik der Technischen Universität Kaiserslautern zur Verleihung des akademischen Grades Doktor der Naturwissenschaften (Doctor rerum naturalium, Dr. rer. nat.) genehmigte Dissertation. Bibliothekskennzeichen: D 386.

Hellen ALTENDORF

November 7, 2011

3D Morphological Analysis and Modeling of Random Fiber Networks

– applied on Glass Fiber Reinforced Composites –

Supervisor: **Prof. Dr. Dominique JEULIN**
Supervisor: **Prof. Dr. Ralf KORN**

JURY

Prof. Dr. Joachim OHSER, Hochschule Darmstadt, University of Applied Science	Referee
Prof. Dr. Jean-Michel MOREL, Ecole Normale Supérieure de Cachan	Referee
Prof. Dr. Karam SAB, Laboratoire Navier, Ecole des Ponts ParisTech	President
Dr. Katja SCHLADITZ, Dept. of Image Processing, Fraunhofer ITWM Kaiserslautern	Examiner
Prof. Dr. Dominique JEULIN, Centre de Morphologie Mathématique, MINES ParisTech	Supervisor
Prof. Dr. Ralf KORN, Dept. of Mathematics, University of Kaiserslautern	Supervisor

THESIS

Technische Universität Kaiserslautern
Fachbereich Mathematik
Gottlieb-Daimler-Straße 47, D-67663 Kaiserslautern

MINES ParisTech
Centre de Morphologie Mathématique
35 rue Saint-Honoré, F-77300 Fontainebleau

Preface

This PhD thesis is part of the cooperation of Mines ParisTech, Technical University of Kaiserslautern and Fraunhofer Institute for Industrial Mathematics in Kaiserslautern. Further financial support was provided by the Institute Carnot M.I.N.E.S. The work of this manuscript includes images recorded at the ESRF in Grenoble, Fraunhofer ITWM in Kaiserslautern, at the synchrotron BESSY in Berlin and at the Ecole Polytechnique in Saclay. The focus lies on glass fiber reinforced polymers from samples provided by the IVW in Kaiserslautern.

Softwares and libraries as Morph-M and Morph-Hom (developed at CMM - Center of Mathematical Morphology in Fontainebleau) as well as MAVIlib and MAVI (developed at the Fraunhofer ITWM in Kaiserslautern) serve as toolboxes for the creation of algorithms presented in this thesis. Visualizations use the open source VTK library.

Abstract

The various uses of fiber-reinforced composites, for example in the enclosures of planes, boats and cars, generates the demand for a detailed analysis of these materials. The final goal is to optimize fibrous materials by the means of “virtual material design”. New fibrous materials are virtually created as realizations of a stochastic model and evaluated with physical simulations. In that way, materials can be optimized for specific use cases, without constructing expensive prototypes or performing mechanical experiments. In order to design a practically fabricable material, the stochastic model is first adapted to an existing material and then slightly modified. The virtual reconstruction of the existing material requires a precise knowledge of the geometry of its microstructure.

The first part of this thesis describes a fiber quantification method by the means of local measurements of the fiber radius and orientation. The combination of a sparse chord length transform and inertia moments leads to an efficient and precise new algorithm. It outperforms existing approaches with the possibility to treat different fiber radii within one sample, with high precision in continuous space and comparably fast computing time. This local quantification method can be directly applied on gray value images by adapting the directional distance transforms on gray values. In this work, several approaches of this kind are developed and evaluated.

Further characterization of the fiber system requires a segmentation of each single fiber. Using basic morphological operators with specific structuring elements, it is possible to derive a probability for each pixel describing if the pixel belongs to a fiber core in a region without overlapping fibers. Tracking high probabilities leads to a partly reconstruction of the fiber cores in non crossing regions. These core parts are then reconnected over critical regions, if they fulfill certain conditions ensuring the affiliation to the same fiber.

In the second part of this work, we develop a new stochastic model for dense systems of non overlapping fibers with a controllable level of bending. Existing approaches in the literature have at least one weakness in either achieving high volume fractions, producing non overlapping fibers, or controlling the bending or the orientation distribution. This gap can be bridged by our stochastic model, which operates in two steps. Firstly, a random walk with the multivariate von Mises-Fisher orientation distribution defines bent fibers. Secondly, a force-biased packing approach arranges them in a non overlapping configuration. Furthermore, we provide the estimation of all parameters needed for the fitting of this model to a real microstructure.

Finally, we simulate the macroscopic behavior of different microstructures to derive their mechanical and thermal properties. This part is mostly supported by existing software and serves as a summary of physical simulation applied to random fiber systems. The application on a glass fiber reinforced polymer proves the quality of the reconstruction by our stochastic model, as the effective properties match for both the real microstructure and the realizations of the fitted model.

This thesis includes all steps to successfully perform virtual material design on various data sets. With novel and efficient algorithms it contributes to the science of analysis and modeling of fiber reinforced materials.

KEYWORDS: Fiber Quantification, Single Fiber Separation, Stochastic Modeling, Physical Simulation, Directional Distance Transform, Inertia Moments, Random Walk, Force-Biased Packing, Parameter Estimation.

Danksagungen

Als erstes möchte ich mich bei meinen Betreuern bedanken: Dominique Jeulin, Katja Schladitz und Ralf Korn. Es war mir eine große Ehre an Ihrer Seite zu arbeiten und von Ihrem reichhaltigen Wissen zu profitieren. Besonders dankbar bin ich Dominique Jeulin für sein herausragendes Engagement als Betreuer, seine zahlreichen Tipps und Wegweisungen, aber auch für seine persönliche Art. Ich danke weiterhin Joachim Ohser und Jean-Michel Morel für das Interesse an meiner Arbeit und die Großzügigkeit, den Auftrag als Gutachter zu akzeptieren, und Karam Sab als Präsident der Jury.

Den Erfolg meiner Doktorarbeit habe ich auch viel meinen Kollegen zu verdanken, die mir bei zahlreichen Problemen immer hilfreich zur Seite standen und mir mit ihrer Heiterkeit den Arbeitsalltag versüßten. Danke also an alle Mitarbeiter des CMM und der BV-Gruppe des Fraunhofer ITWM, ganz besonders an die Kollegen, die mit mir ein Büro teilten: Rebekka Malten, Michael Godehardt, Matthieu Faessel, Charles Peyrega und Serge Koudoro. Rebekka danke ich darüber hinaus für unsere gemeinsame Zeit in Fontainebleau, und dafür, dass sie mich davon überzeugt hat, diese Fahrt überhaupt anzutreten. Anderenfalls wäre diese Arbeit wohl so nie entstanden.

Ein großes Dankeschön für die Unterstützung bei technischen Problemen und wissenschaftlichen Fragen geht an Stephan Didas, Björn Wagner, Oliver Wirjadi, Claudia Redenbach, Martin Braun, Christophe Clienti, Etienne Decencière, François Willot und Michel Bilodeau. Außerdem danke ich meinem Chef Ronald Rösch mit dem ich einige Messen verbracht habe und der sich immer für mich eingesetzt hat. Ganz besonders herzlich danke ich auch Catherine Moysan, die mit ihrem Einsatz weit über ihre Aufgaben hinaus ging und immer einen Weg fand, meine oft sehr ausgefallenen Probleme zu meistern. Sie ist die Perle des CMM, ohne die hier nichts laufen würde.

Vielen Dank auch an Alexander Rack der mir bei einem Besuch am ESRF in Grenoble die Aufnahmetechniken näher gebracht hat und mich des öfteren hilfreich unterstützt hat, sei es mit interessanten Artikeln oder auch mal einem Film für zwischendurch.

Ein großes Dankeschön an alle Freunde, die diese Zeit mit mir geteilt haben – auf zahlreichen Feten, bei Kinobesuchen, in Restaurants und auch bei sportlichen Aktivitäten. Ganz besonders danke ich Jean Stawiaski, der mich in der gesamten Doktorandenzeit in jeder erdenklichen Art und Weise unterstützt hat. In professioneller Sicht für die Mithilfe bei den französischen Übersetzungen und der eleganten Formulierung einiger Paragraphen. Aber vielmehr danke ich ihm für die vielen aufbauenden Worte und das Ertragen meiner – gegen Ende – doch häufigen Stimmungswechseln. Auch an Edy und Francine Stawiaski ein großes Dankeschön für Ihre herzliche Gastfreundschaft und die Verköstigungen bei meiner Verteidigung.

Mein größter Dank geht an meine Eltern, Helga und Hans-Walter Altendorf, die mich stets motivierten mein Bestes zu geben und mich auf diesem langen Weg immer unterstützten. Ohne sie wäre ich sicherlich nie so weit gekommen. Ich danke auch meinen Großeltern, Anna Obenauer, Maria und Johannes Altendorf, für ihre liebevolle Sorge und Teilnahme an all meinen Aktivitäten. Dafür habe ich heute die Ehre, diese Doktorarbeit meiner Familie zu widmen und mich für all das zu bedanken, was sie die vergangen Jahre für mich getan haben und immer noch tun.

Table of Contents

Preface i

Abstract iii

Danksagungen v

Table of Contents vii

1. Introduction 1

2. Materials & Imaging 5
- 2.1. Imaging 5
  - 2.1.1. Micro Computed Tomography (µCT) 6
  - 2.1.2. Synchrotron Radiation 7
  - 2.1.3. Second Harmonic Generation (SHG) 8
  - 2.1.4. Scanning Electron Microscopy (SEM) 8
  - 2.1.5. Scanning Acoustic Microscopy (SAM) 9
- 2.2. Materials 9
  - 2.2.1. Glass Fiber Reinforced Polymer (GRP) 9
  - 2.2.2. Carbon Fiber Reinforced Polymer (CRP) 10
  - 2.2.3. Ultra-High Performance Concrete (UHPC) 11
  - 2.2.4. Collagen Fibers in a Hydrogel Matrix 13

I. Image Analysis for Fiber Quantification 15

3. Local Orientation and Radius Analysis 17
- 3.1. Preprocessing 18
- 3.2. Analysis on Binary Images 20
  - 3.2.1. Inertia Axes of Directed Distance Transform 20
  - 3.2.2. Deviation in the Orientation Estimate and its Correction 22
  - 3.2.3. Radius Estimation 25
  - 3.2.4. Improvement by Adaptive Smoothing 27
  - 3.2.5. Application 27
  - 3.2.6. Evaluation and Comparison on Synthetic Images 27
- 3.3. Analysis on Gray-Value Images 35
  - 3.3.1. Quasi Distance Transform 35
  - 3.3.2. Maximal-Mean Gradient 36
  - 3.3.3. Classification into Foreground and Background 38
  - 3.3.4. Alternative Approaches 39
  - 3.3.5. Comparison of the Different Approaches on a Gray Value Line 40
  - 3.3.6. Comparison of the Different Approaches on a 2D Slice 42
  - 3.3.7. Application 46

4. Presentation and Interpretation of the Local Information 51
4.1. Visualization of Direction Map . . . 51
4.1.1. 2D Colorization . . . 51
4.1.2. 3D Colorization . . . 52
4.2. Estimation of Empirical Distribution Densities . . . 52
4.2.1. Number-, Length- and Volume-Weighted Distributions . . . 53
4.2.2. Radius Distribution . . . 56
4.2.3. 3D Orientation Histograms . . . 57

5. Single Fiber Separation 69
5.1. Probability Maps . . . 70
5.1.1. Probability from Mean Filter with Adapting Structuring Element . . . 70
5.1.2. Probability from Mean Filter with Propagating Structuring Element . . . 72
5.1.3. Probability from Euclidean Distance Transform . . . 73
5.1.4. Comparison of Different Approaches . . . 74
5.2. Core Parts . . . 74
5.2.1. Initializing Core Parts . . . 76
5.2.2. Expanding Core Parts . . . 76
5.2.3. Reconnecting Core Parts . . . 77
5.2.4. Reconnection Graph . . . 77
5.3. Application on Synthetic Images . . . 78
5.4. Application on Real Datasets . . . 78
5.5. Conclusion . . . 79

II. Stochastic Modeling and Physical Simulation 81

6. Stochastic Modeling 83
6.1. Orientation Distributions . . . 85
6.1.1. von Mises-Fisher Distribution . . . 86
6.1.2. multivariate von Mises Fisher Distribution . . . 88
6.1.3. β Distribution . . . 88
6.1.4. Variations of the von Mises Fisher distribution . . . 89
6.2. RSA and Cherry-Pit Fiber Model . . . 90
6.3. Random Walker . . . 91
6.4. Force Biased Fiber Packing . . . 93
6.4.1. Repulsion Force . . . 94
6.4.2. Recover Force . . . 94
6.4.3. Application of Force . . . 96
6.4.4. Stop Criterion and End Step . . . 96
6.4.5. Implementation Details . . . 98
6.4.6. Realizations . . . 98
6.4.7. Discussion . . . 101
6.4.8. Conclusion and Perspectives . . . 105
6.5. Placing Strategy . . . 105
6.6. Parameter Estimation . . . 108
6.7. Statistics . . . 112
6.7.1. Orientation Covariance . . . 113
6.7.2. Tortuosity . . . 117

7. Physical Simulation 119
7.1. Linear Elasticity . . . 119
7.1.1. Isotropy . . . 120

7.1.2. Transverse Isotropy . . . 120
7.1.3. Orthotropic Materials . . . 122
7.2. Conductivity . . . 123
7.3. Simulation via the FFT-based method . . . 123
7.4. Bounds for Effective Properties . . . 125
7.5. Representative Volume Element . . . 126

III. Application 129

8. Application of the Overall Process on a Glass Fiber Reinforced Polymer 131
8.1. Presentation of the Sample . . . 131
8.2. Local Radius and Orientation Analysis . . . 133
8.3. Single Fiber Separation . . . 135
8.4. Stochastic Modeling . . . 138
8.5. Physical Simulations . . . 140
8.5.1. Verification of the Symmetry Cases . . . 140
8.5.2. Results for the Mechanical and Thermal Responses . . . 143
8.5.3. Calculation of the Representative Volume Element . . . 149
8.6. Conclusion . . . 155

9. Conclusion and Perspectives 157
9.1. Contributions . . . 157
9.2. Perspectives . . . 158

A. Calculation of Theoretical Inertia Moments 161

B. Publications 165
B.1. Articles - Journals and Conference Proceedings . . . 165
B.2. Presentations and Conferences . . . 166

C. Curriculum Vitae 169

Bibliography 171

1

Chapter 1.

Introduction

The increasing interest in fibrous materials expands to a large variety of use cases. The most common fiber-reinforced polymers are currently contained in the enclosure of aircrafts, boats, and cars; furthermore, wound-disinfection tissues and thermal insulations make also use of fibrous media. The macroscopic physical properties of these materials are highly influenced by the fiber geometry, in particular by the orientation distribution of the fibers. This thesis is motivated by the demand for a detailed analysis of such materials, which is based on image analysis, stochastic modeling and physical simulation.

The final goal of our studies is to optimize the physical properties of the material by adapting the microstructure respectively. This process is called “virtual material design“. The aim is to create virtually new innovative materials with optimal physical properties in order to propose their structure and design before they are practically available. This approach replaces expensive prototypes and mechanical experiments. Hence, the costs of development can be substantially reduced with the help of numerical simulation. To this end a realistic stochastic model is created and fitted to a particular material using image analysis techniques.

This work includes three main parts:

- 3D image analysis of micro computed tomography datasets for fiber quantification,
- stochastic modeling and simulation of the physical properties,
- an application of the overall process on a particular glass-fiber reinforced polymer.

Image Analysis for Fiber Quantification. We first present some image analysis methods developed in order to locally analyze and segment single fibers in 2D or 3D datasets. This first task consists basically in automatically recognizing and tracking fibers with a circular cross section. Our solution for local analysis is based on the stereological idea that a cylindrical shape is well-defined by the knowledge of one dimensional cuts in several directions. This knowledge is derived from a directional distance transform in a fixed amount of orientations (4 in 2D and 13 in 3D). The main inertia axis of the endpoints, given by the local centralized chords, provide an estimate of the local orientation. In contrast to most of the existing approaches, our method does not require a fixed fiber radius, moreover it computes the local fiber radius. Furthermore, we study how to optimize the measurements by an orientation correction (due to directional sampling error) and an adaptive smoothing based on a weighting with the ratio of inertia moments.

This method can be extended to operate directly on gray level images, by replacing the distance transform (on binary images) with a similar method on gray value images. Different approaches are developed and evaluated within this thesis. The thresholded quasi distance and the maximal-mean gradient have proven to be the most stable approaches in practical use. This first processing step permits to obtain accurate orientation and radius measurements on various images including 2D and 3D, binary and gray level images.

In Chapter 4, we study the visual representation of the local radius and orientation maps. In 2D, the orientation information reduces to an angle that can be visualized by a color on a periodic rainbow spectrum. In the 3D case, one can imagine a similar coloring of the surface rendering of fibers. Still, the task of mapping a three-dimensional orientation to a color space is in fact quite complex. We developed an adequate mapping for a certain amount of orientations of interest. However, a general color mapping, taking into account all possible orientations on the unit sphere without assigning two independent orientations to the same color, remains in the perspectives of this work. Furthermore, we describe how empirical distributions can be estimated from the map of local measurements. Describing an orientation distribution is equivalent to computing a density function on the unit sphere, which raises a non trivial task. An empirical orientation distribution can be presented as a histogram on the unit sphere, which requires a regular tessellation of the sphere surface. We study and describe some existing approaches and propose a new efficient tessellation algorithm. Classical tessellations are based the Voronoi mosaic of a certain amount of well placed points on the sphere, which implies a comparison of the distances to all points in order to assign an arbitrary orientation to its Voronoi cell. Our tessellation permits a direct classification of any arbitrary orientation and a refinement of the tessellation by one parameter.

Chapter 5 proposes a new approach to separate and track single fibers in a binary image. The method is based on probability maps, indicating for each pixel the probability that it belongs to a fiber core in a region without overlapping fibers. Parts of the fibers are then reconstructed by tracking high probabilities and later on pairs of core parts are reconnected over the critical regions, if they affiliate to the same fiber.

At the end of this first part of the thesis, we are able to efficiently analyze real fibrous materials and synthesize useful information needed for the steps of modeling and the physical simulations.

Stochastic Modeling and Physical Simulations. There exist several stochastic models in the literature: systems of straight non overlapping fibers, systems of overlapping bending fibers, or fiber systems created by sedimentation. However, there is a lack of models providing dense, non overlapping fiber systems with a given random orientation distribution and a controllable level of bending. The limitation of volume fraction in non overlapping systems is closely linked to the problem of computing a packing of predefined rigid shapes. In Chapter 6, we introduce a new stochastic model that generalizes the force-biased packing approach to fibers represented as chains of balls, which have a flexible behavior during the packing process. The starting configuration is modeled using random walks, where two parameters in the multivariate von Mises-Fisher orientation distribution control the bending. The fibers can be placed intelligently by evaluating the overlap at several placements. The final fiber configuration is obtained as an equilibrium between repulsion forces avoiding crossing fibers and recover forces ensuring a correct fiber structure. This approach provides high volume fractions up to 72%. Furthermore, we study the estimation of the parameters included in the stochastic model. We developed a new estimator for the von Mises-Fisher distribution parameter κ, that works out to have more stable and less biased estimates than the known one. Moreover, we develop an approximation of the parameters in the multivariate von Mises-Fisher distribution used for the random walk.

In Chapter 7, we recall the theory of physical simulation based on homogenization using the FFT method. Two main physical properties are tested for the real material and the model realizations:

the linear elasticity and thermal conductivity. Furthermore, we recall the bounds for the effective properties and explain how the representative volume element can be calculated.

Application Finally in Chapter 8, we apply the overall process of virtual material design to a sample of a glass fiber reinforced polymer. The local fiber radii and orientations are quantified on the binary image. Furthermore, we separate single fibers with the algorithm proposed in Chapter 5. The reconstructed fiber system yields the possibility to estimate the parameters for the stochastic model. Two kinds of stochastic models are taken into account: the force-biased fiber packing presented in Chapter 6 and the classical Boolean model of cylinders. With that knowledge, we create realizations of the stochastic models with the same parameters as well as realizations with slightly modified parameters. From physical simulations, we observe the effective properties of the virtually created material and we evaluate the different microstructures. The effective properties of the real microstructure and the realizations of our stochastic model match, which proves the quality of the fitted stochastic model.

2

Chapter 2.

Materials & Imaging

Originally this work was dedicated to the application of three dimensional images of glass fiber reinforced polymer acquired with micro computed tomography (µCT) using either laboratory-based X-ray sources or hard synchrotron radiation. This application fixed some basic assumptions about the material, as e.g. fibers with a spherical cross section and low to medium bending. Furthermore, the resolution is assumed to be high enough to sample a fiber radius with at least two pixels. During several projects, the algorithms were tested on various applications as for example collagen fibers in a hydrogel, imaged by second harmonic generation (Altendorf *et al.*, 2011). We can generalize that the algorithms are applicable in a large field of materials and imaging techniques as long as the basic assumptions are respected. In this chapter, we present some of the materials, we worked with, and briefly recall some imaging techniques.

2.1. Imaging

Traditionally, imaging and quantification of a material microstructure was based on 2D section images. These techniques are still in use and adequate for planar structures. When it comes to random fiber systems, the fiber orientations in 3D are essential for the behavior of the material. It is nowadays possible to achieve directly images of the three dimensional structure via second harmonic generation or micro computed tomography using either laboratory-based X-ray sources or hard synchrotron radiation. All of these methods have the great advantage to be non invasive and non destructive, at least to some extent.

Still, for some application on materials with mainly planar fiber distributions, 2D imaging (as scanning electron microscopy (SEM) or scanning acoustic microscopy (SAM)) may be sufficient or simply chosen to reduce costs. Those imaging techniques, taking surfacial images, have the disadvantage that fibers are overlapping, which poses some problems in the analysis part as fibers are cut in several part. One consequence is that border artifacts increases. Furthermore, fibers from lower levels are shining through, while lying out of focus, which biases in general analysis results.

Further imaging techniques, that are not described here in detail are the phase contrast CT, confocal laser scanning microscopy, electron tomography or FIB-tomography. The chosen technique needs to respect the requirements of the analysis approach: The algorithms presented in this work assume fibers with a gray value (on the whole fiber volume) differing from the one of the matrix (e.g. white fibers on black background or vice versa). This assumption already rules out phase contrast techniques on composites with similar absorption coefficient, as the object boundaries show the contrast, whereas the object volume does not. Furthermore, the imaging technique needs to be chosen with respect to the material, that induces a certain resolution (that samples the fiber radius with at least two pixels).

2.1.1. Micro Computed Tomography (µCT)

The general scheme of computed tomography is to illuminate a sample with penetrating radiation and to detect the transmitted beam downstream of the object. Frequently, these images present the projection of the X-ray absorption. Figures 2.1(a) and 2.1(b) show a sketch of the assembly for µCT imaging and the projection of an object. The projections represent line integrals of the 3D microstructure. By rotating the table, on which the sample is positioned, different angles of the material are imaged. The inner mass distribution of the object can be reconstructed by an inversion of the so-called Radon transformation. Different approaches for the latter exist. Typically, the filtered-back projection is used in parallel beam geometry. A micro computed tomograph operates commonly a X-ray source with a spot size in the micrometer range. Achievable spatial resolution can reach up to 1 µm. The great advantage of those systems is that they achieve high resolutions of the full 3D microstructure without destroying the specimen. The technique is called non destructive as the imaging does not include cutting apart the sample, but there are some limitations in time and energy. The ionized radiation has well known side effects on living tissue and also on chemical bonds: long molecules are being cracked, which results in a color falsification (as e.g. bleaching or glass getting brown or enamel getting black). For more details on computed tomography, see Banhart (2008) and Stock (2008).

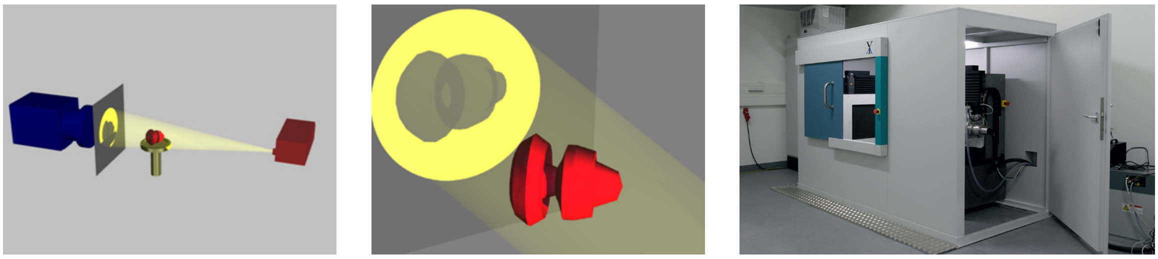
(a) (b) (c)

Figure 2.1.: Sketch of a cone beam computed tomography and image of µCT at Fraunhofer ITWM in Kaiserslautern. (a) Assembly of computed tomography, with X-ray source on the right, the specimen on the rotating table in the middle and the detector on the left. (b) Projection of the X-ray absorption of the red specimen. (c) Industrial µCT at the Fraunhofer ITWM in Kaiserslautern.

The X-ray light was discovered by Wilhelm Conrad Röntgen in 1901, who received the Nobel Prize in Physics. The reconstruction from integral values was already published by Johann Radon in 1917, but rediscovered for the 3D reconstruction of X-ray projections not until 1963 due to Allan C. Cormack. The first CT for human skulls was performed in 1967 by Godfrey N. Hounsfield. In the following years, resolution and accuracy was essentially increased and the application was expanded to material inspection. The first X-ray micro tomography system was conceived and built by Jim Elliott in the early 1980s.

Nowadays, small industrial computed tomographs are available for large-scaled enterprises. For small-medium enterprises, e.g., specialized on the development of new material systems, operating a micro tomography facility is frequently to cost intensive. Consequently, they subcontract such kind of analysis, e.g. to a research institute like the Fraunhofer ITWM, where a system for 3D micro computed tomography is available (see Figure 2.1(c)). It is suitable for non-destructive analysis of various materials such as foams, fibrous materials, polymer composites, metals, ceramics or concrete. The technical specification of an industrial µCT, as it is available at the Fraunhofer ITWM in Kaiserslautern, is a X-ray tube of 225 kV, two X-ray detectors for high and low absorbing materials (low and high energies). The size of specimens can vary from $1 - 100\,\mathrm{mm}$ cube side length. Larger objects, whose size exceeds the detector field of view in one dimension, can be imaged by stacking tomographic scans. The nominal resolution reaches from 1 to 70 µm voxel side length for images with image sizes up to 2048^3 voxels.

2.1.2. Synchrotron Radiation

A synchrotron is a cyclic particle accelerator, where a synchronized magnetic and electric field accelerate a particle beam in a ring shaped path. The ring energy varies up to 8 GeV. Particles are injected with a substantial energy from a linear accelerator inside the main ring. Synchrotron radiation is based on acceleration of charged particles, i.e. electrons (similar to a dipole antenna), which can be released at several beam lines outside the ring. The relativistic speeds of the electrons result in an emission characteristic tangential to the flight direction: a synchrotron beam propagates nearly parallel in only one direction. Frequently, the radiation passes metal attenuators (to absorb low energy X-rays) and a monochromator. A focusing option can be accessible as well. The emitted photon flux density is intense enough to achieve high resolution images depicting features down to the nanometer scale. Figure 2.2 shows a sketch of the synchrotron light source Soleil, located in Paris (France). Examples of synchrotron images are illustrated in Figures 2.4(a) and 2.5(a).

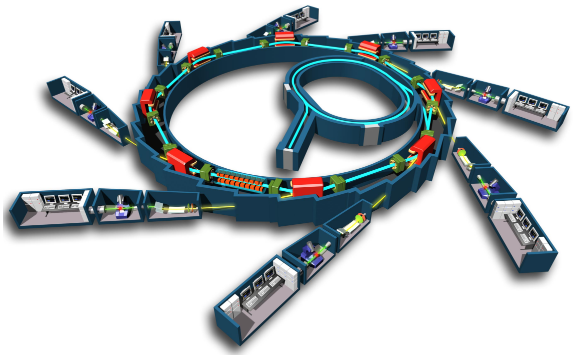

Figure 2.2.: Sketch of the synchrotron light source Soleil, located in Paris (France). The inner circular ring is the actual synchrotron, where electrons are accelerated close to the speed of light. The outer ring is the storage ring where the accelerated electrons are injected when they reached there final speed. The stored electrons in the ring emit "synchrotron radiation" when they pass with their relativistic speed a magnetic field. Depending on the speed and the magnetic field, the wavelength can range from infrared to the hard X-ray regime. The radiation is delivered to the different beamlines (the straight lines branching out of the synchrotron). Each beamline contains scientific instruments, experiments etc. and receives an intense beam of radiation.
Source: Synchrotron Soleil, 18^{th} october 2005, © EPSIM 3D/JF Santarelli, Synchrotron Soleil.

Compared to laboratory X-ray sources, synchrotron radiation offers a significant improvement with its nearly parallel beam propagation, a flux which is several orders of magnitudes higher and the possibility to work with a monochromatic beam (Rack, 2006, Rack *et al.*, 2008). These advantages lead to higher reconstruction qualities, fewer artifacts from beam hardening, shorter acquisition times and improved contrast. With the additional use of X-ray optics to focus the beam, X-ray images with a spatial resolution well below 100 nm can be acquired.

In the scope of this thesis, images were received from the European Synchrotron Radiation Facility ESRF in Grenoble, from the Angströmquelle ANKA in Karlsruhe and from the electron storage ring BESSY in Berlin. X-ray imaging using synchrotron light sources was suggested for the first time in

1980 (Spiller, 1980). The first observation of synchrotron light in a laboratory environment dates back to the 1950s.

2.1.3. Second Harmonic Generation (SHG)

Second harmonic generation (SHG) microscopy is a nonlinear optical process first demonstrated by P. A. Franken, A. E. Hill, C. W. Peters, and G. Weinreich at the University of Michigan, Ann Arbor, in 1961. Laser light is emitted from a source and focused with non linear crystals. The resulting intense laser light is entering the material and non centrosymmetric molecular structure can emerge second harmonic light, which is specified by half wave length and double frequency of the incident light. The pattern of this second harmonic light is detected by a laser scanning microscope. Non centrosymmetric materials are e.g. biological materials such as collagen, microtubules, and muscle myosin. This imaging technique is also non invasive and non destructive and can even be applied in vivo on living animals. SHG produces optical microscopical images with high resolutions up to 200 nm. Figure 2.3 shows a sketch of the optical chain for SHG microscopy. Examples of SHG images are illustrated in Figure 2.7(a)

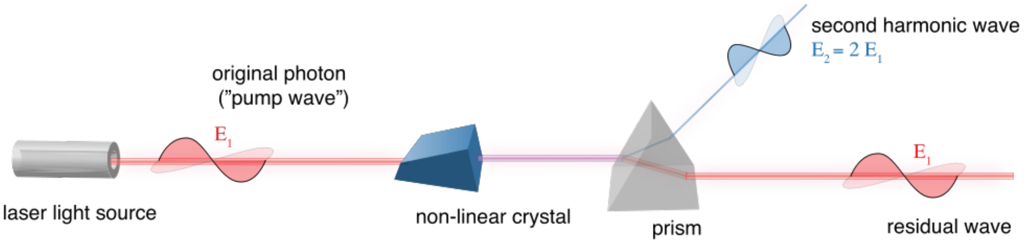

Figure 2.3.: Second-harmonic generation (SHG), also known as frequency-doubling, a non-linear optical process. Source: Jkwchui, Date: 8th january 2011

SHG has been shown to provide highly contrasted 3D images of fibrillar collagen in unstained biological tissues (Campagnola *et al.* (2002), Matteini *et al.* (2009), Pena *et al.* (2007), Strupler *et al.* (2008, 2007), Sun *et al.* (2008), Zipfel *et al.* (2003a)) and in engineered tissues (Bayan *et al.* (2009), Bowles *et al.* (2010), Pena *et al.* (2010), Raub *et al.* (2008)). SHG is indeed a coherent multiphoton process that is specific for dense and aligned structures, such as fibrillar biopolymers (collagen fibrils, myosin thick filaments, microtubules, etc.). It exhibits intrinsic 3D resolution like other multiphoton microscopies and offers increased penetration in scattering tissues compared to confocal microscopy (Zipfel *et al.* (2003b)). Quantitative analysis of SHG images have been reported and aimed at quantifying the density or porosity of the collagen fibrillar network and the directional distribution of the fibrils (Bayan *et al.* (2009), Bowles *et al.* (2010), Matteini *et al.* (2009), Pena *et al.* (2007, 2010), Raub *et al.* (2008), Strupler *et al.* (2008, 2007), Sun *et al.* (2008)). SHG microscopy has the capability to access the 3D architecture of collagen fibrils at a scale finer than 1 µm.

2.1.4. Scanning Electron Microscopy (SEM)

Scanning Electron Microscopy (SEM) is based on an electron microscope. A surface is scanned with a high-energy electron beam in a raster pattern. The electron beam is in general created by heating a filament cathode, which results in electron emission with an energy from 0.5 keV to 40 keV. The electron beam passes condenser lenses, pairs of scanning coils or pairs of deflector plates and typically through a final lens, which diffuses the beam into a rectangular raster pattern. The electrons interact with the material in several ways: there are secondary emitting electrons, back scattered electrons, characteristic X-ray light, specimen current and transmitted electrons. Only parts of these effects are captured. Secondary electron detectors are standard for all SEM, further detectors are optional. The resolution of SEM is extremely high and can reach values finer than 1 nm. The first SEM image was obtained by Max Knoll in 1935.

This imaging technique can only be applied to material with a electrically conductive surface. If this is not the case, materials are coated ultra thinly with electrically-conducting material, commonly gold. Furthermore, for porous material it happens often that structures from a secondary or tertiary layer are shining through and thus are also captured by the microscope even if they are out of focus. This fact often complicates the analysis of the resulting images as the secondary objects are diffuse, but are difficult to blank out.

To get a representative analysis of a material it is not sufficient to analyze the surface, but also the inside of a material. For SEM imaging, the material can be iteratively analyzed by cutting off thin slices and imaging the appearing surfaces in 2D images. This technique destroys the material and it happens (mostly for porous materials) that the specimen does not stand the cutting process, which may result in a destroyed surface, that does not reflect the actual material.

2.1.5. Scanning Acoustic Microscopy (SAM)

Scanning Acoustic Microscopy (SAM) is based on a focused sound from a transducer. Similar to the SEM, there are several interactions of the sound with the surface: the sound is either scattered, absorbed, reflected or transmitted. A detector on a certain position detects the scattered pulses traveling in a certain direction. The distance to the objects is determined by the time when a sound arrives at the detector. The image is taken iteratively with a slight change of the source position. This results in a 2D relief of the material surface, which means a distance information for each point in a 2D image.

The resolution of the image reaches down to 1 µm and is limited by the physical scanning resolution and the width of the sound beam. This imaging technique is non destructive and often used to detect cracks in a material. The first scanning acoustic microscope was developed in 1974 by R. A. Lemons and C. F. Quate at the Microwave Laboratory of Stanford University (Lemons & Quate, 1974).

2.2. Materials

The essential assumptions for our approaches are a spherical cross section of the fibers and a fiber radius relatively large, that it can be sampled with at least two pixels by the chosen imaging technique. Further properties as a extreme high level of bending and high density can also influence the quality of the results, but are not generally limited. In the following, we present some typical applications for our algorithm, that were tested in the scope of these studies.

2.2.1. Glass Fiber Reinforced Polymer (GRP)

Glass fiber reinforced polymer (GRP) consists of a plastic matrix reinforced with thin glass fibers. The plastic matrix may be epoxy, polyester, vinylester or thermoplastic. In order to achieve the extreme strength, known for GRP materials, the glass fibers used to reinforce the matrix need to be free of defect. Full glass material without any defects would have the same strength, but in contrast to glass fibers it is practically impossible to build defect free full glass materials.

There are various ways to inject the glass fibers in the plastic matrix: pultrusion (fibers are pulled trough a liquid bath of polymer, which is then dried out in a heating process), filament winding, gun roving (glass fibers are cut into short lengths and dropped into a jet of resin and positioned onto the surface of a mold), chopped strand mat (made of randomly oriented short fibers), woven fabrics, knit fabrics or uni-directional fabrics.

The main properties of GRP are light weight, extreme strength, and robustness. In comparison to carbon fiber reinforced polymers, the GRP has lower strength and it is less stiff. Still, the GRP is typically far less brittle, and the raw materials are much less expensive. A GRP is stiff and strong in tension and compression along the mean fiber axis. In other directions (orthogonal to their principal axis) the glass fiber is neither stiff nor strong with respect to shear. Therefore, the orientation distribution of the fibers plays a centered role for its physical behavior.

Common uses of GRP include boats, automobiles, baths, hot tubs, water tanks, roofing, pipes, cladding and external door skins. For more details see Mayer (1993) or East Coast Fibreglass Supplies (2010).

Figure 2.4 shows a GRP sample from R. Velthuis (IVW Kaiserslautern) recorded by A. Rack, J. Goebbels at the BAMline (BESSY II, Berlin, Germany) with a resolution of 3.5 µm. We present two slice cuts of the original gray valued image and a surface rendering of the binarization.

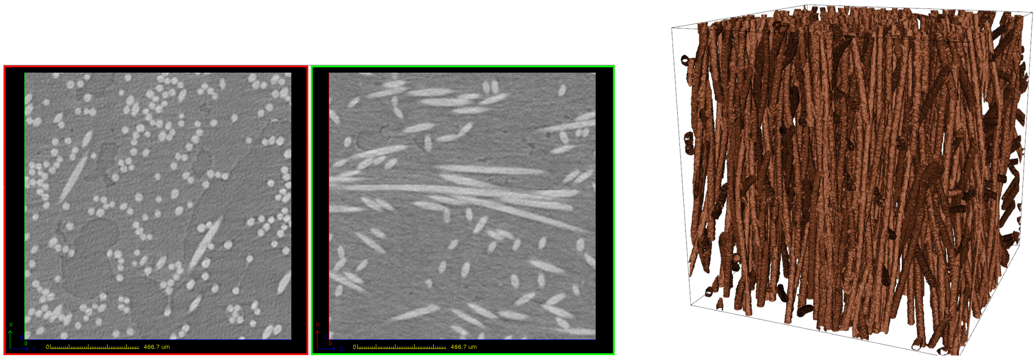

(a) Slice cut of original gray-value image.

(b) Surface Rendering of binarized image.

Figure 2.4.: GRP sample from R. Velthuis (IVW Kaiserslautern) recorded by A. Rack, J. Goebbels at the BAMline (BESSY II, Berlin, Germany) with a resolution of 3.5 µm.

2.2.2. Carbon Fiber Reinforced Polymer (CRP)

Carbon fiber reinforced polymer (CRP) is a very strong and light material, that was invented in 1968 as the new steel (International, 1968, Peters, 1968). It received the name new steel as it has several times the strength of steel, but only a quarter of its weight. Therefore, it was initially used to replace steel modules and thus very interesting for the aerospace industry. The fabrication of this material is relatively expensive, thus its application is limited to cases, where its strength-to-weight ratio and good rigidity is important. The traditional application was in aerospace and automotive fields as well as in sailboats. Nowadays, the applications are also spread to small consumer goods: laptops, tripods, fishing rods, paintball equipment, archery equipment, racket frames, stringed instrument bodies, classical guitar strings, drum shells, golf clubs, and pool/billiards/snooker cues.

The fabrication process of CRP varies, depending on the piece being created. Standard processes are: molding (where fibers form a random mat in the resin), wound continuous filaments, lamination (thin laminations of unidirectional sheets), vacuum bagging or compression mold (of different materials). Figure 2.5 shows an example for a CRP made of different unidirectional layers. Also the choice of the matrix can have an effect on the physical properties of the finished composite. The polymer is most often epoxy, but also polyester, vinyl ester or nylon, are sometimes used. For further details see (Department of Polymer Science at University of Southern Mississippi, 2005).

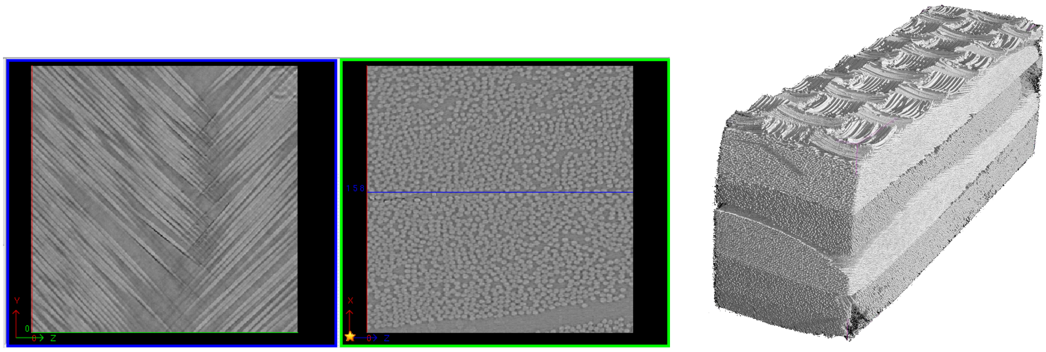

(a) Slice cut of original gray-value image.

(b) Complete specimen.

Figure 2.5.: CRP plate imaged at ESRF Grenoble by L. Helfen (ANKA Angströmquelle Karlsruhe GmbH). The images are taken at beamline ID19 using monochromatic X-rays ($E = 25\,\text{keV}$). The distance between detector and specimen was 3 cm and the resolution is 1.4 µm.

For image processing, this kind of material sets a more difficult task as the filaments are very thin and the system is in general much denser as the fibers are laid in a unidirectional system. Thus, the resolution of the fibers reaches the limit of two pixels per fiber radius and furthermore contours between parallel fibers are not clear enough. Furthermore, the material has a low contrast of absorption between fiber and matrix material, which makes it difficult to distinguish between the two components. Commonly, we observe not single fibers but rovings of fibers that are difficile to segment.

2.2.3. Ultra-High Performance Concrete (UHPC)

Concrete is classified in normal-, high performance-, and ultra-high performance concrete (UHPC) according to its behavior in compression. One of the latest advancements in concrete technology is UHPC: a densely packed concrete material which exhibits increased mechanical performance and superior durability to normal and high strength concretes. UHPC has great potential to be used in the bridge market Ahlborn *et al.* (2008).

The official definition of UHPC is given by Association Française de Génie Civil (2002) as: UHPC is a cementitious composite material composed of an optimized gradation of granular constituents, a water-to-cementitious materials ratio less than 0.25, and a high percentage of discontinuous internal fiber reinforcement. The mechanical properties of UHPC include compressive strength greater than 21.7 ksi (ksi = kilopounds per square inch) (150 MPa) and sustained postcracking tensile strength greater than 0.72 ksi (5 MPa).

UHPC shows very brittle fracture behavior with an abrupt breakdown under compression. In order to improve the ductile behavior in compression and tension as well as to increase crack control, it can be reinforced with steel fibers. The steel fibers are usually thrown in the liquid concrete and thus they are randomly distributed in the matrix. Still, the orientation distribution of the fibers are essential for the physical behavior of the resulting composite. Therefore, this material is a potential candidate for the fiber quantification proposed in this work. Furthermore, the deformation of the fibers (e.g. the reduction in radius) in a crack is related to the load energy the fibers absorbed. Therefore, this material is a potential candidate for the fiber quantification proposed in this work.

For more details see Nawy (2001) or Schuler *et al.* (2007). Figure 2.6 show some different examples of fiber reinforced concrete.

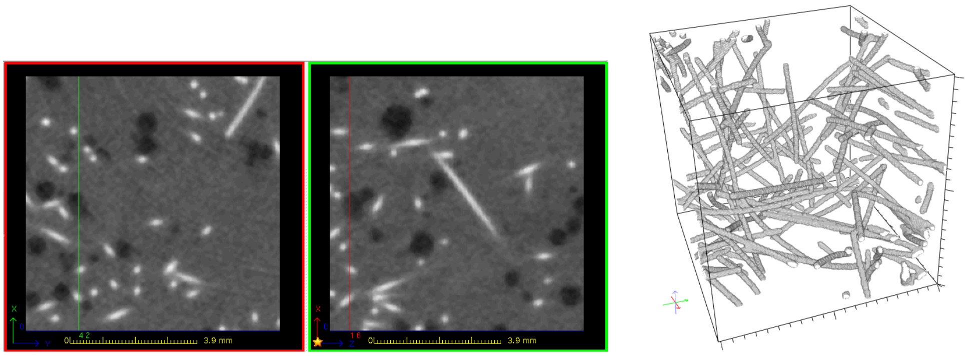

(a) Slice cut of original gray-value image.

(b) Surface Rendering

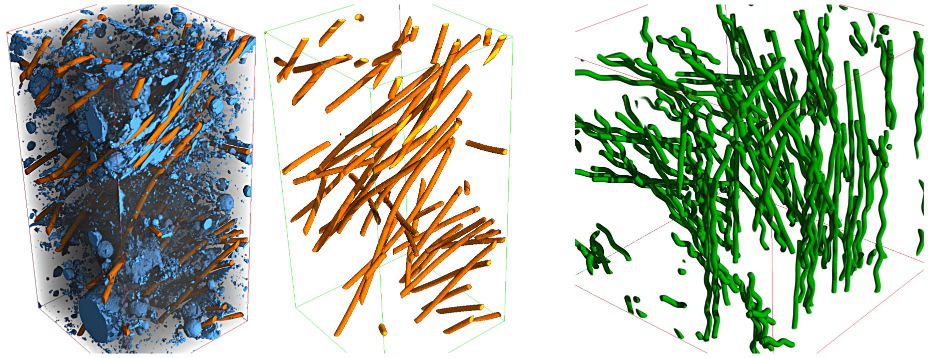

(c) Concrete with steel fibers, left with inclusions, right only fibers.

(d) Rendering of curved fibers in a SFTB concrete.

Figure 2.6.: Examples of fiber reinforced concrete.

2.2.4. Collagen Fibers in a Hydrogel Matrix

Also biological tissues can be an application for fiber quantification, as we showed in Altendorf *et al.* (2011) for collagen fibrils. In this work, the fibrils were inserted in a hydrogel matrix with the following fabrication process:

Collagen I was purified from Wistar rat-tails tendon as previously described (Gobeaux *et al.* (2007)). Purity and homogeneity of the solution were verified by SDS-PAGE electrophoresis. Collagen I diluted solutions were then concentrated by centrifugation at 14 000 g using 3 kD filters tubes (VIVASPIN 20, Sartorius). These concentrated collagen solutions were checked for their hydroxyproline amount and adjusted to 100 mg/ml. The concentrated solutions were then deposited in Teflon crucibles (3 mm wide, 5 mm long and 2 mm deep). The outer surface was gently flattened out longitudinally using a glass coverslip. Subsequently, the Teflon molds were tightened into a dialysis membrane and dipped into a phosphate-buffer saline (PBS) solution to induce the collagen fibrillogenesis and synthesize fibrillated matrices. On the basis of conditions already published (Gobeaux *et al.* (2008)), two different PBS concentrations were used to vary the size of the collagen fibrils: 50 mM and 100 mM, at pH = 7.4. After a few days, the collagen fibrillated matrices were taken off the molds and were directly plunged into the buffer solutions and stored at 4 °C until used.

Figure 2.7 shows a typical slice cut and surface rendering of collagen images taken with SHG.

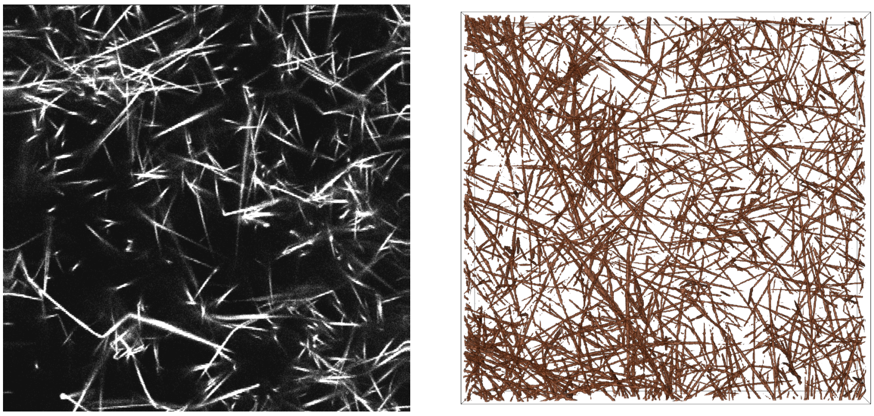

(a) Slice of original gray-value image.

(b) Surface rendering of the binarization.

Figure 2.7.: Example of Collagen. Imaged with SHG at the Ecole Polytechnique in Paris.

Part I.

Image Analysis for Fiber Quantification

3

Chapter 3.

Local Orientation and Radius Analysis

Some fabrication processes of fibrous material reinforce the matrix randomly with fibers. Therefore, the distribution of the fibers in the material is not known. In the case of post-processing, like burning and cooling or compressions, the fibers may deform in an uncontrolled way. Thus, it can happen that the fiber radii do not stay constant during the fabrication process. Still, those characteristics highly influence the physical behavior of the material in performance. The quantification of the fiber system yields the opportunity to verify the required distributions and to evaluate the quality of the material. It also helps to better understand the material forming, as we can compare the outcomes of different fabrication processes or different configurations of one process.

The imaging techniques for material samples vary from 2D surface imaging (as scanning acoustic or electron microscopy, SAM and SEM) to 3D scanning (as micro computed tomography µCT or second harmonic generation SHG). The results of those imaging techniques are 2D or 3D gray-level images, which may be filtered and segmented to binary images. We provide algorithms for binary images as well as gray-level images with a relatively good contrast. Preprocessing steps, as smoothing filters and contrast enhancement, can be applied to improve the image quality. Studies of discretization artifacts have shown that the resolution of the fiber radius should correspond to at least 2 pixels. All approaches are based on the assumption of solid fibers with circular cross sections (in the 3D structure), which is e.g. met by glass fibers. In the case of bending fibers, the analysis adapts locally to the fiber orientation.

Several methods have been proposed in the literature to deal with fiber quantification in 3D images. The chord length transform (Sandau & Ohser, 2007) works on binary images of nearly straight fibers with a significant thickness. The orientation of a foreground point is defined as one of a fixed amount of directions, having the longest chord length. The approach of the Gaussian Orientation Space (Robb *et al.*, 2007, Wirjadi, 2009, Wirjadi *et al.*, 2009) works on both binary or gray-level images with fibers of nearly constant thickness. Oriented Gaussian filters are applied with a fixed amount of directions and the local orientation in a voxel corresponds to the orientation yielding the highest filter response. The oriented Gaussian filters are highly stable to image noise, but just as the chord length transform the fixed amount of directions in 3D is limited caused by highly increasing computing times. Therefore, also the accuracy of the method is limited.

Further approaches for orientation estimation in local windows are the inertia moments (Bigun & Granlund, 1987, Reuze *et al.*, 1993), quadrature filters (Granlund & Knutsson, 1995) and the Hessian Matrix (Frangi *et al.*, 1998, Tankyevych *et al.*, 2008). All three methods (just as the Gaussian orientation space) suppose similar radii of the objects and work on gray-level images. The first two methods can also be applied on binary images. The limitation to a fixed radius restricts the application to a certain class of materials, whereas our method is applicable on various radii and even calculates the radius in the same step.

In the field of radius estimation there is the granulometry (Beucher, 2007), which considers the changes of gray values for openings of increasing size. The estimated radius is the size with the highest difference of the opening results to the next size. This approach is applicable for several kinds of objects with a significant size, as the discretization effect is high on small structuring elements. It is not precise enough for thin fibers or low resolution, as often the case in our applications.

This chapter starts with an introduction in preprocessing steps to improve the image quality or even to binarize the image, followed by the description of the fiber quantification method, beginning with the initial idea on binary images, including studies about improvement of the results and discretization artifacts. We present several ideas to generalize the method for gray-value images, we compare the approaches and explore the best choices for different use cases. Finally, we show how the resulting local orientation maps can be visualized and how distribution functions can be calculated, including studies about regular tessellations of the unit sphere.

3.1. Preprocessing

Every image brings along a certain amount of background noise according to the imaging technique, to the configuration of the imaging tool and also to the composition of the material (e.g. difference of absorption coefficients of the components for CT-imaging). It is advisable (and in some cases necessary) to apply some image processing to reduce the noise before segmenting or analyzing the microstructure.

The first step usually integrates a smoothing filter. The basic filters are the mean or Gaussian filter (with a small structuring element compared to the object size). This kind of filter smoothes over all gray values and therefore does also blur the boundaries of objects. The median filter has less blurring artifacts, however it also merges close fibers with thin contour lines. In contrast, non linear diffusion filters (Catté *et al.*, 1992, Perona & Malik, 1990, Weickert, 1998) smooth over similar gray values and enhance the contrast on boundaries. The following presentation of the diffusion filters is taken from Altendorf *et al.* (2010).

For the input image $f : I \to \mathbb{R}$, $I \subseteq \mathbb{N}^d$, the filtered image u is computed as the solution of the non linear isotropic heat conduction equation

$$\begin{aligned} \partial_t u &= \operatorname{div}\big(g(|\nabla u_\sigma|^2)\nabla u\big) \\ \partial_\nu u &= 0 \qquad \text{for all } x \in \partial I \\ u(\cdot,0) &= f. \end{aligned} \tag{3.1}$$

In this equation, $u_\sigma := K_\sigma * u$ denotes a pre-smoothed version of the data, which is received by a convolution with a Gaussian kernel K_σ with standard deviation σ. g stands for some diffusivity function and ν is the normalized vector in outer orthogonal direction. The equation introduces a time parameter $t \in \mathbb{R}_0^+$, which adjusts the level of filtering. The simplified versions of the image with varying t form a scale space with established properties of simplification (Iijima, 1962, Perona & Malik, 1990, Weickert, 1998, Weickert *et al.*, 1999, Witkin, 1983). Typical diffusivity functions are (Perona & Malik, 1990)

$$g_1(s^2) := \frac{1}{1+\frac{s^2}{\lambda^2}} \quad \text{or} \quad g_2(s^2) := \exp\left(-\frac{s^2}{2\lambda^2}\right) \quad . \tag{3.2}$$

In the application considered in this thesis we make use of g_1. The contrast parameter $\lambda > 0$ controls the preservation and enhancement of the edge contrast. Edges having a gradient norm $|\nabla u|$ higher than the value of λ are not only preserved, but even enhanced. Figure 3.1 shows an example of this

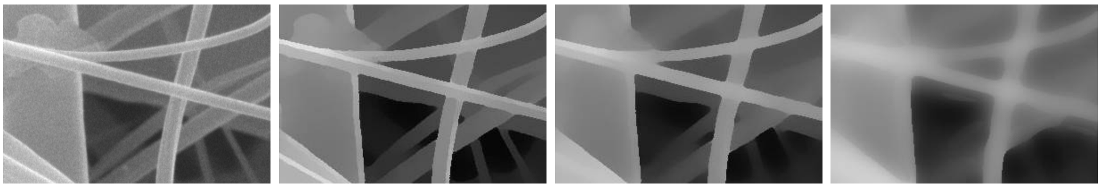

(a) Input Image (b) $\lambda = 1$ (c) $\lambda = 2$ (d) $\lambda = 5$

Figure 3.1.: Influence of the contrast parameter λ in the preprocessing by linear diffusion (fix parameters: $\sigma = 1$ and $t = 100$). The filter is applied on a cutout of a 2D SEM image of a non-woven produced with meltblown.

behavior for varying λ (all other parameters are fix: $\sigma = 1$ and $t = 100$).

This filtering reduces noise in the data and in the case of 2D SEM images, fades out blurred fibers that lie out of focus. We make us of an additive operator splitting (Weickert *et al.*, 1998), which yields efficient implementation and sufficient accuracy. Further improvement in the efficiency of the implementation are possible (Grewenig *et al.*, 2010).

Another additional possibility for datasets with a lot of background noise is the white top hat filter (Meyer, 1979, 1986), which is defined as the difference between original image and an opening $\mathrm{th}(f) = f - \gamma f$. The structuring element should be chosen slightly bigger than the largest interesting diameter of the fibers. The opening removes the fibers from the image and leaves background noise behind. After the subtraction, just the fibrous structures are left, excluding the background noise. The top hat filter can be especially useful for the approach of the maximal-mean gradient (presented in Section 3.3.2). Here, it is necessary to spread the image such that fibers are white on a black background. Generally, a linear spread between the typical foreground and background gray value can also reduce background noise in a pre-smoothed image.

For all gray level approaches presented in this work, we advise to terminate the preprocessing with a toggle mapping (Serra (1989) and Fabrizio *et al.* (2009)), also called morphological shock filter (Osher & Rudin, 1990). Every pixel receives adaptively the result of an erosion or dilation, depending on which resulting gray value is closer to the original pixel value:

$$S_B(f) \ := \begin{cases} \delta_B(f) & , \text{ for } \Delta_B f < 0 \\ \epsilon_B(f) & , \text{ for } \Delta_B f > 0 \\ f & , \text{ for } \Delta_B f = 0 \ . \end{cases} \tag{3.3}$$

B denotes the structuring element of the dilation $\delta_B(f)$ or erosion $\epsilon_B(f)$ and morphological Laplace operator

$$\Delta_B f \ := \ (\delta_B(f)) - 2f + (\epsilon_B(f)) \ . \tag{3.4}$$

We usually use an approximative ball as structuring element with a radius adapted on the fiber dimension. The resulting prefiltered images are convenient for the use of the gray value quantification methods proposed in the following sections. At the same time they yield a suitable starting point for binarization.

Generally, preprocessing needs to be chosen very carefully in order to maintain the object structure. With simple smoothing filters, it is possible that fibers are enlarged, which leads to an overestimation of the fiber radius. The non linear diffusion with reasonable parameters and the toggle mapping in general do not distort the fibers and are therefore a suitable possibility for preprocessing.

3.2. Analysis on Binary Images

In the literature, there are a lot of approaches testing different fiber orientations and choosing the one fitting the best (like the chord length transform (Sandau & Ohser, 2007)). Most of the time, more than 100 directions are sampled to achieve a sufficient precision. The idea leading to our approach is that even with much less information the geometrical object is already well defined. Mathematically, a fiber in form of an infinite cylinder in 2D can be defined by 4 variables: the orientation given by the angle $\theta \in [0, \pi)$, the radius $r \in \mathbb{R}^+$ and a point on the core line $(x, y)^T \in \mathbb{R}^2$. In 3D, the fiber is defined by 6 variables: the orientation given by a point on the upper half unit sphere $v \in S^2_+$, the radius $r \in \mathbb{R}^+$ and a point on the core line $(x, y, z)^T \in \mathbb{R}^3$. We define a d-dimensional orientation space as the upper half of the unit sphere $S^{d-1} = \{x \in \mathbb{R}^d; |x| = 1\}$:

$$S^{d-1}_+ = \{(x_1, \dots, x_d)^T \in S^{d-1};\ \exists\, i_0 \in 1, \dots, d : (x_{i_0} > 0) \wedge (x_i = 0; \forall\, i > i_0)\}. \tag{3.5}$$

Thinking of solving an equation system, we need to sample at least 4 directions in 2D and 6 in 3D. This stereological idea, to sample on differently directed lines in order to conclude to the geometric properties of the whole structure, can be applied to any evaluation method for a given direction in a given image point (e.g. the oriented Gaussian filters or the chord length transform).

This section is structured as follows: We first describe the general idea of using inertia moments to extract the fiber orientation from the sampled information. We discuss the deviation, caused by sampling few directions, and the possibility to correct it in 2D and to approximate it in 3D. The directed distances or chord lengths together with the information of the fiber orientation yield also an approximation of the fiber radius. Finally, we describe how the results can be improved by smoothing adaptively the orientation and radius maps and how the discretization influences the estimates.

3.2.1. Inertia Axes of Directed Distance Transform

In this section, we present the fiber quantification by the local orientation and radius from binary images. The algorithms are based on computing the directional distances to the background for every object point. The sampled directions of the distance transform are chosen as the complete adjacency system (in 2D 8 neighbors, in 3D 26 neighbors). For details on adjacency systems see Altendorf (2007). That means for a chosen direction vs_i, we measure the distance $d(vs_i)$ between the actual image point and the background as drafted in Figure 3.2. The chord length defined in (Sandau & Ohser, 2007) is essentially the sum of the distances of two inverse directions:

$$d_c(vs_i) = d(vs_i) + d(-vs_i). \tag{3.6}$$

A useful observation is that the chord lengths in 2D stay constant for all points inside one straight fiber (except for border effects on the ends of a fiber). This fact is shown in Figure 3.2(a), where two different points are sampled. The star of the centered chords is drafted outside the fiber to demonstrate the equality. In Figure 3.2(b), the cut of a 3D cylinder is shown, where the chords do not stay constant for two arbitrary points with different distances to the fiber core. The most reliable results are those taken near to the fiber core. Therefore, we try to approach to the fiber core by relying on the estimates at the center of mass g of the extremities. That means for a 3D image point, we calculate the center of mass:

$$g = \frac{1}{26} \sum_{i=0}^{25} d(vs_i) vs_i, \tag{3.7}$$

and continue the calculation with the distance information on that point, where we consider only the centered chord lengths. Which means the information relevant for the next steps are the extremities

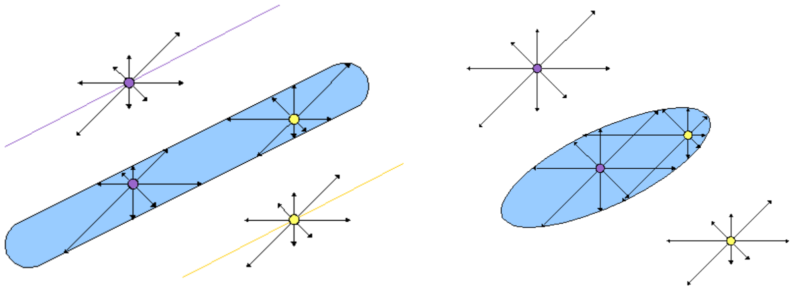

(a) Constant chord lengths in 2D.

(b) Varying chord lengths in section of a 3D fiber.

Figure 3.2.: Illustration of the constant chord lengths in a 2D fiber vs. the variation in a section of a 3D fiber. In both images chord lengths are drawn for two foreground points. The centralized chord lengths are presented additionally outside the fibers, with the main inertia axes in color.

P_i of the centered chords defined by $P_i = \frac{1}{2}d_c(vs_i) \cdot vs_i$. In the following, we will refer to the centralized distances as $d_i = \frac{1}{2}d_c(vs_i)$.

Implementation Details: The directed distance transform can be calculated efficiently following an adapted version of the algorithm introduced by (Rosenfeld & Pfaltz, 1966). We are splitting up the set of neighbors in two classes: forward and backward neighbors, according to the order in which the image will be processed. Assuming the standard storage order for a digital image, we define an order on the pixel coordinates: $p_1 < p_2 \Leftrightarrow z_1 < z_2 \vee [(z_1 = z_2) \wedge (y_1 < y_2)] \vee [(z_1 = z_2) \wedge (y_1 = y_2) \wedge (x_1 < x_2)]$. The backward neighbors are all those neighbors, which were already processed in the marching before arriving at the center pixel. If the set of all neighbors is N_c, the backward neighbors are $n_b \in N_c | n_b < \vec{0}$. The forward neighbors are those still to be processed: $n_f \in N_c \,|\, \vec{0} < n_f$. This classification is shown in Figure 3.3. To determine the directional distances in every pixel, we need to march twice through the image: the first time we process the image in forward order, while increasing the directional distances assigned to the backward neighbors; the second time we process the image in backward order, while increasing the directional distances assigned to the forward neighbors. This algorithm runs in linear time with respect to the number of image pixels. The results are 8 distance maps in 2D and 26 distance maps in 3D.

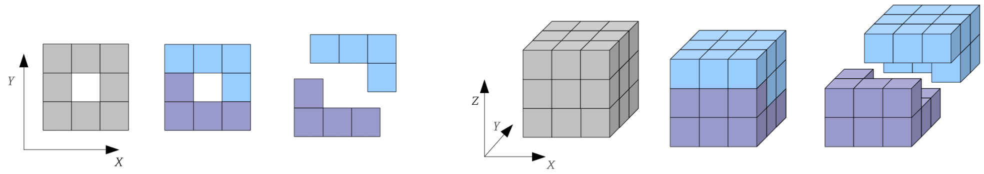

(a) 2D Classification

(b) 3D Classification

Figure 3.3.: Classification of forward (blue) and backward (violet) neighbors.

From the endpoints P_i, derived from the centralized chords in all sampled directions, we calculate the moments (Duda & Hart, 1973). In our case, the moments can be reduced to:

$$M_{pq} = \sum_{i=0}^{7} (P_{i,x})^p (P_{i,y})^q \qquad \text{for 2D and} \tag{3.8}$$

$$M_{pqr} = \sum_{i=0}^{25} (P_{i,x})^p (P_{i,y})^q (P_{i,z})^r \qquad \text{for 3D.} \tag{3.9}$$

Note that the centralization of the chords has the effect, that the center of inertia or gravity is the origin. Therefore, it yields $M_{10} = M_{01} = M_{100} = M_{010} = M_{001} = 0$ and also $M_{00} = 8$ and $M_{000} = 26$. To achieve the direction of elongation of the endpoints, it is necessary to solve the eigenvalue problem of the inertia tensor (Bakhadyrov & Jafari, 1999) or the covariance matrix. Both matrices have the same eigenvectors and their eigenvalues can be transformed to one another (McCartin, 2007). The covariance matrices adapted to our case are:

$$C_2 = \frac{1}{8} \begin{pmatrix} M_{20} & M_{11} \\ M_{11} & M_{02} \end{pmatrix} \qquad \text{for 2D and} \tag{3.10}$$

$$C_3 = \frac{1}{26} \begin{pmatrix} M_{200} & M_{110} & M_{101} \\ M_{110} & M_{020} & M_{011} \\ M_{101} & M_{011} & M_{002} \end{pmatrix} \qquad \text{for 3D.} \tag{3.11}$$

The direction of the concentration ellipsoid or the main inertia axis is the eigenvector to the highest eigenvalue (which indicates the elongation in the according direction). The direction defined in that way gives a first estimate of the fiber orientation.

3.2.2. Deviation in the Orientation Estimate and its Correction

Evaluation of the presented method shows a certain deviation in the orientation estimate as presented in Figure 3.4. The maximal possible deviation is limited to ≈ 10° in both cases 2D and 3D. By considering the endpoints just in a few sampled directions, those directions receive a high weight. This causes an attraction to the sampled directions, explaining the deviation. The orientation estimate is perfect in those orientations lying on or in the middle of two sampled directions.

The regular nature of the bias motivated a theoretical study of the problem. The fiber is assumed to be a spherical cylinder with radius r, infinite length and orientation v, represented by the angle θ (in 3D θ and ϕ, derived from the spherical coordinates). The centralized distances are therefore:

$$d_i = \frac{r}{\sin(\angle(v, vs_i))} \overset{\text{in 2D}}{=} \frac{r}{|\sin(\theta_i - \theta)|} \tag{3.12}$$

from which we can calculate the endpoints

$$P_i = \begin{pmatrix} d_i \cos\theta_i \\ d_i \sin\theta_i \end{pmatrix} \quad \text{for 2D and} \quad P_i = \begin{pmatrix} d_i \sin\theta_i \cos\phi_i \\ d_i \sin\theta_i \sin\phi_i \\ d_i \cos\theta_i \end{pmatrix} \quad \text{for 3D.} \tag{3.13}$$

To calculate the eigenvalues of the 2D covariance matrix and the main axis (given by the angle θ' of the eigenvector to the highest eigenvalue), we use the existing formula (Hu, 1962) adapted to our case:

$$\lambda_{1,2} = \frac{M_{20} + M_{02} \pm \sqrt{4M_{11}^2 + (M_{20} - M_{02})^2}}{16} \tag{3.14}$$

$$\tan(2\theta') = \frac{2M_{11}}{M_{20} - M_{02}} \tag{3.15}$$

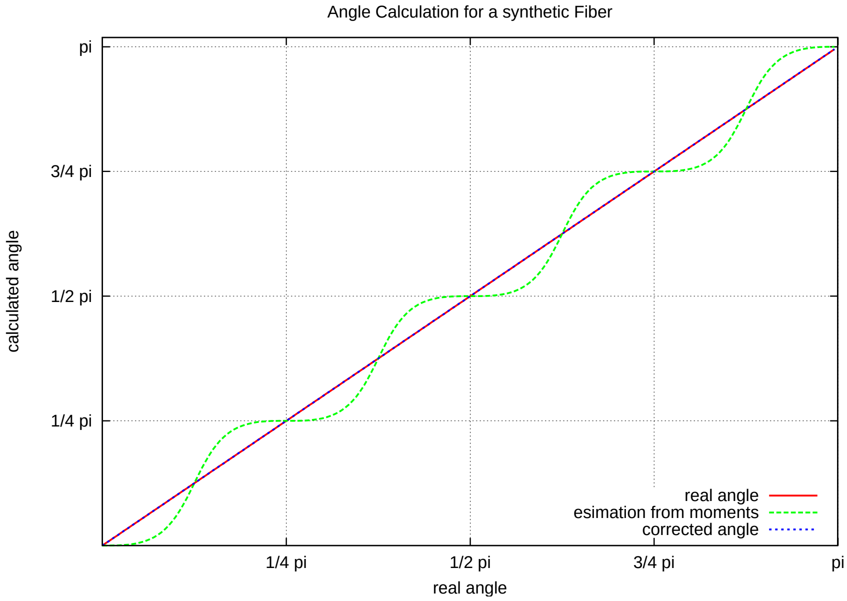

(a) 2D case

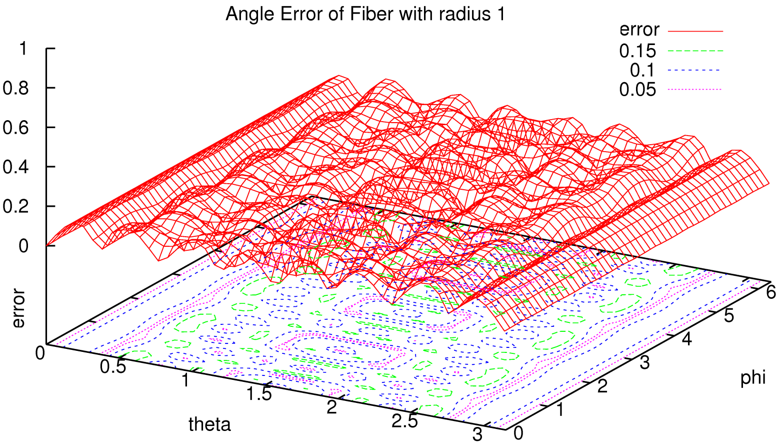

(b) 3D case

Figure 3.4.: Deviation of the orientation estimate based on covariance or inertia moments. (a) True angle of a fiber with length-radius ratio of 1000 vs. calculated angle and corrected angle. The grid indicates the sampled directions. (b) Relief of the angle error (true direction vs. direction calculated from the moments), for a fiber with direction $(1, \theta, \phi)$ in spherical coordinates.

We enter the formula for M_{pq} depending on the fiber parameters r and θ. After applying multiple steps of simplification for trigonometric functions, it was possible to achieve the following equations, which depend only on the main parameters r and θ. The detailed simplification can be found in the appendix A (page 161ff.).

$$\lambda_1 = r^2 \left(\frac{2 + \sqrt{3\cos^2(4\theta) + 1}}{\sin^2(4\theta)} \right) \tag{3.16}$$

$$\lambda_2 = r^2 f(\theta) \qquad \text{with} \quad f(\theta) = \begin{cases} \left(\frac{2 - \sqrt{3\cos^2(4\theta)+1}}{\sin^2(4\theta)} \right) & , \sin^2(4\theta) \neq 0 \\ \frac{3}{4} & , \text{otherwise} \end{cases} \tag{3.17}$$

$$\tan(2\theta') = \tan^3(2\theta). \tag{3.18}$$

From formula (3.18) it is possible to correct the deviation by inverting it with respect to the periodicity in the inversion of the tangent. The orientation can be derived from the estimate θ' as follows:

$$\theta = \frac{1}{2} \arctan\left(\sqrt[3]{\tan(2\theta')} \right) + i\frac{\pi}{2}, \tag{3.19}$$
$$\text{for} \;\; i\frac{\pi}{2} \leq \theta' + \frac{\pi}{4} < (i+1)\frac{\pi}{2},\; i \in \mathbb{N} \left(\Rightarrow i = \left\lfloor \frac{2\theta'}{\pi} + \frac{1}{2} \right\rfloor \right).$$

The deviation and the corrected angle are shown in Figure 3.4(a). The eigenvalue curve dependent on the fiber orientation is shown in Figure 3.5.

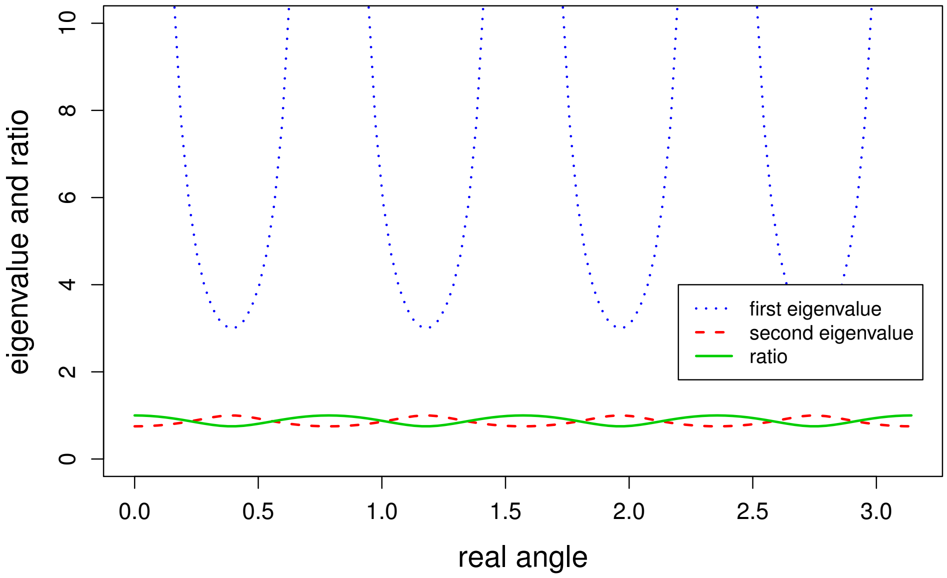

Figure 3.5.: Eigenvalues $\lambda_{1,2}$ and ratio $\frac{\lambda_1}{\lambda_1+\lambda_2}$ of 2D covariance matrix dependent on fiber orientation θ.

There exist also theoretical solutions for the eigenvalue problem in 3D (Jeulin & Moreaud, 2008a). With this, it is possible to deduce an equation for the inertia moments and the inertia vectors. However, simplification of these complex equations and reduction to the main parameters, which provides the possibility to correct the orientation, was not possible. The deviation in 3D is shown in Figure

3.4(b).

Still it is possible to improve the orientation estimate also in the 3D case. Based on the idea of the correction in 2D, we reduce the deviation of the calculated direction by pushing it away from the surrounding sampled directions. First of all, we define the force strength that influences the direction dependent on the distance to the sampled direction. This formula emerged from several tests based on the two dimensional correction curve.

$$t(d) = \begin{cases} -0.2\sin(\pi(4d/\pi)^{0.424}) & d < \pi/4 \\ 0 & \text{otherwise} \end{cases} \tag{3.20}$$

To complete the approach, we need to define the direction in which the force operates: the projections pn of the sampled directions vs_i on the 2D subspace orthogonal to the calculated orientation v. This projection is defined by: $\mathrm{pn}(vs_i, v) = vs_i - (v \cdot vs_i)v$. The approximated orientation v' is then calculated as follows:

$$v' = v + \sum_i t(\angle(vs_i, v))\mathrm{pn}(vs_i, v) \tag{3.21}$$

This procedure reduces the maximal error from 9.97° to 4.78° and the mean error from 6.40° to 1.27°. The reduction of the deviation is visualized in figure 3.6 on the unit sphere in colors from 0° in dark blue to 10° in dark red.

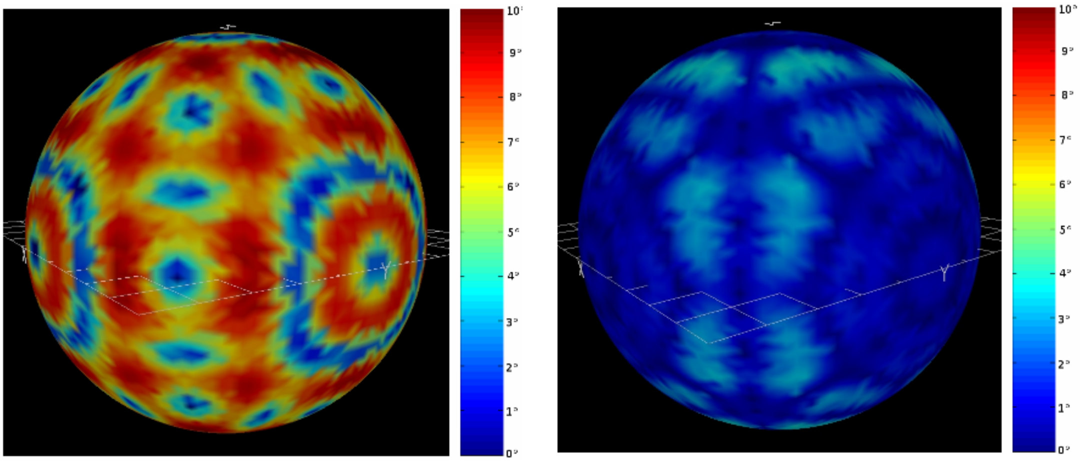

(a) Deviation of main inertia axes

(b) Deviation of approximated orientation

Figure 3.6.: Visualization of the deviation of the calculated fiber orientation on the unit sphere. The maximal error could be reduced from 9.97° to 4.78° and the mean error from 6.40° to 1.27°. The deviation is visualized on the unit sphere in colors from 0° in dark blue to 10° in dark red.

3.2.3. Radius Estimation

Most of the existing approaches to estimate the local fiber orientations need to be adapted to the fiber radius. This parameter often needs to be computed by hand or guessed from an image visualization. If the fiber radii vary to a large scale in the image, those approaches can not create stable results. A great advantage of our quantification method is not only that the orientation estimate is working for varying radii, but that a local radius estimation is practically included in the information.

The eigenvalues and eigenvectors from the covariance matrix describe a concentration ellipsoid (McCartin, 2007). The radii of the ellipsoid are determined by the square root of the eigenvalues, that are in increasing order $\lambda_{\text{min}} \leq \lambda_{\text{mid}} \leq \lambda_{\text{max}}$. Assuming a cylindrical object, we could estimate the radius by $\sqrt{\lambda_{\text{min}}}$ (in 3D also by $\sqrt{\lambda_{\text{mid}}}$, as it holds theoretically $\lambda_{\text{min}} = \lambda_{\text{mid}}$). This theory is based on the concentration ellipsoid of a cloud of points forming the cylindrical volume. In our case, a limited amount of points describe the surface of the object. Still, the 2D fiber radius is highly related to the stable value of the minimal eigenvalue ($\lambda_2/r^2 \in [0.75, 1]$) and can be calculated according to our theoretical studies (Formula 3.17). Thus, the radius can be computed as

$$r' = \sqrt{\lambda_2/f(\theta)} \tag{3.22}$$

with $f(\theta)$ from Formula 3.17.

According to our knowledge, there is no equivalent formula in 3D, thus we present a second method to estimate the radius, which is based on the centralized distances d_i. Equation 3.12 shows that the distances d_i hold the information of the radius. Therefore, each endpoint leads to an estimate of the radius:

$$\tilde{r}_i = d_i \sin(\angle(v', vs_i)). \tag{3.23}$$

An example is shown in Figure 3.7.

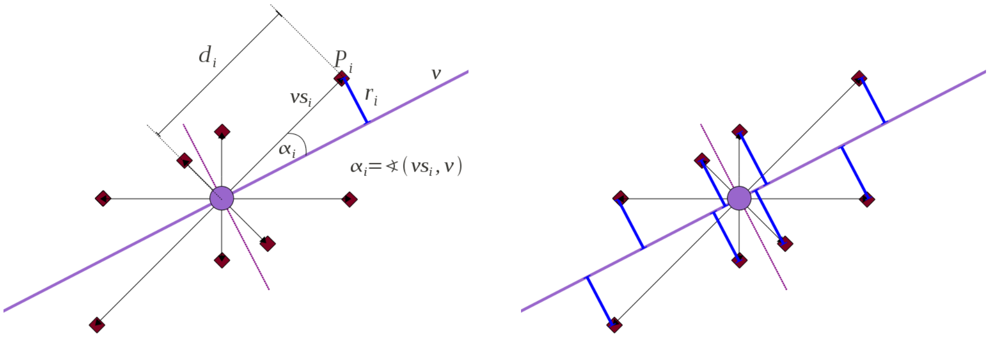

Figure 3.7.: Radius estimation from centralized endpoints.

Based on these radius estimates, there are various possibilities to choose the final radius approximation. We have chosen a trimmed mean, which is a mixture of the mean and median value: discarding the lower radius estimates reduces wrong estimates due to noise or border regions and discarding the higher radius estimates reduces wrong estimates due to crossing regions. The final estimate is computed as follows:

$$r' = \frac{1}{8} \sum_{i=10}^{17} \tilde{r}_{(i)}, \tag{3.24}$$

based on the ordered sequence of the radius estimates:

$$\tilde{r}_{(1)} \leq \tilde{r}_{(2)} \leq \ldots \leq \tilde{r}_{(26)}. \tag{3.25}$$

This approach is also an alternative for the radius estimation in the 2D case, The evaluation on synthetic data has shown that this method yields even better results than the recalculation from the eigenvalues. This can be explained by the fact that the trimmed mean is less sensible to outliers, which occur for example in fiber crossings.

3.2.4. Improvement by Adaptive Smoothing

The resulting direction and radius maps can be locally smoothed by using a smoothing filter (e.g. mean or Gaussian). In addition, filter weights can be based on the ratio of eigenvalues, which indicates the elongation of an object. We define the moment ratio as

$$MR(\lambda_1, \lambda_2) = \frac{\lambda_1}{\lambda_1 + \lambda_2} \in [0.5, 1). \tag{3.26}$$

For a ball, all eigenvalues are the same, whereas for a fiber the first eigenvalue λ_1 differs significantly from the second (in 3D the second and third are similar). In a point where two fibers cross, the first and second eigenvalues are similar. In such crossing regions, the main inertia axis is a mixture of the orientations of the two fibers and thus not reliable. The mixture of information also leads to a non-reliable radius estimate. Therefore, we use the moment ratio of the first two inertia moments to indicate the relevance of the estimated information.

To smooth the orientation and radius information of neighbor pixels, we apply a mean filter with an adapting structuring element (a ball with radius given by the radius map) and filter weights given by the moment ratio. It is advisable to apply this smoothing first on the radius map and then on the orientation information to avoid too big structuring elements for the orientation map, due to a too large radius estimate in crossing regions.

3.2.5. Application

In Figure 3.8 the method is applied on a 2D SAM-image (Scanning Acoustic Microscopy) of a glass-fiber reinforced polymer used for the wheel rim of cars. The sample has a volume fraction of 30% of 1 inch long fibers. Imaged is the projection of a thin slice focussed in a depth of 0.1 mm.

The cutout in Figure 3.8(d) illustrates, that also for very thin fibers we can get a reasonable direction estimate. Nevertheless, as mentioned earlier, in too thin fibers the estimated directions are reduced to the sampled directions. This effect is visible in the direction distribution shown in Figure 3.8(e). For the 4 sampled directions we get unreasonable high peaks, which are caused by discretization limits.

In Figure 3.9, we apply our method to the CRP plate introduced in Chapter 2. In the direction distribution on the unit sphere, shown in Figure 3.9(f), the two main orientations from the different layers are indicated by red marks. The θ angle maps can be used to separate the layers. A 3D rendering of the separated layers is shown in Figure 3.9(e).

3.2.6. Evaluation and Comparison on Synthetic Images

In this section, we study in detail the discretization artifacts and limits for reasonable quantifications. Furthermore, we compare the results of our approach with the Gaussian orientation space and the chord length transform on synthetic data. The tested images are realizations of a boolean model of isotropically oriented cylinders. We compare the different approaches by evaluating pixelwise the angle error, that is presented in an error histogram.

Discretization Artifacts

In this subsection, we will discuss the error of the estimation due to discretization artifacts, which will lead us to the necessary resolution to apply our algorithms. In order to answer this question, we

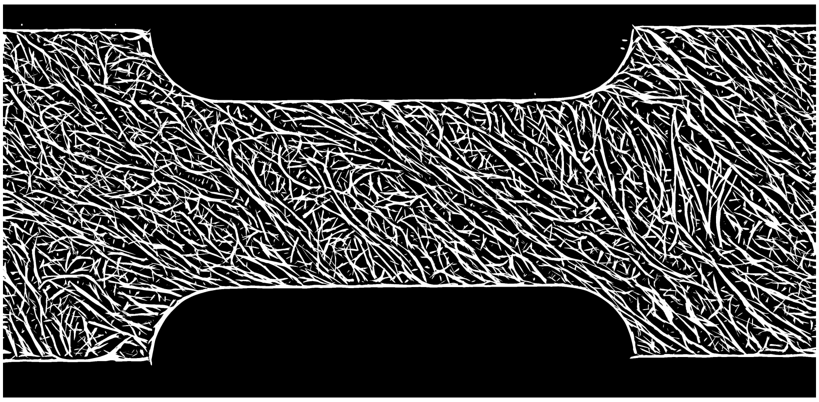

(a) Initial binary image

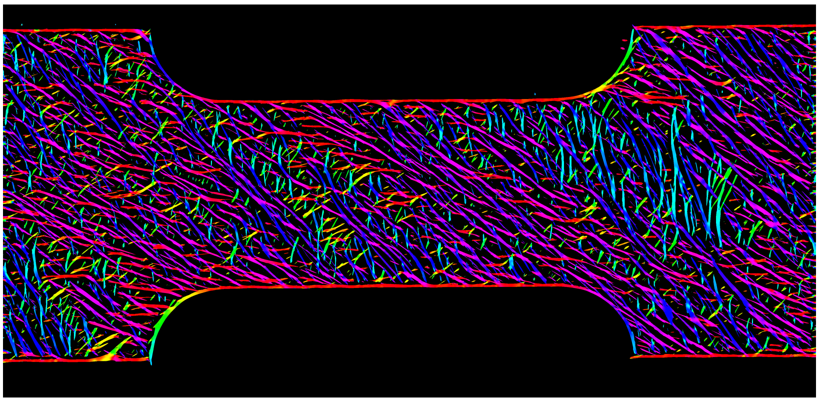

(b) Color coded direction map

(c) Color coding

(d) Zoomed cutout, with reasonable orientations even in thin fibers

(e) Rose of directions

Figure 3.8.: Application of the local analysis to a 2D SAM-image of a glass fiber reinforced polymer used in a car wheel rim.

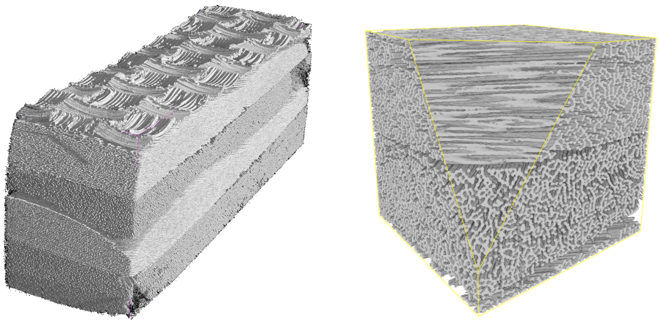

(a) CRP plate (b) Rendering of cutout

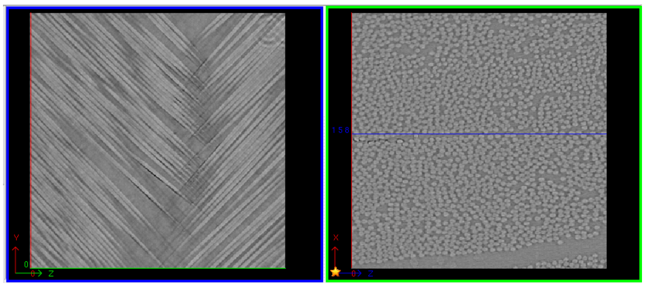

(c) CT data of cutout

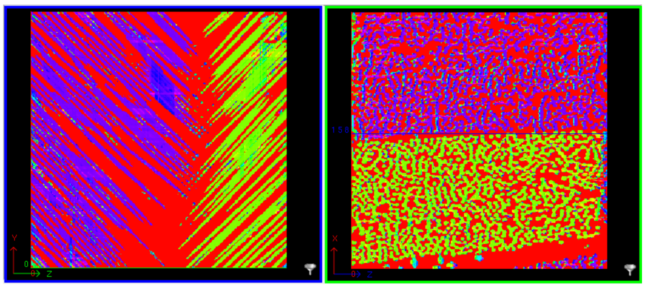

(d) θ angle map

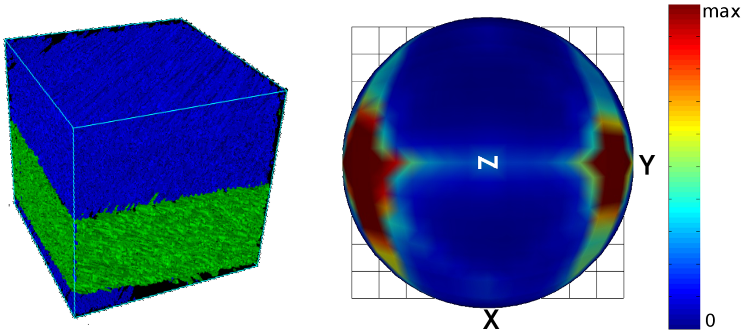

(e) Separated layers (f) Empirical density function of the Orientations on the unit sphere

Figure 3.9.: Application to a 3D CRP Plate: (a) visualization of the whole specimen, where the structure of the four layers is visible, (b) 3D rendering of the treated cutout (cube of 300 pixel side length), (c) structure of the original CT image, (d) colored presentation of the θ angle map (ϕ is in this material nearly constant): red the background, blue and green the two different layers. (e) rendering of the separated layers, (f) direction distribution on the unit sphere, where red indicates a high and blue a low presence of these directions.

have measured the maximal and mean angle error for the fiber orientation estimate over all possible directions, depending on the relative radius (in pixels).

From the resulting curves presented in Figure 3.10, we can conclude that the deviation is acceptable for a resolution, where the fibers appear with a radius ≥ 2 pixel. We show the measures for the main inertia axis and for the corrected angles (in 2D) and the approximated orientation (in 3D). These plots indicate also the improvement of the orientation correction and approximation.

Evaluation with Error Histogram

Working on synthetic data and knowing the ground truth yields the possibility to evaluate and to compare methods. The evaluation method is an error histogram, showing the quantity (amount of pixels) for a certain error. Perfect results would show just one peak on 0. The method, which has a high peak near 0 and decreases fast, provides good results.

The error histograms of the angle maps for synthetic images (Figure 3.11 and 3.12) show the improvement between the different steps of our method. In 2D: the main inertia axis, the corrected or approximated orientation and the result after adaptive smoothing. In 3D: the main inertia axis in every pixel, the main inertia axis in the centers of gravity and the results after approximating the real angle. Smoothing of the 3D image was not yet applied here.

Comparison to Gaussian Orientation Space

Furthermore, we compare our method to the Gaussian orientation space, which uses several elongated Gaussian filters in given directions and assumes the local orientation to be the one, which yields the highest filter response (Robb *et al.*, 2007, Wirjadi, 2009, Wirjadi *et al.*, 2009). The results are limited to the chosen directions, whereas the moments compute angles in the continuous space. That implies that the Gaussian method will need much more directions to achieve comparable results, which increases computation time, especially in 3D. The evaluated error histograms are shown in Figure 3.13 for 2D and in Figure 3.14 for 3D synthetic images. The advantage of this method is that it can be applied directly to the gray-level images and it is highly robust according to noise.

On the chosen 3D model, our method finishes in about one minute, whereas the Gaussian method with 98 orientations needed two hours for comparable results.

Comparison to Chord Length Transform

The chord length transform (Sandau & Ohser, 2007) computes the chord lengths of a certain amount of directions in a binary image. The local direction is the one yielding the longest chord lengths. The results are again limited to the chosen directions. This implies again a long computing time in the 3D case. Figure 3.15 shows, that the results in 2D are outstanding, as it is possible to scan a large amount of directions and the designed objects as cylinders are the optimal application for this approach. Furthermore, in crossing regions this method decides for the orientation of the longest fiber instead of mixing the informations. In 3D, the calculation time limits the amount of direction to a too small number (same as for the Gaussian orientation space) which leads to low precision and high deviations from the real fiber orientation.

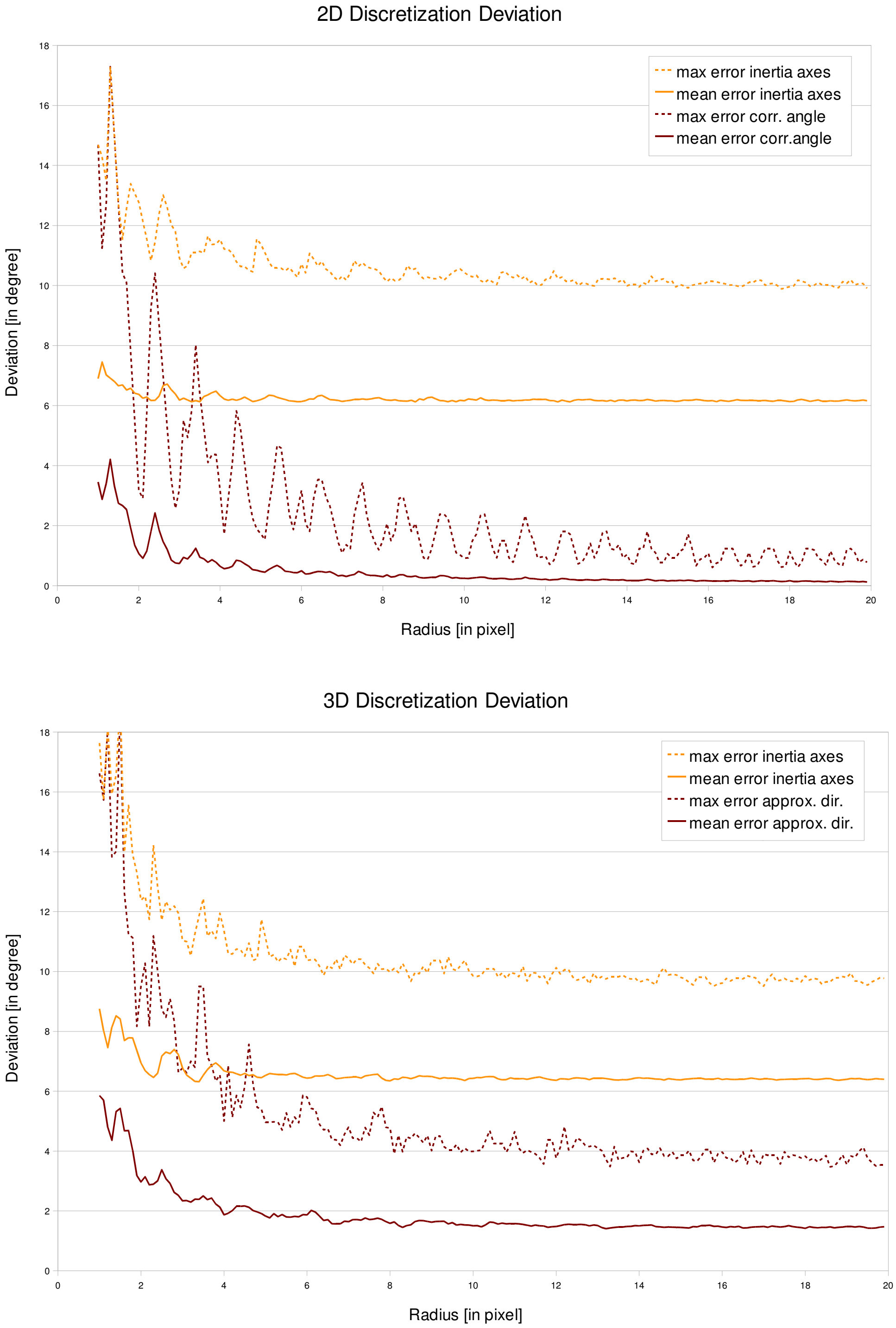

Figure 3.10.: Deviation of calculated direction dependent on resolution of discretization. We show the mean and maximal error over all fiber orientations for the main inertia axis, deriving directly from the covariance matrix, and for the corrected (2D) or approximated (3D) orientation estimates.

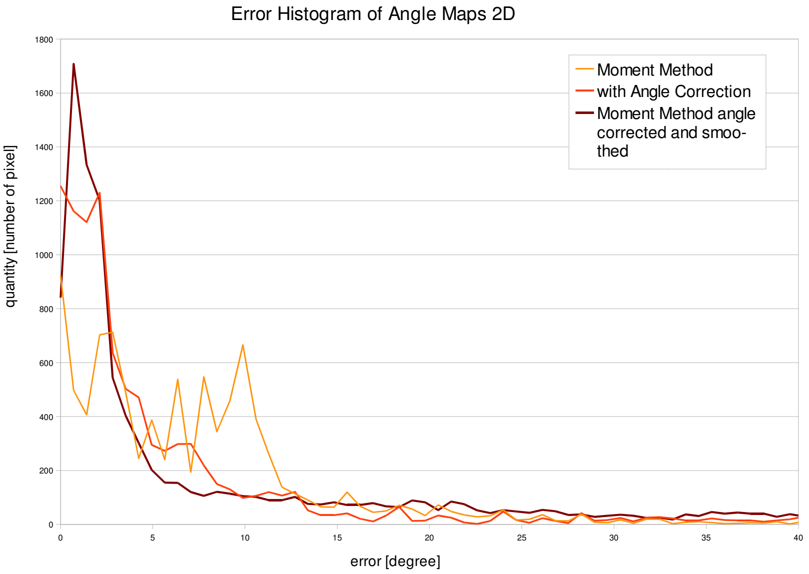

Figure 3.11.: Error Histogram of the angle maps on 2D synthetic data: in orange the first estimate by the inertia moments, in red the corrected angle results and in dark red the results after smoothing.

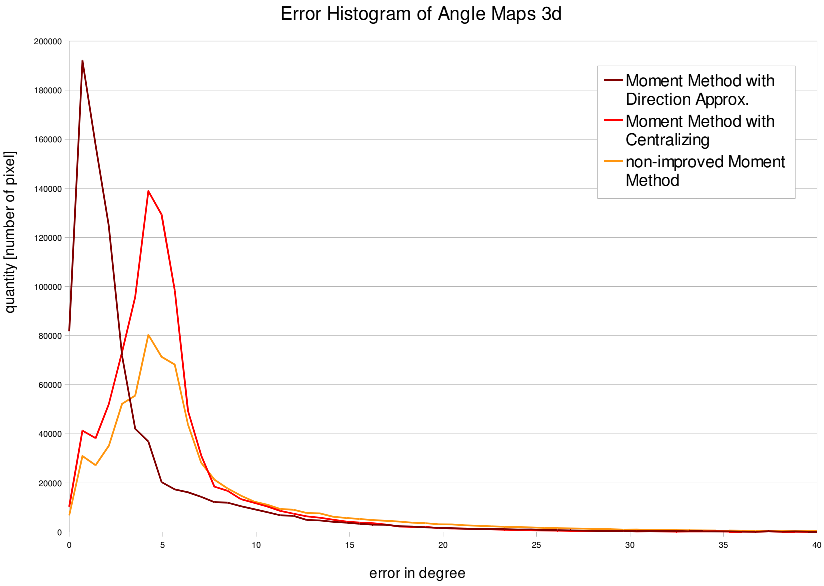

Figure 3.12.: Error Histogram of the angle maps on 3D synthetic data: in orange the first estimate by the inertia moments, in red the error after centralizing by the center of mass from inertia calculation and in dark red the results after approximation of deviation correction.

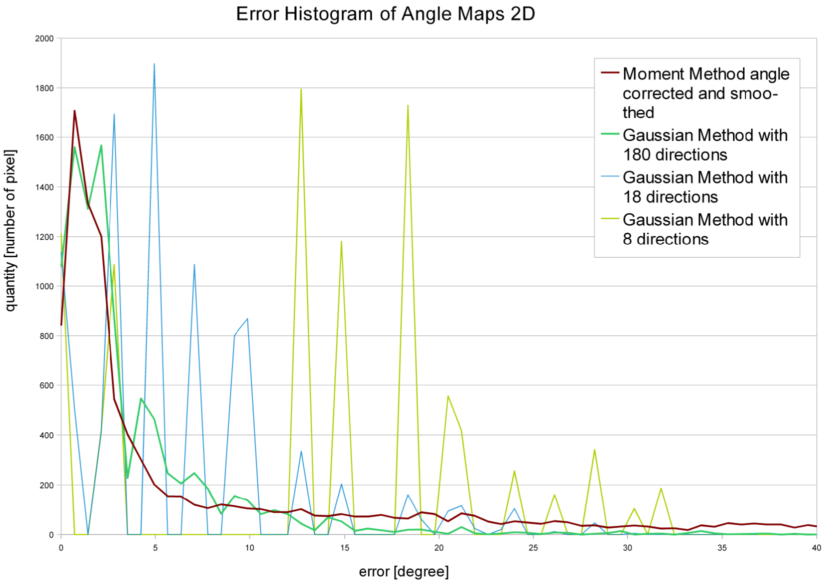

Figure 3.13.: Comparison of our method (4 sampled directions) to the Gaussian orientation space with 8, 18 and 180 directions on a synthetic 2D model.

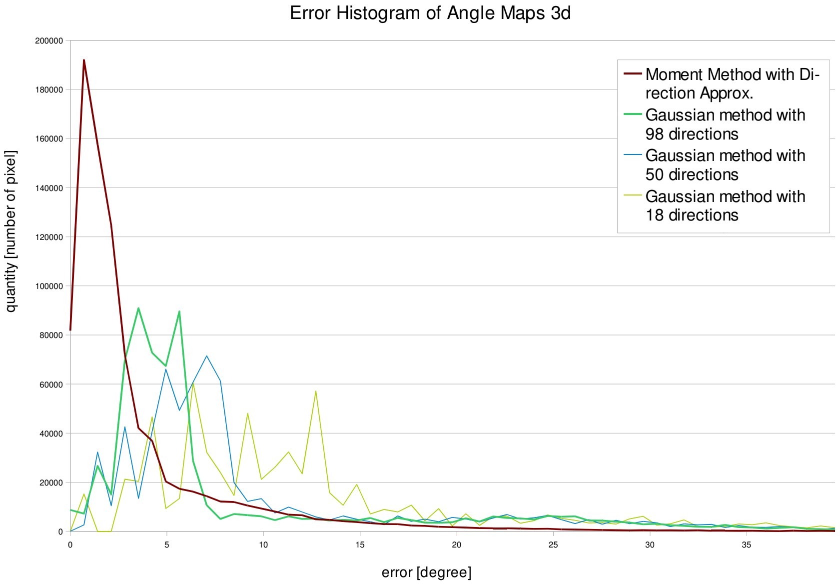

Figure 3.14.: Comparison of our method (13 sampled directions) to the Gaussian orientation space with 18, 50 and 98 directions on a synthetic 3D model.

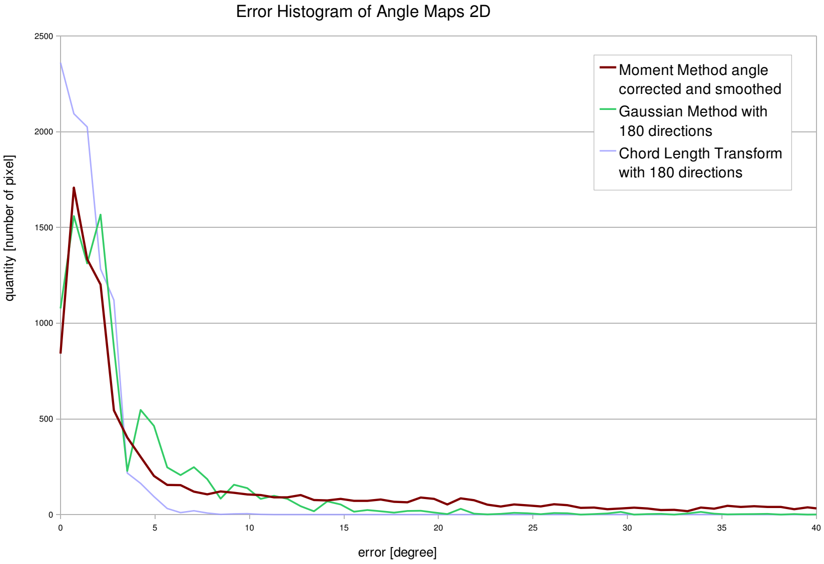

(a) 2D Comparison: our method (4 sampled directions), Gaussian orientation space and chord length transform (both 180 directions).

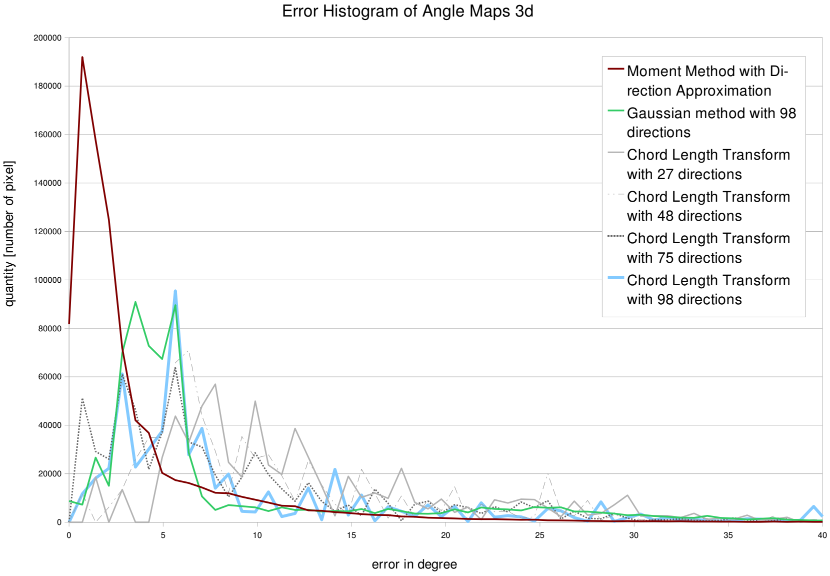

(b) 3D Comparison: our method (13 sampled directions), Gaussian orientation space and chord length transform (both 98 directions).

Figure 3.15.: Comparison of our method and the Gaussian orientation space to the chord length transform.

3.3. Analysis on Gray-Value Images

In dense parallel fiber networks, it often appears that fibers merge or approach very closely and that thin frontiers disappear during the binarization process. Applying the directional distance transform directly to the gray level images could yield the advantage to detect these thin frontiers.

In order to explore this idea, different approaches are proposed. The first possibility to measure distances on gray level images is the quasi distance transform, invented by Beucher (2007), with an additional contrast threshold. The second approach is based on the max-mean gradient, which is an extension of the morphological gradient with different size. Alternatively, we explored two other ideas: the Gaussian filters of adapting size and the comparison of a shape model. We define the four approaches, evaluate them and work out the most adequate applications (Altendorf & Jeulin, 2009a).

3.3.1. Quasi Distance Transform

The quasi distance is based on a residual operator τ, evaluating the difference of erosions or dilations. For each pixel, the maximal change between an operation with structuring element of size $i \in \mathbb{N}$ and $i+1$ is required. The associated function yields the smallest size $i_d \in \mathbb{N}$, which gives the maximal value for the residual operator. In this case, the associated function is called quasi distance:

$$\tau = \sup_{i \in I}(\epsilon_{i+1} - \epsilon_i, \delta_i - \delta_{i+1}). \tag{3.27}$$

The quasi distance is the size i_d for which the dilation or erosion yields the highest residue when compared to the next size $i_d + 1$. In our case, as we want to measure the directional distance, the structuring element is a directed segment. In this case, the image can be treated as several 1D signals. For a 1D signal or gray level function $f : \mathbb{R}^+ \to \mathbb{R}$ we can define the distance for a point x_0 in -x direction with the help of the underbuild function

$$\hat{f}_{x_0} = \sup_{\substack{g:[0,x_0]\to\mathbb{R}, \\ g \text{ increasing}}} (g \leq f). \tag{3.28}$$

This function is increasing and keeps the value in x_0: $\hat{f}_{x_0}(x_0) = f(x_0)$. The definition of $\hat{f}_{x_0}$ equals the reconstruction by dilation from the point x_0, as known in mathematical morphology (Salembier & Serra, 1995, Vincent, 1993). The quasi distance is the distance to the point with the highest gradient:

$$d(x_0) = \inf\left\{h \in (0, x_0) | g_{x_0}(x_0 - h) = G^{\max}_{x_0}\right\} \text{ with} \tag{3.29}$$

$$G^{\max}_{x_0} = \sup_{y \in (0,x_0)} \{g_{x_0}(y)\}, \tag{3.30}$$

$$g_{x_0}(y) = \max(|\hat{f}_{x_0}(y) - \hat{f}_{x_0}(y-1)|, |\hat{f}^c_{x_0}(y) - \hat{f}^c_{x_0}(y-1)|) \tag{3.31}$$

and f^c the inverted image (in theory -f, on 8-bit images 255-f). The implementation can be simplified by defining an image walker in the requested direction and buffering the gray level values in a decreasing and in an increasing vector for one line, which needs to be updated respectively.

In the case of fiber systems, it often appears that single fibers are separated by a weakly contrasted line, whereas the end of a fiber bundle has a very high contrast. Therefore, the quasi distance would detect the end of the fiber bundle, even if there is a closer significant contrast. The distance can be influenced by giving a threshold for the significant gradient G_l. Thus the distance is defined as

$$d_{G_l}(x_0) = \inf\left\{h \in (0, x_0) | g_{x_0}(x_0 - h) \geq \min(G^{\max}_{x_0}, G_l)\right\}. \tag{3.32}$$

This threshold treats the case where regions are separated just by a weakly contrasted line and a larger region of background further away is higher contrasted. In the standard case, the distance will cross the low contrasted background line and stop at the higher contrasted background, thus wrongly measuring the distance. If the threshold is lower than the contrast of the line separating the regions, the distance measure will stop at that line and detect the fiber end correctly. The significance limit G_l needs to be adapted to a kind of image with a certain prefiltering (e.g. a linear spread can change the optimal choice of G_l essentially). The choice of this parameter can be evaluated with the stability of the radius map or the classification map, which will be presented in Section 3.3.3. An example is shown in Figure 3.16.

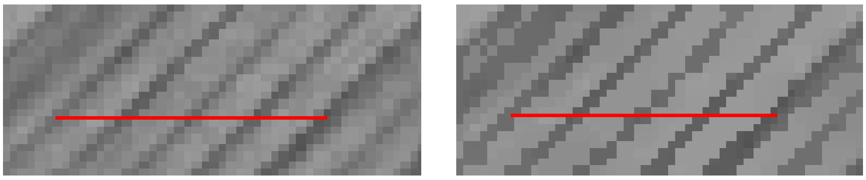

(a) Original CRP image. (b) Prefiltered image with toggle mapping.

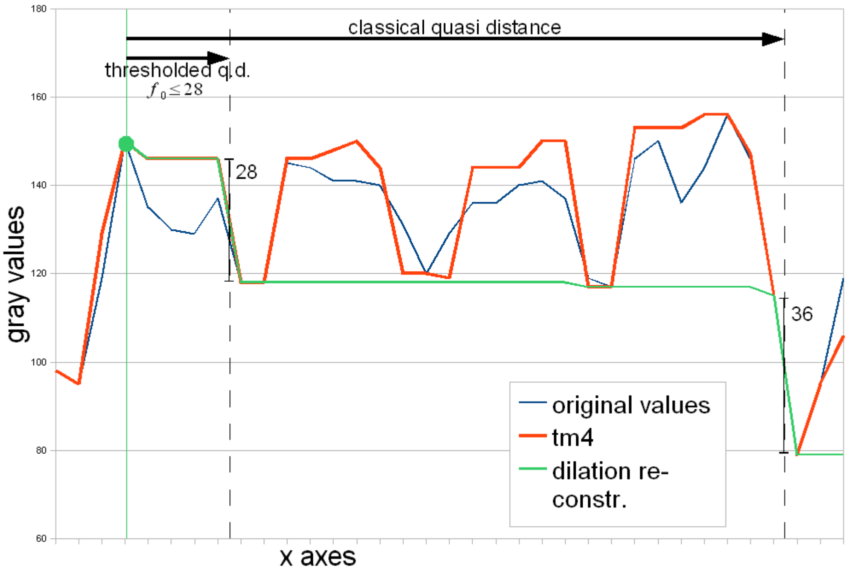

(c) Gray value relief with quasi distance.

Figure 3.16.: Quasi distance with significance threshold. We treat the gray value relief on the horizontal red lines in (a) and (b). The curves in (c) are: blue = original gray value relief, red = gray value relief after applying the toggle mapping filter and green = underbuild function of the red curve from the green point at $x = 4$. There are two high gradients on the green curve: one at the fiber end with residue 28 and one at the end of a bundle with residue 36. The classical quasi distance would prefer the higher residue, which is false in this example. By choosing a significance limit ≤ 28, the single fiber end is recognized correctly.

3.3.2. Maximal-Mean Gradient

The thresholded quasi distance transform, defined in the previous subsection, takes into account every change of gray values. In the case of tomographic images of two phase materials, we can specialize the method to find borders between foreground and background. For this purpose, we developed the maximal-mean gradient approach, inspired by the morphological gradient. The input of this approach is a gray-level line $l : \{1, \ldots, n\} \to \mathbb{R}$, which is extracted from a 3D image. Zeros are added at the front and the back of the line, and intermediate points are introduced with the average value of their two neighbors. This results in an up-sampled line $l^2 : \{1, \ldots, 2n+3\} \to \mathbb{R}$, which is defined as follows:

$$l^2(i) = \begin{cases} l((i-1)/2) & \text{, for } (i-1)/2 \in \{1, \ldots, n\} \\ 0 & \text{, for } i = 1 \text{ or } i = 2n+3 \\ (l^2(i-1) + l^2(i+1))/2 & \text{, else.} \end{cases} \tag{3.33}$$

The gradient in a point i with step size s is $g(i,s) = l^2(i+s) - l^2(i-s)$. Note that this gradient can be positive or negative, respectively if the gray values on the line are increasing or decreasing. The classical morphological gradient is $|g(i,1)|$. On a gray-level line cutting through a fiber, the increase or decrease of the gray values depends highly on its angle with respect to the fiber orientation. If the line is perpendicular to the fiber, the gray-level change will be abrupt; with decreasing angle the gray value change will protract over several pixels, thus $g(i,1)$ will only recognize a part of the increase. To detect boundaries of different levels of increase, the average over gradients with various step sizes is computed. This can also improve the robustness with respect to salt and pepper noise.

The mean gradient in a point i for the step size s is

$$G_{\text{mean}}(i,s) = \frac{1}{s} \sum_{k=1}^{s} g(i,k). \tag{3.34}$$

For too high step sizes s the peaks will flatten down or merge with surrounding peaks. To keep high peaks, we introduce the maximal-mean gradient, which increases with the step size. With respect to salt and pepper noise, a minimal step size s_0 is defined for the initial mean gradient. Then the maximal-mean gradient is recursively defined as:

$$G_{\text{mean}}^{\text{max}}(i,s) = \begin{cases} G_{\text{mean}}(i,s) & \text{, for } s \le s_0 \\ G_{\text{mean}}(i,s) & \text{, for } (s > s_0) \text{ and } |G_{\text{mean}}(i,s)| > |G_{\text{mean}}^{\text{max}}(i,s-1)| \\ & \quad \text{and } \Big(\text{sign}(G_{\text{mean}}(i,s)) = \text{sign}(G_{\text{mean}}^{\text{max}}(i,s-1))\Big) \\ G_{\text{mean}}^{\text{max}}(i,s-1) & \text{, else.} \end{cases} \tag{3.35}$$

The meaningful extrema of $i \mapsto G_{\text{mean}}^{\text{max}}(i,s)$, for a given s, are extracted in three steps: First, the extrema between two changes of sign are considered, and only the main one is kept. That gives us a sequence of peaks with alternating signs. Then peaks with an amplitude lower than a given gradient limit G_0 are deleted, as they are not significant. This sequence is again reduced to an alternating one by extracting the extrema of neighbors with the same sign. The resulting sequence of peaks represents the significant boundaries on the line and defines a foreground and background classification.

Figure 3.17 shows an example of an extracted line from one of the collagen images (Altendorf *et al.*, 2011). The relief of the gray values is presented by the thick black line. The thin colored lines represent the maximal-mean gradient for different step sizes. The minimal step size is chosen as $s_0 = 4$ and the final maximal-mean gradient for step size $s = 10$ is presented in thick red, with the first sequence of alternating peaks. The thick blue line represents the final estimated boundaries. The parameters $s_0 = 4$ and $s = 10$ showed up to be a good choice for various kinds of images and materials. The significant lower limit for the gradient is dependent on the difference of gray values of foreground and background in the original image. Therefore, it needs to be adapted according to the imaging technique and to the material type.

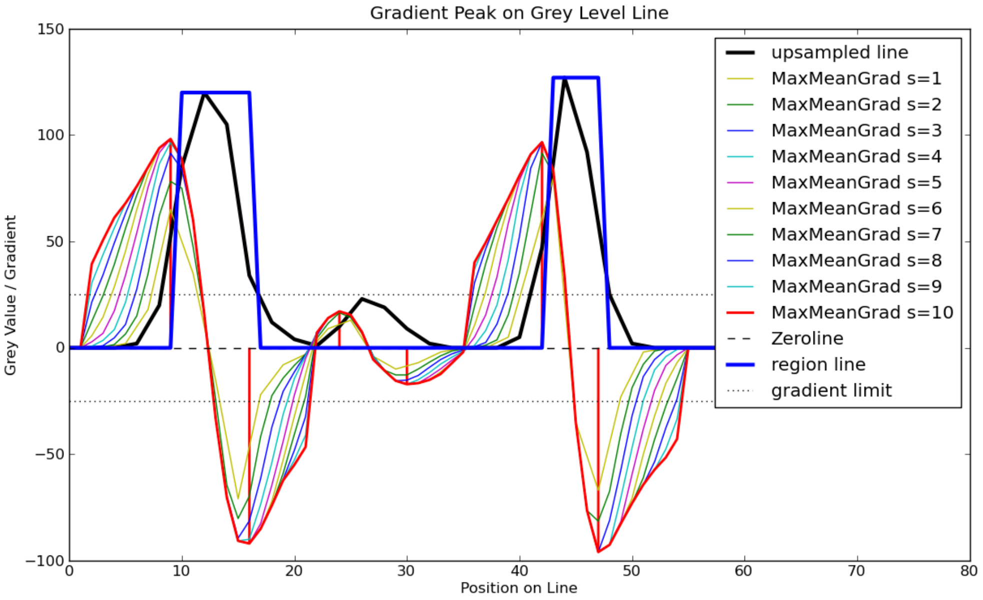

Figure 3.17.: Grey value line from a collagen image with maximal-mean gradients, peak sequence and estimated boundaries.

3.3.3. Classification into Foreground and Background

Assuming bright fibers in a dark matrix, we can classify the treated pixels in foreground or background in every sampled direction for both approaches. We consider a gray-value line in an arbitrary sampled direction. The associated function of the quasi distance finds its maximum in the difference of either erosions or dilations (see Equation 3.27). Bright fibers will disappear with erosion, thus if the maximum in the quasi distance is received from an erosion, the according pixel is in the object and classified as foreground. In the approach of the maximal-mean gradient, we observe the sign of the peak. A positive peak indicates a rise in the gray-value, thus the following pixels are considered as foreground and vice versa.

Thus for every sampled direction, we have classified the pixel as foreground or background. In the 2D case, we sample 8 directions ($N_{\mathrm{2D}} = 8$) and in the 3D case 26 directions ($N_{\mathrm{3D}} = 26$). The number of sampled direction in which the pixel was indicated as foreground gives us a classification rating with the mapping $c : I \to \{0, \ldots, N_d\}$. The optimal outcome would be that a pixel has the same classification in every sampled direction. A misclassification leads to a non reasonable distance measure in that direction and can influence the analysis. In 3D this happens mostly for boundary pixels where the sample line touches the object tangentially. In this case, there is only a slight increase of the gray-values which is considered as noise. The quantification can compensate few misclassifications, if the corresponding distance is set to zero.

It is assumed that the analysis is meaningful, if the classification rating is higher than a limit c_0. In the present case, we propose $c_0 = 6$ for the 2D case and $c_0 = 20$ in the 3D case. The classification can be used in two ways: first, the classification gives a quality measure and second, the thresholding of the classification map with the limit c_0 defines a mask for the foreground voxels. For c_0 close to the maximum N_d, the foreground pixels mainly include bright pixels localized in the inner part of a fibers, this generates a high specificity of the measure but thins the fibers in the mask. Note, that this does not affect the radius estimate, as it is based on the distances calculated from the gray-level images.

3.3.4. Alternative Approaches

Apart from the already presented approaches, we developed and studied two alternatives: the difference of Gaussian filters and the shape model. In comparison, we will see that these approaches do not give as nice results as the quasi distance or the maximal-mean gradient. Still, we include this study to show the variety of possibilities (published in Altendorf & Jeulin (2009a)).

Gray Value Distances by Adapting Difference of Gaussian Filters

This approach makes use of the difference of Gaussian filters of varying size of filter mask. More precisely, the mask size is adapted to the distance s to the point of interest x_0. The function for the Gaussian filter weights is defined as:

$$h_s(x) = \frac{1}{\sigma_s\sqrt{2\pi}} e^{-\frac{x^2}{2\sigma_s^2}}, \tag{3.36}$$

where s denotes the filter size. The parameters are chosen as with $\sigma_s = (s+1)/4$ and $\mu = 0$. The filter is applied to the reconstruction by dilation $\hat{f}_{x_0}$ with respect to the distance to x_0: $s = \sqrt{x_0 - y}$. The filter response is then

$$\tilde{f}_{x_0}(y) = \frac{\int_y^{y+\sqrt{x_0-y}} \hat{f}_{x_0}(x) \cdot h_{\sqrt{x_0-y}}(x-y)dx}{\int_0^{\sqrt{x_0-y}} h_{\sqrt{x_0-y}}(x)dx}. \tag{3.37}$$

The distance should yield the highest difference in $\tilde{f}_{x_0}(y)$:

$$d_g(x_0) = \inf\left\{h \in (0, x_0) | \tilde{f}_{x_0}(x_0 - h) = G_g^{\max}(x_0)\right\} \tag{3.38}$$

with $G_g^{\max}(x_0) = \sup_{y\in(0,x_0)} |\tilde{f}_{x_0}(y) - \tilde{f}_{x_0}(y-1)|$. Increasing the size of the filter with increasing distance, results in a stronger smoothing of the borders further away, thus close distances are preferred.

Gray Value Distances by Shape Model Comparison

The third approach considers a shape model for the fiber, which takes not only into account the local decrease of the gray level, but also the regularity of the values considered to be fiber foreground. The evaluation of a certain distance h from x_0 is dependent on the regularity of the values between $x_0 - h$ and x_0 and the decrease at the point $x_0 - h$. The gray values are expected to be constantly high on fiber foreground (between $x_s(h) = (x_0 - h) + s/2$ and x_0), whereas they should decrease from $x_s(h)$ to $x_e(h) = x_s(h) - s$. The strength of the decrease can be chosen with respect to the image. On the treated images the minimal choice of $s = 2$ was optimal. The smoothed model decrease is considered to be like $h_s(x) = \frac{1}{2}\sin(\frac{(x-(x_0-h))\pi}{s}) + \frac{1}{2}$. We evaluate a distance h according to the adapted model structure. We define two penalty functions: $I_1(x_0, h)$ for the regularity in the foreground and $I_2(x_0, h)$ for the form of the decrease (evaluation is done with the squared deviation from the expected model). In order to honor high difference in foreground and background gray values, we take into account the integral of the minimum of model and real structure with $I_g(x_0, h)$. The final rating $I_t(x_0, h)$ is a combination of these three values.

$$\begin{aligned}
I_t(x_0, h) &= \max(0, I_g(x_0, h) - \sqrt{I_1(x_0, h)^2 + I_2(x_0, h)^2})\\
I_1(x_0, h) &= \frac{f_\Delta}{x_0 - x_s(h)} \int_{x_s(h)}^{x_0} (\frac{f(x) - \bar{f})}{f_\Delta})^2 dx\\
I_2(x_0, h) &= \frac{f_\Delta}{x_s(h) - x_e(h)} \int_{x_e(h)}^{x_s(h)} (\frac{f(x) - f_{\min}}{f_\Delta} - h_s(x))^2 dx)\\
I_g(x_0, h) &= \frac{\sqrt{f_\Delta}}{x_0 - x_s(h)} \int_{x_s(h)}^{x_0} \min(1, \frac{f(x) - f_{\min}}{f_\Delta}) dx\\
&\quad + \frac{\sqrt{f_\Delta}}{x_s(h) - x_e(h)} \int_{x_e(h)}^{x_s(h)} \min(h_s(x), \frac{f(x) - f_{\min}}{f_\Delta}) dx
\end{aligned}$$

with the mean value $\bar{f} = \frac{1}{x_0 - x_s(h)} \int_{x_0}^{x_s(h)} f(x)dx$. The minimal value, the curve does decrease to, is $f_{\min} = \inf_{x \in (x_e(h), x_s(h))} f(x)$ and the difference between these two values is $f_\Delta = \bar{f} - f_{\min}$. The final distance is then defined as

$$d_I(x_0) = \inf\{h \in (0, x_0) | I_t(x_0, h) = \max_{d \in (x_0, h)} I_t(x_0, d)\}. \tag{3.39}$$

3.3.5. Comparison of the Different Approaches on a Gray Value Line

The presented approaches are evaluated on an original and preprocessed gray value line from the CRP data set. As preprocessing we used toggle mapping to enhance the contrast. The main idea of this filter is to build upper and lower bounds by dilation and erosion, and fit the original gray level in every point to the nearest of the bounds. For more details, see Fabrizio & Marcotegui (2006). Note that this operator can enhance salt and pepper noise.

On a preprocessed gray value line, the thresholded quasi distance as well as the shape model are showing perfect results as presented in Figure 3.18 as well as the approach of the maximal-mean gradient as shown in Figure 3.20. For the approach with the Gaussian filters we can already see, that the results are not as stable in neighboring points as for the other approaches. On the original gray value line (without preprocessing) the approach of the integral model shows acceptable results (Figure 3.19). The thresholded quasi distance and the maximal-mean gradient both work fine on the first three fibers and split the fourth fiber up in two. This behavior is not necessarily wrong. We know from the 2D image that it actually is one fiber, but from the gray value line it could be interpreted as two.

In Figure 3.19(b), we can see the most important weak point in the local approaches (quasi distance, integral model and Gaussian filters). Those three approaches search for the highest gray value difference from a local point of view. That means for two neighbor pixels, the next highest difference may be at a different place and thus in one foreground component, the distance function is not regularly increasing, as it should be. In contrast, the maximal-mean gradient detects the highest changes globally on the whole line and assures therefore a coherent design of the distance function.

Regarding the computational complexity, the fastest approach is the maximal-mean gradient with linear time ($\mathcal{O}(n)$), directly followed by the approach of quasi distance which runs in nearly linear

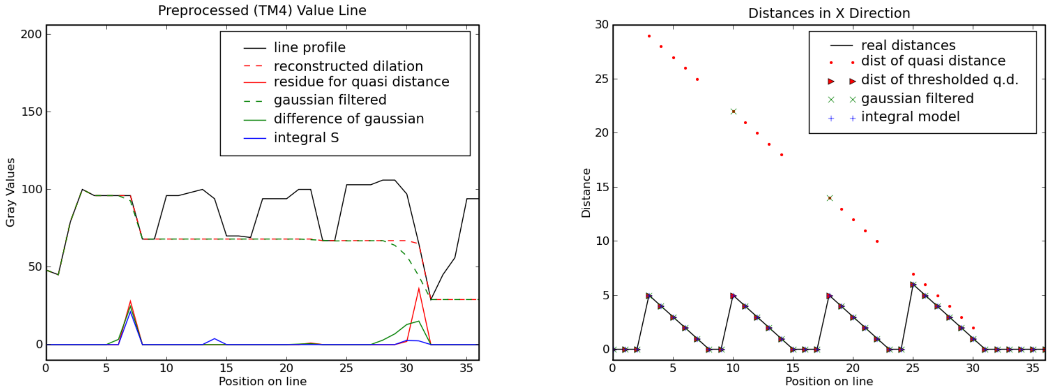

(a) Distances for $x_0 = 4$ in X-direction

(b) Distances in every point

Figure 3.18.: Comparison of the approaches on a TM4 preprocessed value line. (a) seeks the distance to the background from the point $x = 4$ in x direction, we present the values of different residual functions for increasing distances. The highest value of each function indicates the most probable distance. (b) presents the distance to the background in x direction from every point and for different approaches.

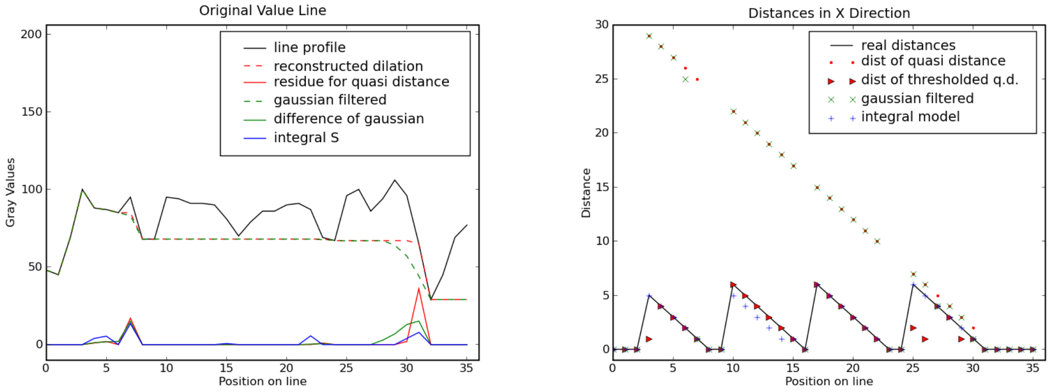

(a) Distances for $x_0 = 4$ in X-direction

(b) Distances in every point

Figure 3.19.: Comparison of the approaches on the original value line. Same structure as in Figure 3.18 applied on the non filtered image values and shows therefore less stable results.

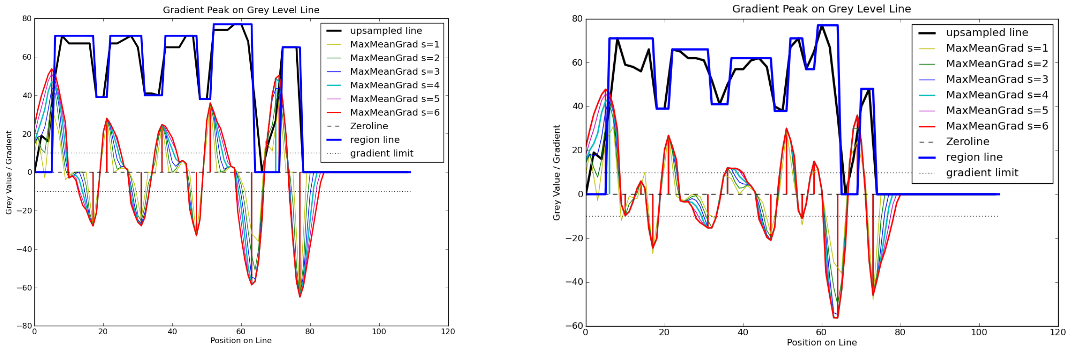

(a) Prefiltered with toggle mapping.

(b) Original gray value line.

Figure 3.20.: Results of the approach based on the maximal-mean gradient.

time (average case $\mathcal{O}(n)$, worst case $\mathcal{O}(n \log n)$). Those two approaches yield an advantage compared to the approaches with Gaussian filters ($\mathcal{O}(n^2)$) or with model shape ($\mathcal{O}(n^2 \log n)$). The given times are estimated for one line with length of n pixels.

3.3.6. Comparison of the Different Approaches on a 2D Slice

In the previous section, we applied the approaches to a very limited example. In this section, we would like to evaluate the performance for real datasets. In general, synthetic data sets are used to evaluate algorithms in comparison to the ground truth. For the analysis of fiber systems in gray value images, we experienced that most of the time synthetically generated images are created too homogeneous and do not reflect the natural artifacts in imaging. We have chosen a 2D section of a 3D CT image of the carbon fiber reinforced polymer, which was introduced in Figure 3.9. This data set presents a rather complex example, as we have the natural noise and artifacts. Still, we are able to evaluate the results as it can be manually segmented in regions with nearly constant orientations.

It is revisable to use a gray value method on this example, because thin and low contrasted contours between fibers are getting lost during the binarization process (see Figure 3.21(c)). Therefore, distance measures can cross several fibers, which distorts the calculation results. The orientation analysis is still reasonable, as the fiber bundles have the same orientation as the single fibers. The radius analysis fails completely as the fiber bundles are measured as one fiber and have therefore a much higher radius.

Figure 3.21 shows the original gray value image, a prefiltered version and the binarization. The thin frontiers between the fibers visible in the gray level image are enhanced by morphological toggle mapping with a disc of radius 4 as structuring element (Figure 3.21(b)). Figure 3.23 shows the results of the radius analysis and Figure 3.22 the angle maps from the orientation analysis, colored in a periodic rainbow presentation (see Section 4.1.1).

For the standard quasi distance it is still possible that the contrast between fiber and thin division line is too low, thus a higher contrast at the end of the fiber bundle is considered as object end. This circumstance causes similar problems in the measurement as in the binary case. The resulting angle

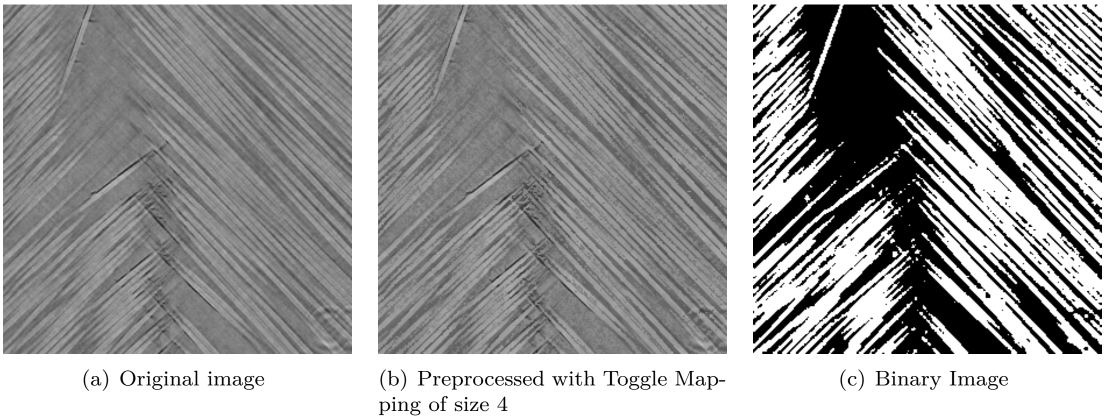

(a) Original image

(b) Preprocessed with Toggle Mapping of size 4

(c) Binary Image

Figure 3.21.: Preprocessed gray level image and binarization of dense parallel fibers in CRP slice.

maps for the standard quasi distance are shown in Figure 3.22(b).

By using the threshold $G_l = 15$ as sufficient gradient (in a domain of gray values reaching from 0 to 255), the thin boundary lines between the fibers can be detected as object ends and improve the measurements for the thresholded quasi distance (see Figure 3.22(c)). The significance level G_l was chosen empirically be evaluating stability of the classification rating (see Section 3.3.3). The method using the maximal-mean gradient (see Figure 3.22(d)) gives visually the same results as the thresholded quasi distance. The difference of Gaussian filters (see Figure 3.22(e)) has slightly worse results and the shape model (see Figure 3.22(f)) seems to fail completely. For comparison, we also applied the oriented Gaussian filters (see Figure 3.22(g)), which reach their best results for the ellipsoid filter sizes of 4 vs. 0.5.

In Figure 3.23 the resulting radius maps are presented, which yield the possibility to evaluate the detection of fiber ends. We can observe the real radius in a medium gray value, whereas the white spots indicate an overestimation of the radius due to merged fibers. Too high estimates for the radius result from errors in the detection of fiber ends. In parallel fiber systems, the measurement error caused by merged fibers has a higher influence on the radius calculation than on the direction calculation. Therefore, evaluation of the correct detection of fiber boundaries is more reasonable on the radius maps. Obviously, the approaches using the thresholded quasi distance and the maximal-mean gradient (presented in Figure 3.23(c) and 3.22(d)) show the most stable results here. Unfortunately, they do not agree in the mean radius (see Table 3.2).

Despite good expectations from the results on the gray value line (from Section 3.3.5), the approach of the model shape does not show convincing results in Figure 3.22(f). The problem with such dense fiber systems is that if the detection of the foreground end fails in just one direction, this direction will carry a too large weight, and intensively influence the estimated orientation.

We evaluated the mentioned approaches on this example with a manual classification of the regions having the same orientations (see Figure 3.22(h)). We receive three regions: the left part with a mean angle of $\pi/4 \approx 0.785$, the right part with a mean angle of $3\pi/4 \approx 2.355$ and the single fiber on the top left, which differs slightly in its angle of ≈ 1.9809. In Table 3.1, we show for every approach the mean orientation for each region and the deviation to it, as well as the mean deviation to the region mean in the whole image and the mean error with respect to the manual classification. The order of

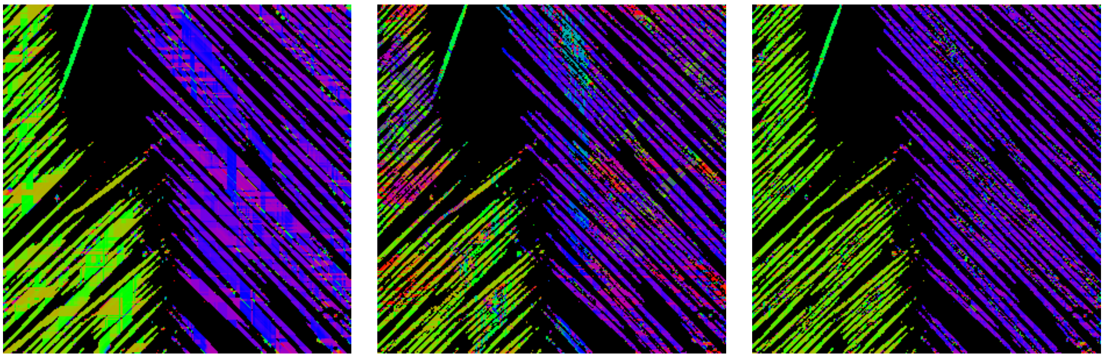

(a) Binary Version

(b) Standard Quasi Distance

(c) Thresholded Quasi Distance ($f_0 = 15$)

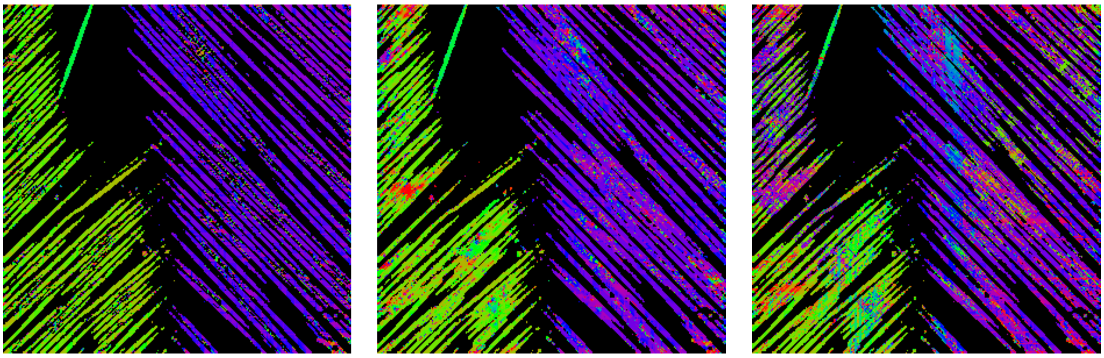

(d) Maximal-Mean Gradient

(e) Difference of Gaussian Filters

(f) Shape Model

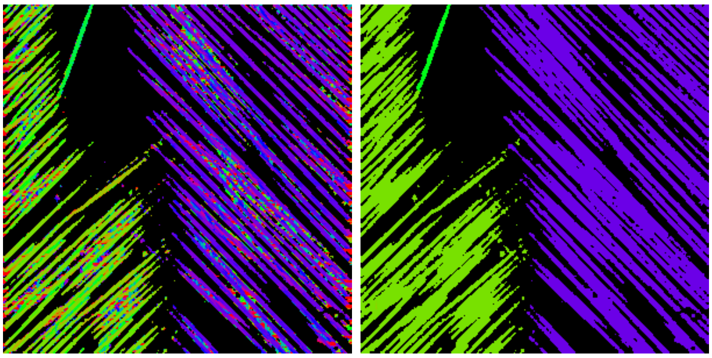

(g) Gaussian Orientation Space with size $(0.5, 4)$

(h) Manual Classification

Figure 3.22.: Direction analysis for binary image and preprocessed gray level images (Figure 3.21(b)) with different approaches.

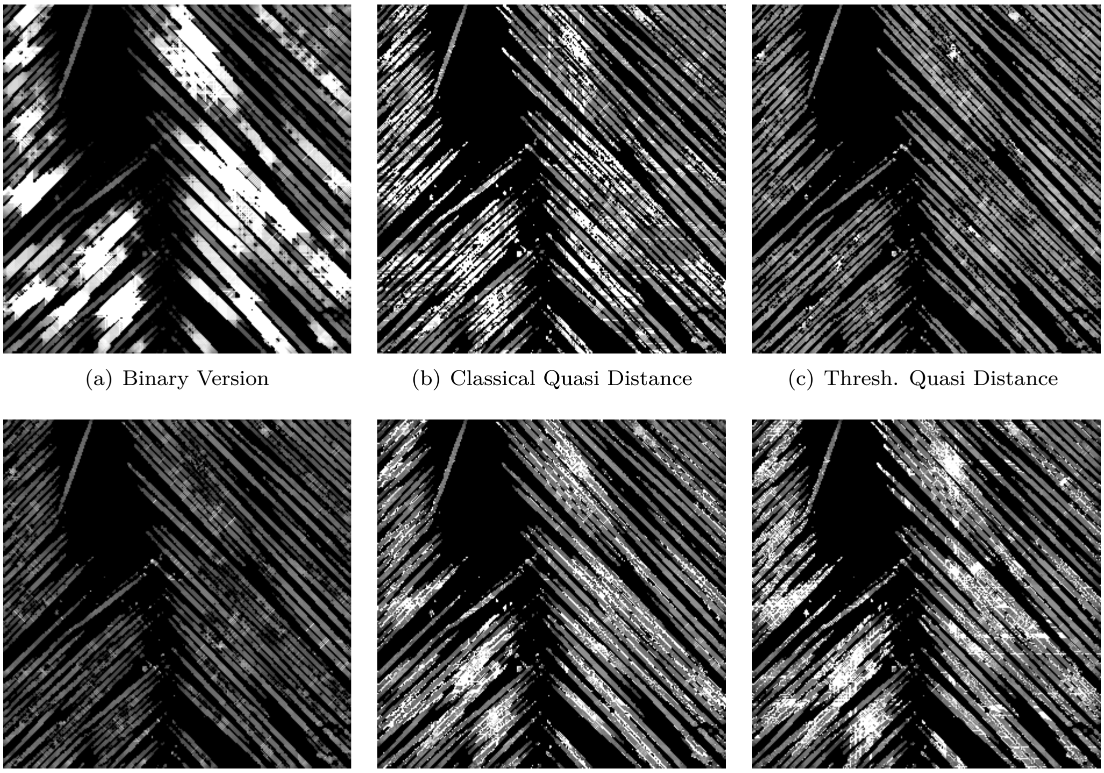
(a) Binary Version (b) Classical Quasi Distance (c) Thresh. Quasi Distance

(d) Maximal-Mean Gradient (e) Difference of Gaussian (f) Shape Model

Figure 3.23.: Radius analysis for binary image and preprocessed gray level images (Figure 3.21(b)).

Approach	Left Part Mean	 (Dev.)	Right Part Mean	 (Dev.)	Single Fiber Mean	 (Dev.)	Mean Error	Mean Dev.
Manual Classification	$\pi/4 \approx 0.785$		1.9809		$3\pi/4 \approx 2.355$			
Maximal-Mean Gradient	0.781	(0.123)	1.906	(0.089)	2.371	(0.154)	0.134	0.133
Thresholded Quasi Distance	0.778	(0.138)	1.905	(0.157)	2.364	(0.173)	0.15	0.149
Binary	0.79	(0.132)	1.938	(0.079)	2.363	(0.192)	0.153	0.154
Difference of Gaussian	0.769	(0.159)	1.91	(0.129)	2.385	(0.226)	0.183	0.183
Gaussian Orientation Space	0.776	(0.235)	1.913	(0.151)	2.374	(0.276)	0.249	0.249
Standard Quasi Distance	0.769	(0.243)	1.874	(0.242)	2.48	(0.443)	0.312	0.309
Shape Model	0.745	(0.316)	1.841	(0.345)	2.446	(0.543)	0.397	0.402

Table 3.1.: Evaluation of different orientation analysis methods. Manual classification enables comparison of the automatic analysis. Three classes were defined: right part, left part and the single fiber on the top left, whose orientation differs from the one of the surrounding fibers. For every class we compute the mean orientation and the deviation from these values. We finally evaluate the method by comparing the mean error over all foreground pixels according to the manual classification.

Approach	Mean Radius	Deviation	Mean Error to 2
Maximal-Mean Gradient	1.69914	0.27106	0.465954
Thresholded Quasi Distance	2.7078	0.384283	0.720088
Difference of Gaussian	2.35981	4.12308	0.814177
Shape Model	2.50726	5.33168	0.936004
Binary	2.71203	3.39907	1.23598
Standard Quasi Distance	3.24365	7.64946	1.33518

Table 3.2.: Evaluation of different radius analysis methods on gray value image. We compute the mean radius with deviation and the mean deviation from the manually defined real radius of 2.

the approaches in the table equals their rank in the evaluation for the chosen data set. We observe that the maximal-mean gradient performs the best, followed by the thresholded quasi distance.

In Table 3.2, we show the mean radius, the deviation, and the mean error assuming the real radius is equal to 2. We manually measured some fibers in the image and concluded that 2 is approximately the mean radius. Still, the radius is not constant in the image as we see cuts of 3D fibers. Thus, it is hard to estimate the radius manually as we tend to take into account only the middle part of the nicely reconstructed ones, which would result in an overestimation. The evaluation of the mean error with respect to the radius 2 shows again the maximal-mean gradient and the thresholded quasi distance on the first two ranks, which have also the most stable radius maps. Unfortunately, they do not agree in the measure of the mean radius.

Irregularities in the measurements can be smoothed with the adaptive smoothing depending on the moment ratio (introduced in Section 3.2.4). Smoothing will decrease the error in the evaluation, but will keep the ranks nearly equal.

3.3.7. Application

In the following, we have chosen two applications treated in the context of project collaborations. Both studies are published (reference given in the corresponding sections below).

2D SEM Images of a Meltblown Non Woven

In the following application on 2D SEM images of a meltblown non woven, the quality of the final product is highly dependent on the mean fiber diameter. In this case, our software could replace stultifying manual measurements, that even deviates essentially between different test persons. Six different probands manually estimated the empirical diameter distribution of one image, by choosing 50 points in the image, measuring the diameter by clicking on both opposed fiber boundaries and noting the diameter in an Excel worksheet. Figure 3.24 shows that the empirical distribution functions of the automatic analysis perfectly lie in the range of those of the probands. Thus, the quality can be controlled much more efficient automatically and the results can be reproduced at any time.

Figure 3.25 shows an example for varying enlightening techniques for the SEM imaging. Different configurations were tested on the same specimen. The distribution densities of test $1, 2, 4$ show similar curves, whereas test 3 overestimates the diameter. This effect is equivalent to the one in binarized images: in overlapping regions the fibers merge and form a larger object, which yields a higher local radius estimate. The other enlightening configurations create a contrast between superposing fibers and the boundaries can be identified.

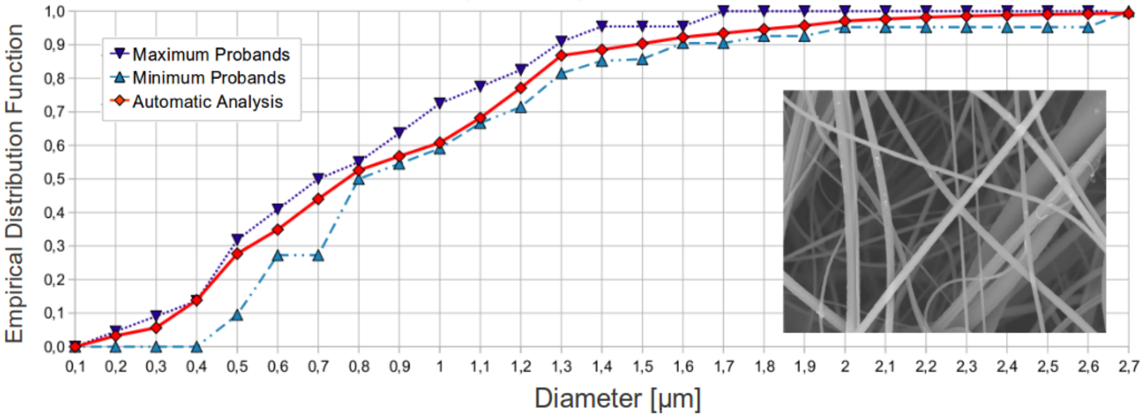

Figure 3.24.: Empirical distribution function of diameter estimation on 2D SEM image of a meltblown non-woven. Comparison to range of manual measurement by six probands.

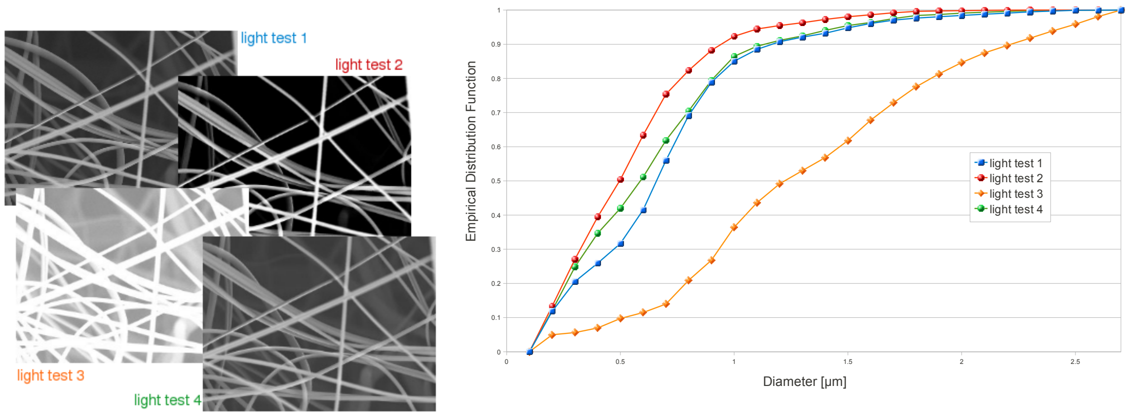

(a) 4 differently enlightening images of the same specimen

(b) Empirical distribution functions of the fiber diameter

Figure 3.25.: Test of robustness for differently enlightening.

For further details see Altendorf *et al.* (2010).

3D SHG Images of Collagen

The gray value method can also be applied on 3D images of collagen in a phosphate-buffer saline (PBS) solution. The imaging technique is Second Harmonic Generation (SHG) producing stacks of 2D images, that can be interpreted as a 3D image with a non cubic lattice. A collection of results was created, including (a) volume rendering of the original gray level image, (c) calculated orientation distribution and (f) diameter distribution. The main orientations are classified and a color was assigned to each class, which is visualized on the unit sphere (d). The choice and size of the classes is defined manually, thus their their fraction of the sphere surface is not corresponding to the distribution density. Additionally, the surface rendering of the c_0-thresholded classification has been overlaid with the colors of the main orientation classes (b) and a color-coded depth profile of the densities of the main orientations was created (e). The overall density is presented in black and the non assigned pixels in gray.

Concerning the diameter distributions (Figure 3.26(f)), it should be stressed that the first classes ($0.0 - 0.4\,\mu\text{m}$) are just within the lateral resolution of the microscope, and probably correspond to the sharp extremities of the fibers. Concerning the depth profile of the main orientations (e), the two peaks in the curves of the main orientations are essentially formed by the red curve, where the first peak is accentuated by the green curve. The other main orientations are uniformly distributed in depth.

For further details see Altendorf *et al.* (2011).

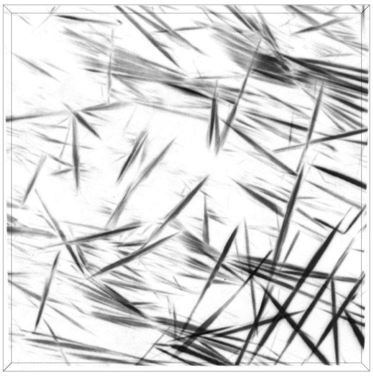

(a) Volume rendering of original image.

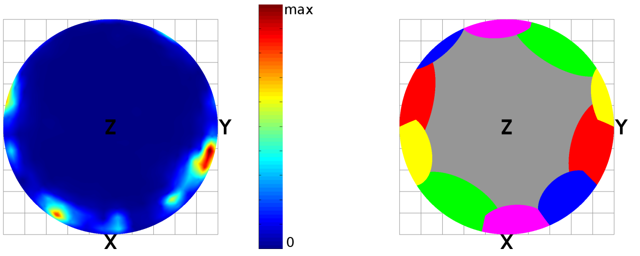

(c) Empirical orientation density function on unit sphere in stereographic view.

(d) Manual classification of main orientations.

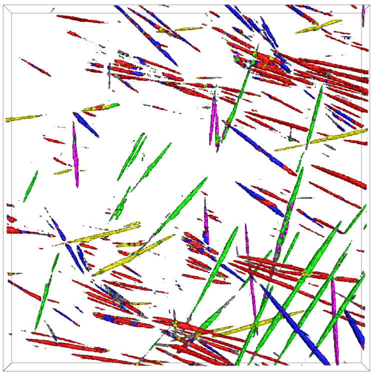

(b) Surface rendering superposed with main orientation colors.

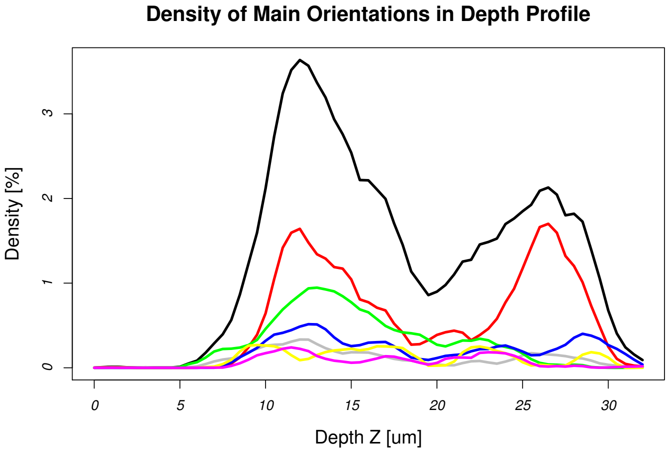

(e) Density profile of main orientations in z direction, for all fibrils (black) and for main orientations (same colours as (d)).

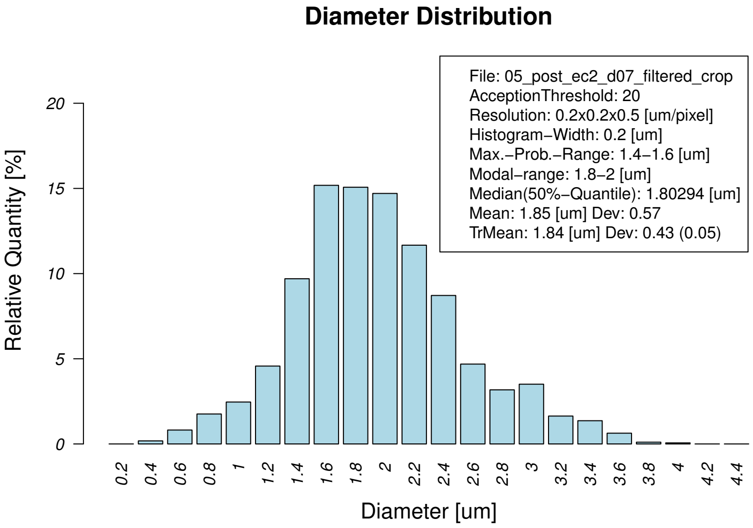

(f) Diameter Distribution

Figure 3.26.: Results for 2D SHG image of collagen. 100 mg/ml collagen in 100 mM phosphate buffer, imaged at the edge of Teflon side with 10 mW at 860 nm excitation.

4

Chapter 4.

Presentation and Interpretation of the Local Information

In the previous chapter, we presented the local analysis of fiber orientation and radius. The result of these approaches are maps including the local information for every foreground pixel. In this chapter, we discuss how the local orientations can be presented using a color coding, which is a non trivial problem in 3D. Furthermore, we estimate the empirical distribution density by a histogram. This rises two problems: first the weighting of the local information, that may distort the histogram, and second the division of the S^2 sphere surface in regular cells.

4.1. Visualization of Direction Map

In this section, we treat the question how to visualize the results of the local orientation. One possibility is the representation of tensorial data as ellipsoids at each pixel or for a coarser resolution. Here, we chose a color representation for every pixel in 2D and on a surface rendering in 3D. The presentation of three dimensional orientation data is difficult and often confusing. Nevertheless, we present a possibility to define a color code, which is useful to represent the variation with respect to some given preferred directions.

4.1.1. 2D Colorization

The visualization of a 2D direction map in color is quite straight forward. It suffices to define a π-periodic color function $f_c : \mathbb{R} \to [0, 255)^3$ for the angle θ, which fulfills $f_c(\theta) \neq f_c(\theta')$ for $\theta, \theta' \in [0, \pi)$ and $\theta \neq \theta'$. There are various functions fulfilling these conditions, we have chosen

$$f_c(\theta) = \begin{pmatrix} g_{\cos}(\theta/\pi) \\ g_{\cos}(\theta/\pi - 1/3) \\ g_{\cos}(\theta/\pi + 1/3) \end{pmatrix} \tag{4.1}$$

with

$$g_{\cos} = \begin{cases} g_{\cos}(x+1) & , x < 0 \\ 1 & , 0 \leq x < 1/6 \\ 1 + \cos(6\pi(x - 1/6)) & , 1/6 \leq x < 2/6 \\ 0 & , 2/6 \leq x < 4/6 \\ 1 - 1/2(1 + \cos(6\pi(x - 4/6))) & , 4/6 \leq x < 5/6 \\ 1 & , 5/6 \leq x < 1 \\ g_{\cos}(x-1) & , x \geq 1 \end{cases} . \tag{4.2}$$

The curves of $f_c(\theta)$ and the colorization of a centralized ring are shown in Figure 4.1.

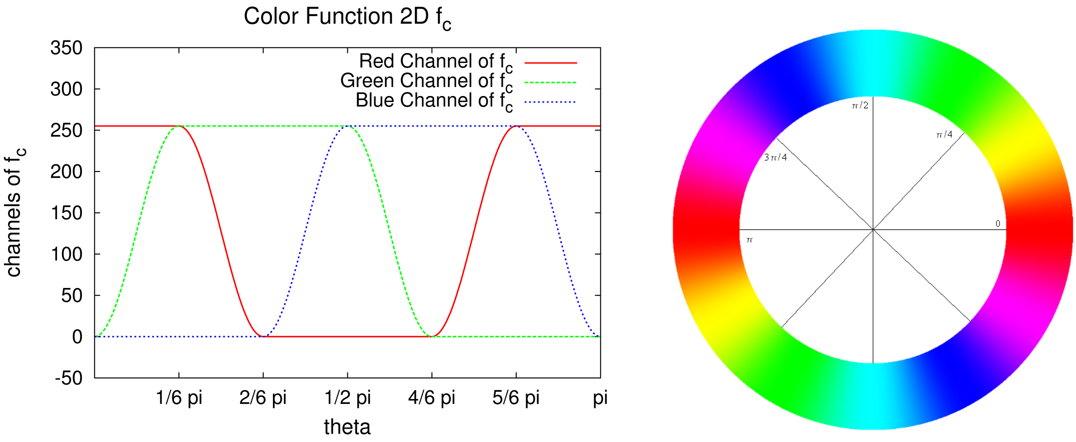

(a) 2D Color Function f_c

(b) Color on Unit Circle

Figure 4.1.: Colorized 2D angle.

4.1.2. 3D Colorization

The color assignment for 3D orientation information is not as trivial as in 2D. The conditions for the function to be periodic and injective are harder to fulfill. One possibility is to choose fix points $P_1, \dots, P_n \in S_+^{d-1}$ on the upper half sphere, assign fix colors $C_1, \dots, C_n \in \mathbb{R}^d$ to these points and compute the color for an arbitrary direction $v \in S^{d-1}$ dependent on the distances to the fixed points or its inverses.

$$C(v) = \frac{255 \cdot c(v)}{|c(v)|} \quad \text{with } c(v) = \begin{cases} C_i & \text{, for } v \in \{P_i, -P_i\} \\ \sum_{i=1}^{n} \left(\frac{\pi}{\angle_{\min}(P_i, v)} \right)^k C_i & \text{, otherwise} \end{cases}, \tag{4.3}$$

with $\angle_{\min}(p, v) = \min\{\angle(p, v), \angle(-p, v)\}$. The parameter k in the Equation (4.3) defines the influence of the surrounding points. For $k = 0$ all surrounding points participate with their colors in equal weights, disregarding the distance to the point v. For $k = \infty$ the closest point defines the color and the color mapping defines regions according to the Voronoi tessellation. The color distribution on the unit sphere and in plane cuts (for $k = 3$) is shown in Figure 4.2.

With this color definition for unit vectors in $\mathbb{R}^3$ it is possible to colorize the surface rendering. An example for random 3D synthetic data is shown in Figure 4.3. Note, that it still might happen that two different orientations are assigned to the same color. Furthermore, the sharp color transitions for $k = 3$, that we used here, yield a wide range of orientations with similar color as well as high alternation around the boundaries between two color cells. This method serves nicely to be adapted to the case of several (at most 6) preferred directions. The colored representation can then be seen as a classification into the main directions.

4.2. Estimation of Empirical Distribution Densities

Once the local radius and orientation information are computed, a convenient representation of the underlying distribution is required. There are different possibilities to find these distributions (e.g. a histogram, a kernel density function and an empirical distribution function). The easiest way to collect real-valued information like the radius is a histogram on an interval division of the region of interest. The shape and significance of a histogram depends highly on the chosen width of the

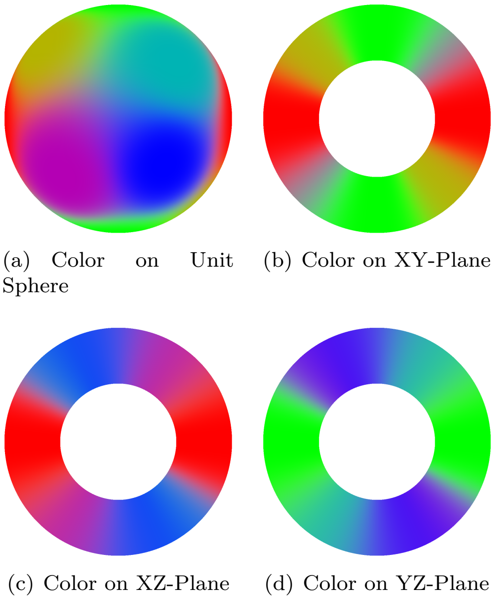
(a) Color on Unit Sphere
(b) Color on XY-Plane
(c) Color on XZ-Plane
(d) Color on YZ-Plane

Figure 4.2.: Colorized 3D orientation.

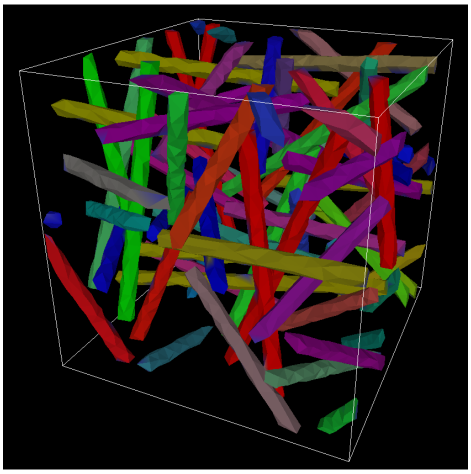

Figure 4.3.: Visualization of 3D direction map for synthetic data. Thanks to C. Kessler for the implementation and integration in the stl-viewer.

intervals used to create the histogram bins. A smoother representation can be achieved by the kernel density estimation (Parzen, 1962), which is the sum of continuous kernels centered in the particular local estimate. The resulting distribution is smoothed according to the width of the kernel. Note that the distribution will be flattened: the distribution of an underlying model has a higher variance. Another possibility is to observe the distribution instead of the density function. The empirical distribution function builds a step function of the ordered local estimates.

We have chosen the histogram for our application, as it reduces the amount of data to the number of histogram bins. This is a great advantage when dealing with large images, producing an enormous amount of local information. In the case of spherical data, received from the orientation analysis, the division of the sample space (which is the sphere surface S^2) rises a non trivial question, which will be discussed in Section 4.2.3. Collection of local information from a discretized image directly results in a volume-weighted distribution, contrary to a number-weighted one used for stochastic modeling. This topic is discussed in the following section.

4.2.1. Number-, Length- and Volume-Weighted Distributions

While discretizing an object in an image, it receives a certain amount of pixels which is related to the volume of the object. Quantification of the object creates local information at every pixel in the foreground. If we are collecting these informations from every pixel with equal weights, we end up with a volume weighted image. This can distort the distribution function, if we are observing a characteristic, which depends on the object volume. For example we can think of a size distribution of random hard spheres. Imagine two spheres with different radii $R_1 \ll R_2$. Two peaks appear in the volume-weighted distribution function with different heights. The volume of a sphere is $\frac{4}{3}\pi R^3$, thus the second peak has a much higher amplitude than the first. For those not aware of this effect, it seems that the probability of a radius R_2 is higher than those for R_1. Also for statistics as the mean radius this can cause a distortion towards higher values.

In the case of cylindrical fibers, we can convert the volume-weighted measure to a length-weighted one by dividing by a weight according to the cross section of the cylinder, thus a disc with the given radius. In the same manner, we could divide by the volume of the cylinder to achieve a number-weighted distribution. This requires the knowledge of the fiber length, which is often not available. Given a sample space Ω, divided in n classes $\omega_1, \ldots, \omega_n \subset \Omega$ and a measure $\lambda : I \to \Omega$, which assigns every pixel in a d-dimensional image $I \subset \mathbb{N}^d$ a certain statistics.
The volume-weighted histogram is calculated as

$$H_V(\omega_j) = C_V \sum_{i \in I, \lambda(i) \in \omega_j} 1,$$

the length-weighted histogram is calculated as

$$H_L(\omega_j) = C_L \sum_{i \in I, \lambda(i) \in \omega_j} \frac{1}{\pi r(i)^2}$$

and the number-weighted histogram is calculated as

$$H_N(\omega_j) = C_N \sum_{i \in I, \lambda(i) \in \omega_j} \frac{1}{\pi r(i)^2 l(i)}.$$

The values C_V, C_L and C_N are normalizing constants, such that the integral of the histogram over the sample space is equal to one: $\sum_{j=1}^{n} H(\omega_j) = 1$. Figure 4.4 shows the number-, length-, and volume-weighted version of 10 000 realizations of capsules (cylinders with round caps) with fix length and fiber radius distributed with the uniform or normal distribution.

In our approach of fiber quantification, we do not know the length of the fibers, thus we cannot calculate the number-weighted histogram. A prerequisite for computing the fiber length is to identify single fibers, which is not always possible in the application. For high resolution images with low density, we still propose a single fiber separation method in Chapter 5. For other cases, we prove in the following that if radius, length and orientation of a fiber are independent, the volume-weighted orientation distribution, as well as the length-weighted radius distribution, do not differ from their number-weighted versions (Altendorf *et al.*, 2011).

We consider a population of fibers with random radius R, length L, and orientation Ω. The number and volume weighted multivariate distributions $f(r, l, \omega)$ and $g(r, l, \omega)$ are related as follows:

$$g(r, l, \omega) = k_1 r^2 l f(r, l, \omega) \tag{4.4}$$

with a normalization constant k_1 given by

$$k_1 = \frac{1}{\iiint r^2 l f(r, l, \omega) \, \mathrm{d}r \, \mathrm{d}l \, \mathrm{d}\omega}. \tag{4.5}$$

The marginal distributions of the orientation $f(\omega)$ and $g(\omega)$ are related by the following expression, deduced from Equation (4.4):

$$g(\omega) = k_1 \iint r^2 l f(r, l, \omega) \, \mathrm{d}r \, \mathrm{d}l. \tag{4.6}$$

If, for each fiber, the orientation is statistically independent of the radius and of the length, we have the decomposition

$$f(r, l, \omega) = f(\omega) f(r, l) \tag{4.7}$$

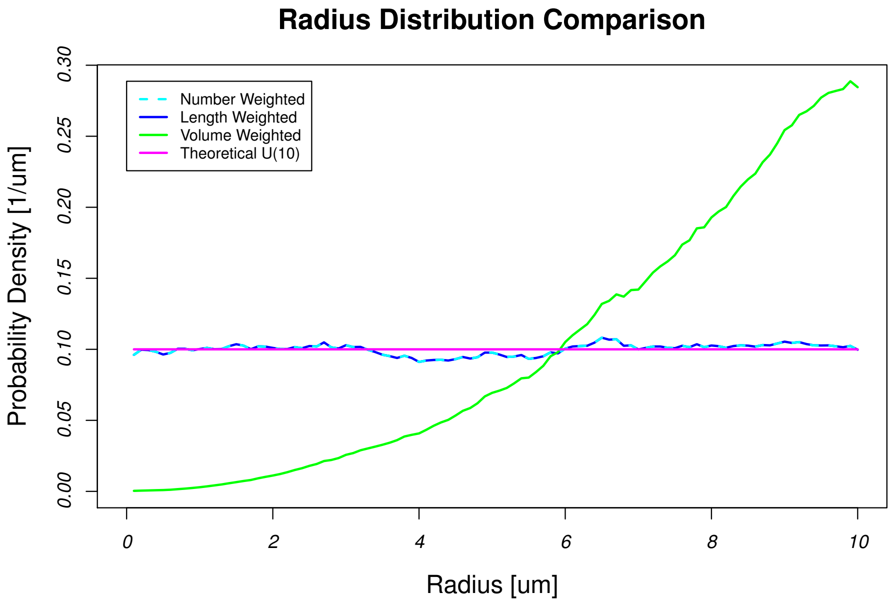

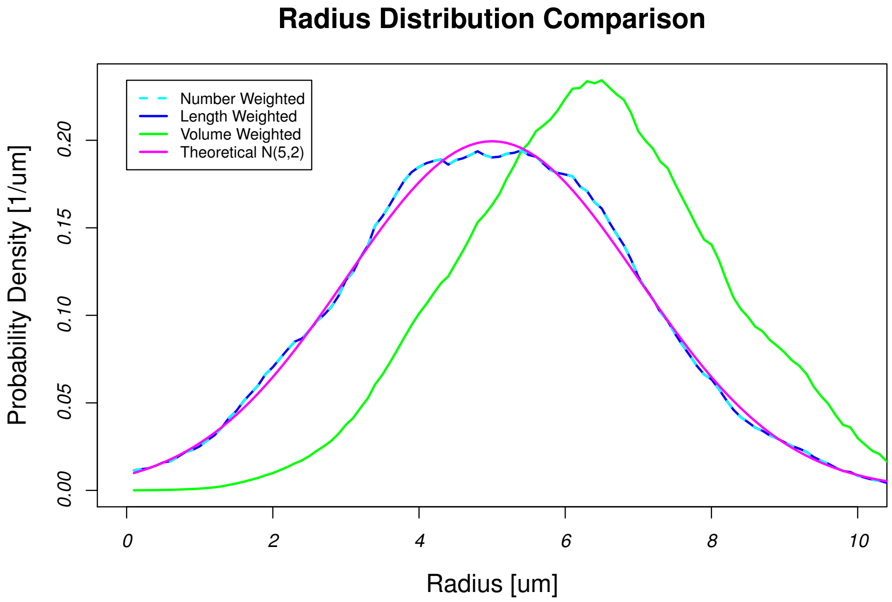

Figure 4.4.: Comparison of number-, length-, and volume-weighted version of a theoretical uniform and normal distributed radius.

and

$$g(\omega) = f(\omega)k_1 \iint r^2 l f(r,l)\,\mathrm{d}r\,\mathrm{d}l = f(\omega), \tag{4.8}$$

as

$$k_1^{-1} = \iiint r^2 l f(r,l) f(\omega)\,\mathrm{d}r\,\mathrm{d}l\,\mathrm{d}\omega = \iint r^2 l f(r,l) \left(\int f(\omega)\,\mathrm{d}\omega \right) \mathrm{d}l\,\mathrm{d}r. \tag{4.9}$$

Per definition $f(\omega)$ is normalized, thus $\int f(\omega)\,\mathrm{d}\omega = 1$. It follows that

$$k_1^{-1} = \iint r^2 l f(r,l)\,\mathrm{d}l\,\mathrm{d}r, \tag{4.10}$$

which eliminates the second constant in Equation (4.8). Therefore, the assumption of independence involves that the volume- and number-weighted distributions are the same. This result is true, even if the length and the radius of fibers are not independent.

Similarly, we can derive a relationship between the length ($h(r,l)$) and number ($f(r,l)$) weighted joint distributions of the random radius R with the random length L. We have

$$h(r,l) = k_3 \int l f(r,l,\omega)\,\mathrm{d}\omega = k_3 l \int f(r,l,\omega)\,\mathrm{d}\omega = k_3 l f(r,l), \tag{4.11}$$

with

$$k_3 = \frac{1}{\iint l f(r,l)\,\mathrm{d}l\,\mathrm{d}r}. \tag{4.12}$$

When the random length L is independent of the radius R, we have the decomposition

$$f(r,l) = f(l) f(r) \tag{4.13}$$

and therefore $k_3 = \frac{1}{\int_0^\infty l f(l)\,\mathrm{d}l} = \frac{1}{E[L]}$, with $E[L]$ being the number-weighted expectation of the fiber length. The marginal radius distribution becomes

$$h(r) = k_3 \int_0^\infty h(r,l)\,\mathrm{d}l = f(r) k_3 \int_0^\infty l f(l)\,\mathrm{d}l = k_3 E[L] f(r) = f(r). \tag{4.14}$$

Thus, the length and number weighted joint distributions of the random radius R are the same. This result is true, even if the radius and length are not independent of the orientation of fibers.

4.2.2. Radius Distribution

The radius distribution is represented by a weighted histogram with bin sizes h_w. Additionally, to the weight transforming the histogram in a length-weighted version, we can make use of the quality measures. In Equation 3.26 (page 27), we presented the ratio of eigenvalues R_λ as a quality measure for the local orientation and thus indirectly also for the local radius. In Section 3.3.3, the classification in foreground and background is presented, which yields another quality measure c. We can respect both by defining the weight of quality $q(i) = R_\lambda(i)c(i)$.

Thus, the masked foreground voxels contribute to the histogram with a weight of quality $q(i)$ divided by the approximated fiber cross section $\pi r(i)^2$. The relative quantity of a histogram bin $b(k) = ((k-1)h_w, kh_w]$ is then defined as:

$$H_r(k) = C_r \sum_{i \in I, r(i) \in b(k), c(i) > c_0} \frac{q(i)}{\pi r(i)^2}, \tag{4.15}$$

where C_r is a normalizing factor, such that the integral over the whole histogram is equal to one: $\sum_{k=1}^{\infty} H_r(k) = 1$. The histogram is mostly presented as the histogram step function:

$$h(r) = H_r(\lceil r/h_w \rceil). \tag{4.16}$$

It is often difficult to choose a reasonable interval for the histogram. If the observation is split in too many bins (h_w small) the trend of the overall distribution is not visible. For a too large value for h_w, it may happen that several peaks merge to one and furthermore the accuracy of the maxima is decreasing. A more smooth progression can be achieved by the empirical distribution function with a rather small value for h_w:

$$F(r) = \sum_{k=1}^{\lceil r/h_w \rceil} H_r(k). \tag{4.17}$$

A smooth approximation of the density function is the numerical derivative of F_r, with an interval width parameter $h_d \geq h_w$:

$$f(r) = \frac{F(r + h_d/2) - F(r - h_d/2)}{h_d}. \tag{4.18}$$

We advise to choose a small value for h_w around one tenth of the pixel sampling and h_d equal to the pixel sampling. The parameter h_d represents the level of smoothing for the empirical density function f. For $h_d \leq h_w$ there is no smoothing and the empirical density function equals the histogram step function h. For a too large value for h_d, the smoothing can again merge close peaks, but in contrast to the histogram the accuracy of the maximum positions keeps intact.

4.2.3. 3D Orientation Histograms

For the orientation histogram, the sphere surface is divided in m cells $C_1, \ldots, C_m \subset S^2$. The partition in equally sized and formed cells is a non trivial task and discussed in detail in the following section. Again, the masked foreground voxels contribute to the histogram with a weight set to their quality index, so the distribution is defined by:

$$H_o(k) = C_o \sum_{i \in I, o(i) \in C_k, c(i) > c_0} q(i), \tag{4.19}$$

where C_o is the normalizing factor, so that the integral over the distribution is equal to one. The orientation distribution is volume-weighted. The division of the sphere surface in equally cells is not trivial and discussed in the following section.

Division of Sphere Surface

For some directional operations on 3D images and for creating a histogram on the sphere surface, it is necessary to divide the surface in a finite number of evenly formed cells or to define evenly placed points. In 2D this is trivial as we can divide the circle in an arbitrary number of equal sectors. Unfortunately, it is nontrivial to transfer this to the 3D case.

In the following, we discuss the state-of-the-art of this problem and assign a name to every method, that will reappear in the section of comparison.

Fliege. Fliege & Maier (1996) propose a method based on a forced bias packing, which starts with a certain amount of random points. By applying forces of repulsion, the distances between neighbors are maximized iteratively. Wirjadi (2009) adapted this approach to evenly place points on the upper hemisphere.

Sloane. Furthermore, Hardin *et al.* (2000) developed a method to optimize one of three different aspects for a set of n points:

- **Packing:** maximize the distance between pairs of the n points.
- **Covering:** minimize the distance between any point on the sphere surface to one of the n points.
- **Maximal Volume Arrangement:** maximize the volume of the convex hull on the n points.

This method can generally optimize any amount of points, but their are certain amounts of points having better properties in the given aspects. Therefore, it only makes sense to work with the points given on their website (Hardin *et al.*, 1994).

HEALpix. A third approach is given in Górski *et al.* (2005), where a diamond pattern is projected on the sphere surface. In the following, we will describe an even simpler approach, which projects a grid from the unit cube.

QuadSphere. The idea of mapping the cube faces on the sphere surface was already studied by the NASA (Chan & O'Neill, 1975, O'Neill & Laubscher, 1976, White & Stemwedel, 1992) and was called the Quadrilateralized spherical cube (QuadSphere). The fundamental difference between the QuadSphere and our approach is the mapping, which we will discuss in detail in the paragraph on page 62.

The last three methods have similar ideas and the great advantages that for an arbitrary point on the sphere surface, the index of the according cell can be computed directly in constant time.

Grid Projection

The division of the 2D circle can be projected on the surrounding unit square. If we expand this division to a grid on the unit cube, we can project it on the unit sphere to get a division of the sphere surface. This construction is visualized in Figure 4.5. Later we observe that the area fraction of the cells can be optimized by displacing minimally the division lines of the grid. There are now different ways to define points and cells on this grid:

Config. 1: points = grid points, cells = their Voronoi cells

Config. 2: cells = grid cells, points = middle grid nodes of a twice finer grid

Config. 3: points = points from Config. 2., cells = their Voronoi cells

Config. 4: cells = optimized grid cells, points = middle grid nodes of a twice finer grid

Config. 5: points = points from Config. 4., cells = their Voronoi cells

First, we studied the nodes of the grid and their Voronoi cells on the unit sphere, which build a partition of the sphere surface.

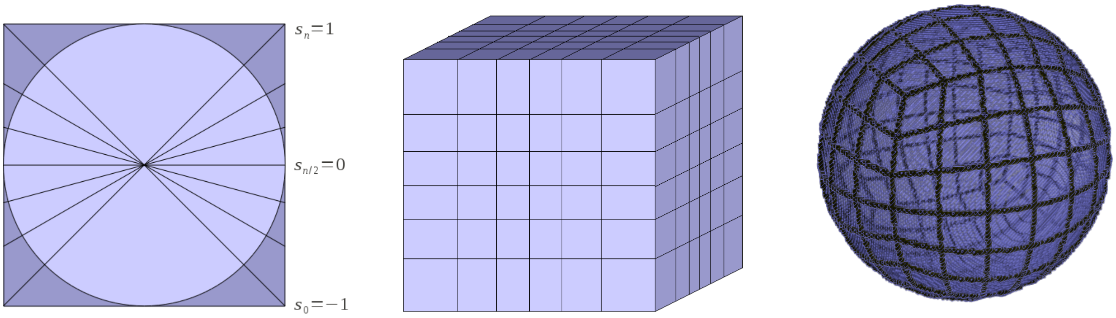

Figure 4.5.: Transfer of the 2D angle division over the 3D cube to the sphere.

For a division index $n \in \mathbb{N}^+$, meaning the cube or square side is divided into n segments, we have the following steps on the side of the square $\in [-1, 1]$:

$$t(i) = \tan\left(\frac{(2i-n)\pi}{4n}\right), \text{ for } i \in I_{n+1} = \{0, \dots, n\}\,. \tag{4.20}$$

The grid nodes on the cube (Config. 1) are therefore:

$$P_{\text{cube}}(n) = \{\pm(t(i), t(j), 1) \mid i, j \in I_{n+1}\} \cup \{\pm(t(i), 1, t(j)) \mid i, j \in I_{n+1}\} \cup \{\pm(1, t(i), t(j)) \mid i, j \in I_{n+1}\}\,. \tag{4.21}$$

The points on the unit sphere are the normalized vectors of $P_{\text{cube}}(n)$:

$$P_1(n) = \left\{\frac{v}{|v|}, v \in P_{\text{cube}}(n)\right\} \tag{4.22}$$

The number of points is $|P_1(n)| = |P_{\text{cube}}(n)| = n^2 * 6 + 2$, except for $n = 0$ in which case there are 6 points.

For a set of points on the unit sphere without given division, we define a division by the Voronoi cells. Let $P = \{p_i, i \in \{1, \dots, m\}\} \subset S^2$ be the set of points on the unit sphere surface. We define the Voronoi cell $V_P(p_i)$ generated by a point p_i as all points on the sphere surface having p_i as the closest point to a metric d:

$$V_P(p_i) = \{p \in S^2 \mid d(p, p_i) = \min_{j \in \{1,\dots,m\}} d(p, p_j)\}. \tag{4.23}$$

Division of the Sphere Surface Created by a Grid

For Config. 2 and 4, we consider the division defined by the grid projection itself. Therefore, the sphere surface is divided in $6n^2$ cells with the indices $(s, i, j), s \in \{0, 1, 2\}, i, j \in I_n = \{0, \dots, n-1\}$ and supporting vectors

$$p(s,i,j) = \begin{cases} (1, t(i+\frac{1}{2}), t(j+\frac{1}{2})) & , \text{ for } s = 0 \\ (t(i+\frac{1}{2}), 1, t(j+\frac{1}{2})) & , \text{ for } s = 1\,. \\ (t(i+\frac{1}{2}), t(j+\frac{1}{2}), 1) & , \text{ for } s = 2 \end{cases} \tag{4.24}$$

Figure 4.6 shows an example of the cell indices, the supporting vectors and the projection on the unit sphere, where the cube side is divided in $n = 6$ areas. The black grid on the cube represents the division lines of the cells, whereas the grid nodes of the red grid indicate the supporting vectors,

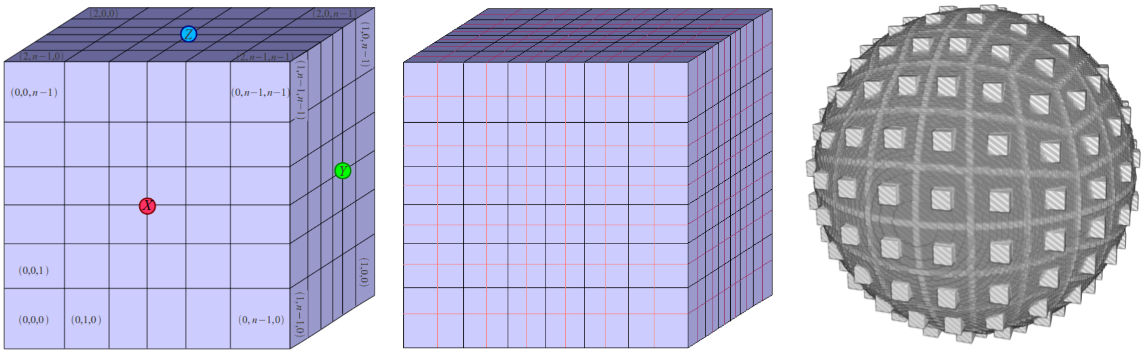

(a) Indices given to the cells

(b) Division grids on the unit cube

(c) Divsion grid and supporting center on the unit sphere

Figure 4.6.: Division of the unit sphere with $n = 6$

which are presented as little cubes on the unit sphere.

This division can be used to efficiently calculate the histogram of a direction distribution in linear time with respect to the amount of continuous directions. The supporting vectors of each cell enable a smooth surface rendering of the direction distribution on the unit sphere. The inverse function, to calculate the cell index for an arbitrary direction $v \in S^2$, projects v from the unit sphere on the unit cube $w = \frac{v}{max\{v_x, v_y, v_z\}}$. From this point w it is possible to compute the index of the cell, which is represented by a vector (s, i, j), where $s \in \{0, 1, 2\}$ indicates the cube face and i and j the division index on the plane. The cell index is derived from w as follows:

$$\text{Cell}(w) = \begin{cases} (0, \text{Index}(w_y), \text{Index}(w_z)) & , |w_x| = 1 \\ (1, \text{Index}(w_x), \text{Index}(w_z)) & , |w_y| = 1 \\ (2, \text{Index}(w_x), \text{Index}(w_y)) & , |w_z| = 1 \end{cases} \tag{4.25}$$

with

$$\text{Index}(t) = min\left\{ \left\lfloor \frac{1}{2} \left(\frac{4n}{\pi} tan^{-1}(t) + n \right) \right\rfloor , n - 1 \right\}. \tag{4.26}$$

Optimal Division

It turns out that the cells in the center of a cube face tend to be larger than those on the border of the cube face. Therefore, we tried to optimize the equality of the size of the cell surfaces by choosing the division lines of the grid accordingly. The surface of one projected cube face is $\frac{4\pi}{6}$, thus the first line on the cube face cuts a slice with an optimal area of $\frac{4\pi}{6n}$. The surface of a spherical quadrangle, with inner angles α, β, γ and δ, is $A = \alpha + \beta + \gamma + \delta - 2\pi$. In the slice of a projected cube face, there is twice the angle α_0 between the cube boundaries and twice the angle β_1, between the first line and the cube boundary (as shown in Figure 4.7). Thus, the surface is $A_0 = 2\alpha_0 + 2\beta_1 - 2\pi$. The angles between two crossing grid lines are computed from the orthogonal vectors n_1 and n_2 of the plane defined by the line and the origin: $\cos\beta = n_1 \cdot n_2$. Note, that we still need to be aware of which side of the crossing is concerned.

To define the grid division, we consider first the positive x face of the cube. The upper cube boundary (in z direction) has the orthogonal vector $n_\perp$ defined by the spherical coordinates $\theta_\perp = 3\pi/4$ and $\phi_\perp = 0$. The left cube boundary (in -y direction) has the orthogonal vector n_0 defined by $\theta_0 = \pi/2$

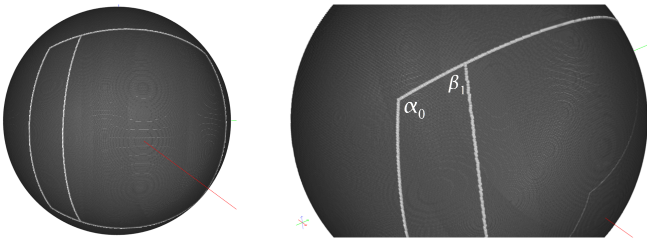

Figure 4.7.: Angles α_0 and β_1 in optimal grid division.

and $\phi_0 = \pi/4$; the right cube boundary extends to $\phi_n = 3\pi/4$. A vertical line keeps $\theta = \pi/2$ and $\phi = l\pi$ with $l \in \left[\frac{1}{4}, \frac{3}{4}\right]$. For the included angle between the upper cube boundary (orthogonal to $n_\perp$) and a vertical line (orthogonal to n), it yields

$$\begin{aligned}
\cos\beta &= n_\perp \cdot n && (4.27)\\
&= \sin\theta_\perp \cos\phi_\perp \sin\theta \cos\phi + \sin\theta_\perp \sin\phi_\perp \sin\theta \sin\phi + \cos\theta_\perp \cos\theta && (4.28)\\
&= \sin\left(\tfrac{3\pi}{4}\right)\cos(0)\sin\left(\tfrac{\pi}{2}\right)\cos(l\pi) + \sin\left(\tfrac{3\pi}{4}\right)\sin(0)\sin\left(\tfrac{\pi}{2}\right)\sin(l\pi) + \cos\left(\tfrac{3\pi}{4}\right)\cos\left(\tfrac{\pi}{2}\right) && (4.29)\\
&= \frac{1}{\sqrt{2}}\cos(l\pi) && (4.30)
\end{aligned}$$

To calculate the edge angle α_0, we consider $\pi - \beta$ for $l = \frac{1}{4}$. Thus, it yields $\cos(\pi - \alpha_0) = \frac{1}{\sqrt{2}}\cos(\frac{\pi}{2})$. This implies $\alpha_0 = \frac{2\pi}{3}$.

Considering the desired area for A_0, we receive the equation

$$2\beta_1 - 2\alpha_0 - 2\pi = \frac{4\pi}{6n} \quad \Leftrightarrow \quad \beta_1 = \frac{\pi}{3}(\frac{1}{n} + 1). \tag{4.31}$$

We can generalize this for the ith line, which cuts a slice of area $\frac{4i\pi}{6n}$ and has therefore

$$\beta_i = \frac{\pi}{3}(\frac{i}{n} + 1). \tag{4.32}$$

Note, that we can expand i to the real-valued interval $[0, n]$, which is used to compute the supporting vectors of the cell. By inverting the Equation 4.30, we obtain

$$l_i = \frac{\cos^{-1}(\sqrt{2}\cos\beta_i)}{\pi}. \tag{4.33}$$

By respecting the index ordering defined in Equation 4.24 and presented in Figure 4.6(a), we define the orthogonal vectors of the division lines by their polar coordinates as

$$\begin{aligned}
n_i:&\quad \theta_i = \frac{\pi}{2},\ \phi_i = l_i\pi && (4.34)\\
n_j:&\quad \theta_j = (\frac{3}{2} - l_j)\pi,\ \phi_j = 0. && (4.35)
\end{aligned}$$

The supporting vector of the cell (s, i, j) is

$$v(s,i,j) = \begin{cases} -n_{i+0.5} \times n_{j+0.5} & \text{, for } s = 0 \\ (v_y(0,i,j), v_x(0,i,j), v_z(0,i,j)) & \text{, for } s = 1 \\ (v_y(0,i,j), v_z(0,i,j), v_x(0,i,j)) & \text{, for } s = 2 \end{cases}. \tag{4.36}$$

Assuming that the inverse tangent function $\tan^{-1}$ is mapping in $(-\pi/2, \pi/2]$, we can calculate the cell index for an arbitrary vector $v \in S^2$ by:

$$Cell_{\mathrm{opt}}(v) = \begin{cases} (0, Index_i(-\frac{v_x}{v_y}), Index_j(-\frac{v_z}{v_x})) & \text{, for } |v_x| = \max\{|v_x|, |v_y|, |v_z|\} \\ (1, Index_i(-\frac{v_y}{v_x}), Index_j(-\frac{v_z}{v_y})) & \text{, for } |v_y| = \max\{|v_x|, |v_y|, |v_z|\} \\ (2, Index_i(-\frac{v_z}{v_x}), Index_j(-\frac{v_y}{v_z})) & \text{, for } |v_z| = \max\{|v_x|, |v_y|, |v_z|\} \end{cases} \tag{4.37}$$

with

$$Index_i(t) = \begin{cases} \left\lfloor \left(\frac{2\tan^{-1}(t)}{\pi} - \frac{1}{2} \right) n \right\rfloor & \text{, for } \tan^{-1}(t) \geq 0 \\ \left\lfloor \left(\frac{2\tan^{-1}(t)}{\pi} + \frac{3}{2} \right) n \right\rfloor & \text{, for } \tan^{-1}(t) < 0 \end{cases} \tag{4.38}$$

$$Index_j(t) = \left\lfloor \left(\frac{1}{2} - \frac{2\tan^{-1}(t)}{\pi} \right) n \right\rfloor \tag{4.39}$$

Quadrilateralized Spherical Cube - Similarities and Differences

The idea of mapping a grid from the cube face to the sphere was firstly studied by Chan & O'Neill (1975), O'Neill & Laubscher (1976) and detailed in Patt (1993), White & Stemwedel (1992). The main edges of the cube are projected in the same manner as explained in our approach. The great difference lies in the mapping from the face to the sphere surface. In our approach, we use a tangential mapping treating x and y direction independently. The QuadSphere approach uses a rather complex mapping defined in Patt (1993) for Cartesian coordinates $(x, y) \in [0, 1]^2, x > y$ on the 2D square ($[-1, 1]^2$) (representing the x cube face) to coordinates $(q, r, s) \in S^2$ of the sphere surface by:

$$\frac{s}{r} = \frac{\sin\left(\frac{\pi}{12}\frac{y}{x}\right)}{\cos\left(\frac{\pi}{12}\frac{y}{x}\right) - \frac{1}{\sqrt{2}}} \tag{4.40}$$

$$q = 1 - x^2 \left(1 - \frac{1}{\sqrt{2 + \left(\frac{s}{r}\right)^2}} \right) \tag{4.41}$$

$$r = \frac{x}{|x|} \sqrt{\frac{1 - q^2}{1 + \left(\frac{s}{r}\right)^2}}. \tag{4.42}$$

These equations are defined only on an eighth of the square, other values can be achieved by intelligently reflecting or rotating to this case (switching x and y as well as the results r and s, or inverting signs respectively). The mapping from the sphere to the square is then defined by:

$$x = \sqrt{\frac{1 - q}{1 - \frac{1}{\sqrt{2 + \left(\frac{s}{r}\right)^2}}}} \tag{4.43}$$

$$\frac{y}{x} = \frac{12}{\pi} \left[\tan^{-1}\left(\frac{s}{r}\right) - \sin^{-1}\left(\frac{2}{\sqrt{2r^2 + 2s^2}}\right) \right]. \tag{4.44}$$

Note, that this kind of mapping distorts structure as shown in Figure 4.8. In our approach straight lines on the square are projected to lines on the sphere (intersections between a plane through the origin and the sphere), presented by the red lines. The QuadSphere approach distorts the original lines. The result is presented by the gray lines.

The number of cells in the division of the QuadSphere is defined to $6 \cdot 2^{2N}$, with $N \in \mathbb{N}_0^+$. Still, with the defined mapping we can easily generalize it to the finer division rate of $6n^2$ as used before.

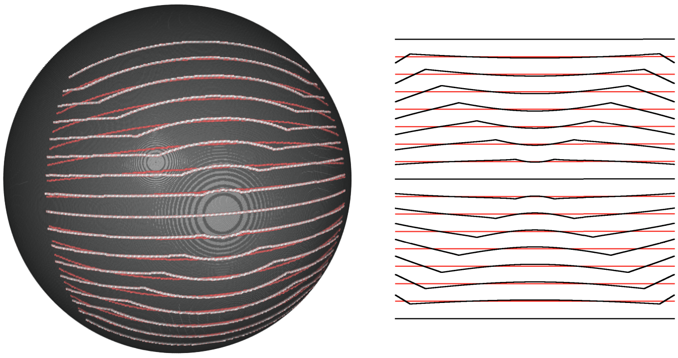

Figure 4.8.: Distortion of lines by the QuadSphere approach. In red: projected lines with our approach, in gray: projected lines with the QuadSphere approach.

Comparison of the Different Approaches

Figure 4.9 shows a rendering of the sphere surface partition of different approaches, for approximately 200 points. As every approach can realize only specific numbers of points, the values vary from 192 to 272. Note, that the visualization of Config. 2 and 3 are skipped as they are visually nearly identical to Config. 4 and 5.

For Config. 4 (Figure 4.9(b)), the regular structure of the cubic division grid is observed very nicely. For Config. 2 and 4, the HEALpix and the QuadSphere, we can define a reasonable adjacency systems on the points (or cells) with a fix number of 4 neighbors. Config. 5 shows the Voronoi cells with the same points as Config. 4. We observe that the Voronoi division is surprisingly far from the grid division. That means for an arbitrary point on the sphere surface, the assignment to a grid cell is not always the one with the closest supporting vector. This is a disadvantage of the grid division against the Voronoi division, but one needs to take into account that the assignment of a vector is computable in constant time, whereas with the Voronoi division we need to calculate m distances to assign the vector to one of the m points.

The points from the approach of the HEALpix project a diamond structure on the sphere surface. On the original division, there is also the possibility to define an adjacency system with fix amount of neighbors, with the same disadvantage, that the assignment is not always to the closest point. In Figure 4.9(f), the Voronoi cells of the HEALpix points are shown, which have (similar to Config. 3 and 5) a quite irregular structure. The Voronoi cells of Fliege & Maier (1996) as well as Hardin *et al.* (2000) are made of pentagons and hexagons (like a truncated icosahedron, used for the pattern of a soccer ball). The structure seems to be very regular.

To compare the division of the sphere, we create some statistics on the cell area, perimeter, number of nodes, length of edges, the inner angles between cell edges and the circular shape factor (circularity, Stoyan & Stoyan (1992)). Let m be the number of cells and A_i their area for $i \in \{1, \dots m\}$. The expectation of the cell area $\mathbb{E}[A]$ is desired to be stable around the theoretical mean value $4\pi/m$. The variance $\mathrm{Var}(A) = \frac{1}{m}\sum_{i=1}^{m}(A_i - \mathbb{E}[A])^2$ indicates the stability of the cell area. To get a comparable measure independent of the number of points m, we consider the variation coefficient $\sqrt{\mathrm{Var}(A)}/\mathbb{E}[A]$. For a cell limited by the k points $v_0, \dots, v_{k-1}$ with supporting vector p, we compute the variation coefficient of the following properties:

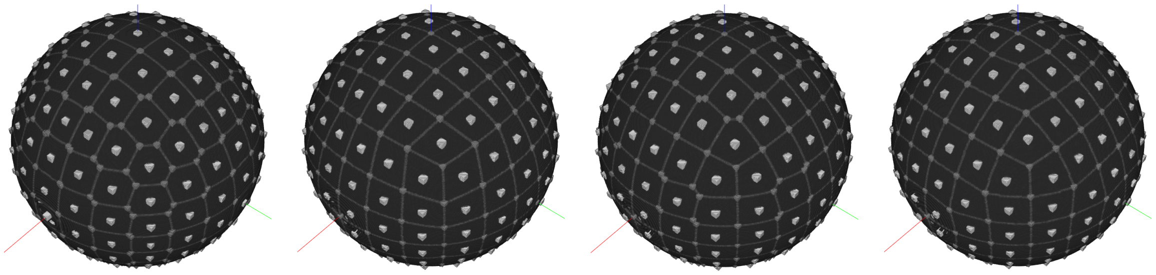

(a) Config. 1: grid nodes, $n = 6$, 218 points

(b) Config. 4: optimal cell points with grid faces, $n = 6$, 216 points

(c) Config. 5: optimal cell points with Voronoi cells, $n = 6$, 216 points

(d) QuadSphere division, 216 points

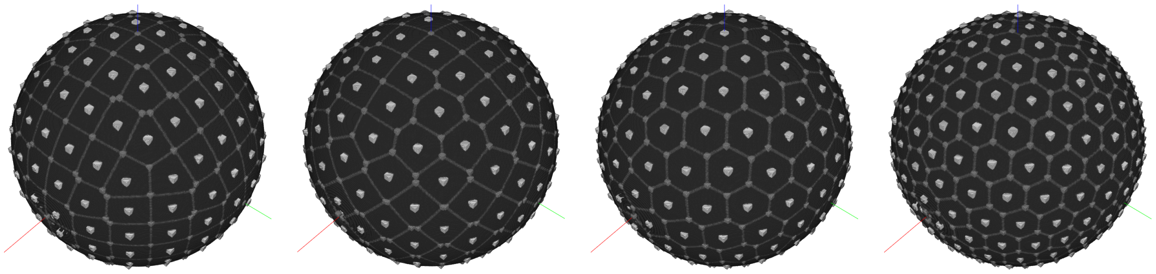

(e) QuadSphere points with Voronoi cells, 216 points

(f) HEALpix, 192 points

(g) Fliege, 196 points

(h) Sloane - Covering, 272 points

Figure 4.9.: Visualization of division for different approaches for approximately 200 points.

Perimeter	P	$= \sum_0^{k-1} l_i$
Lengths	L	$= \{l_0, \dots, l_{k-1}\}$
Number of Nodes	k	
Inner Angles	Θ	$= \{\alpha_0, \dots, \alpha_{k-1}\}$
Area	A	$= \sum_0^{k-1} \alpha_i - (k-2)\pi$
Circularity	f_{circ}	$= 4\pi A / P^2$

with $l_i = d(v_i, v_{[(i+1) \mod k]})$, $\alpha_i = \pi - \cos^{-1}(n_i \cdot n_{[(i+1) \mod k]})$ and $n_i = \pm v_i \times v_{[(i+1) \mod k]}$ such that $n_i \cdot p > 0$.

Figure 4.10 shows the variation coefficient of the cell area for different approaches. This was the characteristic optimized in Config. 4, which means for a mapping, treating the coordinates x and y independently and therefore conserving the line structure, these are the best possible results. We can observe that the optimal grid division can compete with the alternative existing approaches. We also see that the Voronoi cells (dashed lines) are slightly better than the grid division. Similar results yield the statistics of the perimeter in Figure 4.11.

In Figure 4.12, all the grid division approaches win, as the amount of cell nodes is fixed to 4, this would also yield for the HEALpix, considering the grid division (which we did not implement). Considering the length of all cell edges (Figure 4.13), we see that the Voronoi cells have high variations as the edges are varying. For the grid divisions edge lengths are more stable, just as well as for the icosahedral divisions. The last obviously have the lowest variation in the inner angles (Figure 4.14), followed by the grid division and the Voronoi cells are on the last positions. This ranking is also applicable on the statistics of the circular shape factor in Figure 4.15.

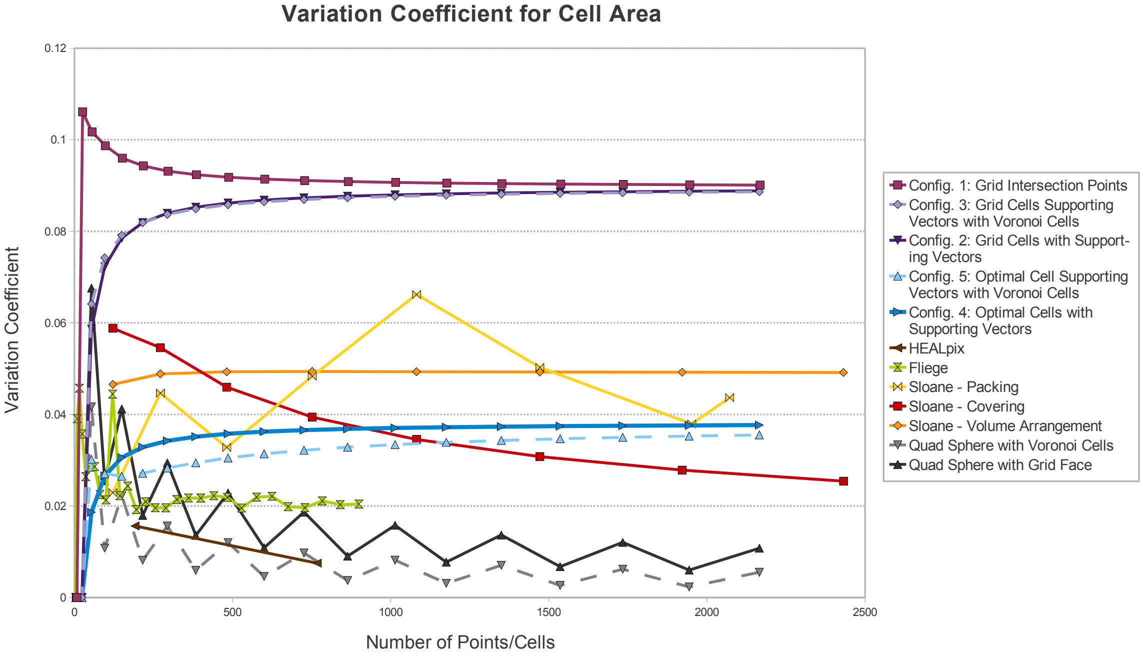

Figure 4.10.: Comparison of the variance coefficient of the cell area of the different tessellations of the unit sphere surface.

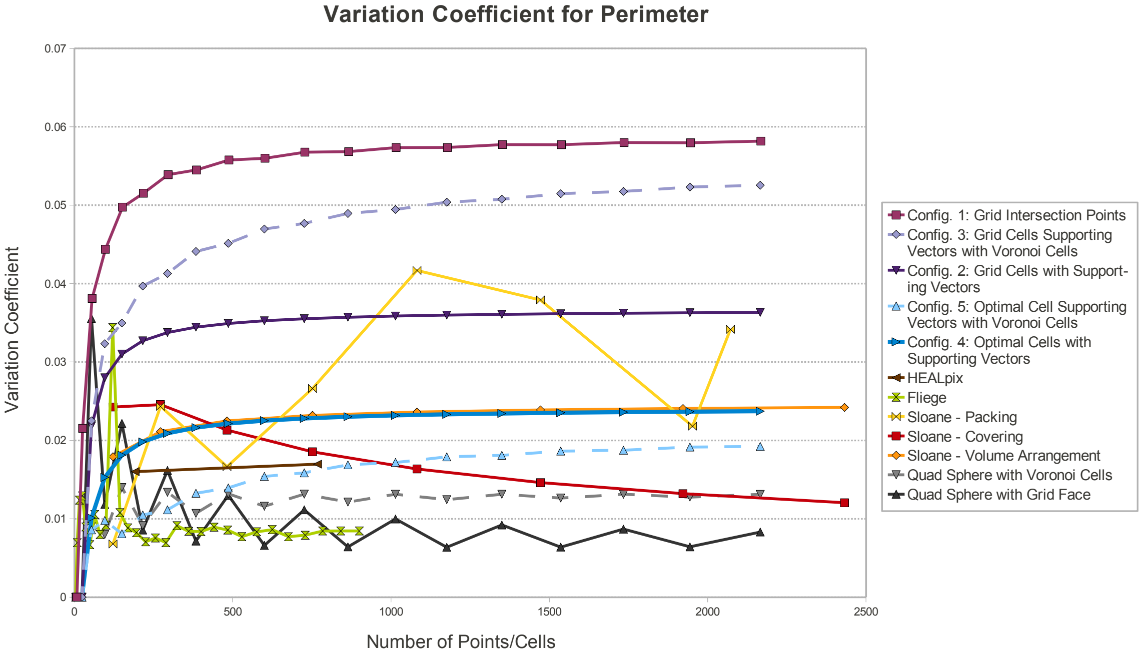

Figure 4.11.: Comparison of the variance coefficient of the cell perimeter of the different tessellations of the unit sphere surface.

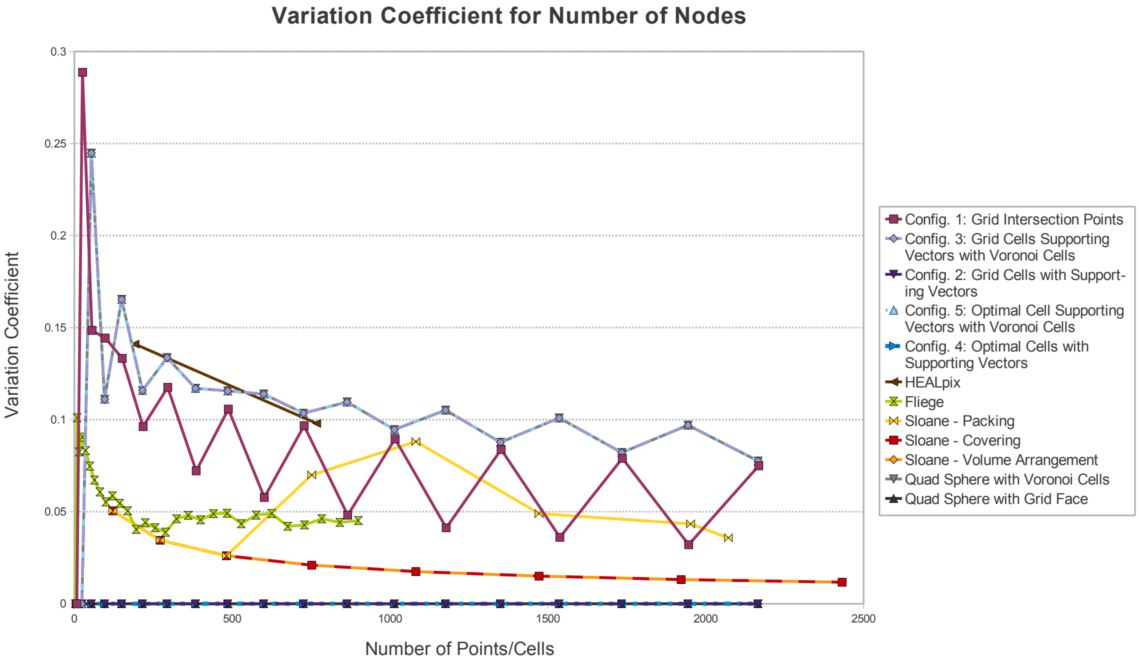

Figure 4.12.: Comparison of the variance coefficient of the number of nodes of the cells in the different tessellations of the unit sphere surface.

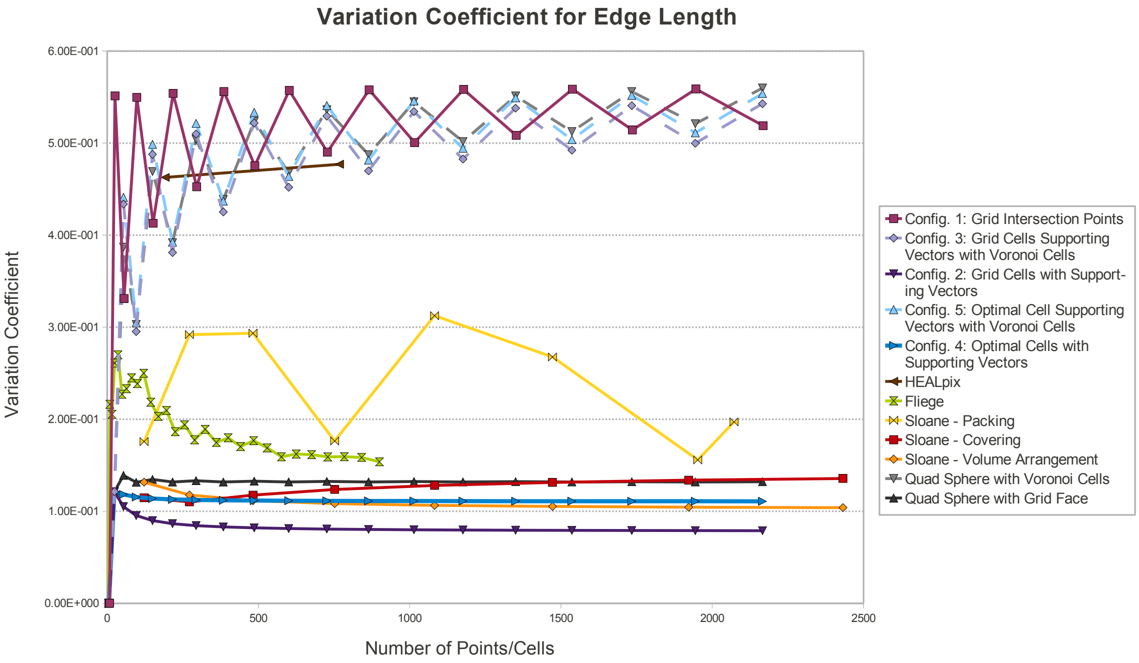

Figure 4.13.: Comparison of the variance coefficient of the length of the edges of the cells in the different tessellations of the unit sphere surface.

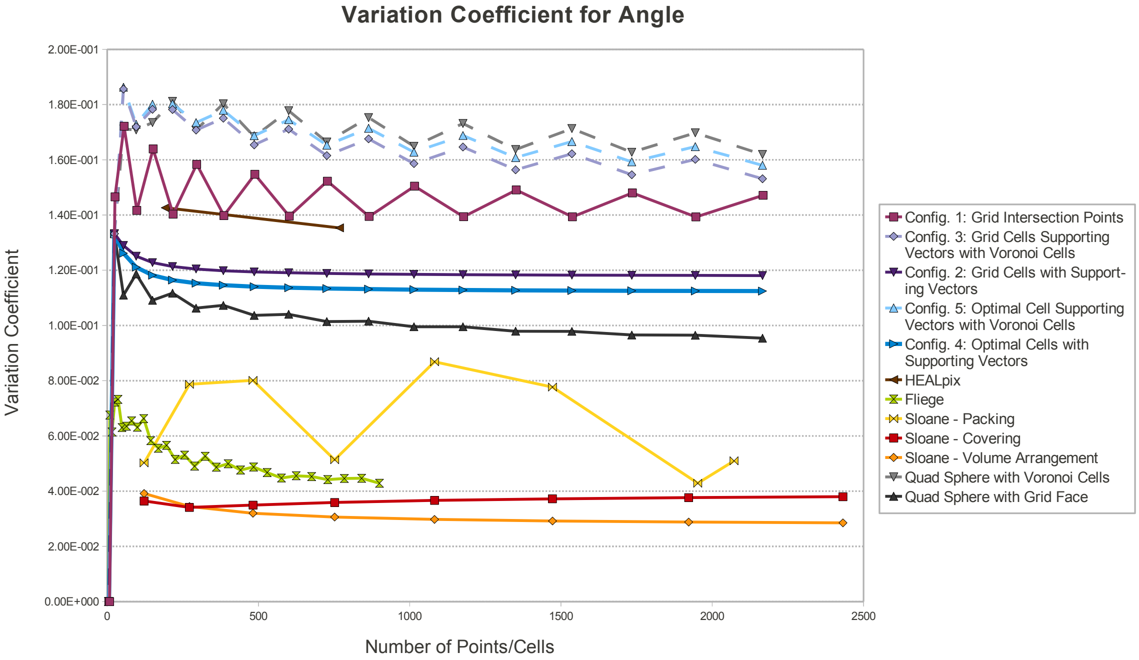

Figure 4.14.: Comparison of the variance coefficient of inner angles in the cells of the different tessellations of the unit sphere surface.

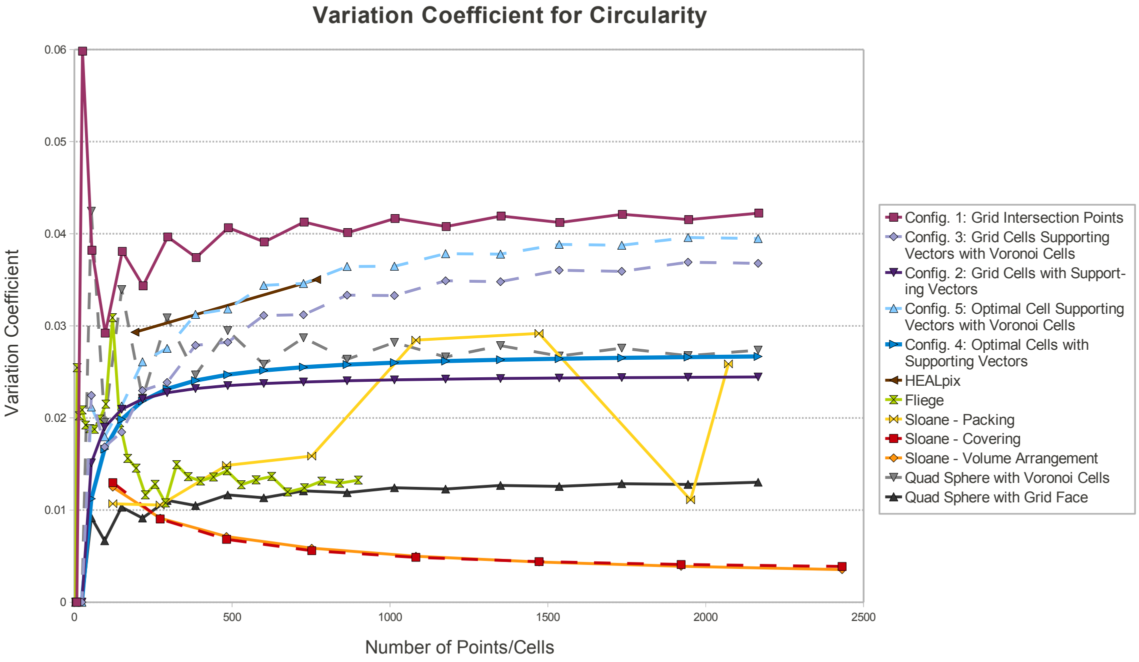

Figure 4.15.: Comparison of the variance coefficient of circularity shape factor of the cells of the different tessellations of the unit sphere surface.

Considering the advantage of the grid division in simple construction and direct cell assignment, the choice of the optimal cell division is recommended. In the following example of direction distributions, we will make use of the presented method.

5

Chapter 5.

Single Fiber Separation

In the previous chapter, we presented approaches for local analysis of fiber orientation and radius. Further characteristics of the fiber system remain unknown, as fiber length and curvature or the number-weighted distribution of orientation and radius. To achieve this kind of knowledge, it is necessary to recognize each fiber, which rises the problem of fiber separation. Fibrous materials usually form multiply connected networks. Thus, standard labeling techniques for connected components are not suitable to separate fibers.

Talbot *et al.* (2000) propose a method on 2D images, which recognizes parts of the fiber cores from the skeleton and reconnects them afterwards. The skeletonization of fibers already poses a great problem, as even slight fiber contacts or noisy images can distort the skeleton. Another approach (Sandau & Ohser, 2007) relies on the chord length transform to lift 2D fibers into 3D space, where the z-coordinate is derived from the orientation. The lifted fibers are in general not connected and can be separated by standard labeling techniques. Unfortunately, the generalization of the method to a 3D fiber system is non trivial. In materials with cellulose fibers (Axelsson, 2009, Bache-Wiig & Henden, 2005, Walther *et al.*, 2006), the non-crossing lumen can be used as markers to separate the fibers with standard labeling techniques.

In this chapter, we present a fiber separation approach based on probability maps indicating the probability for each point to be inside the core of a fiber in a non-crossing region (published in Altendorf & Jeulin (2009b). We define the core parts, which are initialized in locally maximal probabilities and expand along the fiber core, indicated by high probabilities. The core parts stop at crossing regions and will be reconnected in a second step. To decrease the amount of comparisons of pairs of core parts during reconnection, we developed a reconnection graph, which refers only to those pairs as reconnection candidates, which hold a connecting line in the foreground of the image. The decision of reconnection is made according to the orientations of the core parts and their connection line, as well as the length and the image values of the connection line.

Our studies are mainly focused on glass fiber reinforced polymers, where we can assume fibers with low bending, no branching and circular cross section. The algorithm is based on binary images and uses the local orientation map and a knowledge of the local radius (from a local radius map or a fix global radius).

The chapter starts with several possibilities to calculate the probability maps, followed by a study of the core parts: definition, initialization, expanding and reconnection over crossing regions. We terminate the chapter with applications on synthetic and real data.

5.1. Probability Maps

In this section, we present three approaches to compute the probability maps: the original idea based on mean filters with adapting structuring element, the mean filter with a propagating structuring element and a method based on the Euclidean distance transform. The probability maps include two types of information: the probability of a pixel being on a fiber core (called inner probability) and the probability for a pixel to be in a non-crossing region (called outer probability).

5.1.1. Probability from Mean Filter with Adapting Structuring Element

The fiber core is formed by the centers of maximal balls. Thus, a ball with given fiber radius fits in the fiber only if the center is situated on the fiber core. While moving this ball away from the fiber core, the intersection of the ball and the foreground decreases. To evaluate if a point is situated in a non-crossing region, we consider a ring around the point of interest, where the inner radius equals the fiber radius and the outer radius equals twice the fiber radius. In a core point situated in a non-crossing region, we observe that the surface or volume of this ring is covered to 52% with background in 2D and to 74% in 3D, see equations 5.2 and 5.5. If the point is situated in a crossing region, the ring hits another fiber and the intersection of ring and background decreases. This ball-ring-theory is illustrated in Figure 5.1 and the given percentages are computed as follows.

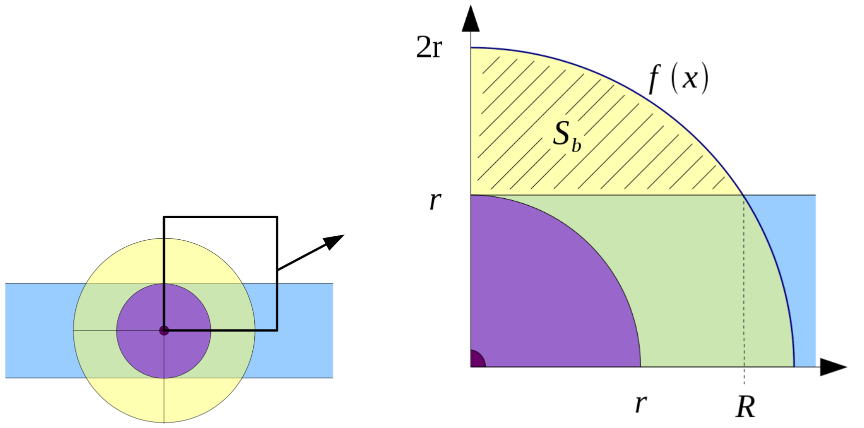

(a) blue - fiber, violet - ball with fiber radius fitting completely in the fiber, yellow - ring with 52% of its surface in the background

(b) cutout of one quarter of the ring surface, serves to calculate the percentage of the background

Figure 5.1.: Ball-ring-theory on a 2D fiber.

Surfaces in the 2D case (notation and formula derived from Figure 5.1(b)):

$$S_b = \int_0^R \sqrt{4r^2 - x^2}dx - Rr = r^2(-\sqrt{3}/2 + 2\pi/3) \tag{5.1}$$

In the case of no overlap, the maximal percentage of the surface of the ring, that lies in the background is

$$\rho_2^{\max} = 4S_b/S_{\text{ring}} = \frac{4r^2(-\sqrt{3}/2 + 2\pi/3)}{\pi((2r)^2 - r^2)} = \frac{8}{9} - \frac{2\sqrt{3}}{3\pi} \approx 52.13\%. \tag{5.2}$$

In the case of two orthogonal overlapping fibers, the percentage decreases to

$$\rho_2^{\min} = \frac{4\int_r^R \sqrt{4r^2 - x^2}dx - Rr}{S_{\text{ring}}} = \frac{4r^2(\frac{\pi}{3} + 1 - \sqrt{3})}{3\pi r^2} \approx 13.36\%. \tag{5.3}$$

The volume for the 3D case is derived from the function $f(x)$ (in Figure 5.1(b)) rotating around the x axes. The following integral builds half of the volume of the intersection of the ring and the background:

$$V_b = \pi \int_0^R 3r^2 - x^2 dx = 2\pi r^3 \sqrt{3} \tag{5.4}$$

In the case of no overlap, the maximal percentage of the volume of the ring, that lies in the background is

$$\rho_3^{\max} = 2V_b / V_{\text{ring}} = \frac{4\pi r^3 \sqrt{3}}{\frac{4}{3}\pi((2r)^3 - r^3)} = \frac{3\sqrt{3}}{7} \approx 74.23\%. \tag{5.5}$$

In the 3D case, it is not that trivial to compute the minimal percentage in the case of overlapping fibers. We approximate this minimal percentage by assuming the foreground percentage as twice the percentage in the case of a single fiber. This minimal percentage is

$$\rho_3^{\min} = 1 - 2(1 - \rho_3^{\max}) \approx 48,46\%, \tag{5.6}$$

which is slightly higher than the real percentage, as it neglects the overlapping volume of the two orthogonal fibers inside the ring element.

The percentage of the intersection of a structuring element with the foreground or background can be easily computed with the mean filter, assuming the foreground to have value 1 and the background value 0. Applying the mean filter to the foreground with a structuring element of a ball with radius equal to the fiber radius, we achieve the percentage of intersection and save it in the inner probability map. The boundary points still yield 50% of the ball in the foreground. Therefore, we spread the probability from $[0.5, 1]$ to $[0, 1]$, which defines:

$$P_{\text{inner}}(x) = \frac{2}{\|B_{r(x)}(x)\|} \left(\sum_{y \in B_{r(x)}(x)} b(y) \right) - 1, \tag{5.7}$$

where $b : \mathbb{N}^d \to \{0, 1\}$ defines the binary image and $B_r(x) = \left\{ y \in \mathbb{N}^d \mid |y - x| \leq r \right\}$ the ball with radius r centered in $x \in \mathbb{N}^d$.

The outer probability is computed by applying the mean filter to the background with a ring as structuring element, which results in

$$\rho(x) = \frac{1}{\|R_{r(x),2r(x)}(x)\|} \left(\sum_{y \in R_{r(x),2r(x)}(x)} 1 - b(y) \right), \tag{5.8}$$

with $R_{r_1,r_2}(x) = B_{r_2}(x) \backslash B_{r_1}(x)$ the ring element. The outer probability is spread according to its minimal and maximal values:

$$P_{\text{outer}}(x) = \frac{\rho(x) - \rho_d^{\min}}{\rho_d^{\max} - \rho_d^{\min}}, \tag{5.9}$$

where d defines the dimension of the image.

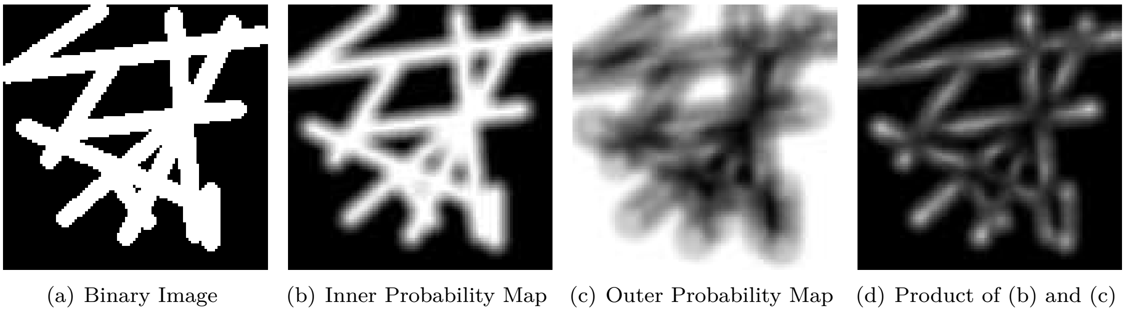

Figure 5.2.: Example of probability maps.

Assuming these two incidences to be independent, the product of the probabilities equals the combined probability of being inside a core in a non-crossing region. An example is shown in Figure 5.2.

By varying the structuring elements, we can include the information of the local fiber orientation. Different examples are visualized in Figure 5.3. The structuring elements are drawn on a blue fiber, the violet region indicates the structuring element for calculating the inner probability, whereas the yellow region indicates the structuring element (on the background) for calculating the outer probability. Note, that in the case of oriented structuring elements, the accuracy of the local orientation influences the probability maps.

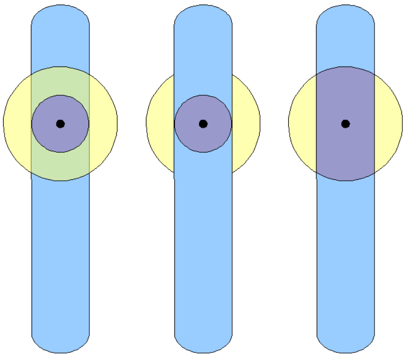

Figure 5.3.: Structuring elements for calculating the probability maps. The structuring elements are drawn on a blue fiber, the violet region indicates the structuring element for calculating the inner probability, whereas the yellow region indicates the structuring element (on the background) for calculating the outer probability. From left to right: original structuring element, ring element limited to the expected background and additionally an elongated inner structuring element (defined by the intersection of the ball with radius $2r$ and the expected foreground).

5.1.2. Probability from Mean Filter with Propagating Structuring Element

The approach using the mean filter over the entire structuring element has the great disadvantage that close fibers influence the surrounding probabilities. To avoid this, we define a propagating structuring element, which acts like a radial underbuild function or a radial reconstruction by dilation. Let $f : W \to \mathbb{R}$ be any real valued image. The radial underbuild function is defined on a window $W \in \mathbb{N}$

with center $x \in W$ and an adjacency system $\mathbf{N}$ as:

$$f_{\hat{r}}(y) = \begin{cases} f(y) & \text{, for } y = x \\ \min\{f(y)\} \cup \{f(z) \mid z \in \mathbf{N}(y) \wedge [d(z,x) < d(y,x)]\} & \text{, otherwise.} \end{cases} \tag{5.10}$$

In binary images, this radial underbuild function is included in the connected component of x. This means close parallel fibers do not influence the probability and even in crossing regions the crossing fiber has less influence on the probability.

5.1.3. Probability from Euclidean Distance Transform

The calculation of the probability maps in 3D, especially the propagating one, is very time-consuming, therefore we try to find a faster method to achieve the probability maps. In a first step, we treat the probability $\mathsf{P}_{\text{inner}}$ of being in the fiber core. The definition of this normalized probability that x is inside a fiber core is given in equation 5.7. The key properties, we want to keep, are $\mathsf{P}_{\text{inner}}(x_{\text{core}}) = 1$ and $\mathsf{P}_{\text{inner}}(x_{\text{border}}) = 0$. We observe that optically the Euclidean distance transform (EDT) gives similar results as the inner probability map and can be calculated much faster. We can define an inner probability dependent on the EDT and the local radius map $r : \mathbb{R}^d \to \mathbb{R}^+$ as:

$$\mathsf{P}_{\text{EDT}}(x) = \min\left\{\frac{\text{EDT}(x)}{r(x)}, 1\right\}. \tag{5.11}$$

This definition fulfills the key properties:

$$\text{EDT}(x_{\text{core}}) = r(x_{\text{core}}) \;\Rightarrow \mathsf{P}_{\text{EDT}}(x_{\text{core}}) = 1 \text{ and } \text{EDT}(x_{\text{border}}) = 0 \;\Rightarrow \mathsf{P}_{\text{EDT}}(x_{\text{border}}) = 0. \tag{5.12}$$

For further discussion of the crossing regions, we need to distinguish between the 2D and 3D case and between an exact or approximated radius, because the calculation of the EDT and the radius map differs in those cases. In the 2D case, the EDT increases in the crossing regions, whereas in 3D this is in general not the case. In 2D we can define a formula for the outer probability knowing the exact radius $r(x)$:

$$\mathsf{P}_{\text{EDT,outer}} = \min\left\{e^{-10(\frac{\text{EDT}(x)}{r(x)}-1)}, 1\right\}. \tag{5.13}$$

The crossing regions with higher EDT values naturally yields a boundary where the EDT value equals the radius. This undesirable effect can be eliminated by some simple morphological operations on the outer probability map. Practical tests showed good results after applying an erosion followed by an opening, both with $B_{r(x)}$ as structuring element. Figure 5.4 shows the results of the enlarged probability maps.

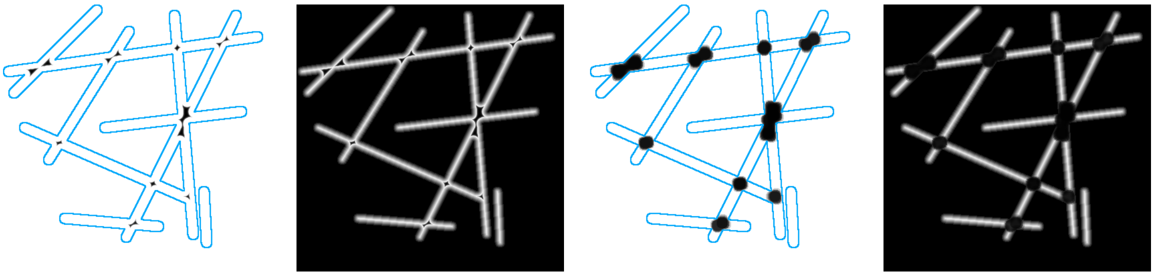

(a) $\mathsf{P}_{\text{EDT,outer}}$ (b) $\mathsf{P}_{\text{EDT,outer}} \cdot \mathsf{P}_{\text{EDT}}$ (c) enlarged $\mathsf{P}'_{\text{EDT,outer}}$ (d) $\mathsf{P}'_{\text{EDT,outer}} \cdot \mathsf{P}_{\text{EDT}}$

Figure 5.4.: Example of EDT probability maps.

In the 3D case, there is normally no indication of crossing regions from the EDT, thus we can only compute the inner probability. Considering that in practical applications fibers are solid and significant penetration of fibers does not occur, the separation of slightly overlapping fiber can be based on the inner probability only.

If the real radius is not known and we use the local radius information, computed by the method presented in chapter 3, we can make use of a main characteristic of this approach: The radius map $\widetilde{r}$ yields an overestimation of the radius in crossing regions. This can be useful for the probability map, as it yields:

$$\mathrm{EDT}(x_{crossing}) \ll \widetilde{r}(x_{crossing}) \;\Rightarrow \mathsf{P}_{\mathrm{EDT}}(x_{crossing}) \ll 1. \tag{5.14}$$

That implies that we could interpret the probability $\mathsf{P}_{\mathrm{EDT}}$ as $\mathsf{P}_{\mathrm{inner}} \cdot \mathsf{P}_{\mathrm{outer}}$, which defines the basis for the fiber separation algorithm.

We can summarize the properties of $\mathsf{P}_{\mathrm{EDT}}$ as follows:

- ⊖ in 3D or for approximated radius, not applicable to calculate $\mathsf{P}_{\mathrm{outer}}(x)$
- ⊕ for approximated radius in a crossing region $\mathsf{P}_{\mathrm{EDT}}$ decreases
  $\Rightarrow \mathsf{P}_{\mathrm{EDT}}$ can be interpreted as $\mathsf{P}_{\mathrm{inner}} \cdot \mathsf{P}_{\mathrm{outer}}$
- ⊖ more influenced by dark noise in the fibers (could be reduced by prefiltering)
- ⊕ EDT is locally limited to connected components ⇒ not influenced by other close fibers and therefore more stable in dense fiber fields
- ⊕ EDT is much faster to compute than mean filtering

5.1.4. Comparison of Different Approaches

Figure 5.5 shows the resulting multiplied probability map $\mathsf{P}_{\mathrm{inner}} \cdot \mathsf{P}_{\mathrm{outer}}$ of all the approaches for a synthetic 2D data set. The first row makes use of the fixed real radius $r = 4$, the second row uses the approximation of the radius with the approach presented in chapter 3 and the third row yields the same results as the second row with spread gray values, to make the accuracy of the method more visible.

The effect of close fibers can be observed at the parallel fibers at the bottom right of the images. With the propagating ball or the EDT approach this effect vanishes. In real datasets, the case of approaching parallel fibers occurs very often, which advises to apply one of those approaches. As the EDT is the fastest and the propagating ball the slowest method, we suggest to use the EDT approach.

5.2. Core Parts

Based on the probability maps, we build an algorithm tracking high probabilities. The fibers are reconstructed in the form of chains of spheres, called core parts. The structure of core parts is defined as a sequence of points, where a radius and an orientation are assigned to each point. The assigned orientation should be chosen as the local orientation of the fiber. Figure 5.6 shows an example of

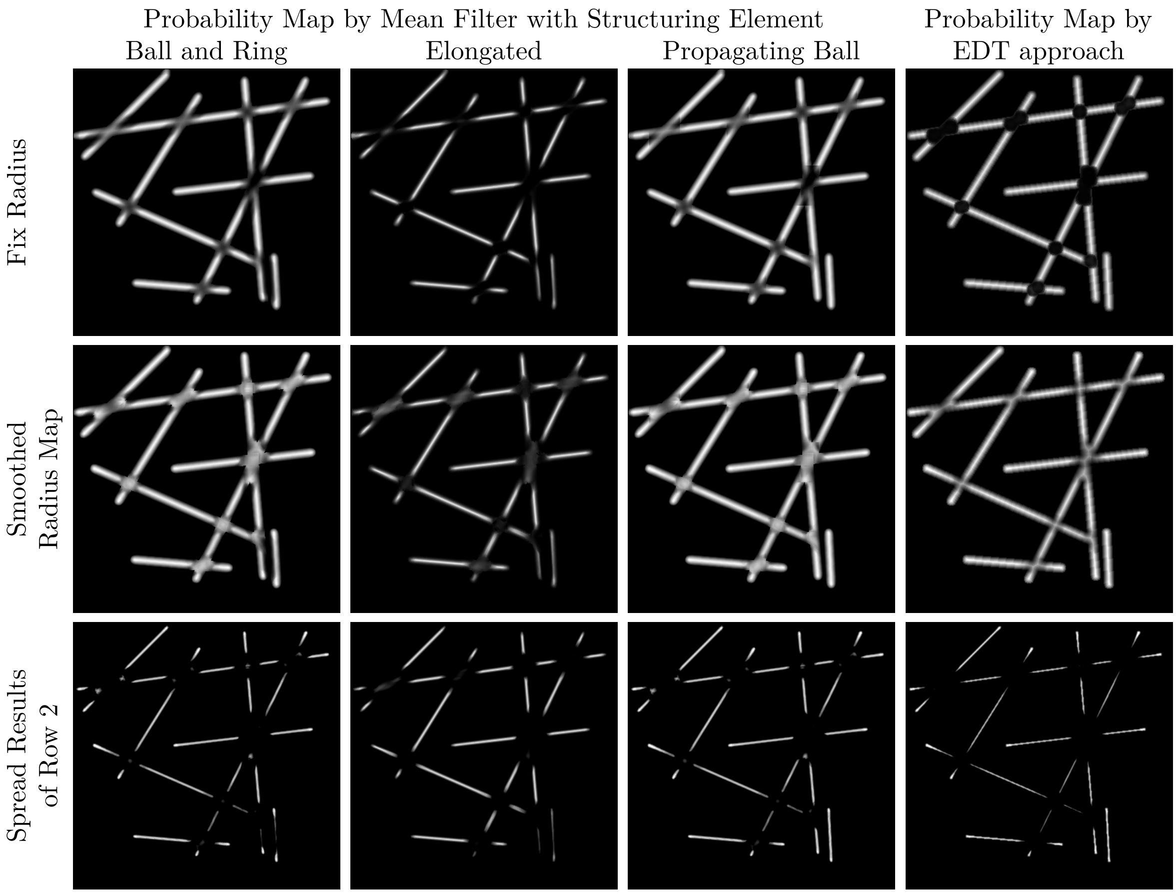

Figure 5.5.: Comparison of probability maps for different approaches. The first row makes use of the fixed real radius $r = 4$, the second row uses the approximation of the radius with the approach presented in chapter 3 and the third row yields the same results as the second row with spread gray values, to make the difference in the gray values more visible.

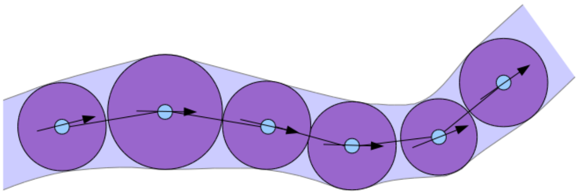

Figure 5.6.: Structure of a core part. The small circle indicates the location of the point, the big circle refers to the radius and the arrows show the orientation in that point.

a core part. Defining the core of a fiber this way, instead of using straight lines, allows bending of the fiber and variation of the local radius. In the following, we build the core parts such that the distance between two points equals approximately the fiber radius. We describe, how the core parts are initialized, expanded along the fiber core and reconnected over crossing regions.

5.2.1. Initializing Core Parts

The core parts should be initialized on the fiber core in regions, where the orientation and radius information is reasonable, which is the case in non-crossing regions. Thus, we start the initialization process on the local maxima of the probability map, presented by a marker map as shown in Figure 5.7. The local maxima are processed in the order of decreasing probability higher than the lower threshold $\mathsf{P}_{\min}$. This limit needs to be chosen carefully and may vary in different applications. If $\mathsf{P}_{\min}$ is too low, the core parts can depart from the fiber core or enter in crossing regions, which can imply a disorientation of the core part ends and therefore a problem in the reconnecting process. If $\mathsf{P}_{\min}$ is too high, parts of the fiber can be missed, because all points in the fiber part under-run the limit.

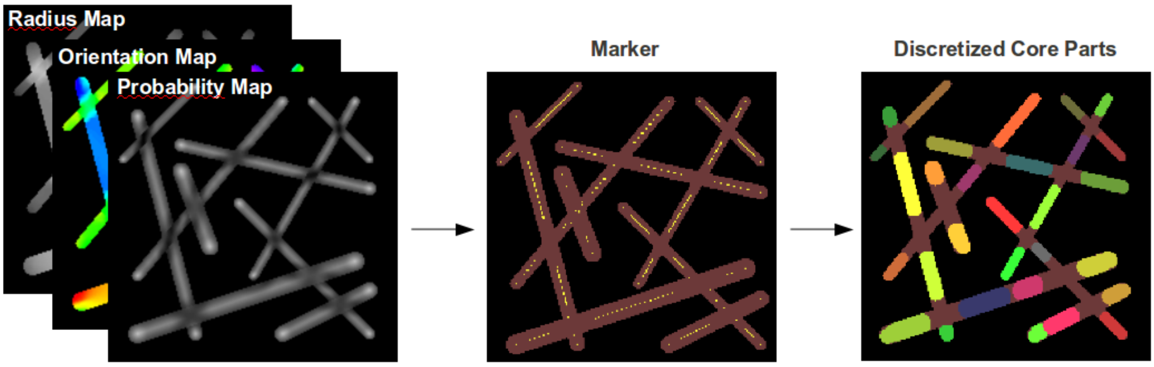

Figure 5.7.: Initializing of core parts. Basis: orientation, radius and probability map; marker from local maxima of the probability map; discretized core parts from expanded markers.

The markers create core parts, consisting of one point with radius and orientation given by the according maps. The core parts are created in decreasing order of probability. Each created core part is directly expanded and sets the values of the probability map in its influence zone to zero. This procedure assures the uniqueness of core parts and increases the efficiency of the algorithm.

5.2.2. Expanding Core Parts

A core part should be expanded along the fiber core as long as it does not enter a crossing region. The decision to expand is based on the probability given by the probability map. We expand from both ends of the core part in the direction of the assigned orientation and in the distance given by the assigned radius. Allowing a certain variation in those parameters, we obtain an area, in which we search for the highest probability value. The variation parameter in the expanding direction controls the accepted bending of the fibers. We expand a core part as long as the probability values are higher than the limit $\mathsf{P}_{\min}$. The expanding process is illustrated in Figure 5.8.

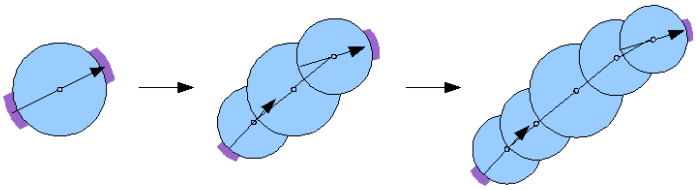

Figure 5.8.: Expanding of the core parts.

5.2.3. Reconnecting Core Parts

Two core parts should only be reconnected over a crossing region, if they are direct neighbors in the same fiber, which defines the reconnection candidates. For a pair of core parts, we decide about their reconnection by comparing the orientations and position of their closest ends. Having chosen two reasonable endpoints, we evaluate the angle between their orientations as well as the angle between their orientations and the orientation of the connection line. The evaluation value for the orientation is defined by $\mathsf{V}_{\text{Dir}} \in [0,1]$. We also take into account the distance between the core parts, evaluated with $\mathsf{V}_{\text{Dist}} \in [0,1]$, and the intersection of the connecting line with the foreground, evaluated with $\mathsf{V}_{\text{Line}} \in [0,1]$. The mentioned values are computed from the endpoints p_1, p_2 and their orientations v_1, v_2 as follows:

$$f(v,w) = 1 - \frac{\sqrt{\max\{\angle(v,w) - 0.3, 0\}}}{\pi} \in [0,1] \tag{5.15}$$

$$\mathsf{V}_{\text{Dir}} = \frac{f(v_1,v_2) + f(v_1,\overrightarrow{p_1p_2}) + f(v_2,\overrightarrow{p_1p_2})}{3} \tag{5.16}$$

$$\mathsf{V}_{\text{Line}} = \frac{\text{Volume}[\text{Foreground} \bigcap \text{CorePart}(p_1,p_2)]}{\text{Volume}[\text{CorePart}(p_1,p_2)]} \tag{5.17}$$

$$\mathsf{V}_{\text{Dist}} = \left(\frac{|\overrightarrow{p_1p_2}|}{100} + 1\right)^{-1} \tag{5.18}$$

$$\Rightarrow \mathsf{V}_{\text{Total}} = \frac{\mathsf{V}_{\text{Dir}} + \mathsf{V}_{\text{Line}} + \mathsf{V}_{\text{Dist}}}{3} \tag{5.19}$$

If any of those values under-run the lower bound V_{min}, the connection is directly denied. The connecting process is performed in decreasing order of the evaluation values $\mathsf{V}_{\text{Total}}$. After a connection, the values of the surrounding core part pairs can change and need to be recomputed.

5.2.4. Reconnection Graph

The straightforward approach of evaluating every pair of core parts exceeds very fast an acceptable runtime. Therefore, it is necessary to find a reasonable way to choose candidates for the connecting process. Core parts should only be connected through the foreground without crossing any other core part. So we define, that two core parts are connection candidates, if there exists a path in the foreground connecting them, which does not cross another core part.

This approach can be implemented on the mosaic of labeled core parts, including an additional label for the background. The region graph yields all connections between neighbor regions and can therefore indicate candidates for reconnection. An example of such a mosaic and the resulting region graph is shown in Figure 5.9(c) and 5.9(d).

5.3. Application on Synthetic Images

The presented algorithms are tested on synthetic datasets, where the result can be compared to the ground truth. Examples are shown in Figure 5.9 for the 2D case and in Figure 5.10 for the 3D case, where the fiber system is achieved by a cherry-pit RSA cylinder process. The results are nearly perfect, as all synthetic fibers could be recognized and separated from other colliding fibers. There remain some assignment problems at the fiber ends or in crossing regions.

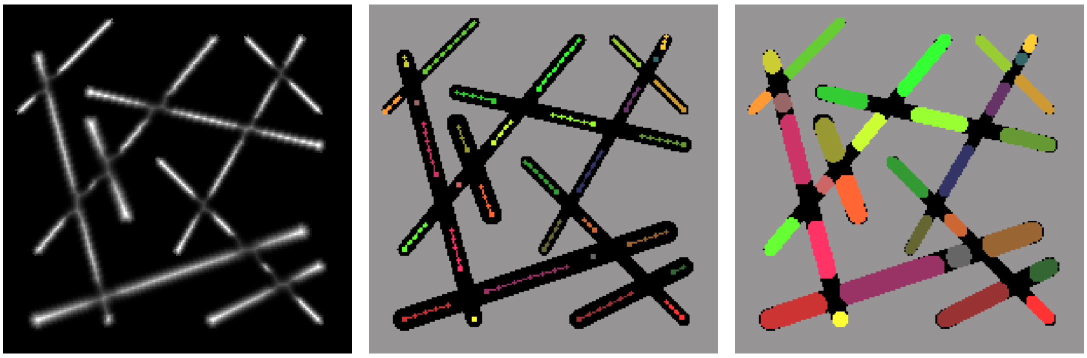

(a) Probability Map (b) Center Line of Core Parts (c) Labeled Core Parts

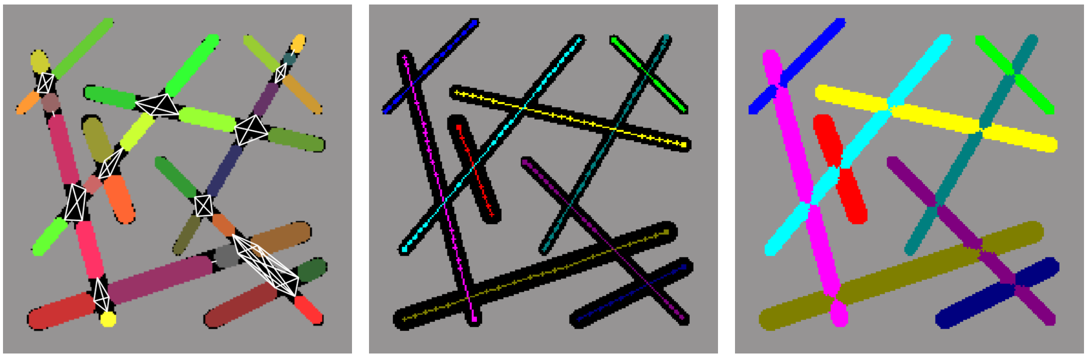

(d) Reconnection Graph (e) Reconnected Core (f) Separated Fibers

Figure 5.9.: Example for the separation of fibers on a 2D fiber model

5.4. Application on Real Datasets

We can now apply the fiber separation on real datasets. In Figure 5.11, the method is applied to a glass fiber reinforced polymer, where standard labeling techniques fail, because of the multiple connections in the fiber system. The probability $\mathsf{P}_{\text{outer}}$ is low in dense regions and therefore some fibers may remain undetected (especially in the low left corner in the sample shown in Figure 5.11(b)). The EDT probability is not influenced by close fibers and could therefore detect those missing fibers (see 5.11(c)).

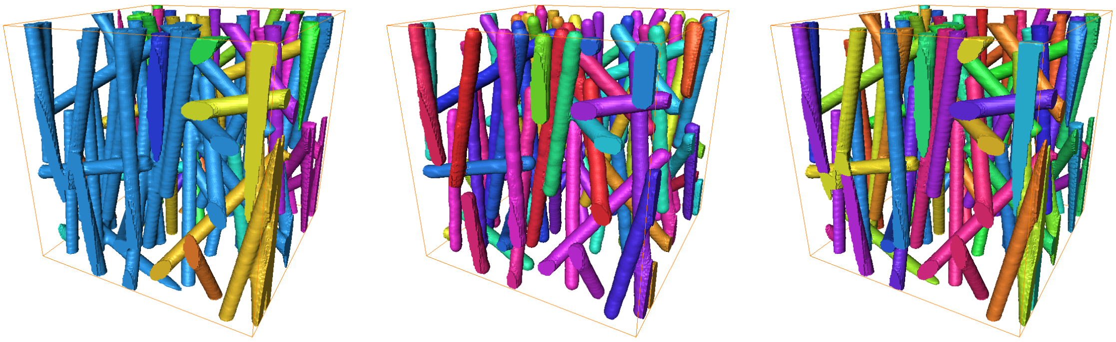

(a) Labeled Fibers

(b) Reconstructed Sphere Chains

(c) Labeling of Foreground by Region Growing from Fiber Cores

Figure 5.10.: Example for the separation of fibers on a 3D model. Labeled 3D Rendering visualized with Amira software.

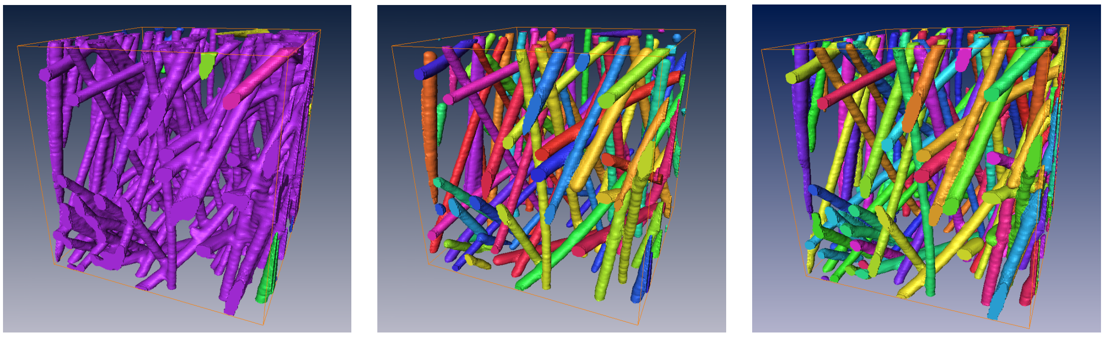

(a) Standard Labeling

(b) Separation with Probability Map $P_{inner} \cdot P_{outer}$

(c) Separation with Probability Map P_{EDT}

Figure 5.11.: Application of separation approaches on IVW glass fibers. GRP Sample from R. Velthuis (IVW Kaiserslautern) recorded by A. Rack, J. Goebbels at the BAMline (BESSY II, Berlin, Germany) with a resolution of 3.5 µm.

5.5. Conclusion

The algorithm shows reasonable results on synthetic data. In the application on CT datasets, the majority of fibers is detected. The problem of undetected fibers in dense regions of GRP got resolved by the EDT probability. Still it remains to verify, if the method is adaptable to highly dense and parallel fiber system, as often seen in carbon fiber reinforced polymer. The method was tested on materials as glass fiber reinforced polymers and steel fiber reinforced concrete with a volume fraction up to 15%. For a sufficiently high resolution, volume fraction up to 30% should be even possible to treat. For higher volume fraction or carbon fiber reinforced polymers, it remains to check the limits of density and resolution, for which the method still yields acceptable results.

Part II.

Stochastic Modeling and Physical Simulation

Chapter 6.

6 Stochastic Modeling

Thanks to the analysis from the previous chapter, the microstructure of a fibrous material is known in details. In this chapter, we design a suitable stochastic model for a random fiber system and show how it can be fitted based on the knowledge of the microstructure of a real material. The stochastic model is published in Altendorf & Jeulin (2011a) and the model fitting in Altendorf & Jeulin (2011b).

In the area of stochastic geometry models, we distinguish between soft-core and hard-core systems. A hard-core system forbids overlap between the objects, which is strongly required, as such penetrations are not realistic in the case of solid glass or carbon fibers. Concerning random fiber systems, there exist several approaches providing either hard-core fiber systems with a low volume fraction, soft-core systems and sedimentation algorithms, providing hard-core systems with restrictions on the orientation distribution.

We recall in detail the state of the art in fiber modeling: The classical approach called the dilated Poisson line process was introduced in Matheron (1975) and creates infinite straight cylinders in a soft-core network. Since then, fiber modeling has evolved into more flexible approaches. In order to achieve hard-core systems, the random sequential adsorption model was created in Widom (1966), which iteratively generates objects and tries to place them in the system such that they do not overlap with already existing objects. This approach was applied for cylinders in Feder (1980). Two other random fiber-packing methods have been developed: one for ellipsoids presented in Bezrukov & Stoyan (2006) and one for spherocylinders in Williams & Philipse (2003). All three random packing approaches produce straight fibers in a hard-core system and achieve only low volume fractions of about $10\% - 15\%$ for isotropic orientation distribution and a fiber aspect ratio of 10. For long fibers, as is the case for fiber-reinforced composites (aspect ratio of about 200), the producible volume fraction goes down to 5%, while $15\% - 55\%$ is required. Furthermore, long fibers cannot be realized with cylinders in a periodic window, as fibers tend to overlap themselves. Still, periodic boundary conditions are often required for simulations of physical properties.

There are also more physically motivated approaches of fiber sedimentation, which achieve, in general, high volume fractions but are limited in realizing a given orientation distribution. The fiber deposition model in Provatas *et al.* (2000) generates fibers oriented in the plane and deposes them with a certain bending parameter on the existing system. In this approach, high volume fractions can be achieved, but the most important parameter, the orientation distribution, is limited to the plane. The sequential deposition algorithm in Coelho *et al.* (1997) realizes a fall of random particles until they reach a local minimum of their potential energy. During the fall, rotation and displacement are not restricted. Therefore, the particle can change its orientation arbitrarily, and it cannot be assured that the desired orientation distributions will be achieved. This approach allows up to a 59% volume fraction for cylinders with an aspect ratio of 10.

Another hard-core bending fiber model was proposed in Pan *et al.* (2008). The representative volume element is divided into sublayers. Fibers are randomly oriented in the xy plane, and in the case of overlap, the newly added fiber changes the sublayer to avoid the existing fiber. The resulting chains of polyhedra with ellipsoid cross sections achieve a volume fraction of $35\% - 40\%$. Still, the buckled polyhedra do not appear to be very realistic, and again, the orientation distribution is restricted to the xy plane.

Our model uses four major inspirations: Firstly, model bended fibers as ball chains by a random walk (initiated by Joachim Ohser). Secondly, a combination of the ideas from Wirjadi (2009) and Karkkainen *et al.* (2008) to control the orientation distribution in spite of the bending. Thirdly, the force-biased approach on sphere packings (Mościński & Bargieł (1989) and Bezrukov *et al.* (2002)). Fourthly, the design of energies in molecular dynamics to define the forces (Mościński & Bargieł, 1989).

Soft-core bending fiber systems can be achieved by random walks introduced in Wirjadi (2009) with the von Mises-Fisher distribution, controlling the smoothness of the bending. In this approach it is possible that long fibers bend to a circle; thus, the final orientation distribution cannot be controlled. The approach of Karkkainen *et al.* (2008) provided 2D random walks with the multivariate von Mises-Fisher distribution, which also controls the deviation from the main fiber orientation, assuring a certain loyalty to a given orientation distribution. Furthermore, in Faessel *et al.* (2005) a bending fiber model is proposed based on dilated cores made of curvature points connected by spline interpolation. The last three models are soft-core systems.

The idea to represent fibers as chains of spheres was already considered in Karayiannis & Laso (2008). An irregular assembly of chains of tangent hard spheres (like in a pearl necklace) were studied to build dense packings with Monte Carlo simulation schemes. Hard-core configurations with low density are packed with a “box shrinkage” algorithm and relaxed in Monte Carlo algorithms by localized moves as flip, rotation, reptation, and intermolecular reptation. The aim of the approach in Karayiannis & Laso (2008) is a highly dense packing, which was successfully achieved with a volume fraction of 63.9%, which corresponds to the densest packing of hard spheres. To this end, the restrictions on the fiber structure are very low, and thus, the approach is not suitable for reconstructing fiber-reinforced composites.

Material properties are highly influenced by the fiber structure, particularly its orientation distribution. This correlation is studied in Schulgasser (1985), Chin *et al.* (1988), Jain & Wetherhold (1992), Hine *et al.* (1995), Fu & Lauke (1996) and Favier *et al.* (1997). Furthermore, Berhan and Sastry (Berhan & Sastry (2007a) and Berhan & Sastry (2007b)) studied the influence of model characteristics on percolation simulation for different high-aspect-fiber systems. In Berhan & Sastry (2007a), the influence of soft-core and hard-core systems is examined, while Berhan & Sastry (2007b) focuses on the waviness of the fibers. Berhan states that the frequently used straight and overlapping fiber systems are inappropriate to model fiber-reinforced materials, and he suggests using hard-core bending fiber systems. Those studies enhance the need for stochastic models, creating realistic fiber systems dedicated to fiber composite materials. In the previous chapters, we proposed quantification methods to analyze the most important characteristics of fiber systems. Now, a stochastic model is required to realize the measured properties. In contrast to physical simulations dedicated to systems of liquid crystals (e.g. Cinacchi & Gaetani (2008)), we are only interested in the final configuration of the stochastic model and its properties, instead of the behavior of the fibers during the simulating process.

The aim of this chapter is to provide a random hard-core fiber model with a controllable bending and high volume fractions. For this purpose, random walks are used to create a realistic system of bending fibers. The level of bending is controlled by two parameters in the multivariate von Mises-Fisher distribution. The created points are provided with a radius and the current orientation. The balls, defined by the points and the assigned radii, are connected in chains according to the paths of the random walks. This approach results in a soft-core system of bending fibers, modeled as chains of balls. In a second step, we apply a force-biased approach to achieve a hard-core configuration of the fiber system. Force-biased algorithms on spheres were introduced in Mościński & Bargieł (1989) and statistically analyzed in Bezrukov *et al.* (2002). The forces in our approach were inspired by the energy-reducing models known from molecular dynamics (Mościński & Bargieł, 1989). The mentioned forces describe the necessary displacement of the balls to relax the system. They do not act like mechanical forces. Two kinds of forces are applied to the ball centers: repulsion and recover forces. The repulsion force arises in the case of a fiber overlap and displaces the balls to a non overlapping position. The recover force maintains the fiber structure between the balls. It keeps the distance and the angles between a ball and its neighbors, allowing only a small deviation.

The approach works in a closed cubic window $W \subset \mathbb{R}^3$ with periodic boundary conditions. Overlap checks are effectively computed in subdivisions of the window W, where only neighboring cells need to be compared. Therefore, the algorithm has low computing time. We ensured the quality of the realization by evaluating the parameters of the final configuration.

Although ball chains are considered as the second type of ideal amorphous solids, they are purely used in modeling fibrous material. As stated in Laso *et al.* (2009), in the case of non overlapping neighbor spheres, the maximal possible volume fraction rises up to the one of individual spheres: ≈ 0.64. With decreasing distance between neighboring spheres and increasing alignment of fibers, we approach a system of parallel cylinders. In this case, the problem reduces to a random packing of 2D disks, for which the maximal volume fraction can reach up to 0.78 (Hinrichsen *et al.*, 1990). In our approach, the distance between neighboring spheres is approximately $r/2$, where r is the sphere radius. This distance is one-quarter of the distance of non overlapping neighbor spheres. Thus, the maximal possible volume fraction may lie between the values 0.64 and 0.78. As we include higher restrictions to the fiber structure than the random packing of tangent sphere chains of Karayiannis & Laso (2008), it is probable that we will not reach such high volume fractions for every set of parameters. Still, volume fractions around 50% were achieved for several input parameters. The maximal volume fraction of our experiments was 72.0075 %, achieved for a z axis preferred orientation distribution and an aspect ratio of 9.

We start this chapter with a presentation of the orientation distributions used in this studies: the standard and multivariate von Mises-Fisher distribution (Fisher, 1953, Karkkainen *et al.*, 2008) and the β girdle orientation (Ohser & Schladitz, 2009, Schladitz *et al.*, 2006). In the following, we first introduce the rather classical approach of hardcore cylinders organized with the RSA algorithm (random sequential absorption). We generalize the approach by adding a soft-shell ratio, which keeps the fiber core solid and allows overlap on the shell. The idea of the soft-shell ratio is taken from the cherry-pit model introduced by Rikvold & Stell (1985), Torquato (2002) and analyzed in Elsner *et al.* (2009). In Section 6.3, we introduce the random walker creating a soft-core system of bended fibers. Section 6.4 presents the force-biased fiber packing bringing the bended fibers in a non overlapping configuration. We terminate the chapter with a study on the estimation of the model parameters and further statistics on the created model.

6.1. Orientation Distributions

In this chapter, we recall some three-dimensional orientation distributions, which are used in the following studies. In the definition of the distributions, we make use of the spherical coordinates

$(\theta, \phi) \in [0, \pi) \times [0, 2\pi)$. The conversion to Cartesian coordinates $(x, y, z) \in S^2 \subset \mathbb{R}^3$ is the following:

$$x = \sin\theta\cos\phi, \quad y = \sin\theta\sin\phi, \quad z = \cos\theta. \tag{6.1}$$

Thus θ describes the deviation from the positive z axis, while ϕ describes the deviation from the positive x axis in the xy plane projection in clockwise order. We will refer to the presentation in polar coordinates with square brackets and the index PC: $(x, y, z)^T = \langle\theta, \phi\rangle_{\mathrm{PC}}$. There are various alternatives to describe an orientation with angles like the geographical, geological or astronomical coordinates (see Fisher *et al.* (1993)). Note that also the definition of the spherical coordinates is not always identical in the literature.

There are two classes of distributions on the unit sphere, considering either directed vectors or axial data, where inverse directions yield the same probability. This difference is essentially important for statistical analysis of the data as well as for parameter estimation. In the case of fibers, the fiber orientation is generally not directed. This axial data reduces the orientation space to the half sphere S^2_+ described by the spherical coordinates in $[0, \pi/2) \times [0, 2\pi)$. For global orientation distributions, we take into account only those distributions having equal probabilities for inverse directions. Still, for the stochastic model based on random walks, we need to consider a distribution for preferred directed orientations. For this approach, we choose the multivariate von Mises-Fisher distribution.

Furthermore, the presentation of the orientation distributions need to be discussed. We choose the same specification as in Fisher *et al.* (1993) by probability density function (pdf) and probability density element (pde). The pde $h(x)$ describes the probability for a certain range around the point x. The distribution specified by the pdf $f(x)$, which is not a probability, serves for integration. The relation of both functions is: $h(x) = f(x)\ \mathrm{d}x$, which differs just in the multiplication by the elemental range $\mathrm{d}x$ for $x \in \mathbb{R}$. In the case of 3D orientation, the elemental area for spherical coordinates is the unit spherical surface having Θ between θ and $\theta + \mathrm{d}\theta$ and Φ between ϕ and $\phi + \mathrm{d}\phi$. The element of surface $\mathrm{d}S$ in spherical coordinates is

$$\mathrm{d}S = \sin\theta\ \mathrm{d}\theta\ \mathrm{d}\phi. \tag{6.2}$$

Therefore, a pde $h(\theta, \phi)\ \mathrm{d}S$ has the pdf $f(\theta, \phi) = h(\theta, \phi)\sin\theta$.

In the following, all presented orientation distributions have one preferred direction μ and are isotropic in rotation around that preferred direction. Thus, they can be defined by the marginal distribution only dependent on the angle θ between a direction v and the preferred direction μ. It yields $\cos\theta = \mu \cdot v$, where "·" represents the scalar product (also called inner vector product).

6.1.1. von Mises-Fisher Distribution

The most common orientation distribution with preferred direction $\mu \in S^2$ and reliability parameter $\kappa > 0$ is the von Mises Fisher distribution defined by its probability density element (see pages 86 ff. in Fisher *et al.* (1993))

$$h_{\mathrm{vMF}}(v) = \frac{\kappa}{2\pi(e^{\kappa} - e^{-\kappa})} e^{\kappa(\mu \cdot v)}\ \mathrm{d}S \tag{6.3}$$

or by the probability density function in polar coordinates ($\mu = \langle\theta_0, \phi_0\rangle_{\mathrm{PC}}$)

$$f_{\mathrm{vMF}}(\theta, \phi) = \frac{\kappa}{2\pi(e^{\kappa} - e^{-\kappa})} e^{\kappa(\sin\theta\sin\theta_0\cos(\phi-\phi_0)+\cos\theta\cos\theta_0)} \sin\theta, \tag{6.4}$$

with preferred direction $\mu \in S^{d-1}$ and concentration parameter $\kappa > 0$. $\kappa \to 0$ leads to the uniform distribution and $\kappa \to \infty$ leads to the fixed distribution of μ. Examples of realizations with different

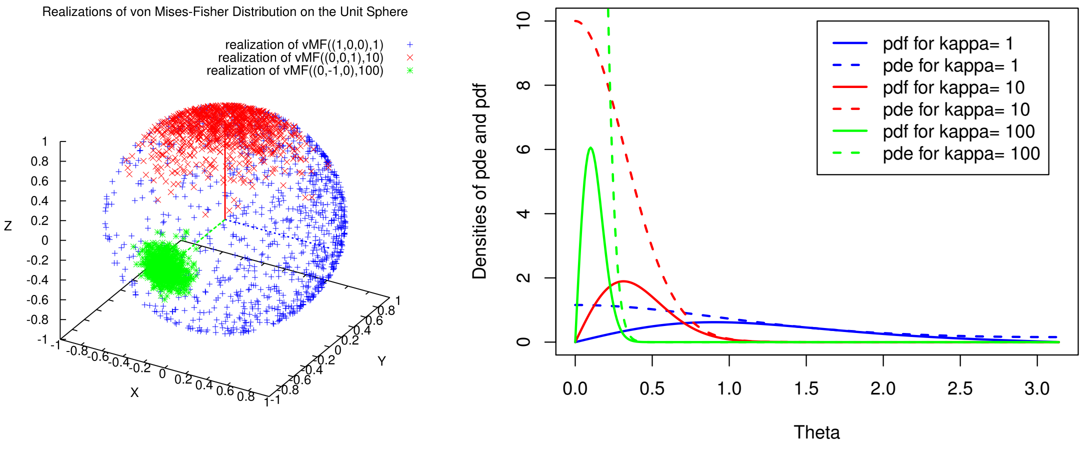

Figure 6.1.: Realizations and density functions of the von Mises Fisher distribution with $\kappa = 1, 10, 100$.

anisotropy parameter κ are shown in Figure 6.1.

The marginal distribution for $\mu = (0,0,1)^T = \langle 0,0\rangle_{\text{PC}}$ or θ representing the angle between μ and v is

$$g_{\text{vMF}}(\theta) = \frac{\kappa}{(e^{\kappa} - e^{-\kappa})} e^{\kappa \cos\theta} \sin\theta. \tag{6.5}$$

Respectively, the cumulative distribution function over θ for a von Mises Fisher distribution is

$$G_{\text{vMF}}(\theta) = \frac{1 - e^{\kappa(\cos\theta - 1)}}{1 - e^{-2\kappa}}. \tag{6.6}$$

We roughly sketch the deduction of the cumulative distribution function:

$$\begin{aligned}
G_{\text{vMF}}(\theta) &= \int_0^{\theta} g_{\text{vMF}}(\alpha)\, \mathrm{d}\alpha && (6.7)\\
&= \frac{\kappa}{(e^{\kappa} - e^{-\kappa})} \int_0^{\theta} e^{\kappa\cos\alpha} \sin\alpha\, \mathrm{d}\alpha && (6.8)\\
&= \frac{\kappa}{(e^{\kappa} - e^{-\kappa})} \left[-\frac{1}{\kappa} e^{\kappa\cos\alpha}\right]_0^{\theta} && (6.9)\\
&= \frac{1}{(e^{\kappa} - e^{-\kappa})} \left(-e^{\kappa\cos\theta} + e^{-\kappa}\right) && (6.10)\\
&= \frac{1 - e^{\kappa(\cos\theta - 1)}}{1 - e^{-2\kappa}} && (6.11)
\end{aligned}$$

The pseudo random generator for $\mu = (0,0,1)^T$ is based on the cumulative distribution function for $\theta \in [0,\pi]$ and the isotropically distributed $\phi \in [0, 2\pi]$:

1. generate X_1, X_2 uniformly in $[0,1]$
2. find θ with $G_{\text{vMF}}(\theta) = P(\Theta \leq \theta) = X_1$: $\quad \theta = \cos^{-1}\left(1 + \frac{\ln[1 - X_1(1 - e^{-2\kappa})]}{\kappa}\right)$
3. find ϕ with $F(\phi) = P(\Phi \leq \phi) = X_2$: $\quad \phi = 2\pi X_2$

Other choices of $\mu = \langle \alpha, \beta \rangle_{\mathrm{PC}}$ can be realized by rotating the z centered realization $\langle \theta', \phi' \rangle_{\mathrm{PC}} \sim \mathrm{vMF}(\langle 0, 0 \rangle_{\mathrm{PC}}, \kappa)$ with the rotation matrix:

$$R_{\alpha,\beta} = \begin{pmatrix} \cos\alpha\cos\beta & -\sin\beta & \sin\alpha\cos\beta \\ \cos\alpha\sin\beta & \cos\beta & \sin\alpha\sin\beta \\ -\sin\alpha & 0 & \cos\alpha \end{pmatrix} \tag{6.12}$$

It yields $\langle \alpha, \beta \rangle_{\mathrm{PC}} = R_{\alpha,\beta} \langle 0, 0 \rangle_{\mathrm{PC}}$ and the rotated direction $\langle \theta, \phi \rangle_{\mathrm{PC}} = R_{\alpha,\beta} \langle \theta', \phi' \rangle_{\mathrm{PC}}$ is distributed with $\mathrm{vMF}(\langle \alpha, \beta \rangle_{\mathrm{PC}}, \kappa)$.

6.1.2. multivariate von Mises Fisher Distribution

The multivariate von Mises Distribution was first defined in Karkkainen *et al.* (2008) for the 2D case. The generalization to higher dimensions has the pde:

$$h(x|x_1, \kappa_1, x_2, \kappa_2)\ \mathrm{d}S = c(x_1, \kappa_1, x_2, \kappa_2)\ e^{\kappa_1 x_1^T x + \kappa_2 x_2^T x}\ \mathrm{d}S, \tag{6.13}$$

where $x_1, x_2 \in S^{d-1}$ are two preferred directions and $\kappa_1, \kappa_2 \in \mathbb{R}^+$ are the reliability parameters towards the preferred directions. The factor $c(x_1, \kappa_1, x_2, \kappa_2)$ serves for the normalization, such that the integral over S^{d-1} is equal to 1.

A useful observation is that every multivariate von Mises Fisher distribution can be written as a classical von Mises Fisher distribution with the parameters

$$\kappa = |\kappa_1 x_1 + \kappa_2 x_2| \quad \text{and} \quad x_0 = \frac{\kappa_1 x_1 + \kappa_2 x_2}{\kappa}, \tag{6.14}$$

which can be easily checked by inserting those parameters in the classical von Mises Fisher density function. This simplifies the generation of the pseudo random variables to the standard case, which has been described before. Furthermore, this defines the normalization factor in S^2

$$c(\kappa) = \frac{\kappa}{2\pi(e^{\kappa} - e^{-\kappa})} \tag{6.15}$$

$$\Rightarrow c(x_1, \kappa_1, x_2, \kappa_2) = \frac{|\kappa_1 x_1 + \kappa_2 x_2|}{2\pi(e^{|\kappa_1 x_1 + \kappa_2 x_2|} - e^{-|\kappa_1 x_1 + \kappa_2 x_2|})}. \tag{6.16}$$

As the multivariate von Mises Fisher distribution can be written as a classical vMF distribution, it is not very interesting to observe realizations of this distribution with fixed parameters. This case could be replaced by the classical von Mises Fisher distribution. The multivariate version is required during the random walk, where the first preferred direction is fixed to the global mean direction of the walk, whereas the second preferred direction refers to the last direction in the walk. Therefore, this parameter changes during the process other than the remaining three parameters.

6.1.3. β Distribution

For the global orientation distribution, we have applied the β orientation distribution (Schladitz *et al.* (2006), (Ohser & Schladitz, 2009, p. 252)) with one parameter $\beta \in \mathbb{R}^+ \backslash \{0\}$. For $\beta = 1$ it results in the uniform distribution on the sphere, for $\beta \to 0$ it concentrates on the z axis, and for $\beta \to \infty$ the orientations are distributed isotropically in the xy plane. The probability density function of the β orientation distribution is

$$f_{\mathrm{B}}(\theta, \phi) = \frac{\beta \sin\theta}{4\pi(1 + (\beta^2 - 1)\cos^2\theta)^{3/2}}. \tag{6.17}$$

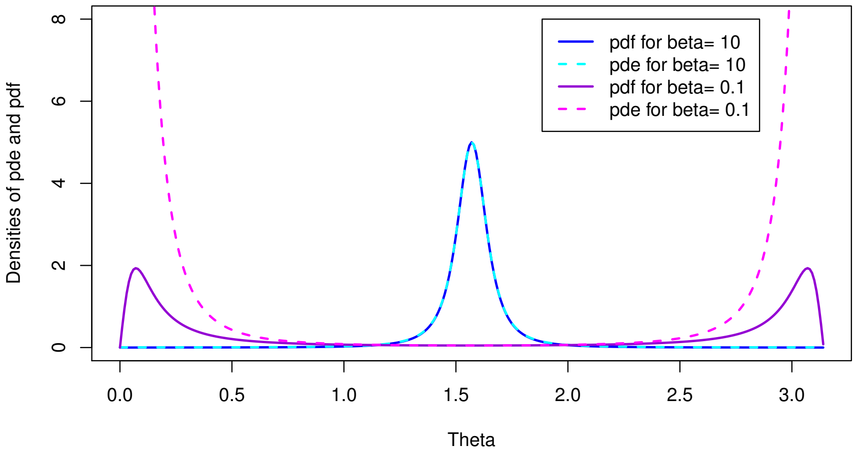

Figure 6.2.: Probability densities (pdf and pde) for the β distribution with parameters $\beta = 0.1$ and $\beta = 10$.

Figure 6.2 shows the probability density elements and functions for the β distribution with parameters $\beta = 0.1$ and $\beta = 10$.

In difference to the von Mises Fisher distribution, the girdle distribution treats inverse directions equally. Thus, it yields $f_{\mathrm{B}}(v) = f_{\mathrm{B}}(-v)$ for all $v \in S^2$. This behavior is important for a fiber orientation, as the sense of the orientation is not defined. Furthermore, this orientation distribution yields the possibility to describe a concentration on a girdle in the xy plane, which appears quite often in real materials, as e.g. in non woven or in CRP.

The marginal probability density function is

$$g_{\mathrm{B}}(\theta) = \frac{\beta \sin\theta}{2(1 + (\beta^2 - 1)\cos^2\theta)^{3/2}}, \tag{6.18}$$

and the cumulative distribution function over $\theta \in [0, \pi)$ is

$$G_{\mathrm{B}}(\theta) = \frac{1}{2} - \frac{\beta}{2\sqrt{\cos^{-2}\theta + (\beta^2 - 1)}}. \tag{6.19}$$

The inversion of the cumulative distribution function serves to create the pseudo random generator:

1. generate X_1, X_2 uniformly in $[0, 1]$
2. find θ with $G_{\mathrm{B}}(\theta) = X_1$: $\quad \theta = \cos^{-1}\left(\frac{X_1}{\sqrt{X_1^2 - \beta^2 X_1^2 + \beta^2}}\right)$
3. find ϕ with $F(\phi) = X_2$: $\quad \phi = 2\pi X_2$

The created pseudo random vector $v = \langle\theta, \phi\rangle_{\mathrm{PC}}$ can also be rotated according to a preferred orientation or axis with the rotation matrix (see Equation 6.12).

6.1.4. Variations of the von Mises Fisher distribution

There are also several approaches to generalize the von Mises Fisher distribution, in order to achieve equality for inverse directions and to create a distribution, which covers bipolar and girdle preferences.

One possibility of expanding the von Mises Fisher distribution to create a girdle distribution was introduced by Watson (1965). The Watson density element is

$$h_{\mathrm{W}}(\theta, \phi) = C_{\mathrm{W}}(\kappa) e^{\kappa \cos^2 \theta} \, \mathrm{d}S, \quad \text{with} \quad C_{\mathrm{W}}(\kappa) = \left(4\pi \int_0^1 e^{\kappa u^2} \, \mathrm{d}u \right)^{-1}. \tag{6.20}$$

The normalizing constant includes solving the integration of the Gaussian function, which can not be ascribed to an antiderivative and therefore needs to be approximated numerically by the so called error function. One may think of the possibility to compress the von Mises Fisher distribution on polar coordinates from $\theta \in [0, 2\pi]$ to $\theta \in [0, \pi]$ by making use of $\cos(2\theta)$, which leads to the probability density element

$$h_{\mathrm{DF}}(\theta, \phi) = C_{\mathrm{DF}}(\kappa) e^{\kappa \cos 2\theta} \, \mathrm{d}S, \quad \text{with} \quad C_{\mathrm{DF}}(\kappa) = \left(2\pi \int_0^\pi e^{\kappa \cos 2\theta} \sin\theta \, \mathrm{d}\theta \right)^{-1}. \tag{6.21}$$

As it yields $\cos 2\theta = 1 - 2\cos^2\theta$, we end up with the same unsolvable problem as for the Watson distribution. The probability density elements and function of the doubled Fisher distribution h_{DF} and the Watson distribution are shown in Figure 6.3 for $\kappa = 10$ and $\kappa = -10$. Both yield similar, smooth curves.

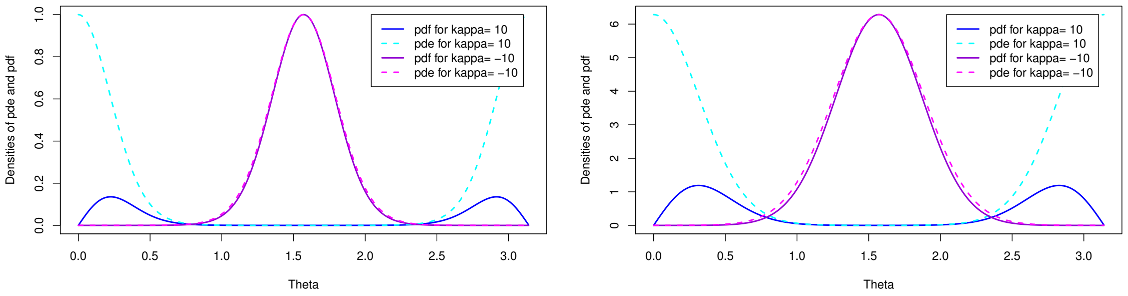

(a) Watson Distribution

(b) Doubled Fisher Distribution

Figure 6.3.: The probability density elements and function for the Watson and the doubled von Mises Fisher distributions for $\kappa = 10$ and $\kappa = -10$.

However, there is a way to create a variation of the von Mises Fisher distribution with nice integration properties by using the absolute value of the cosine $|\cos(\theta)|$. The probability density element is defined as

$$h_{\mathrm{FA}}(v) = C_{\mathrm{FA}}(\kappa) e^{\kappa |\mu^T \cdot v|} \, \mathrm{d}S, \quad \text{with} \quad C_{\mathrm{FA}}(\kappa) = \frac{\kappa}{4\pi(e^\kappa - 1)}. \tag{6.22}$$

For $\kappa > 0$ the distribution concentrates around the axis μ, with equal probabilities for inverse directions and for $\kappa < 0$ the distribution concentrates isotropically around the plane orthogonal to μ. Figure 6.4 shows an example of the probability density function and elements for $\kappa = 10$ and $\kappa = -10$. The probability density is continuous, but unfortunately it is not differentiable in the point $\theta = \pi/2$.

6.2. RSA and Cherry-Pit Fiber Model

A classical approach to model random fiber networks is a cylinder process. The basis is a hard-core germ grain process realized with the RSA algorithm (random sequential adsorption, see Feder

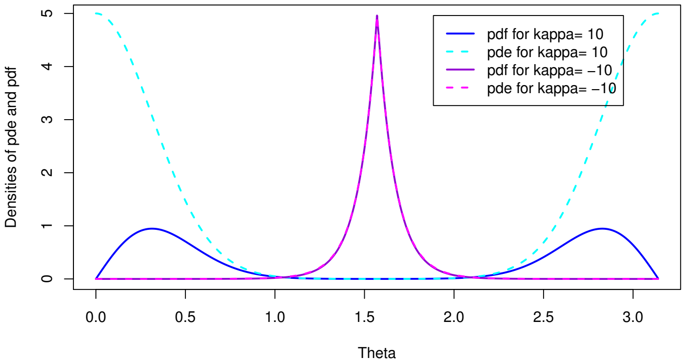

Figure 6.4.: Fisher absolute distribution with $\kappa = 10$ and $\kappa = -10$.

(1980)). To achieve a certain degree of overlap the collision check is performed on thinned fibers, similar to the cherry-pit model.

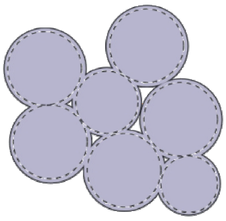

Figure 6.5.: Cherry-pit model in 2D.

Fibers are defined as cylinders with starting point $x \in \mathbb{R}^d$ uniformly distributed, orientation $v \in S^{d-1}$ with specific orientation distribution (here we used β orientation distribution) and radius $r \in \mathbb{R}^+$. The fiber model is provided with an overlap ratio $\rho \in \mathbb{R}^+$. Collision checks are accomplished for the realized fibers with adapted radius $\rho \cdot r$. With that extension we can allow a certain overlap of the fibers for $\rho < 1$ or assure a free surrounding of each fiber for $\rho > 1$.

Figure 6.6 shows some realizations of the cherry-pit fiber model for varying orientation distributions and a soft-shell ratio of 0.5.

6.3. Random Walker

In this section, we present a model to create bended fibers in a soft-core system. Each fiber of the initial fiber system is modeled as a random walk. A random walk is a Markov process on $\mathbb{R}^3$ producing a chain of points. We assign to every fiber point the current direction and a radius. The result of a random walk is a sequence of points in $\mathbb{R}^3 \times S^2 \times \mathbb{R}^+$, describing the fiber:

$$P = \{p_0, \dots, p_l\}, \; p_i = (x_i, \mu_i, r_i) \in \mathbb{R}^3 \times S^2 \times \mathbb{R}^+. \tag{6.23}$$

The starting point $p_0 = (x_0, \mu_0, r_0)$ and the path length l could be generated from four distributions for the starting coordinate, the principal fiber orientation, the fiber radius, and the fiber length. In general, the initial coordinate x_0 is uniformly distributed in a cubic window with periodic edge treatment $x_0 \sim U(W \subset \mathbb{R}^3)$. The other three distributions describe the main parameters of the fiber

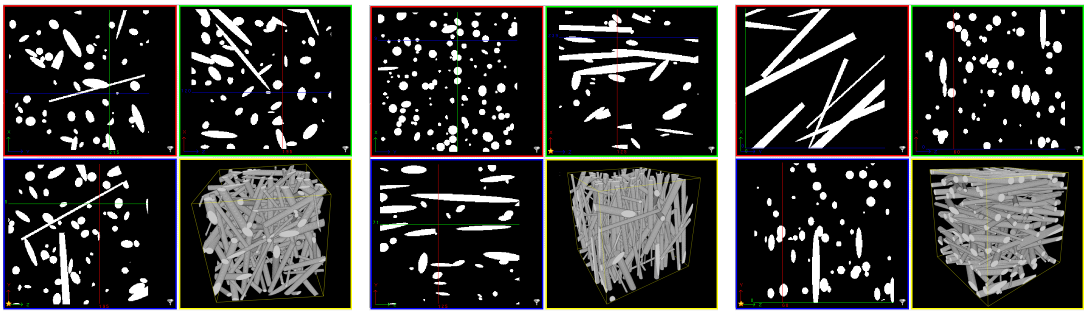

(a) $\beta = 1$, uniformly distributed (b) $\beta = 0.2$, z preferred (c) $\beta = 50$, girdle distribution

Figure 6.6.: Examples of realizations of the cherry-pit fiber model. Modeling Parameters: image size = 300^3, amount of fibers = 200, overlap ratio = 0.5, radius $\in [2, 10]$ and length $\in [200, 300]$. The direction distribution (girdle distribution) is controlled by different values of β.

system. For the orientation distribution, we have applied the β orientation distribution, described in Section 6.1.3. The radius and length can be simulated from any distribution on $\mathbb{R}^+$. The radius can either be fixed for the whole system or chosen once for each fiber or for every point during the random walk with some strategy for smooth variation. The number of fibers for the system is chosen depending on the required volume fraction. Another main characteristic of the fiber system is the bending of the fibers, which is indirectly controlled by two parameters, κ_1 and κ_2, in the multivariate von Mises-Fisher distribution.

During the random walk, the generation of a new point p_{i+1} requires three steps: First, the new orientation μ_{i+1} is generated according to the multivariate von Mises-Fisher distribution, with the last orientation μ_i and the main fiber orientation μ_0 as parameters. Second, the new radius r_{i+1} is generated. Finally, the new coordinate is calculated as $x_{i+1} = x_i + \frac{r_{i+1}}{2}\mu_{i+1}$. The distance between the points is a trade-off between a representative fiber structure and a treatable number of points.

We specify the multivariate von Mises-Fisher distribution in our approach as follows: the first preferred direction is the main fiber orientation μ_0 and the second preferred direction is the orientation of the previous point μ_{i-1}. Therefore, κ_1 describes the reliability to the main fiber orientation, whereas κ_2 describes the reliability to the last orientation and hence specifies the smoothness of the bending. The probability density element for the ith step in the random walk (with $i \geq 1$) is

$$h(\mu_i) = c(\mu_0, \kappa_1, \mu_{i-1}, \kappa_2)\; e^{\kappa_1 \mu_0^T \mu_i + \kappa_2 \mu_{i-1}^T \mu_i}\; \mathrm{d}S. \tag{6.24}$$

Realizations of the soft-core fiber model created by random walks with varying choices of reliability parameters κ_1 and κ_2 are shown in Figure 6.7.

The mean fiber orientation of a created ball chain $P = \{p_0, \dots, p_l\}$ is defined as $\bar{\mu}(P) = \frac{p_l - p_0}{|p_l - p_0|} \in S^2$. The mean orientations of the created fibers are supposed to be realizations of a global orientation distribution for the fiber system. The starting orientations μ_0 are chosen with respect to the global orientation distribution, but the mean orientation differs from μ_0 with a deviation depending on the reliability parameters κ_1 and κ_2. To ensure the global orientation distribution, we rotate the chosen fiber, so that the mean fiber orientation equals the originally chosen main fiber orientation: $\bar{\mu}(P) = \mu_0$. The fiber structure (length, radii, bending) remains constant during the rotation. Every

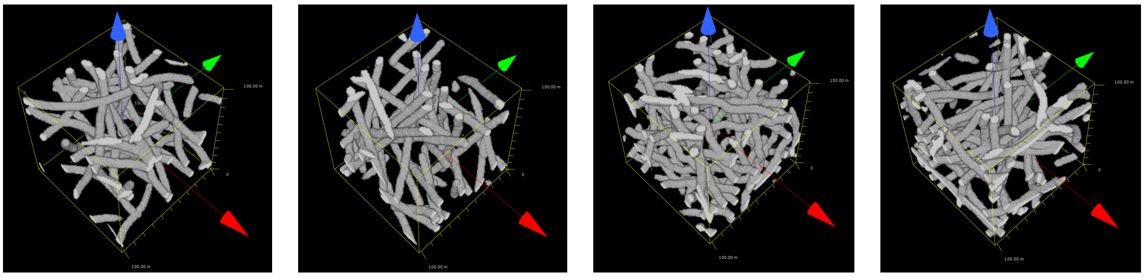

(a) $\kappa_1 = 1, \kappa_2 = 100$ (b) $\kappa_1 = 100, \kappa_2 = 1$ (c) $\kappa_1 = 10, \kappa_2 = 10$ (d) $\kappa_1 = 10, \kappa_2 = 100$

Figure 6.7.: Realizations of the fiber model created by random walks. Common parameters are as follows: number of fibers $n = 10$, window side length $s = 100$, fixed fiber length $l = 300$ and fixed fiber radius $r = 3$, and isotropic orientation distribution ($\beta = 1$).

ball $p_i = (x_i, \mu_i, r_i)$ is adjusted to $p'_i = (x'_i, \mu'_i, r_i)$ with

$$x'_i = x_0 + \mathrm{Rot}(x_i - x_0, n, \alpha) \tag{6.25}$$

$$\mu'_i = \mathrm{Rot}(\mu_i, n, \alpha) \tag{6.26}$$

$$n = \mu_0 \times \bar{\mu}(P) \tag{6.27}$$

$$\alpha = \measuredangle(\mu_0, \bar{\mu}(P)) \tag{6.28}$$

$$\mathrm{Rot}(\mu, n, \alpha) = (n \cdot \mu)n + \cos\alpha((n \times \mu) \times n) + \sin\alpha(n \times \mu), \tag{6.29}$$

where the center dot "·" denotes the scalar product (or inner vector product) and the sign "×" indicates the cross product (or vector product). The random walks create a stochastic fiber model made of overlapping ball chains. The system is defined by the graph (P, E), where

$$P = \{p_{1,1}, p_{1,2}, \ldots, p_{1,l_1}, p_{2,1}, \ldots, p_{n,l_n}\} \subset \mathbb{R}^3 \times S^2 \times \mathbb{R}^+ \tag{6.30}$$

yields the created points and

$$E = \{(p_{i,j}, p_{i,j+1}) \mid i \in \{1, \ldots, n\}, j \in \{1, \ldots, l_i\}\} \tag{6.31}$$

yields the connections between the points according to the n paths of the random walks. l_i is the number of points for the ith fiber. Furthermore, we define

$$C = \{(q, p, q') \in P^3 \mid (q, p) \in E \wedge (p, q') \in E\} \tag{6.32}$$

as the joints between two edges. For further steps, we need to remember the original distance between two neighboring points and the original angle in every joint. Thus, we define an original distance and an original angle function,

$$\begin{array}{rccc} D_{orig}: & E & \to & \mathbb{R}^+ \\ & (p, q) & \to & |x_p - x_q| \end{array} \tag{6.33}$$

$$\begin{array}{rccc} A_{orig}: & C & \to & [0, \pi] \\ & (q, p, q') & \to & \measuredangle(x_q, x_p, x'_q) \end{array} \tag{6.34}$$

and fix the mappings before the fiber packing process starts.

6.4. Force Biased Fiber Packing

To achieve a hard-core fiber system, the fiber packing applies two kinds of forces to the ball centers given by the soft-core fiber model from the previous section: the repulsion force to separate overlapping balls and the recover force to keep the fiber structure. The reconfiguration of the ball chains is realized in several steps. In each step, the forces are calculated for the current configuration of the system, and displacements are performed, respectively.

6.4.1. Repulsion Force

The repulsion force for a pair of overlapping balls describes the necessary displacement to make them non penetrating. An overlap between two balls is permitted if the balls are close neighbors in the same fiber. In this case, we define the two points $p, q \in P$ as related:

$$p \sim q \Leftrightarrow \exists \text{ path between } p \text{ and } q \text{ with length} \leq 5. \tag{6.35}$$

The value of 5 is an approximation for the minimal distance of two balls in the same chain that do not naturally overlap. The distance between the ball centers of two direct neighboring balls is chosen as $r/2$. In this case, balls in the same chain connected by a path with length less than 4 do overlap naturally. In order to take care of small deviations in the radius or additional curvature, we increase the minimal path length to 5.

Let $p_1 = (x_1, d_1, r_1)$ and $p_2 = (x_2, d_2, r_2) \in P$ be two arbitrary points in the fiber system. The overlap between those two points is

$$\text{Overlap}(p_1, p_2) = \max\left[0, r_1 + r_2 - d(x_1, x_2)\right] \tag{6.36}$$

with the distance function $d(x_1, x_2)$ respecting the periodic edge treatment. The repulsion force given by

$$F_{\text{rp}}(p_1, p_2) = \mathbb{1}_{p_1 \nsim p_2} \frac{\text{Overlap}(p_1, p_2)}{2} \frac{x_1 - x_2}{|x_1 - x_2|}, \tag{6.37}$$

is applied if the points are not related as defined in Equation (6.35). The force on p_1 works in the opposite direction to p_2, with a strength linearly dependent on the overlap. The total repulsion force for the point p_1 is cumulated over all points in P:

$$F_{\text{rp}}(p_1) = \sum_{q \in P} F_{\text{rp}}(p_1, q). \tag{6.38}$$

6.4.2. Recover Force

The recover force keeps the distance between neighboring points by modeling springlike forces between them, and it keeps the angle in the joints by modeling open springs between the connections. Open springs describe the fact that there is a force for decreasing but none for increasing angles. Thus, a fiber can be straightened but not folded into a clew.

The recover force is induced by a displacement of the original ball coordinate as an effect of the applied repulsion force. By applying the recover forces to one ball it induces recover forces on its neighbors. Even if the strength of the indicated forces is decreasing, a kind of domino effect has started, and the process does not stop. In order to stabilize the movement, we introduce a smoothing factor, which acts like a starting friction. We define a minimal change x_s, which is necessary to induce a force, and a change x_e when the force regains its full strength. The friction factor is defined as

$$f_{x_s, x_e}(x) = \begin{cases} 0 & , x < x_s \\ \frac{1}{2} - \frac{1}{2}\cos\left(\frac{|x| - x_s}{x_e - x_s}\pi\right) & , x_s \leq x \leq x_e \\ 1 & , x_e < x \end{cases} . \tag{6.39}$$

The curve $f_{x_s, x_e}(x)$ is given in Figure 6.8.

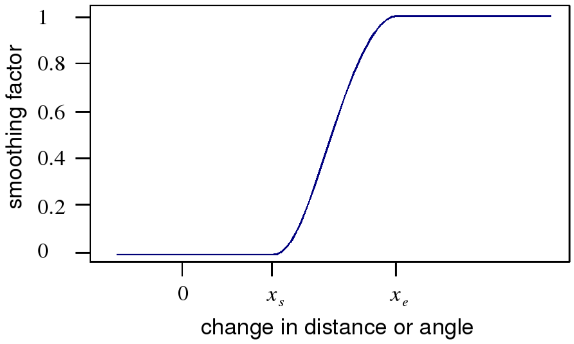

Figure 6.8.: Friction factor for recover forces.

Spring Force: In order to keep the distances between the balls in a fiber, we define a force between the centers of the balls, with a strength linearly dependent on the change of distance. This kind of force can be interpreted as a spring between the ball centers. Let $p = (x_p, d_p, r_p)$ and $q = (x_q, d_q, r_q)$ be two neighboring points. The change of distance is

$$\Delta D(q,p) = \ D_{orig}(q,p) - |x_q - x_p| \tag{6.40}$$

and the unit vector for the direction of the force is

$$v(p,q) = \frac{x_p - x_q}{|x_p - x_q|}. \tag{6.41}$$

Thus, the recovery spring force F_{rs} on a point p is defined as

$$F_{\mathrm{rs}}(p) = \sum_{q \in P} \left\{ [\mathbb{1}_E(p,q) + \mathbb{1}_E(q,p)]\, f_{d_s,d_e}\left(\frac{|\Delta D(q,p)|}{D_{orig}(q,p)}\right) \times [\Delta D(q,p)]\, v(p,q) \right\}. \tag{6.42}$$

The spring force is applied to p for every direct neighbor (at most two). It is linear to the distance change and multiplied by the friction factor on the ratio of distance change. For the realizations created in our applications, the friction parameters were chosen as $d_s = 5\,\%$ and $d_e = 10\,\%$.

Angle Force: In order to keep the angle between joints, we define a recover force on each point having two direct neighbors. Let $(q_1, p, q_2) \in C$ be a joint in the point $p = (x, d, r)$ with the neighbors $q_1 = (x_1, d_1, r_1)$ and $q_2 = (x_2, d_2, r_2)$. We define

$$\alpha_0 = A_{orig}(q_1, p, q_2) \tag{6.43}$$

$$m = \overline{x_1 x_2} \cap \mathrm{Plane}\,(x, \perp(x_1 - x_2)) \tag{6.44}$$

$$h_1 = |m - x_1|,\ h_2 = |m - x_2|,\ z = |m - p| \tag{6.45}$$

$$\alpha_1 = \tan^{-1}(h_1/z),\ \alpha_2 = \tan^{-1}(h_2/z) \tag{6.46}$$

$$\tan\alpha = \tan(\alpha_1 + \alpha_2) = \frac{z(h_1 + h_2)}{z^2 - h_1 h_2} \tag{6.47}$$

$$z_0 = \frac{h_1 + h_2 + \sqrt{(h_1 + h_2)^2 + 4 h_1 h_2 \tan^2\alpha}}{2\tan\alpha}. \tag{6.48}$$

Now, the recovery angle force F_{ra} on a point p is defined as

$$F_{\mathrm{ra}}(p) = \mathbb{1}_{\exists q_1, q_2 \in P, (q_1, p, q_2) \in C}\ f_{\alpha_s, \alpha_e}(\alpha_0 - \alpha)\ (z - z_0) v(m,p). \tag{6.49}$$

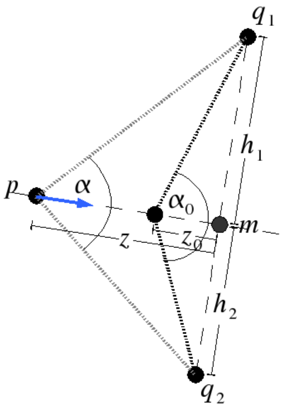

Figure 6.9.: Geometry for angle force.

The angle force is linearly dependent on the necessary displacement to regain the original angle, and it is multiplied by the friction factor, depending on the angle change. For the realizations created in this work, the friction parameters were chosen as $\alpha_s = 0.1\,°$ and $\alpha_e = 0.2\,°$. The geometrical construction is visualized in Figure 6.9.

6.4.3. Application of Force

The total force on an arbitrary point $p \in P$ is composed of the sum of all mentioned forces:

$$F_{\text{total}}(p) = \sum_{q \in P} F_{\text{rp}}(p, q) + \rho F_{\text{rs}}(p) + \rho F_{\text{ra}}(p), \tag{6.50}$$

where ρ is a factor in $[0, 1]$ leading to a smooth development of the recover forces, favoring the repulsion forces in the first steps. For the realizations created in this thesis, we chose $\rho = 0.2$. In order to limit the possible displacement of a point, we define an upper bound $F_{\max}$ for the final force strength:

$$F_{\text{final}}(p) = \frac{F_{\text{total}}(p)}{|F_{\text{total}}(p)|} \min(|F_{\text{total}}(p)|, F_{\max}). \tag{6.51}$$

In each step, the ball center of p is displaced by the limited final force:

$$x'_p = x_p + F_{\text{final}}(p). \tag{6.52}$$

After a displacement step, the forces are recalculated for the new configuration and applied in the following step.

6.4.4. Stop Criterion and End Step

During the packing process the forces decrease very quickly in the beginning and converge slowly to zero in the end. The process should be stopped by a criterion dependent on the force strength. In our implementation, the algorithm terminates with a solution if the total force strength $\sum_{p \in P} F_{\text{total}}(p)$ falls below a certain limit and the displacements become negligible. For the realizations created in this work, we chose the limit as $0.002\, s\, n$, where n is the number of fibers and s the side length of the window. That means the mean sum of necessary displacements in a fiber is smaller than 0.2%

of a unit size. When the volume fraction is chosen too high, it is possible that there is no configuration with low force strength. In this case, the process will not converge, and we need to add a stop criterion. We have chosen an upper bound for the number of steps of 10 000. If the process reaches this limit, it will terminate unsuccessfully. This stop criterion varies from the idea in the force-biased sphere packing, where the radius is directly reduced to a non interacting size and the volume fraction of the sphere system with reduced radii decides about the termination of the process.

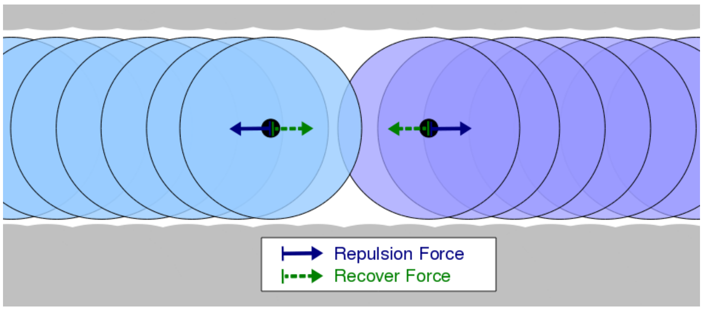

(a) Trade-off between repulsion and recover forces.

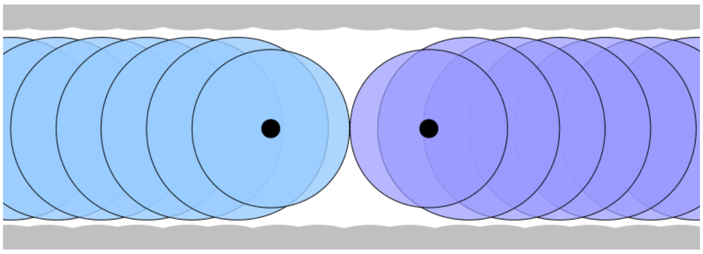

(b) Solution 1: Reducing the radius.

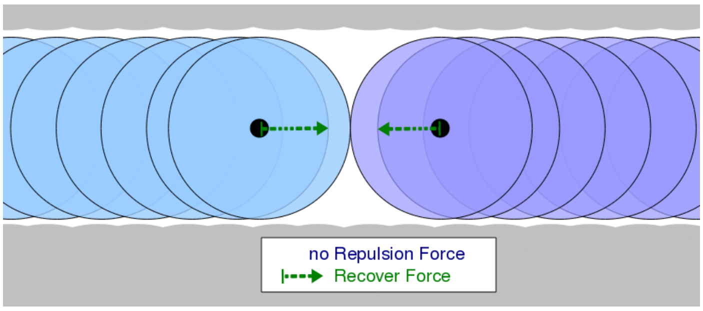

(c) Solution 2: Endstep regarding only the repulsion forces.

Figure 6.10.: Trade-off problem in the final configuration with two possible solutions: reducing the radius or applying an end step considering only the repulsion forces. Note that force vectors are elongated for visualization reasons; they do not correspond to the necessary displacements.

In the case of a successfully completed process, the total force strength is negligible. Still, one should be aware that the total force on a point is a sum of different forces. Thus, even if the sum of forces is zero, it is not sure that every specific force is negligible in its strength. In particular, for the repulsion force, it may happen that the recover force acts in the opposite direction with exactly the same strength [as shown in Figure 6.10(a)]. As the repulsion force is linear to the overlap, we conclude that the fiber packing does not necessarily have a zero overlap, which means that the system may not be totally hard-core.

This effect is similar to the maximal random jammed state, known from random packings (see Laso *et al.* (2009)). In our approach, a ball is never jammed since its displacement is defined by reducing forces and overlap in a following configuration is not strictly forbidden. Still, we have a similar situation if the requested volume fraction is too high for the fiber structure.

To assure a non overlapping system, we accept an outcome only if the maximal overlap falls below a certain limit. Here we chose $0.1\, r_{\min}$, where $r_{\min}$ is the minimal radius in the system. Then, a final step is added, where the radius of each point is reduced according to the maximal overlap with other points. This approach is similar to the idea in the force-biased sphere packing. Let $p = (x, d, r) \in P$ be an arbitrary point of the fiber system; the radius r is reduced to

$$r' = r - \frac{1}{2} \max_{q \in P, q \nsim p} \operatorname{Overlap}(p, q). \tag{6.53}$$

If the accuracy of the radius distribution is very important, the end step can be replaced by a second run of the packing algorithm, where only the repulsion force is active. In this case, the theoretical recover force strength should be checked afterwards, to make sure that the fibers are not drawn apart.

6.4.5. Implementation Details

The periodic distance function for $x = (x_x, x_y, x_z)^T$ and $y = (y_x, y_y, y_z)^T$ and a window $W = [0, w_x] \times [0, w_y] \times [0, w_z]$ is defined as

$$d(x, y) = \left| \begin{pmatrix} \min(|x_x - y_x|, w_x - |x_x - y_x|) \\ \min(|x_y - y_y|, w_y - |x_y - y_y|) \\ \min(|x_z - y_z|, w_z - |x_z - y_z|) \end{pmatrix} \right|. \tag{6.54}$$

The repulsion force on an arbitrary point $p \in P$ is defined as the sum over all points $q \in P$. Still, the repulsion force is equal to zero if balls p and q are not overlapping, which is definitely the case if $q \notin B_{r_p + r_{\max}}(x_p)$, where $r_{\max} = \max_{q \in P} \ r_q$. As proposed in Mościński & Bargieł (1989) we divide the window W into smaller cubic subwindows with a side length $s_i \geq r_{\max}$ with $i \in \{x, y, z\}$. For a window $W = [0, w_x] \times [0, w_y] \times [0, w_z]$ the side lengths of the subwindows are calculated as

$$s_i = \frac{w_i}{n_i}, \quad n_i = \lceil \frac{w_i}{r_{\max}} \rceil. \tag{6.55}$$

Thus, $B_{r_p + r_{\max}}(x_p)$ is included in the union of the subwindow including p and its neighbor subwindows. The overlap check is limited to this union.

Experiments show that the number of iterations can be essentially reduced by including a placing strategy in the initial random walk. For every fiber to be added to the system, we choose several starting points and place the fiber to the one with the lowest overlap to the existing fibers. This strategy avoids multiple clustering of fibers and therefore the fiber packing can start with a more relaxed configuration.

6.4.6. Realizations

Figure 6.11 shows realizations of the presented model with varying input parameters for the fiber aspect ratio χ, the number of objects n and the global orientation distribution. The parameters and the achieved volume fraction V_V are given below for each realization.

The aspect ratio is generally defined as length divided by diameter. In the case of a ball chain $p_1, \ldots, p_n$ with fixed radius r, the aspect ratio χ can be calculated as

$$\chi = \frac{2r + \sum_{i=1}^{n-1} |p_i - p_{i+1}|}{2r}. \tag{6.56}$$

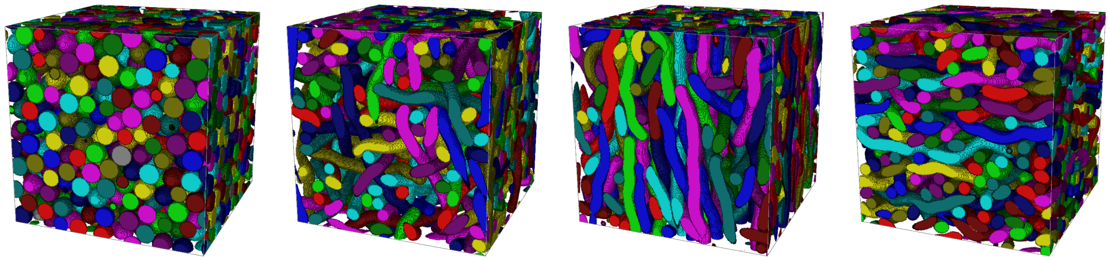
(a) $\chi = 1$, $n = 1146$, $V_V = 57.27\%$
(b) $\chi = 33$, $n = 90$, $V_V = 50.35\%$, isotropic orientation ($\beta = 1$)
(c) $\chi = 17.67$, $n = 170$, $V_V = 49.60\%$, orientation in z-direction ($\beta = 0.1$)
(d) $\chi = 17.67$, $n = 170$, $V_V = 49.95\%$, orientation in xy-plane ($\beta = 10$)

Figure 6.11.: Realizations for packed fiber systems. Common parameters are as follows: window side length $s = 100$ and bending parameters $\kappa_1 = 10$ and $\kappa_2 = 100$.

To evaluate if the final configuration fulfills the required distributions, we observed the changes in the characteristics of the fiber system during the force-biased packing for three realizations with different choices of $\beta \in \{0.1, 1, 10\}$. The remaining parameters are chosen as follows: window size $= 100^3$, length $= 50$, radius $= 5$, number of fibers $= 100$, and required density $= 44.483\%$. The evolution of the characteristics is shown in Figure 6.12. The estimation of the parameters will be discussed in details in Section 6.6, still we roughly sketch the main ideas here: The estimation of length and radius is obvious. The measured density is the volume fraction of the discretized image. The β estimate is the numerical approximation of the maximal likelihood estimator, which cannot be resolved theoretically. The estimation of the bending parameters κ_1 and κ_2 is not that simple, but experiments showed that they can be approximated for $\kappa_2/\kappa_1 > 2$ with the following estimates:

$$\hat{\kappa}_1 = 1/\mathrm{Var}_1 \quad \text{with} \quad \mathrm{Var}_1 = \frac{1}{n}\sum_{j=1}^{n}\left(\frac{1}{l_j}\sum_{i=0}^{l_j}\left[\mu_{j,i} - \bar{\mu}(p_{j,1}, \ldots, p_{j,l_j})\right]^2\right) \tag{6.57}$$

$$\hat{\kappa}_2 = 2/\mathrm{Var}_2 \quad \text{with} \quad \mathrm{Var}_2 = \frac{1}{n}\sum_{j=1}^{n}\left(\frac{1}{l_j - 1}\sum_{i=0}^{l_j-1}\left(\mu_{j,i} - \mu_{j,i+1}\right)^2\right). \tag{6.58}$$

The estimates are not highly accurate. However, they still describe the global and local bending. As long as the measures of the real data set and the measures of the final model configuration are close, the aim of realistically reproducing the fiber structure is fulfilled.

In Figure 6.12, the first steps are mostly driven by the repulsion forces, which evokes changes in the local structure and therefore in the parameter measure. When the repulsion force decreases, the recover forces reconstruct the fiber structure, which results in a convergence of the measures to the requested values. Most measures start with the requested values, except for the density and the global bending parameter κ_1. The low density in the beginning is evident, as the overlapping fiber volume is counted only once. The deviation of the global bending parameter κ_1 or reliability to the principal fiber orientation is caused by different measure conditions: During the realization of the fiber structure, κ_1 represents the reliability to the chosen fiber orientation μ_0, whereas the measure of κ_1 reflects the reliability to the resulting fiber orientation $\bar{\mu}(P)$, which differs slightly. This results in an overestimation of the parameter κ_1. The convergence to the required value is surprisingly good

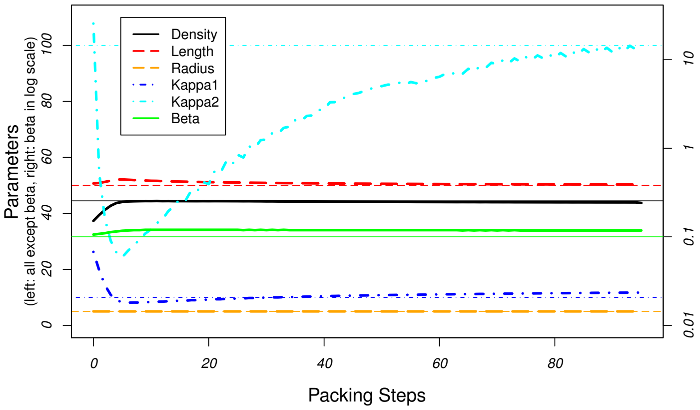

(a) Orientation distribution with $\beta = 0.1$

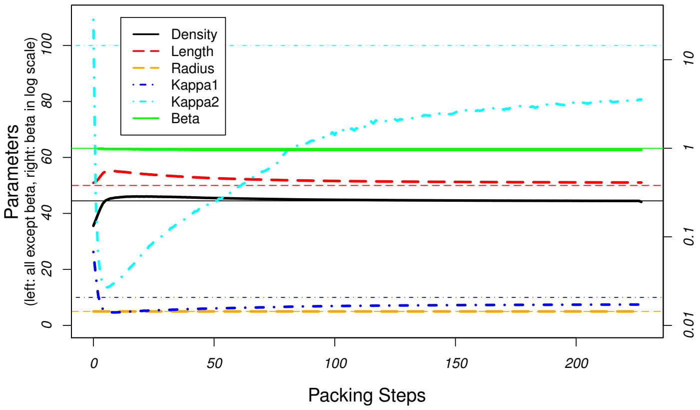

(b) Orientation distribution with $\beta = 1$

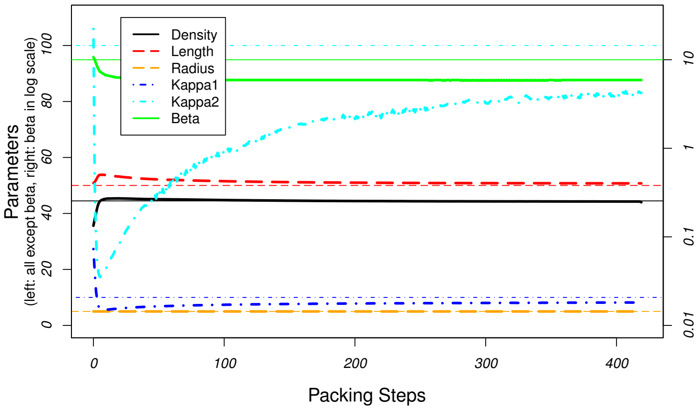

(c) Orientation distribution with $\beta = 10$

Figure 6.12.: Evolution of estimated model parameters during the packing process for different choices of β for the orientation distribution. Fixed parameters are as follows: window size = 100^3, length = 50, radius = 5, number of fibers = 100, and starting density = 44.483%.

and is probably caused by the trade-off between the recover force to the original fiber structure and the tolerance range of local deviation.

We stress once more that the important configuration is the final one, and the geometric characteristics during the process are studied to understand better what happens during the packing process. The evaluation of the quality of our models is only based on the geometric characteristics of the final configuration, as shown in Table 6.1.

	Density	Length	Radius	κ_1	κ_2	β
Required	44.48%	50	5	10	100	various
$\beta = 0.1$	43.94%	50.66	4.99	9.91	96.32	0.134
$\beta = 1$	43.90%	50.75	4.98	8.21	80.95	0.87
$\beta = 10$	44.10%	50.90	4.98	8.03	82.39	5.6

Table 6.1.: Parameter measures for the final configuration of experiments from Figure 6.12.

In both visualizations, we can see that the parameters of length, radius, and density fit perfectly to the requested values. The global and local bending κ_1 and κ_2 are approaching the required values, as expected. As the local orientations have some tolerance during the packing process, it is understandable that the final bending values are lower than the initial ones. If the final bending values are not satisfying, there are two possibilities to improve this: first, one can choose the initial values higher than required, and second, one can reduce the tolerance α_s and α_e in the packing process. The parameter β for the orientation distribution is acceptably approximated for the choices $\beta = 0.1$ and $\beta = 1$, whereas the girdle orientation with $\beta = 10$ could not be maintained that strictly during the packing process. The results would even become worse for higher choices of β. With the described model, we can realize parameters in the range of $0.05 - 5$. If a more restricted orientation distribution is required, recover forces for the orientation of a fiber have to be included. This could be obtained by forces on the extremities of a fiber. As we included no restrictions in changing the mean fiber orientation during the packing process, the system will relax in a less restrictive configuration.

6.4.7. Discussion

In this section, we discuss the volume fractions achieved by numerical simulations and the evolution of the repulsion and recover forces during the fiber packing. Furthermore, we analyze the computing time.

Volume Fraction

The maximal volume fraction depends on the aspect ratio and on the orientation distribution of the system. Figure 6.13 shows the maximal volume fractions, achieved with realizations for the β orientation distribution with $\beta \in \{0.1, 1, 10\}$ and varying aspect ratio $\chi \in [1, 33]$. We achieved the highest volume fraction 72.0075 % for an aspect ratio of 9 and a z axis preferred orientation distribution with $\beta = 0.1$. In general, Figure 6.13 supports the intuitive expectation that fibers can be packed in a particularly dense system, if they are oriented parallel, and that short fibers can be packed more easily.

In Figure 6.14, the ratio of achieved volume fraction to initial volume fraction is shown. The initial volume fraction is the sum of all fiber volumes after the random walk divided by the window size. The change of the distances between the balls is related to a change in the volume fraction. As we allow small deviations in the distances, we allow also small deviation in the volume fraction. Here the deviation of the distances is limited to 10 %. As a consequence, there also exists a limit

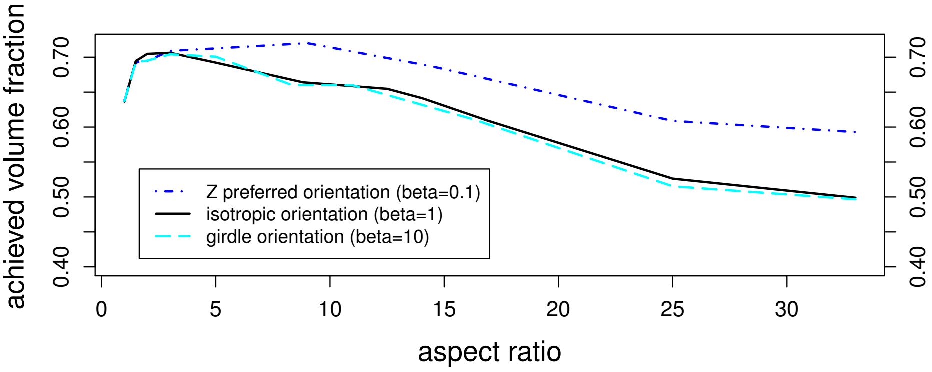

Figure 6.13.: Maximal volume fractions for realizations with varying orientation distributions and aspect ratios.

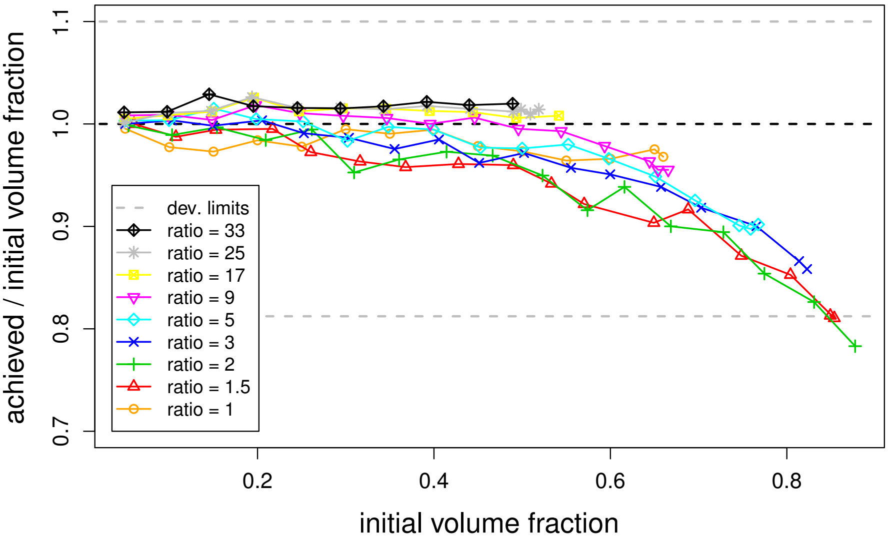

Figure 6.14.: Ratio of the achieved volume fraction and the initial volume fraction for isotropic orientation distribution.

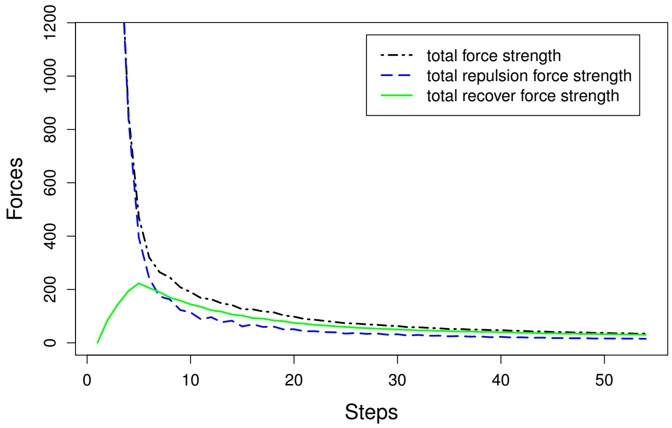

Figure 6.15.: Evolution of force during the fiber packing process. Aspect ratio $\chi = 6$. Isotropic orientation distribution.

for the deviation of the volume fraction caused by the distance change. It ranges from 90 % to 110 % of the initial volume fraction. Another deviation in the volume fraction is caused by the end step, reducing the radii. The maximal overlap is $0.1\,r_{\min}$, and a radius r is maximally reduced by $\frac{1}{2}$Overlap $\leq 0.05\,r_{\min} \leq 0.05\,r$. Therefore, the volume V of a fiber could maximally be reduced to

$$V' \approx l\pi(r')^2 > (0.95)^2 l\pi r^2 \approx 0.9025\,V. \tag{6.59}$$

Thus, a lower limit for the volume fraction would be $0.9 \cdot 0.9025 = 81.225\%$ of the initial volume fraction. The upper limit remains at 110% since the radius is not enlarged in the end step. Note that this is a rough approximation of the limits. Particularly for dense systems, it may happen that bending or force-canceling effects influence the structural arrangement, so that these limits are exceeded. We assume that this effect happened in one of realizations in Figure 6.14: the point with the highest required volume fraction of 90% underruns the lower limit. Note that volume fraction of 90% is impossible to reach for a fiber system with spherical fiber cross-section.

The reduction of the volume fraction is expected for dense systems of fibers with a low aspect ratio, where the packing consists of moving and shortening of the objects, which causes a decrease of the volume fraction. The aspect ratio 1 is a special case, as the “fibers” consist only of one ball and shortening is not possible. For a high aspect ratio, the packing is essentially bending the fibers around each other, which causes elongation of the fibers and rising of the volume fraction.

Evolution of Forces

Figure 6.15 shows the evolution of the repulsion and recover forces during the fiber packing. Initially, the recover force is zero, as the fibers still have the initial structure, whereas the repulsion force is high at the beginning because the fibers can overlap without restriction. The repulsion force is decreasing very quickly, while the recover force rises slightly in the first steps, caused by the displacements according to the repulsion forces, and decreases quite smoothly with respect to the parameter ρ.

Computing Time

In practical applications the algorithm showed good performance. All time measurements are taken with a desktop PC with an Intel(R) Core(TM)2 processor with CPU X6800, 2.93 GHz and 3.8 GB

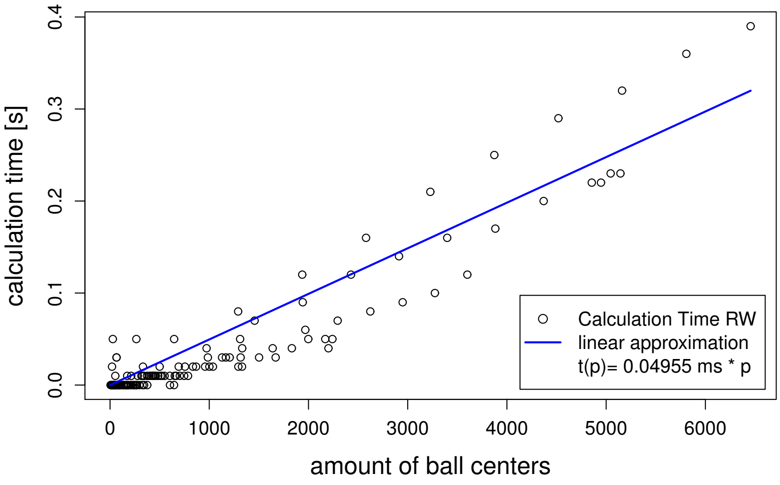

(a) Computing time of random walk vs. amount of ball centers.

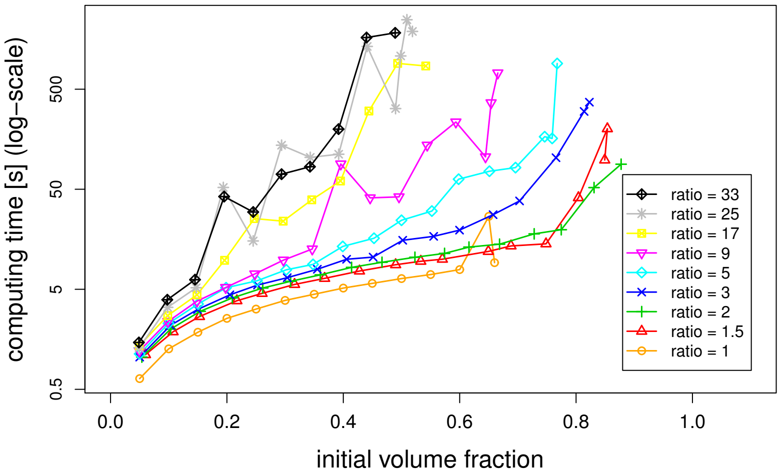

(b) Computing time of fiber packing vs. initial volume fraction.

Figure 6.16.: Computing time of the random walk and the fiber packing for isotropic orientation distribution and constant fiber volume of $0.005\,s^3$, with $s = 100$ window side length.

memory. Realization conditions are an isotropic global orientation distribution and constant fiber volume of $0.005\,s^3$, and $s = 100$ as window side length. The creation time for the random walk progresses approximately linearly with the number of steps, which corresponds to the total number of ball centers in the system. The mean creation time per ball center is approximately 0.05 ms:

$$t_{\mathrm{RW}} \approx 0.05\,\mathrm{ms} \times \text{ number of ball centers.} \tag{6.60}$$

The computing time for the fiber packing increases exponentially with the volume fraction V_V for fixed aspect ratio χ. This is caused by the enormous increase of interaction with increasing volume fraction. Still, the realization with the longest computing time took about 41 min for an aspect ratio $\chi = 25$, an isotropic orientation distribution, and an achieved volume fraction of $V_V = 51.43\%$, which is at the limit of the possible volume fraction for the given parameters. The computing time is acceptable for those circumstances and a standard desktop computer. The computing time for the random walk and the fiber packing are shown in Figure 6.16.

6.4.8. Conclusion and Perspectives

We have presented an algorithm generating bending hardcore fibers, with given orientation, radius, and length distributions. We showed how to evaluate the quality of the final configuration of the fiber system. For the performed realization, we could achieve high convergence to the requested parameters, and for the global orientation distribution, we studied the realizable range for the parameter β. In the future, we will include further recover forces to be able to realize more restricted orientation distributions.

In practical tests, we achieved the highest volume fraction of 72.0075 % for the β orientation distribution ($\beta = 0.1$) and an aspect ratio of 9. Practical applications for isotropic orientation distribution have shown a computing time linearly dependent on the number of points for the random walk and a computing time exponentially increasing with the initial volume fraction for the fiber packing.

A soft-shell ratio can be easily included to allow partial overlap or to keep distances between the objects. In the overlap calculation, each radius would be multiplied by the soft-shell ratio. Further studies will include the observation of additional morphological properties during the packing process and the application and adaption of the model parameters to data sets on real materials.

6.5. Placing Strategy

In the above described stochastic model, there is no strategy for placing the fibers in the initial configuration. Still, the initial placement influences highly the time of stabilization in the packing process. We can make use of the idea of the random sequential adsorption algorithm (RSA, see Feder (1980)) to create the initial configuration.

The RSA algorithm was originally invented for sphere packing, but can be generalized to any kind of objects. In a first step, a finite set of objects is created in a stochastic process. In the second step, the objects are iteratively inserted in the scene of interest with well defined boundary conditions. For every object, which should be inserted in the scene, new placements are randomly chosen and the object is inserted as soon as a placement is found without any collision with the already inserted objects. To assure chosen characteristic distributions of the object (as for example size or orientation distribution) it is important that the object is not recreated, but only displaced. Otherwise, objects with smaller size or aligned orientations would be preferred.

In the case of fiber systems, the RSA algorithm combined with cylindrical objects has the disadvantage, that only low volume fractions can be achieved. However, it can serve to create a less overlapping initial configuration for our stochastic model. The criterion to evaluate a placement for a sphere chain $F_m = \{p_{m,1}, \ldots, p_{m,l_m}\}$ in a scene with $m-1$ already inserted fibers $F_1, \ldots, F_{m-1}$ can be either the maximal overlap or the sum of overlaps of the spheres of the fiber F_m with the already inserted fibers. We define these two criteria as following:

$$C_{\max}(F_m \mid F_1, \ldots, F_{m-1}) = \max_{i,j,k}\{\text{Overlap}(p_{m,i}, p_{k,j})\} \tag{6.61}$$

$$C_{\text{sum}}(F_m \mid F_1, \ldots, F_{m-1}) = \sum_{i,j,k} \text{Overlap}(p_{m,i}, p_{k,j}) \tag{6.62}$$

with $1 \leq i \leq l_m$, $1 \leq k \leq m-1$, $1 \leq j \leq l_k$. We displace the objects as long as the criterion value is higher than a global limit $\text{Overlap}_{\text{min}}$, which serves also as stop criterion for the packing process. After a certain volume fraction, the probability to exceed this limit is quite low (otherwise the packing process would not be necessary). Therefore, we fix a certain number of placements (in the experiments prepared for this work we tested 10 and 100). The object is inserted at those placement, having the lowest value of the evaluation criterion.

Figure 6.17 shows the computation time for the fiber packing with 10 and 100 steps for the initial configuration and the standard Boolean configuration. The model is realized in a unit cube with periodic boundary conditions. The fibers are isotropically oriented and have an aspect ratio of 9 and a volume of 1% of the cube volume. The curvature parameters are chosen as $\kappa_1 = 10$ and $\kappa_2 = 100$. The experiment runs 100 realizations of the stochastic model and averages the extracted characteristics.

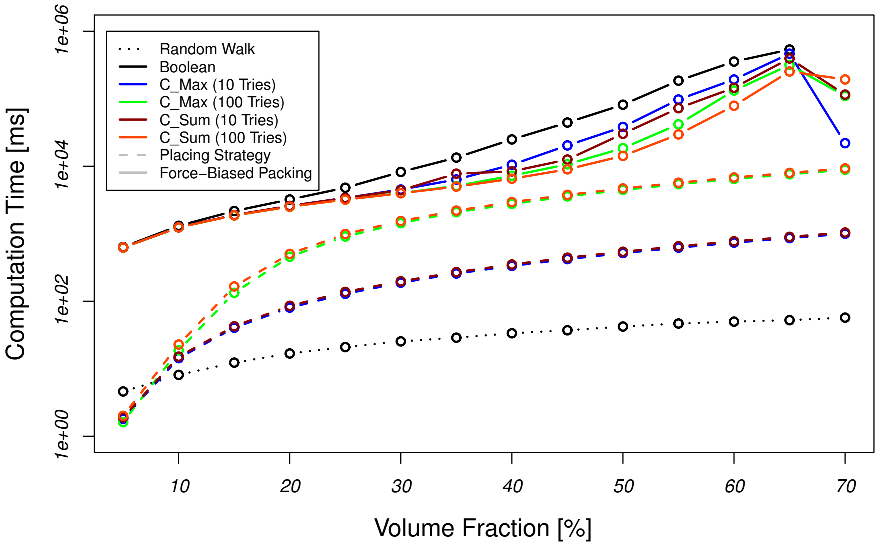

Figure 6.17.: Computation times for the object generation.

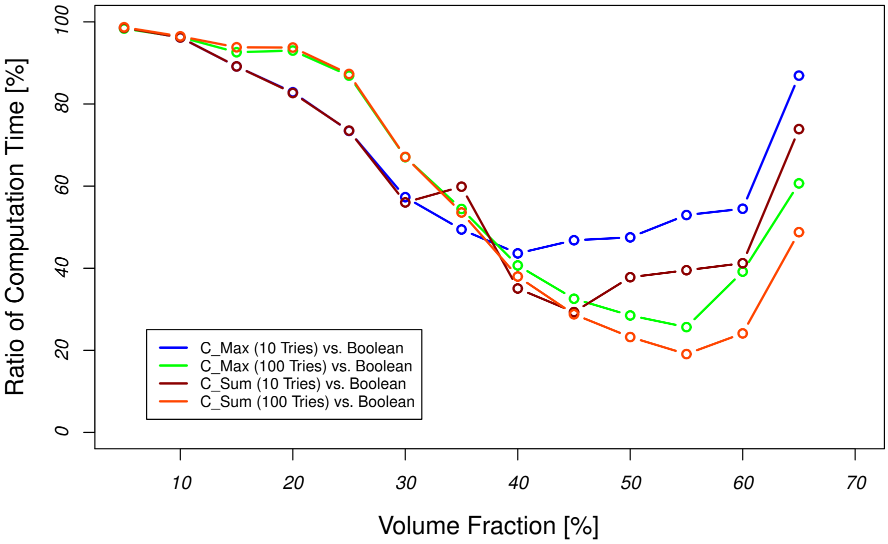

Figure 6.18.: Ratio between the times of fiber packing with and without placing strategy.

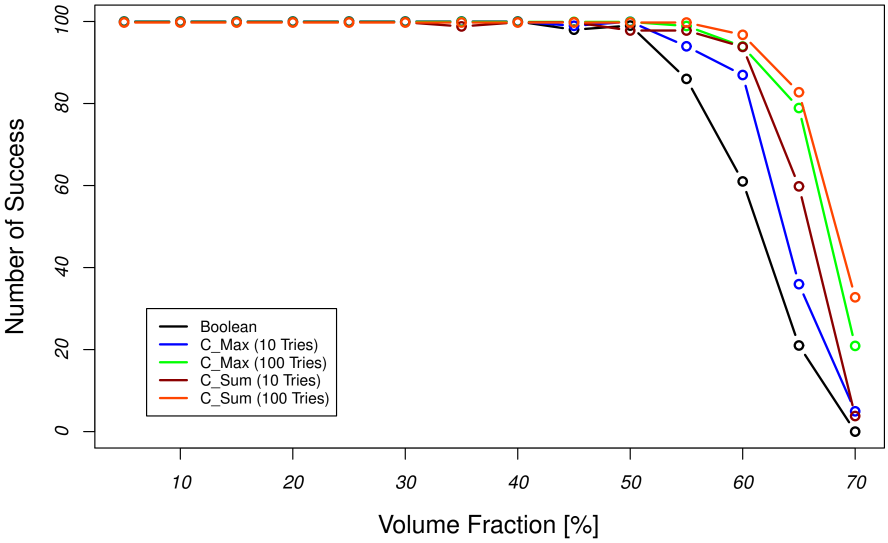

Figure 6.19.: Probability of success for the fiber packing process.

Figure 6.18 shows the ratio of the placing and packing time versus the packing time without strategy for the initial configuration. We observe that the strategy is not very efficient for low volume fractions, as in this case the probability of overlap is very low, thus already the first random placing has low overlap and even in the case of overlap, there is enough free space to displace the fiber in only few steps. The influence of the placing strategy rises with the volume fraction until about $50\% - 55\%$, where the placing strategy results in a more evenly placed systems and decreases the appearance of locally overcrowded areas. When the volume fraction rises over 55%, the influence of the placing strategy decreases again and may even vanish for very dense systems. This effect has two reasons. First, we count only the successfully finished jobs, which results in an underestimation of the computation times for cases with low success rate. Secondly, for a higher volume fraction, we have also a higher amount of fibers, which may be naturally placed more evenly over the image (according to the law of large numbers). Additionally, the placing strategy gets ineffective as with the high density, as there exits no "good" placement any more. Thus the last fibers are placed randomly and the configurations with or without strategy are equally distributed in space.

Still, Figure 6.19 shows that the placing strategy increases the probability to successfully finish the packing process for high volume fractions. For 70% of volume fraction, there remain no successfully finished packings without placing strategy, whereas the probability of the process with the C_{sum} criterion and 100 placing tests is still at 33%. Thus, we conclude that for medium to high volume fractions, the use of a placing strategy is advisable. Still, as this part of the thesis is a very recent study, the placing strategy was not used for the presented applications.

6.6. Parameter Estimation

In order to fit a stochastic model realistically to an existing material, it is important to accurately estimate the model parameters. For the force-biased fiber model this would be: the volume fraction V_V, the distribution of the fiber radius and orientation, the mean fiber length and the curvature expressed by κ_1 and κ_2.

Local information and histograms about the radius and orientation distribution, can be estimated directly from the original CT image (as explained in Chapter 3). Still, we need to fit a stochastic model to the empirical distributions. The volume fraction can be measured from a binarized image, which is created e.g. during the local analysis. Approximation of the mean fiber length and the fiber curvature requests a separation of single fibers (presented in Chapter 5), which is applicable in the case of fiber systems with moderate volume fraction and sufficient resolution. The separation of single fibers results in a reconstruction of the fibers as ball chains (equal to the structure created by the random walk) and is therefore highly qualified for the parameter estimation.

We will also mention here the different possibilities to base our statistics on: the local analysis from the gray value images or the binarized image, the fiber reconstruction from the single fiber separation and the different weighting (number-, length- or volume-weighted). Ideally, all the possibilities agree in the statistics, unfortunately this is not always the case in praxis. The experiments show similar results in the length-weighted statistics from the smoothed and quality-weighted local analysis and from the separated fibers. The length-weighted statistics are preferable to the number-weighted one (which are now possible with the separated fibers), as short fiber with maybe not representable properties are gaining too much interest in the number-weighted evaluation. Thus, in the following we show how to estimate the model parameters from the reconstructed fiber system with length-weighting, that can be realized by taking into account every sphere of the chain (as the number of spheres are linearly dependent on the fiber length).

Radius Estimation

The reconstructed ball chains from the single fiber separation are described by

$$P = \{p_{1,1}, p_{1,2}, \ldots, p_{1,l_1}, p_{2,1}, \ldots, p_{n,l_n}\} \tag{6.63}$$

with $p_{j,i} = (x_{j,i}, \mu_{j,i}, r_{j,i}) \in \mathbb{R}^3 \times S^2 \times \mathbb{R}^+$. The fiber index is $j \in \{1, \ldots, n\}$ and the balls in the fiber j are ordered by the index $i \in \{1, \ldots, l_j\}$. Parameters for the stochastic model can be directly measured from this reconstructed microstructure. The estimation of the mean radius and its standard deviation is evident:

$$\bar{r}(P) = \frac{1}{L} \sum_{j=1}^{n} \sum_{i=1}^{l_j} r_{j,i} \quad \text{with} \quad L = \sum_{j=1}^{n} l_j \tag{6.64}$$

$$\sigma_r(P) = \sqrt{\frac{1}{L} \sum_{j=1}^{n} \sum_{i=1}^{l_j} (r_{j,i} - \bar{r}(P))^2}. \tag{6.65}$$

In general, we try to fit the normal distribution to the empirical radius distribution with the above parameters. Of course, the distribution model needs to be adapted to every application respectively.

Length Estimation

For long fiber reinforced composites as CRP and GRP, the fibers are so long that they emerge the samples prepared for CT with sufficient resolution. Therefore, there is no way to estimate a distribution of the fiber length. The mean fiber length can be approximated from the sum of all fiber lengths divided by half the visible ends, excluding the cuts at image borders:

$$\bar{l}(P) = \frac{2}{\#(\text{visible ends})} \sum_{j=1}^{n} \sum_{i=2}^{l_j} |x_{j,i} - x_{j,i-1}| \tag{6.66}$$

Still, every incorrect reconstruction can highly influence the estimation. It happens quite often that one fiber could not be tracked completely and splits up in two or more parts. This behavior distorts mainly the length estimation, so we suspect the mean fiber length to be underestimated.

Global Orientation Distribution

The global fiber orientation distribution is determined by the parameter β, which can be approximated by the statistic over $|\cos\theta|$ which yields theoretically

$$\mathbb{E}(|\cos\theta|) = \frac{1}{\beta + 1} \quad \text{therefore} \quad \hat{\beta} = \mathbb{E}(|\cos\theta|)^{-1} - 1. \tag{6.67}$$

The deduction of this statistic is sketched in the following:

$$\begin{aligned}\mathbb{E}(|\cos\theta|) &= \int_0^{2\pi}\int_0^{\pi} f_\beta(\theta,\phi)\ |\cos\theta|\ \mathrm{d}\theta\ \mathrm{d}\phi && (6.68)\\ &= \int_0^{\pi/2} \frac{\beta\sin\theta\cos\theta}{(1+(\beta^2-1)\cos^2\theta)^{3/2}}\ \mathrm{d}\theta && (6.69)\\ &= \frac{\beta}{\beta^2-1}\left[(1+(\beta^2-1)\cos^2\theta)^{-1/2}\right]_0^{\pi/2} && (6.70)\\ &= \frac{\beta-1}{\beta^2-1} = \frac{1}{\beta+1} && (6.71)\end{aligned}$$

Unfortunately, this estimator is not very precise. Nevertheless, it can serve as a first guess to numerically approximate β from the maximum likelihood function:

$$ml(\beta) = n\ln\beta - n\ln(4\pi) - \frac{3}{2}\sum_{j=1}^{n}\ln(1+(\beta^2-1)\cos^2\theta_j), \tag{6.72}$$

for θ_j the angle between the j-th mean fiber orientation $\bar{\mu}(P,j) = \frac{p_{j,l_j}-p_{j,1}}{|p_{j,l_j}-p_{j,1}|} \in S^2$ and the global mean fiber orientation $\bar{\mu}(P)$, which can be derived by the main inertia axis of the set of all mean fiber orientations and their inverse: $M(P) = \{\bar{\mu}(P,j), -\bar{\mu}(P,j) \mid j = 1,\ldots,n\}$. For the case of a girdle distribution, the interesting orientation is not the mean orientation, but the mean axis orthogonal to the samples. This mean axis is not the first (the main) but the third inertia axis. According to different applications, it may happen that the global orientation distribution is a mixture of β distributions with varying parameters. In this case, we rougly estimate the different parameters, and classify the orientations to the distribution having the highest probability for the specific orientation. This classification yields the weighting factors for the different distributions. For every class, we recompute the parameter estimation and adapt the classification respectively. Iteratively, we approach the real distribution when the classification and the parameter estimation stabilize.

Curvature Estimation

To estimate the curvature parameters κ_1 and κ_2 appearing in the multivariate von Mises Fisher distribution, we first study the classical von Mises-Fisher distribution. From basic statistics we can derive the following relations ($\mathbb{E}$ being the mathematical expectation):

$$\begin{aligned}\mathrm{Var}(\mu) = \mathbb{E}\left[\|\mu-\mu_0\|^2\right] &= \frac{2}{\kappa} + 2(1-\frac{e^\kappa+e^{-\kappa}}{e^\kappa-e^{-\kappa}}) && (6.73)\\ \mathbb{E}[\cos\theta] &= -\frac{1}{\kappa} + \frac{e^\kappa+e^{-\kappa}}{e^\kappa-e^{-\kappa}}, && (6.74)\\ \mathbb{E}[\cos^2\theta] &= 1 - \frac{2}{\kappa}\frac{e^\kappa+e^{-\kappa}}{e^\kappa-e^{-\kappa}} + \frac{2}{\kappa^2}. && (6.75)\end{aligned}$$

Note, that the first two statistics are directly related as $\|\mu-\mu_0\|^2 = 2(1-\cos\theta)$ for $\theta = \angle(\mu,\mu_0)$. In the following, we will refer to $\mathrm{Var}(\mu)$ as the spatial variance and to $\mathbb{E}[\cos\theta]$ as the deviation cosine. The term $(e^\kappa+e^{-\kappa})/(e^\kappa-e^{-\kappa})$ also known as hyperbolic cotangent ($\coth\kappa$) converges very fast to 1 for $\kappa\to\infty$. Already for $\kappa > 2$ the difference is negligible. This gives us an estimator for $\kappa > 2$:

$$\tilde{\kappa} \approx \frac{2}{\mathrm{Var}} = \frac{1}{1-C} \tag{6.76}$$

with the empirical statistics for the spatial variance $\mathrm{Var} = \frac{1}{n}\sum_i \|\mu_i - \mu_0\|^2$ and the deviation cosine $C = \frac{1}{n}\sum_i \cos\theta_i$. Including an empirical correction term, we achieve an even better estimator for $\kappa > 1$:

$$\tilde{\kappa}_{\text{MLE-A}} = \frac{2}{\mathrm{Var}} - e^{-1.45/\mathrm{Var}} = \frac{1}{1-C} - e^{-0.725/(1-C)}. \tag{6.77}$$

The numerical estimate $\hat{\kappa}_{\text{MLE-A}}$ from the equations (6.73) or (6.74) coincides with the maximum likelihood estimator:

$$\begin{aligned}\mathrm{MLE}(\kappa) &= \sum_i \ln\left[\frac{\kappa}{(e^{\kappa} - e^{-\kappa})} e^{\kappa\cos\theta_i}\right] &(6.78)\\ &= \sum_i \ln\kappa - \ln(e^{\kappa} - e^{-\kappa}) + \kappa\cos\theta_i &(6.79)\\ &= n\ln\kappa - n\ln(e^{\kappa} - e^{-\kappa}) + \sum_i \kappa\cos\theta_i. &(6.80)\end{aligned}$$

To maximize the maximum likelihood function, we set its derivation to zero:

$$0 \overset{!}{=} n\frac{1}{\kappa} - n\frac{e^{\kappa} + e^{-\kappa}}{e^{\kappa} - e^{-\kappa}} + \sum_i \cos\theta_i \quad \Rightarrow \quad \frac{1}{n}\sum_i \cos\theta_i = -\frac{1}{\kappa} + \frac{e^{\kappa} + e^{-\kappa}}{e^{\kappa} - e^{-\kappa}} \tag{6.81}$$

Furthermore, we can make use of the theoretical value of the squared deviation cosine presented in Equation (6.75) to replace the hyperbolic cotangent in the deviation cosine in Equation (6.74). This simplifies the κ estimator to:

$$\hat{\kappa}_{\text{A}} = \frac{2\mathbb{E}[\cos\theta]}{1 - \mathbb{E}[\cos^2\theta]}. \tag{6.82}$$

Experiments will show that this is the best estimation of the real value for κ. Theoretical properties of this estimate are left to be checked.

In the literature (Fisher *et al.*, 1993) the maximum likelihood estimator is denoted as

$$R/n = -\frac{1}{\kappa} + \frac{e^{\kappa} + e^{-\kappa}}{e^{\kappa} - e^{-\kappa}} \quad \text{with} \quad R = \|\sum_i v_i\| \tag{6.83}$$

and described as biased and unstable. Theoretically, we have $\mathbb{E}[R^2] = \mathbb{E}[\cos^2\theta]$ and therefore the two described methods are nearly identical, but in praxis there are not enough realizations and the value R is biased. R does not only take into account the deviation from the mean direction: $\cos\theta_i$, but also the isotropically distributed variation in the orthogonal plane. This variation has the expectation 0, but in the statistic of realizations the value is too biased and therefore biases also the κ estimate. In my opinion, there is no indication why this variation should appear in the maximum likelihood estimate. The probability density function is only dependent on the deviation to the mean orientation: $\cos\theta$.

Table 6.2 shows a comparison of different κ estimates (presented in this work, in Fisher *et al.* (1993) or in Banerjee *et al.* (2005)). The estimates are evaluated with mean relative error $\frac{|\hat{\kappa}-\kappa|}{\kappa}$ over 100 experiments with each 100 realizations. The parameter κ is varying from 0.1 until 100 with step size 0.1. The estimator $\hat{\kappa}_{\text{A}}$ (6.82), developed in this work, shows the best results.

The problem in estimating the parameters for the multivariate von Mises-Fisher distribution (mvMF) is to fix μ_1, while μ_{i-1} is varying during the process. Thus, for each realization of the von Mises-Fisher distribution parameters have changed. A fixed mvMF distribution can be described as a

Name	Formula	all κ	small κ	large κ
Altendorf	$\hat{\kappa}_{\text{A}} = (2\mathbb{E}[\cos\theta])/(1-\mathbb{E}[\cos^2\theta])$	0.0115583	0.016697	0.0112822
Altendorf MLE	$\hat{\kappa}_{\text{MLE-A}}$ numerically solve (6.81)	0.0124714	0.031205	0.0114646
Altendorf MLE approx	$\tilde{\kappa}_{\text{MLE-A}} = 1/(1-C) - e^{-0.725/(1-C)}$	0.022026	0.219301	0.0114243
Fisher MLE	$\hat{\kappa}_{\text{MLE-F}}$ numerically solve (6.83)	0.0237823	0.0923478	0.0200975
Fisher MLE approx	$\tilde{\kappa}_{\text{MLE-F}} = n/(n-R)$	0.0472494	0.552439	0.0201001
Fisher unbiased	$\tilde{\kappa}_{\text{1-F}} = (1-1/n)\tilde{\kappa}_{\text{MLE-F}}$	0.0383229	0.537169	0.0115145
Fisher robust	$\tilde{\kappa}_{\text{R-F}} = 1/(\sum_{i=1}^{n} c_i X_{(i)})$	0.0510952	0.536255	0.0250223
Banerjee	$\tilde{\kappa}_{\text{B}} = (3R-R^3)/(1-R^2)$	0.037771	0.123189	0.0331806

Table 6.2.: Comparison of κ estimates. Evaluation with mean relative error $\frac{|\hat{\kappa}-\kappa|}{\kappa}$ over 100 experiments and with each 100 realizations. The parameter κ is varying from 0.1 until 100 with step size 0.1 and the classification in small and large κ is separated at $\kappa = 5$. Sources for other estimators: Banerjee *et al.* (2005), Fisher *et al.* (1993).

classical von Mises Fisher distribution with a single reliability parameter $\kappa = |\kappa_1\mu_1 + \kappa_2\mu_2|$. For several realizations of mvMF with fixed $\kappa_1, \mu_1, \kappa_2, \mu_2$ and known μ_1, μ_2 the estimator for κ would be trivial, and κ_1 and κ_2 could be derived from the linear combination $\kappa\mu = \kappa_1\mu_1 + \kappa_2\mu_2$. Instead, the random walk realizes $X_i \sim \text{mvMF}(\kappa_1, \mu_1, \kappa_2, \mu_{i-1})$. Thus, we achieve single realizations for varying distributions. Still, we can define spatial variances to each preferred direction μ_1 and μ_{i-1} as:

$$\text{Var}_1(X) = \frac{1}{n-1}\sum_{i=2}^{n} \|\mu_i - \mu_1\|^2 \quad \text{and} \quad \text{Var}_2(X) = \frac{1}{n-1}\sum_{i=2}^{n} \|\mu_i - \mu_{i-1}\|^2. \tag{6.84}$$

Simulations show that

$$\kappa_1 \approx 1/\text{Var}_1 \quad \text{and} \quad \kappa_2 \approx 2/\text{Var}_2 \quad \text{for} \quad \kappa_2/\kappa_1 > 2. \tag{6.85}$$

We are aware of the limitation of this estimator and that it can just be seen as a first guess of the parameters. Still, it is a measure of the curvature of the fiber. If we achieve similar measure values for the real and the virtual material, we can conclude that the model fitting is successful. Some results for the estimation from the variances can be seen in Figure 6.20.

6.7. Statistics

For the evaluation of the models, we introduce a new method: the orientation covariance, which indicates the correlation of orientations in two image points with respect to their distance. We can interpret the covariance as a measure of local alignment. Moreover, the covariance yields the distance where fiber orientations become independent. Some studies of correlations of orientations between vectors are available in the literature (Jupp & Mardia (1989), Fisher *et al.* (1993), Fisher (1996) and Mardia *et al.* (2000)). They are dedicated to statistics for pairs of unit vectors on a circle for the planar case, or on a sphere for the three dimensional case. No statistics have been proposed for the characterization of a random vector field. So far, this is done in this thesis in quite a different and novel way. The statistical tools available in the literature are based on the standard correlation matrix between coordinates of the random vector.

The orientation covariance is a modification of the classical covariance in image processing (Serra, 1982, p. 532). Instead of evaluating the correlation of the binary image with respect to coordinate distance, we evaluate the correlation of the fiber orientations in foreground pixels (Altendorf & Jeulin, 2011b). This approach can be applied to a binary image of a fiber system with the information of

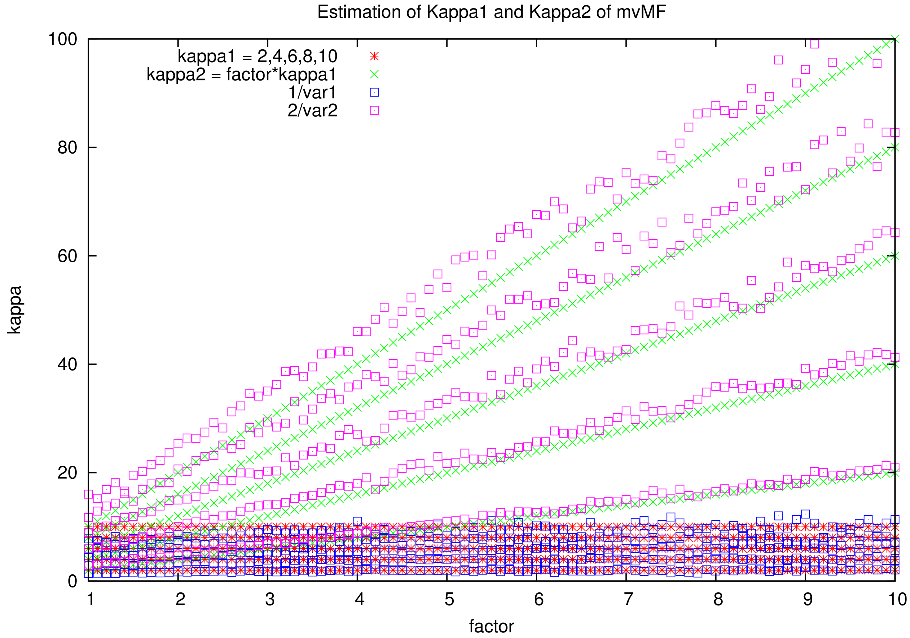

Figure 6.20.: Estimation of κ_1 and κ_2 for multivariate von Mises Fisher distribution.

local orientation, as resulting e.g. from the algorithm introduced in Chapter 3. Furthermore, we are comparing the tortuosity (see Decker *et al.* (1998) and Peyrega *et al.* (2009)) of the fibers, which will be measured on the separated fibers.

6.7.1. Orientation Covariance

The classical covariance ((Stoyan *et al.*, 1987, pp.72), (Serra, 1982, pp. 532) and Matheron (1975)) is defined on a stationary random set $B \subset \mathbb{R}^3$ as the probability that an arbitrary point x and its translation $x + hv$ are part of the set B. We can define the covariance with the following formula:

$$\mathrm{Cov}_B(h, v) = \mathbb{E}[\mathbb{1}_B(\vec{0})\mathbb{1}_B(hv)], \text{ for } v \in S^2 \text{ and } h \in \mathbb{R}. \tag{6.86}$$

For a binary image $b : W \subset \mathbb{R}^3 \to \{0, 1\}$, we define B as the set of foreground points $B = \{x \in W \mid b(x) = 1\}$ and estimate the covariance as average over all image points $x \in W$:

$$\mathrm{Cov}_B(h, v) = \frac{1}{\|W\|} \sum_{x \in W} \mathbb{1}_B(x)\mathbb{1}_B(x + hv). \tag{6.87}$$

The covariance is also known as normalized geometric covariogramm Matheron (1975). It evaluates the similarity of the indicator function on two points depending on their distance h in direction v. The covariance function starts at 1 for $h = 0$ and converges to the squared volume fraction for $h \to \infty$. From the evolution of the covariance function we can interpret the mean width of objects in a given direction and the existence and size of clusters. Comparison of covariance functions for different directions gives indications on the anisotropy of the microstructure.

The covariance can be applied to different characteristics by replacing the indicator function. In particular, the covariance of local fiber orientations can be defined on the scalar product of two orientations as follows:

$$\mathrm{Cov}_o(x, x+hv) = \mathbb{E}[(o(x)o(x+hv))^2 \mid \mathbb{1}_B(x)\mathbb{1}_B(x+hv) = 1], \tag{6.88}$$

where $o : W \to S^2$ is the local orientation map. By equation (6.88), we estimate a scalar, namely the conditional expectation of the square of the scalar product between two vectors located in x and in $x + hv$, knowing that the two points are in the set of interest. For a stationary random field of orientations, the covariance does not depend on the point x and can be written as

$$\mathrm{Cov}_o(h, v) = \mathbb{E}[(o(\vec{0})o(hv))^2 \mid \mathbb{1}_B(\vec{0})\mathbb{1}_B(hv) = 1], . \tag{6.89}$$

In the sequel of this work, we assume stationarity. In that case, the covariance is estimated from the spatial average of the scalar product over the location of x in the image:

$$\mathrm{Cov}_o(h, v) = \frac{1}{\|W^*\|} \sum_{x \in W^*} (o(x)o(x+hv))^2 \quad \text{with} \quad W^* = \{x \in W \mid \mathbb{1}_B(x)\mathbb{1}_B(x+hv) = 1\}. \tag{6.90}$$

It turns out, that this scalar equals the average of $\cos^2 \alpha$, α being the angle between the two vectors $o(x)$ and $o(x + hv)$. The squared cosine is one for equal orientations and drops down to zero for orthogonal orientations. The conditional expectation assures that only foreground points are taken into account. Otherwise, the curve would be a mixture of the classical covariance and the orientation covariance. The orientation covariance starts at 1 for $h = 0$ and converges to 1/3 for $h \to \infty$ in an isotropically distributed fiber system, which is deducted in details in the following.

The orientation covariance converges for $h \to \infty$ to the covariance of two independent random vectors $x, y \in S^2$ distributed with the orientation distribution of the fiber system. In the case of isotropic orientation distribution, the orientation covariance converges to the same value for all $x \in S^2$. Thus, we can assume $x = (0, 0, 1)^T$ without loss of generality. Let θ and ϕ be the angles of the polar coordinates of y. The probability density function for the isotropic distribution is: $f(\theta, \phi) = \frac{1}{4\pi} \sin\theta$. The convergence of the orientation covariance for isotropic orientation distribution can be solved with partial integration as follows:

$$\mathrm{Cov}_o(h, v) \xrightarrow{h \to \infty} \mathbb{E}[(xy)^2] = \mathbb{E}[((0, 0, 1)^T y)^2] = \mathbb{E}[\cos^2\theta] \tag{6.91}$$

$$= \int_0^{2\pi} \int_0^{\pi} \cos^2\theta \frac{1}{4\pi} \sin\theta \,\mathrm{d}\theta \,\mathrm{d}\phi \tag{6.92}$$

$$= \frac{1}{2} \int_0^{\pi} \cos^2\theta \sin\theta \,\mathrm{d}\theta \tag{6.93}$$

$$= \frac{1}{2} \left(\frac{-\cos^3\theta}{3} \right) \Bigg|_0^{\pi} = \frac{1}{3} \tag{6.94}$$

In contrary to the classical statistics on spherical data, the covariance also takes into account the spatial arrangement of the information. It can reveal local alignment and global anisotropy in the orientation distribution. It can be applied directly on data sets with the results from local orientation analysis as well as to realizations from the stochastic modeling. Therefore, it serves as a quality measure of the reconstructed material. Using the square of the scalar product enables a fast estimation by fast Fourier transform of the covariance of orientations for any separation hv. This is an advantage when dealing with images, which was not the scope of earlier statistical studies on populations of vectors.

Figure 6.21 shows an example for the orientation covariance for several orientation models. We observe the theoretical start at 1 for all orientation models and the convergence to one third for the isotropic orientation distribution. The z preferred orientation model yields a slower decrease for the curve in z direction, whereas the decrease of this curve is faster in the case of a girdle distribution. Furthermore, the convergence limit is higher if the orientation distribution is more restricted to one orientation or to the girdle.

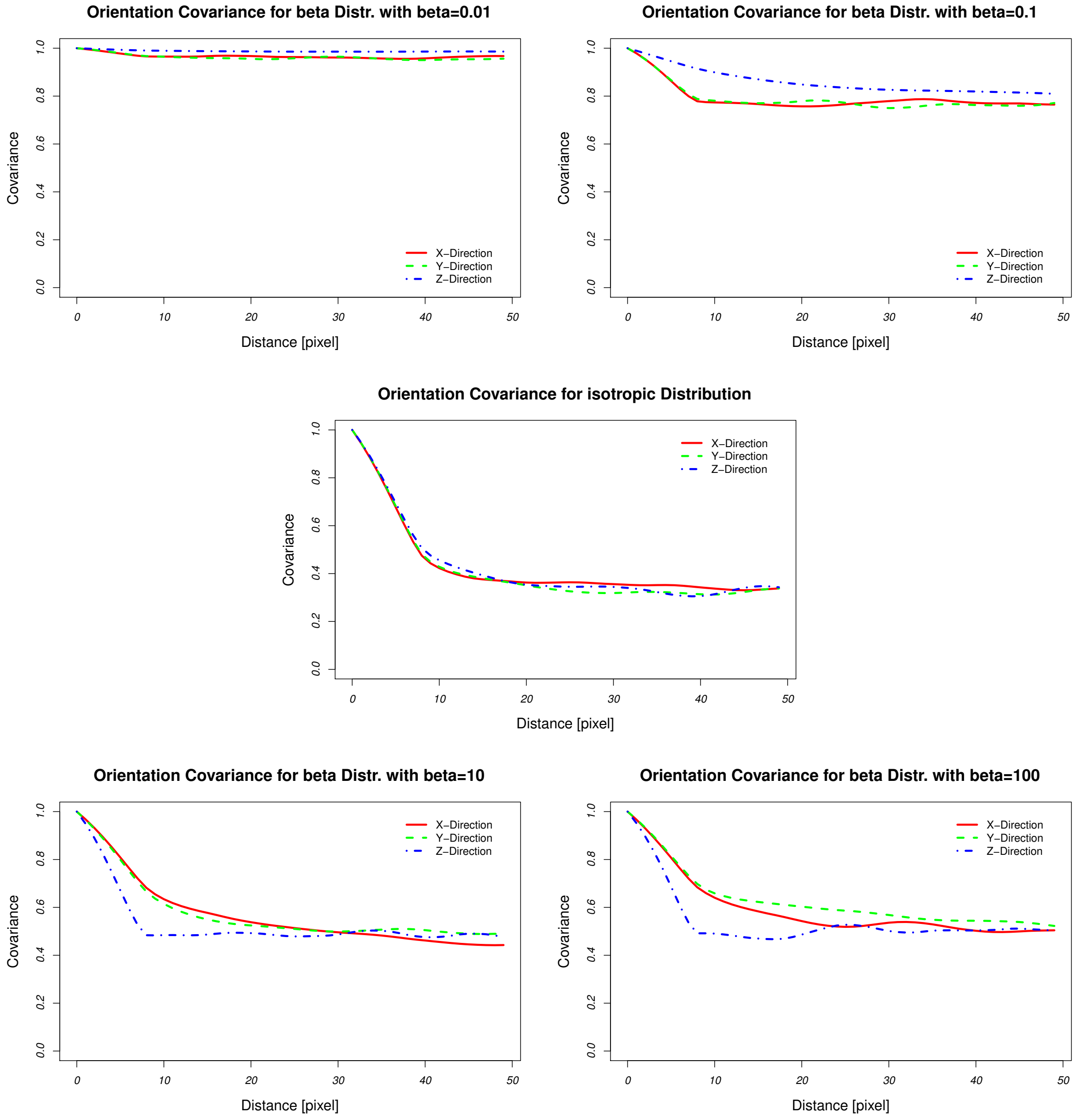

Figure 6.21.: Example for orientation covariance and different orientation models: z preferred orientation distribution (β distribution with $\beta = 0.01$ and $\beta = 0.1$), isotropic orientation distribution, girdle distribution (β distribution with $\beta = 10$ and $\beta = 100$).

Furthermore, the orientation covariance can be generalized for arbitrary directions, which means we are not only evaluating one fixed direction v, but the mean over all directions $v \in S^2$. We call this observation radial orientation covariance and it is defined as

$$\mathrm{Cov}_o(h) = \frac{1}{\|R^*\|} \sum_{(x,y)\in R^*} ((o(x)o(y))^2 \tag{6.95}$$

with $R^* = \{(x,y) \in W \times W \mid (\mathbb{1}_B(x) = 1) \wedge (\mathbb{1}_B(y) = 1) \wedge (d(x,y) \in [h-\epsilon, h+\epsilon])\}$. Figure 6.22 shows an example of the radial orientation covariance for the same realizations as in Figure 6.21.

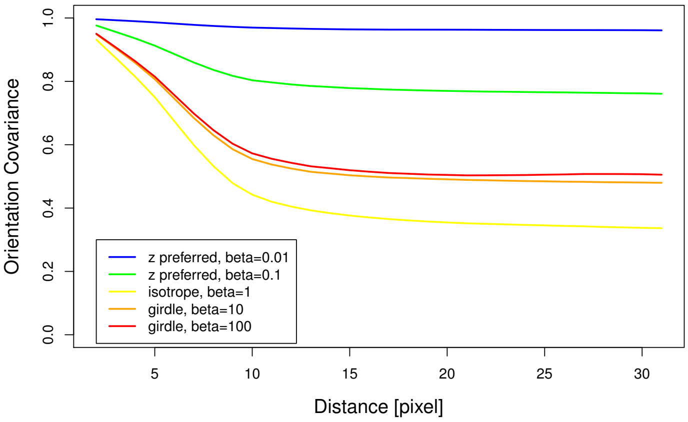

Figure 6.22.: Example for the radial orientation covariance and different orientation models (same as in Figure 6.21).

We show now, that it is possible to estimate the curvature parameters κ_1 and κ_2 directly from the radial orientation covariance. This is a great advantage as the estimation of these parameters are based on the single fiber separation, which is not always possible to perform. The idea is that the radial orientation covariance for h equal to the half fiber radius (which is the distance of balls in the according ball chain) gives us the statistic $\mathbb{E}(\cos^2\theta)$, from which κ_2 could be numerically approximated with the Equation (6.75). And for $h \to \infty$ we can numerically estimate κ_1 from the radial orientation covariance. This study is not yet completely finished, but first experiments show that the parameters could be estimated with the following equations:

$$\hat{\kappa}_1 = \tilde{\kappa}(\mathrm{Cov}_o(10r))/1.1 \tag{6.96}$$
$$\hat{\kappa}_2 = \tilde{\kappa}(\mathrm{Cov}_o(r/2))/7.1 \tag{6.97}$$

with $\tilde{\kappa}(s)$ the numerical approximation of

$$s \overset{!}{=} \mathbb{E}[\cos^2\theta] = 1 - \frac{2}{\kappa}\frac{e^{\kappa}+e^{-\kappa}}{e^{\kappa}-e^{-\kappa}} + \frac{2}{\kappa^2}. \tag{6.98}$$

The results of two first experiments are shown in Figure 6.23. In both versions, we created one fiber for each step with different parameters. Simultaneously, we created the binary image as well as the angle maps and calculated the radial orientation covariance for $h = 2.5$ and $h = 50$ (fiber radius $r = 5$). First experiment: vary κ_1 from 1 to 100, while keeping $\kappa_2 = 100$ fix. Second experiment: keep $\kappa_1 = 10$ fixed and vary κ_2 from 10 to 100. These two experiments are not sufficient to assure the quality of the estimators, but they show a strong correspondence of the radial orientation covariance to the κ estimators.

These results are very promising as the single fiber separation would not longer be necessary for parameter estimation. The only parameter still based on the separated fibers is the fiber length, which cannot be estimated reliably anyway.

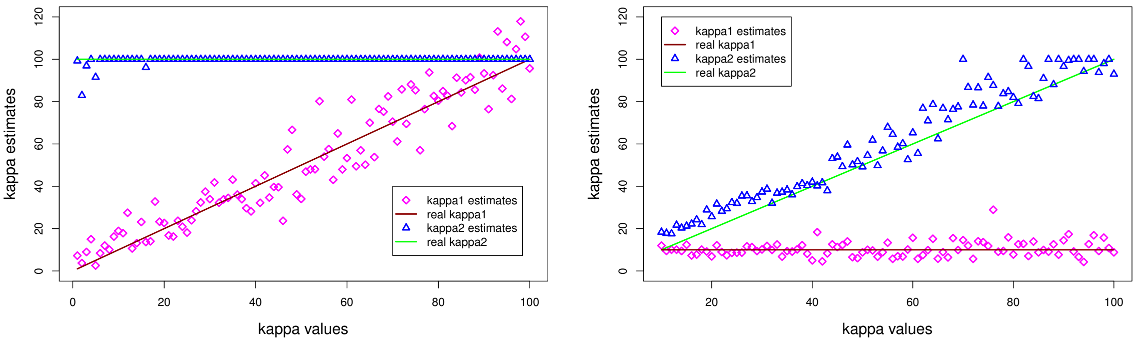

(a) First experiment

(b) Second experiment

Figure 6.23.: Example for the estimation of curvature parameters κ_1 and κ_2 from the radial orientation covariance.

6.7.2. Tortuosity

In order to evaluate the bending of the fibers, we observe an additional characteristic: the tortuosity, which is defined as the ratio between geodesic fiber length and the distance of starting and end point:

$$\hat{T}(P_j) = \frac{\sum_{i=2}^{l_j} |x_{j,i} - x_{j,i-1}|}{|x_{j,1} - x_{j,l_j}|}. \tag{6.99}$$

For totally straight fibers (cylinders) the tortuosity is equal to 1. The higher the bending, the higher the tortuosity.

The theory of this chapter will be applied to a glass-fiber reinforced polymer in a detailed case study in Chapter 8.

7

Chapter 7.

Physical Simulation

The final goal of our studies is to optimize the physical properties of the fiber composites by adapting the microstructure respectively. This process is called virtual material design. The aim is to create virtually new innovative materials with optimal physical properties in order to propose their structure and design before they are practically available. This approach replaces expensive prototypes and mechanical experiments. Therefore, the costs of development can be substantially reduced with the help of numerical simulation.

In this chapter, we recall briefly the theory of physical simulation using the FFT-based method. Two main physical properties of the material and the model realizations are tested: the linear elasticity and thermal conductivity. Applications on a glass fiber reinforced material and on various realizations of stochastic models can be found in the following chapter.

7.1. Linear Elasticity

Elasticity describes the ability of a material to return to its original shape after stress is applied (reversible behavior). The level of deformation in the material is called strain. Linear elasticity is considered, i.e. strain depends linearly on stress (Hooke's law). The classical example for linear elasticity is a spring. The linear elasticity is a simplification of the reality. If the stress passes the elastic limit the material deforms irreversibly, which is called plasticity. Furthermore, viscoelastic behavior is not considered in the simulations.

Linear elasticity is described by the stiffness tensor C_{ijkl}, which is a 4^{th} order tensor. The linear relation between the stress σ_{ij} and strain ε_{kl} tensors is

$$\sigma_{ij} = C_{ijkl} \cdot \varepsilon_{kl} \qquad \text{for } i, j, k, l \in \{1, 2, 3\}. \tag{7.1}$$

Due to tensor symmetries, this relation is classically exposed (in the Voigt notation) as

$$\begin{pmatrix} \sigma_{xx} \\ \sigma_{yy} \\ \sigma_{zz} \\ \sigma_{yz} \\ \sigma_{xz} \\ \sigma_{xy} \end{pmatrix} = \begin{pmatrix} C_{11} & C_{12} & C_{13} & C_{14} & C_{15} & C_{16} \\ C_{12} & C_{22} & C_{23} & C_{24} & C_{25} & C_{26} \\ C_{13} & C_{23} & C_{33} & C_{34} & C_{35} & C_{36} \\ C_{14} & C_{24} & C_{34} & C_{44} & C_{45} & C_{46} \\ C_{15} & C_{25} & C_{35} & C_{45} & C_{55} & C_{56} \\ C_{16} & C_{26} & C_{36} & C_{46} & C_{56} & C_{66} \end{pmatrix} \cdot \begin{pmatrix} \varepsilon_{xx} \\ \varepsilon_{yy} \\ \varepsilon_{zz} \\ \varepsilon_{yz} \\ \varepsilon_{xz} \\ \varepsilon_{xy} \end{pmatrix}, \tag{7.2}$$

with $(C_{rs})_{1 \leq r,s \leq 6}$ is a second-rank symmetrical tensor with 21 components, which is called the stiffness matrix. Symmetrical constraints of the material can reduce the variety of the components, which we will explain in detail in the following subsection. The stiffness matrix is reconstructed by the stress σ necessary to create several deformation, described by the strain tensor ε. We consider the following modes for the strain tensors:

$$\varepsilon^C = \begin{pmatrix} 1 & 0 & 0 \\ & 1 & 0 \\ & & 1 \end{pmatrix}, \qquad \varepsilon^{S1} = \begin{pmatrix} 1 & 0 & 0 \\ & 1 & 0 \\ & & \text{-2} \end{pmatrix}, \qquad \varepsilon^{S1b} = \begin{pmatrix} 1 & 0 & 0 \\ & \text{-2} & 0 \\ & & 1 \end{pmatrix}, \tag{7.3}$$

$$\varepsilon^{S2} = \begin{pmatrix} 0 & 1 & 0 \\ & 0 & 0 \\ & & 0 \end{pmatrix}, \qquad \varepsilon^{S3} = \begin{pmatrix} 0 & 0 & 0 \\ & 0 & 1 \\ & & 0 \end{pmatrix}, \qquad \varepsilon^{S4} = \begin{pmatrix} 0 & 0 & 1 \\ & 0 & 0 \\ & & 0 \end{pmatrix}. \tag{7.4}$$

The simulation responses for the necessary stress tensors $\sigma^C, \sigma^{S1}, \sigma^{S1b}, \sigma^{S2}, \sigma^{S3}, \sigma^{S4}$ serve to reconstruct the stiffness matrix C_{rs}, which is used to extract the Young's moduli E, the Poisson's ratios ν and the shear moduli G for the different symmetry axes.

Furthermore, we calculate the bulk modulus (also known as the modulus of compression), which describes the resistance of a material to uniform compression. In response to the hydrostatic load, the specimen will change its volume. The bulk modulus is defined as the ratio of hydrostatic pressure to the relative volume change (related to the direct strain). For any material and a constant compression σ the bulk modulus is:

$$K = \frac{\sigma}{\Delta V/V} = \frac{\sigma_m}{\varepsilon_{xx} + \varepsilon_{yy} + \varepsilon_{zz}} = \frac{\sigma^C_{xx} + \sigma^C_{yy} + \sigma^C_{zz}}{9}. \tag{7.5}$$

7.1.1. Isotropy

In the case of isotropy, the elasticity tensor is invariant to rotations of the coordinate system, that means the effective properties are independent of the sample adjustment. For fibrous materials this is the case, if the fiber orientations are isotropically distributed. It is the simplest case for physical simulations and the stiffness matrix simplifies to a matrix with two independent values C_{11} and C_{44}. The diagonal values in the first quarter are $C_{11} = \frac{E(1-\nu)}{(1+\nu)(1-2\nu)}$, whereas the non-diagonal values equal $C_{11} - C_{44}$. The lower left and upper right quarters of the matrix vanish, and the lower right quarter has a diagonal form with the three equal entries $C_{44} = \frac{E}{(1+\nu)}$.

It is sufficient to apply two modes of strain: the compression ε^C and a generalized shear strain

$$\varepsilon^S = \begin{pmatrix} 0 & 1 & 1 \\ & 0 & 1 \\ & & 0 \end{pmatrix}. \tag{7.6}$$

The resultant stress tensors σ^C and σ^S are simplified to the values $\bar{\sigma}_d = \frac{\sigma^C_{xx}+\sigma^C_{yy}+\sigma^C_{zz}}{3}$ and $\bar{\sigma}_n = \frac{\sigma^S_{xy}+\sigma^S_{yz}+\sigma^S_{xz}}{3}$, from which the engineering constants can be computed as following:

$$\nu = \frac{\bar{\sigma}_d - \bar{\sigma}_n}{2\bar{\sigma}_d - \bar{\sigma}_n}, \quad E = \bar{\sigma}_n(1+\nu), \quad \text{and} \quad G = \frac{\bar{\sigma}_n}{2}. \tag{7.7}$$

7.1.2. Transverse Isotropy

In the case of transverse isotropy, the stiffness matrix simplifies to 5 independent values. Transverse isotropy means that the material properties do not change if we rotate the material around the z axis, thus the material is symmetric around the z axis. This is always the case for fiber systems with the β distribution as global fiber orientation distribution. Hooke's Law states that the stiffness matrix for transverse isotropic materials is given by

$$C_{rs} = \begin{pmatrix} \frac{1-\nu_{pz}\nu_{zp}}{E_p E_z \Delta} & \frac{\nu_p+\nu_{pz}\nu_{zp}}{E_p E_z \Delta} & \frac{\nu_{zp}+\nu_p\nu_{zp}}{E_p E_z \Delta} & 0 & 0 & 0 \\ \frac{\nu_p+\nu_{pz}\nu_{zp}}{E_p E_z \Delta} & \frac{1-\nu_{pz}\nu_{zp}}{E_p E_z \Delta} & \frac{\nu_{zp}+\nu_p\nu_{zp}}{E_p E_z \Delta} & 0 & 0 & 0 \\ \frac{\nu_{pz}+\nu_p\nu_{pz}}{E_p^2 \Delta} & \frac{\nu_{pz}(1+\nu_p)}{E_p^2 \Delta} & \frac{1-\nu_p^2}{E_p^2 \Delta} & 0 & 0 & 0 \\ 0 & 0 & 0 & 2G_{zp} & 0 & 0 \\ 0 & 0 & 0 & 0 & 2G_{zp} & 0 \\ 0 & 0 & 0 & 0 & 0 & \frac{E_p}{1+\nu_p} \end{pmatrix}, \tag{7.8}$$

with $\Delta = \frac{(1+\nu_p)(1-\nu_p-2\nu_{pz}\nu zp)}{E_p^2 E_z}$. The 5 engineering constants in the stiffness matrix are: the "parallel" and "transverse" Young's modulus E_p and E_z and Poisson's ratios ν_p (along the z axis and in the xy plane) and ν_{pz} as well as the shear modulus G_{zp} in the z direction (Mandel, 1966). With this knowledge, we can simplify the stiffness matrix to

$$C_{rs} = \begin{pmatrix} C_{11} & C_{12} & C_{13} & 0 & 0 & 0 \\ C_{12} & C_{11} & C_{13} & 0 & 0 & 0 \\ C_{13} & C_{13} & C_{33} & 0 & 0 & 0 \\ 0 & 0 & 0 & C_{44} & 0 & 0 \\ 0 & 0 & 0 & 0 & C_{44} & 0 \\ 0 & 0 & 0 & 0 & 0 & C_{11}-C_{12} \end{pmatrix}. \tag{7.9}$$

Note that the formula for the last entry C_{66} often appears with a factor 1/2, which is due to a different definition of the strain tensor.

In general, four modes of strain are sufficient to reconstruct the values of C_{rs} from physical simulations: the compression ε^C and three modes of shear $\varepsilon^{S1}, \varepsilon^{S2}, \varepsilon^{S3}$. The result of the physical simulations are the stress tensors σ^C, σ^{S1}, σ^{S2}, and σ^{S3}. From these results we calculate the characteristics of the stiffness matrix with the following equations:

$$C_{44} = \sigma_{yz}^{S3} \tag{7.10}$$

$$C_{33} = \frac{\sigma_{zz}^C - \sigma_{zz}^{S1}}{3} \tag{7.11}$$

$$C_{13} = \frac{\sigma_{xx}^C - \sigma_{xx}^{S1}}{3} \tag{7.12}$$

$$C_{11} = \frac{1}{3}\sigma_{xx}^C + \frac{1}{6}\sigma_{xx}^{S1} + \frac{1}{2}\sigma_{xy}^{S2} \tag{7.13}$$

$$C_{12} = \frac{1}{3}\sigma_{xx}^C + \frac{1}{6}\sigma_{xx}^{S1} - \frac{1}{2}\sigma_{xy}^{S2}. \tag{7.14}$$

The 5 engineering constants can be calculated as follows:

$$G_{zp} = \frac{1}{2}C_{44} \tag{7.15}$$

$$v_{zp} = \frac{C_{13}}{C_{11}+C_{12}} \tag{7.16}$$

$$E_z = C_{33} - \frac{2C_{13}^2}{C_{11}+C_{12}} \tag{7.17}$$

$$E_p = \frac{(C_{11}-C_{12})(C_{33}(C_{11}+C_{12})-2C_{13}^2)}{C_{11}C_{33}-C_{13}^2} \tag{7.18}$$

$$v_p = \frac{E_p}{C_{11}-C_{12}} - 1. \tag{7.19}$$

7.1.3. Orthotropic Materials

A material is orthotropic if its mechanic and thermal properties are described by three perpendicular axes. The classic example for orthotropy is a partial cutout of wood. The three axes of wood are: the fiber directions, the direction tangential to visual part of the growth rings and the direction normal to the growth rings. This example yields only for a wood panel. A slice of wood with the complete growth rings would be transverse isotropic. Fiber reinforced materials are orthotropic, if the fiber orientation distribution is a mix of β distributions with different axes (out of the x, y or z axes) as preferred direction.

In the case of orthotropic materials, the stiffness matrix is described by 9 values as follows:

$$C_{rs} = \begin{pmatrix} C_{11} & C_{12} & C_{13} & 0 & 0 & 0 \\ C_{12} & C_{22} & C_{23} & 0 & 0 & 0 \\ C_{13} & C_{23} & C_{33} & 0 & 0 & 0 \\ 0 & 0 & 0 & C_{44} & 0 & 0 \\ 0 & 0 & 0 & 0 & C_{55} & 0 \\ 0 & 0 & 0 & 0 & 0 & C_{66} \end{pmatrix}. \tag{7.20}$$

For complete reconstruction of the values of C_{rs}, we need to apply all 6 modes of strain described in Equation 7.4. The values of C_{rs} of the stiffness matrix are computed as follows:

$$C_{44} = \sigma_{yz}^{S3} \qquad C_{13} = \frac{\sigma_{xx}^{C} - \sigma_{xx}^{S1}}{3} \qquad C_{12} = \frac{\sigma_{xx}^{C} - \sigma_{xx}^{S1b}}{3} \tag{7.21}$$

$$C_{55} = \sigma_{xz}^{S4} \qquad C_{23} = \frac{\sigma_{yy}^{C} - \sigma_{yy}^{S1}}{3} \qquad C_{22} = \frac{\sigma_{yy}^{C} - \sigma_{yy}^{S1b}}{3} \tag{7.22}$$

$$C_{66} = \sigma_{xy}^{S2} \qquad C_{33} = \frac{\sigma_{zz}^{C} - \sigma_{zz}^{S1}}{3} \qquad C_{11} = \frac{\sigma_{xx}^{C} + \sigma_{xx}^{S1} + \sigma_{xx}^{S1b}}{3}. \tag{7.23}$$

The inverse of the stiffness matrix, known as the compliance matrix, is described by the essential engineering constants:

$$C_{rs}^{-1} = \begin{pmatrix} \frac{1}{E_x} & -\frac{v_{xy}}{E_x} & -\frac{v_{xz}}{E_x} & 0 & 0 & 0 \\ -\frac{v_{xy}}{E_x} & \frac{1}{E_y} & -\frac{v_{yz}}{E_y} & 0 & 0 & 0 \\ -\frac{v_{xz}}{E_x} & -\frac{v_{yz}}{E_y} & \frac{1}{E_z} & 0 & 0 & 0 \\ 0 & 0 & 0 & \frac{1}{2G_{yz}} & 0 & 0 \\ 0 & 0 & 0 & 0 & \frac{1}{2G_{zx}} & 0 \\ 0 & 0 & 0 & 0 & 0 & \frac{1}{2G_{xy}} \end{pmatrix}. \tag{7.24}$$

The lower right part leads directly to the following relations:

$$G_{yz} = \frac{1}{2}C_{44}, \quad G_{zx} = \frac{1}{2}C_{55}, \quad G_{xy} = \frac{1}{2}C_{66} \tag{7.25}$$

By inverting the upper left part of the stiffness matrix C_{rs}, we achieve the following relations:

$$E_x = \frac{D}{C_{22}C_{33} - C_{23}^2} \qquad v_{xy} = -E_x\frac{C_{13}C_{23} - C_{12}C_{33}}{D} \tag{7.26}$$

$$E_y = \frac{D}{C_{11}C_{33} - C_{13}^2} \qquad v_{xz} = -E_x\frac{C_{12}C_{23} - C_{13}C_{22}}{D} \tag{7.27}$$

$$E_z = \frac{D}{C_{11}C_{22} - C_{12}^2} \qquad v_{yz} = -E_y\frac{C_{13}C_{12} - C_{23}C_{11}}{D} \tag{7.28}$$

with $D = C_{11}C_{22}C_{33} + 2C_{12}C_{13}C_{23} - C_{11}C_{23}^2 - C_{22}C_{13}^2 - C_{33}C_{12}^2$.

The assumption of orthotropic, transverse isotropic, or isotropic material properties can be verified from the disposition of the complete stiffness matrix. This includes simulations for at least 6 load modes, for which the strain tensors are linearly independent. With the 6 resulting stress tensors, all 21 values of C_{rs} of the stiffness matrix can be reconstructed and symmetries can be verified.

7.2. Conductivity

In physics, there are two kind of conductivity: thermal and electrical conductivity. Electrical conductivity is a measure of how strongly a material allows the flow of electric current, whereas thermal conductivity describes how a material allows thermal differences. Fortunately, the computation of both behaviors is identical. It only varies in the input parameters of the two phases and in the interpretation of the results.

The electrical resistivity is $\rho = E/J$, where ρ is the static resistivity (measured in ohm-meters [Ωm]), E is the magnitude of the electric field (measured in volts per meter, [V/m]), and J is the magnitude of the current density (measured in amperes per square meter, [A/m^2]). With respect to the symmetry of the material, there can be three different constants for the three axes: ρ_x, ρ_y and ρ_z.

Thermal conductivity k is the ability of a material to conduct heat. As higher the thermal conductivity as faster the rate of heat transfer across the material. In heat sink applications high thermal conductivity is preferred, whereas for thermal insulation low thermal conductivity is required.

According to the Fourier's law, the relation between an applied temperature gradient and resulting heat transfer is simply linear: $\phi = -k\varrho$, k being a second order tensor and ϱ the temperature gradient. For the different symmetry cases, the conductivities k may equal in specific directions. In the isotropic case, all principal values k_{ii} are equal. In the case of transverse isotropy around the z axis, the conductivity in x or y directions equals to k_p and differs from the one in z direction k_z. In the general case (including orthotropy), all directions needs to be treated separately. The tensors for applied heat differences are just the unit vectors for the threedimensional space:

$$\varrho^{C1} = \begin{pmatrix} 1 \\ 0 \\ 0 \end{pmatrix}, \qquad \varrho^{C2} = \begin{pmatrix} 0 \\ 1 \\ 0 \end{pmatrix}, \quad \text{and} \quad \varrho^{C3} = \begin{pmatrix} 0 \\ 0 \\ 1 \end{pmatrix}. \tag{7.29}$$

In the case of transverse isotropy, the simulation for ϱ^{C1} and ϱ^{C3} is sufficient, and in the case of isotropy, we can reduce the simulation to one case of temperature gradient, we chose ϱ^{C1}.

7.3. Simulation via the FFT-based method

The full-fields computations by means of fast Fourier transforms was realized with the Morph'Hom Software developed by François Willot at the Center of Mathematical Morphology in Fontainebleau. Willot & Jeulin (2009) describe the method as following:

When the "fast Fourier method" was introduced by Moulinec & Suquet (1994), it was considered as a breakthrough in numerical methods for computing the mechanical response of composite materials. It can be applied to many other homogenization problems, as conductivity or permittivity Jeulin

& Moreaud (2008b). The FFT-based method is an iterative fixed-point algorithm derived from the periodic Lippman–Schwinger equation in elasticity (Kroner, 1972). Given an homogeneous elastic reference material with elastic tensor L^0, the strain field ε is the solution of the implicit equation:

$$\varepsilon(x) = \langle\varepsilon\rangle + \int \mathrm{d}^3x' G^0(x-x') : \tau(x'), \quad \tau(x) = \sigma(x) - L^0 : \varepsilon(x), \tag{7.30}$$

where G^0 denotes the Green function, that depends only on the reference tensor L^0. The average of G^0 is set to zero. The polarization stress with respect to the reference L^0 is denoted as τ and $\langle\varepsilon\rangle$ is the prescribed macroscopic strain field. The original scheme of the FFT-based method is a straightforward application of the Lippman-Schwinger equation. Given an image of the strain field with $\varepsilon \equiv 0$, the polarization field τ on the right side equation in (7.30) is computed in the real space, making use of the constitutive law, whereas the convolution on the left side equation is computed in the Fourier space, as a product, yielding a new strain field. The original FFT-based algorithm consists in iterating the two equations, computing forward and backward fast Fourier transforms at each step, on a cubic grid of $\mathcal{L}^3$ voxels. The iterations stop, when the given convergence criterion falls below a fixed limit. It is common to check for stress equilibrium in the Fourier space, i.e.:

$$\frac{\left(\sum_q |q \cdot \hat{\sigma}(q)|^2\right)^{1/2}}{|\hat{\sigma}(0)|} < \eta, \tag{7.31}$$

in our applications, we chose η of order 10^{-2}. The use of an optimal reference elastic tensor L^0 strongly improves convergence, however the number of iterations to achieve convergence is roughly proportional to the contrast between the phases, i.e. this method cannot be applied to infinitely contrasted media.

Subsequently, Eyre & Milton (1999) and Michel *et al.* (2001) have developed refined algorithms which proved more efficient in the case of a high contrast between the phases (see Moulinec & Suquet (2003) for comparisons between the three methods). In this work, we use Michel's "augmented Lagrangian" algorithm, which, among its advantage, is the only one that converges for infinitely contrasted medium. However, no formula for the optimum elastic reference tensor L^0 is known. Worst, numerical computations show that the optimum choice is very sensitive to the contrast, geometry and the required precision, although less to the system size. Consequently, a sub-optimal reference field is numerically estimated at small grid sizes, and applied to larger systems.

The augmented Lagrangian scheme is derived from the minimization of an elastic potential over an auxiliary variable $\mathbf{e}$ with the additional condition that $\mathbf{e} = \varepsilon$ (see Eq. (6) in Moulinec & Suquet (2003)). Contrary to the strain field ε in the original scheme, the compatibility for $\mathbf{e}$ is not enforced at each step. Since the Fourier transform of the stress is not directly available in the augmented Lagrangian algorithm, convergence is checked as a relative difference in the real space between the tensors ε and $\mathbf{e}$, i.e.:

$$\frac{\left(\sum_x \|\varepsilon(x) - \mathbf{e}(x)\|^2\right)^{1/2}}{\|\hat{\sigma}(0)\|} < \eta, \tag{7.32}$$

with $\eta = 10^{-6}$ or $\eta = 10^{-7}$. Attention must be paid to the highest frequencies (e.g. $q = \pm(\mathcal{L}/2+1)$, where $\mathcal{L}$ is the number of voxels along each direction, see Moulinec & Suquet (1998)), at which point the Green function lacks its usual symmetry (i.e. $G*(q) \neq G(-q)$), inducing an edge effect.

7.4. Bounds for Effective Properties

The Hashin-Shtrikman (HS) bounds, used in this work, are theoretical limits for the effective properties of a multiphase material with arbitrary but isotropic microstructure. These bounds are appropriate for the case of fiber systems with isotropic distributed orientations. In the case of transverse isotropy, where fibers are aligned to a preferred direction or oriented in a plane, we consider the 2D bounds for the planar properties (in x or y direction) as the slices orthogonal to the z direction show an isotropic distribution of the objects. In the z direction the properties may exceed the bounds. Still, it serves to check how much the anisotropy of the material influence the physical behavior. In (Bornert *et al.*, 2001, p. 176f.) the following equations are shown to compute the HS bounds in 3D for the bulk modulus K and the shear modulus G for the two phases of the material:

$$p^{HS} = p_1 + c_2 \frac{p_2 - p_1}{1 + c_1 \frac{p_2 - p_1}{p^* + p_1}}, \tag{7.33}$$

where p stands for the shear modulus G or bulk modulus K. The values of p^* are either $K^* = \frac{4}{3} G_0$ or $G^* = \frac{G_0(9K_0 + 8G_0)}{6(K_0 + 2G_0)}$ with K_0 and G_0 equal to one of the two phase constants, one for the lower bound, the other for the upper bound. The constants c_1 and c_2 represent the volume fraction of the two phases, thus it yields $c_1 + c_2 = 1$.

In Peter Wall (1997), a general expression for bounds of shear or bulk modulus is given as:

$$\bar{p}(\xi_p) = p_2 \frac{1 + \xi_p \, \eta \, c_1}{1 - \eta \, c_1} \quad \text{with} \quad \eta = \frac{p_1 - p_2}{p_1 + p_2 \xi_p}, \tag{7.34}$$

where ξ_p distinguishes the values for the upper and lower bounds of different definitions, that can be found in the Table 7.1.

Bound Description	Bulk Modulus			Shear Modulus		
Reuss-Voigt	0	$\leq \xi_K \leq$	∞	0	$\leq \xi_G \leq$	∞
Hashin-Shtrikman 2D	$\frac{G_2}{K_2}$	$\leq \xi_K \leq$	$\frac{G_1}{K_2}$	$\frac{K_2}{K_2 + 2G_2}$	$\leq \xi_G \leq$	$\frac{G_1 K_1}{G_2(K_1 + 2G_1)}$
Hashin-Shtrikman 3D	$\frac{4G_2}{3K_2}$	$\leq \xi_K \leq$	$\frac{4G_1}{3K_2}$	$\frac{9K_2 + 8G_2}{6(K_2 + 2G_2)}$	$\leq \xi_G \leq$	$\frac{G_1(9K_2 + 8G_2)}{6G_2(K_2 + 2G_2)}$

Table 7.1.: Values for ξ_p for the bulk and shear modulus and different bound definitions.

The equality of $\bar{p}(\xi_p)$ and p^{HS} for the 3D Hashin-Shtrikman bounds are not included in Peter Wall (1997), therefore we will shortly sketch the equality for $\xi_p = \frac{p^*}{p_2}$ (which leads to the bounds given in Table 7.1):

$$\begin{aligned}
p^{HS} &= p_1 + c_2 \frac{p_2 - p_1}{1 + c_1 \frac{p_2 - p_1}{p^* + p_1}} & &= p_1 + (1 - c_1) \frac{p_2 - p_1}{1 - c_1 \frac{p_1 - p_2}{p^* + p_1}} \\
&= \frac{p_1 (1 - c_1 \frac{p_1 - p_2}{p^* + p_1}) + (1 - c_1)(p_2 - p_1)}{1 - c_1 \frac{p_1 - p_2}{p^* + p_1}} & &= \frac{-p_1 c_1 \frac{p_1 - p_2}{p^* + p_1} + p_2 - c_1 p_2 + c_1 p_1}{1 - \eta c_1} \\
&= \frac{p_2 + c_1 (\frac{-p_1 (p_1 - p_2) + (p_1 - p_2)(p^* + p_1)}{p^* + p_1})}{1 - \eta c_1} & &= \frac{p_2 + c_1 (p^* \frac{p_1 - p_2}{p^* + p_1})}{1 - \eta c_1} \\
&= p_2 \frac{1 + \xi_p \eta c_1}{1 - \eta c_1} & &= \bar{p}(\xi_p)
\end{aligned}$$

In our case, the 3D Hashin-Shtrikman bounds yield for isotropic orientation distribution of the fibers. For the transverse isotropy, the 2D bounds of Hashin-Shtrikman are optimal for the bulk modulus in the sense that there exist geometries which attain the upper or the lower bound. The 2D bounds of Hashin-Shtrikman hold also for the transverse shear modulus G_{xy} in the case of transverse isotropy. For all other cases, the effective properties are bounded by the Reuss-Voigt bounds for the general case of anisotropic materials.

Furthermore, we can extend the bounds to the Young's modulus E and the Poisson's ratio ν (Jeulin, 2008, pp.VI,30-31). The relation $\frac{1}{E} = \frac{1}{9K} + \frac{1}{3G}$ leads us to the bound:

$$E_{lu} = \left(\frac{1}{9K_{lu}} + \frac{1}{3G_{lu}} \right)^{-1}, \tag{7.35}$$

where l and u represents the lower and upper bound. In the same matter, we can describe the bounds for the Poisson's ratio as

$$\nu_{lu} = \frac{1}{2} - \frac{3}{2} \frac{G_{ul}}{3K_{lu} + G_{ul}}. \tag{7.36}$$

Note, that the bounds for the Poisson's ratio are valid only for the isotropic case.

There are equivalent equations (Hashin & Shtrikman, 1962) for the thermal conductivity in a m-phase composite,

$$\bar{k}(\eta) = \frac{\sum_{t=1}^{m} c_t k_t (\eta + k_t)^{-1}}{\sum_{t=1}^{m} c_t (\eta + k_t)^{-1}}, \tag{7.37}$$

where c_t is the volume fraction and k_t the thermal conductivity of the phase t. Note: $\sum_{t=1}^{m} c_t = 1$. The parameter η equals 0 or ∞ for the Wiener bounds, the maximal or minimal k_t for the 2D Hashin-Shtrikman bounds and twice the maximal or minimal k_t for the 3D Hashin-Shtrikman bounds. This generalization can be simplified for a two phase composite as described in Table 7.2, and can also be found in the following references: Torquato (1991), Trias *et al.* (2006), Markov & Zvyatkov (1995) and Carson *et al.* (2005).

Description	Lower Bound	Upper Bound
Wiener	$\frac{1}{\frac{c_1}{k_1} + \frac{c_2}{k_2}}$	$c_1 k_1 + c_2 k_2$
Hashin-Shtrikman 2D	$k_1 + \frac{c_2}{\frac{1}{k_2 - k_1} + \frac{c_1}{2k_1}}$	$k_2 + \frac{c_1}{\frac{1}{k_1 - k_2} + \frac{c_2}{2k_2}}$
Hashin-Shtrikman 3D	$k_1 + \frac{c_2}{\frac{1}{k_2 - k_1} + \frac{c_1}{3k_1}}$	$k_2 + \frac{c_1}{\frac{1}{k_1 - k_2} + \frac{c_2}{3k_2}}$

Table 7.2.: Bounds for the thermal conductivity in a two phase material.

The application of the bounds to the different isotropy cases is equivalent to those of the previously explained effective properties.

7.5. Representative Volume Element

The representative volume element (RVE) describes which volume a sample of a microstructure should have to show representative behavior in physical simulations. The RVE is dependent on the effective property that should be computed and on the relative error accepted for the deviation. It is possible to compute it on one big image or on several n smaller samples and mean over the results (Kanit *et al.*, 2003, 2006, Oumarou *et al.*, 2011).

We explain stepwise how the RVE can be computed from simulation results concerning a certain effective property Z. One simulation should be applied on a relatively large image size V_0 with a field of the local effective property in each point. The mean of the effective property over all image points is $\bar{Z}$. The image is then separated in different non overlapping regions with smaller volumes $V \ll V_0$, and the variance of the mean property in the m small region $\bar{Z}_j$ to the over all mean property $\bar{Z}$ is calculated as $D_Z^2(V) = \frac{1}{m}\sum_{j=1}^{m}(\bar{Z}_j - \bar{Z})^2$. This variance theoretically has the following relation to the volume:

$$D_Z^2(V) = D_Z^2(1)\ A_3^\alpha / V^\alpha. \tag{7.38}$$

Observing the variance curve to the region volume in a logarithmic scale on both axes, it should have a linear progression. Therefore, the variables A_3 and α can be numerically approximated by fitting a straight line to the logarithmic version:

$$\log D_Z^2(V) = \log D_Z^2(1) + \alpha \log A_3 - \alpha \log V. \tag{7.39}$$

The relative error ϵ_{rel} and the absolute error ϵ_{rel} are dependent on the sample volume of n independent samples or realizations by the following equation:

$$\epsilon_{\text{rel}} = \frac{\epsilon_{\text{abs}}}{\bar{Z}} = \frac{2D_Z(V)}{\bar{Z}\sqrt{n}} \quad \Rightarrow \epsilon_{\text{rel}}^2 = \frac{4\ D_Z^2(1)\ A_3^\alpha}{\bar{Z}^2\ n\ V^\alpha}. \tag{7.40}$$

This implies the limit for the volume of the RVE dependent on a fixed relative error (e.g. 1%) as

$$V_{\text{RVE}} = \left(\frac{4\ D_Z^2\ A_3^\alpha}{\epsilon_{\text{rel}}^2\ \bar{Z}^2\ n}\right)^{1/\alpha}. \tag{7.41}$$

For more details on micro mechanics we refer to the literature, e.g. Gross & Seelig (2011), Mura (1987), Nemat-Nasser & Hori (1998), Aboudi (1991), Zohdi & Wriggers (2008), Schmauder & Mishnaevsky (2008), and Barbero (2007).

Part III.

Application

8

Chapter 8.

Application of the Overall Process on a Glass Fiber Reinforced Polymer

In this chapter, we apply the overall process of virtual material design to a sample of a glass fiber reinforced polymer. We start with a presentation of the sample, the CT-image, the binarization, and its surface rendering. The quantification of the local fiber radii and orientations are performed on the binary image. Furthermore, we separate single fibers with the algorithm proposed in Chapter 5. The reconstructed fiber structure yields the possibility to estimate the parameters for the stochastic model. Two kinds of stochastic models are taken into account: the force-biased fiber packing presented in Chapter 6 and the Boolean model of cylinders. We create realizations of these stochastic models with the same parameters as estimated from the real material, as well as realizations with slightly modified parameters. From physical simulation, we observe the effective properties of the virtually created material and we evaluate the various microstructures.

8.1. Presentation of the Sample

Figure 8.1 shows the original gray value image and the binarization of the glass fiber reinforced polymer sample, provided by R. Velthuis from the IVW in Kaiserslautern. The image was recorded by A. Rack and J. Goebbels at the synchrotron BESSY in Berlin with a pixel sampling of 3.5 µm.

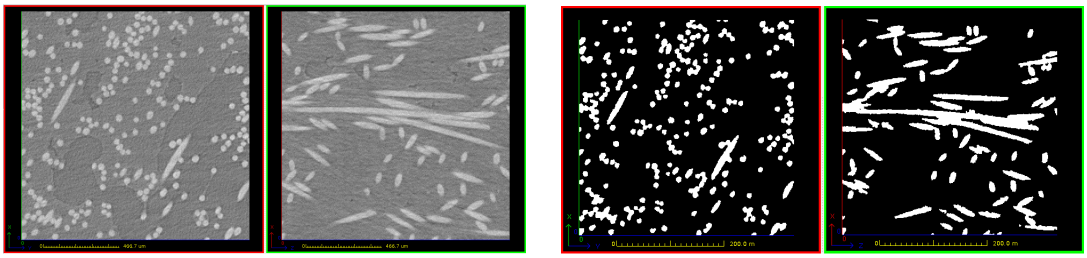

(a) Slice cuts of original gray-value image.

(b) Slice cuts of the binarized image.

Figure 8.1.: GRP sample from R. Velthuis (IVW Kaiserslautern) recorded by A. Rack and J. Goebbels at the BAMline (BESSY II, Berlin, Germany) with a pixel sampling of 3.5 µm.

Furthermore, Figure 8.2 shows surface renderings of the binarized image from all possible angles of the cube. We observe that the first view from the side X gives a wrong impression of straight fibers with only one preferred direction. Taking into account all possible views of the sample, we realize that the structure is actually more complex.

(a) View side X.

(b) View side $-X$.

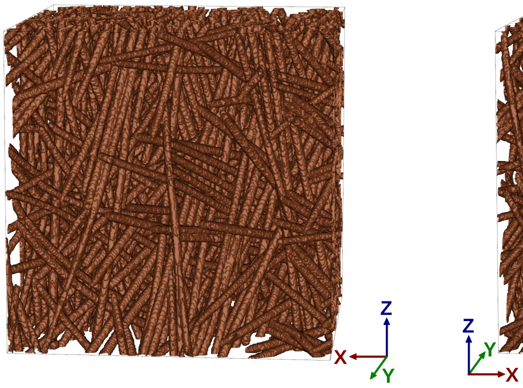

(c) View side Y.

(d) View side $-Y$.

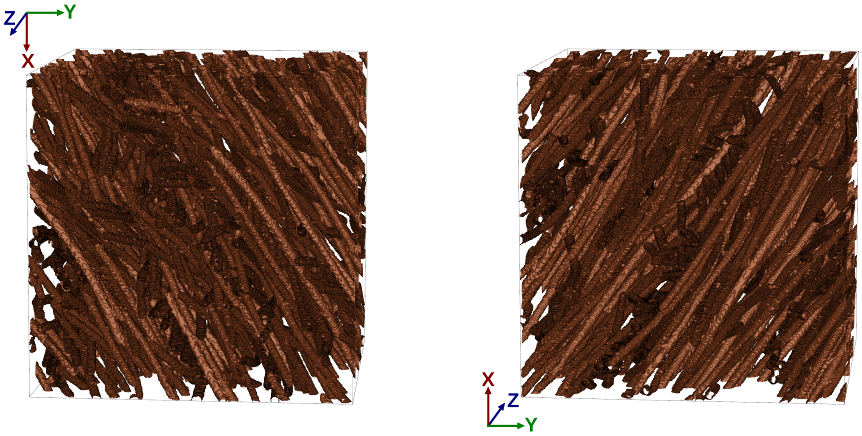

(e) View side Z.

(f) View side $-Z$.

Figure 8.2.: Surface Rendering of binarized imaged of the GRP sample.

8.2. Local Radius and Orientation Analysis

The quantification of the local fiber radius and orientation is based on the binarized image, presented in Figure 8.1(b). The standard approach of orientation correction (Section 3.2.2) is applied as well as a locally adaptive smoothing (Section 3.2.4) with the size of 0.4 times the local radius. From the local maps of radius and orientation, we extract empirical distributions as explained in Sections 4.2.2 and 4.2.3. As already mentioned in Section 4.2.1, the histogram of the radius and orientations can be weighted in different ways. We recall, that in general it is not advisable to observe the volume-weighted histogram of the fiber radius as the volume of a fiber depends on the radius. Figure 8.3 shows the length-weighted empirical distribution function $F(r)$ with a bin width of 0.1 pixel and the empirical derivative $f(r)$ for $h_d = 1$ pixel. Furthermore, we estimate the mean radius and the standard deviation (given in Figure 8.3) to fit the normal distribution to the results.

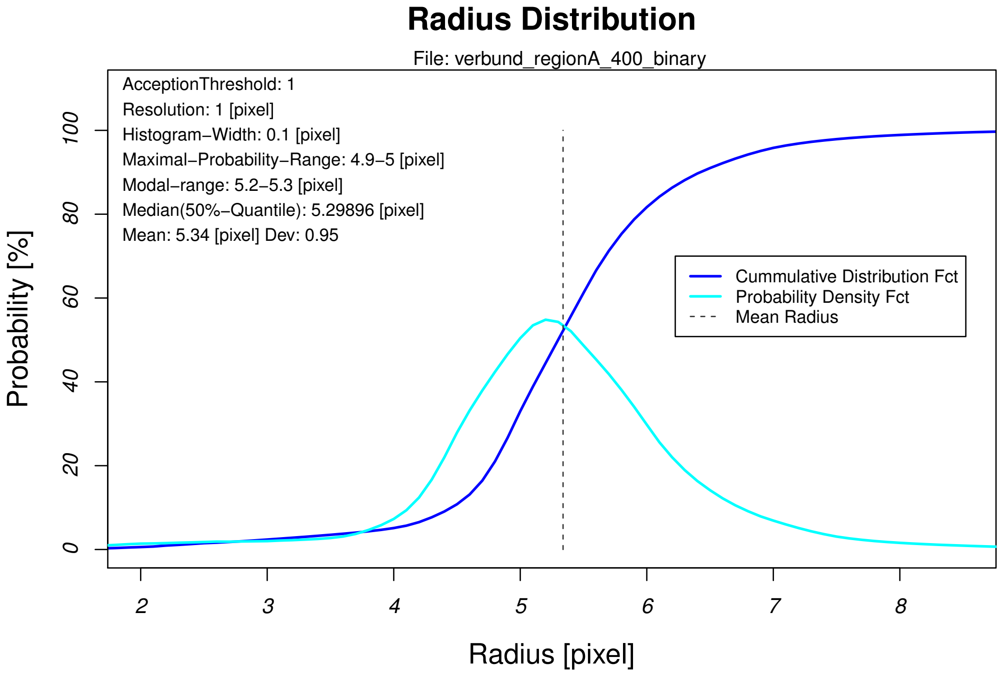

Figure 8.3.: Empirical distribution and density function from local analysis on the binary image of the GRP sample.

In Figure 8.4 we compare different weightings of the radius distribution: the length-weighted version with or without the quality weighting and the volume-weighted version. We observe that the volume-weighted version is distorted to larger radii as expected. The quality weights reduce the participation of pixels in crossing regions, where the radius is overestimated, as well as those of pixels at the boundary between fiber and matrix, where there might be some discretization effect influencing the radius estimation. The dashed light-blue curve shows the radius distribution without the quality measure, which is slightly distorted to larger radii as the overestimation in crossing regions participates with a higher weight. We conclude that the quality- and length-weighted radius distribution is the most reliable.

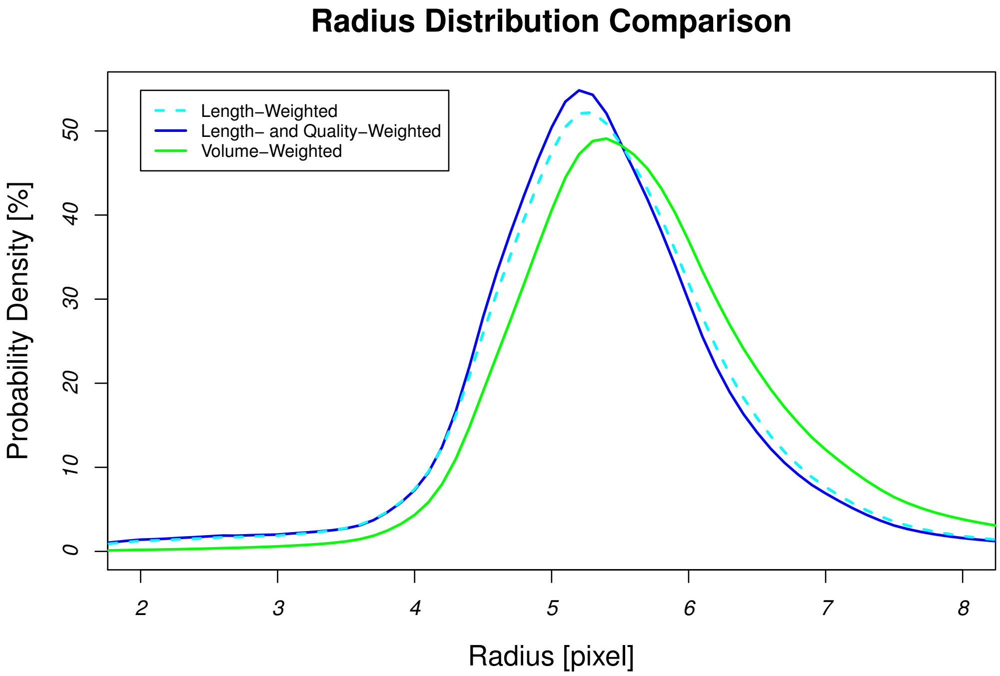

Figure 8.4.: Comparision of the different weightings of the radius distribution. Dashed light-blue: length-weighted, blue: length- and quality-weighted, green: volume-weighted.

Figure 8.5 shows the orientation distribution of the fiber system on the unit sphere from three view angles. Note that the orientation distribution is volume- and quality-weighted and that it is point symmetric in the origin, i.e. if $p(v)$ gives the probability density for the direction $v \in S^2$, it yields $p(v) = p(-v)$. We observe a frequented direction on the z axis and a faint increase on a girdle passing the z axis. From this visualization, we assume a mixture of two β orientation distributions: one with preferred orientation close to the z axis and a girdle distribution. In the following section, we show how to fit this mixture of two β distributions to the empirical orientation distribution.

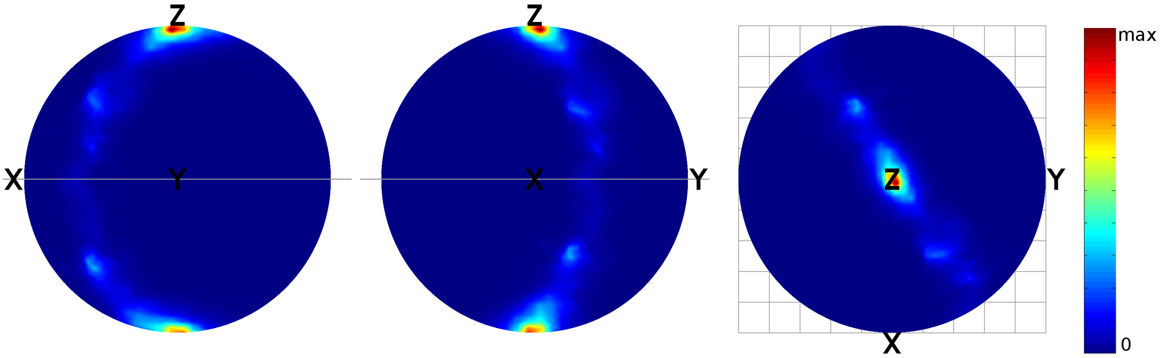

Figure 8.5.: Orientation distribution from local analysis.

8.3. Single Fiber Separation

To separate the single fibers, we have chosen the EDT approach with a fixed radius of approximative 5 pixels. As in this sample fibers have approximately the same width, the probability map from a fixed radius is more stable than the approximation by the radius map. Furthermore, crossing regions can be directly eliminated. However, this restriction is only used to compute the probability map, the local radius of the reconstructed chain of spheres is set to the local radius estimate.

Figure 8.6 shows surface renderings of the reconstructed and labeled fibers versus the surface rendering of the original sample. We observe that most of the fibers could be reconstructed, but it happens that they are split up in two parts. This effect influences mainly the length estimation, which is anyway hardly reliable in a sample where nearly all fibers extend over both boundaries. Also the volume fraction may differ in the reconstructed version, if not all fibers are found or are reconstructed with a slightly various radius. Therefore, the volume fraction should be measured from the original binary image. In the following, we describe a configuration of the fiber system by

$$P = \{p_{1,1}, p_{1,2}, \dots, p_{1,l_1}, p_{2,1}, \dots, p_{n,l_n}\} \tag{8.1}$$

with $p_{j,i} = (x_{j,i}, \mu_{j,i}, r_{j,i}) \in \mathbb{R}^3 \times S^2 \times \mathbb{R}^+$. The fibers are indexed with $j \in \{1, \dots, n\}$ and the spheres in one fiber are ordered by the index $i \in \{1, \dots, l_j\}$.

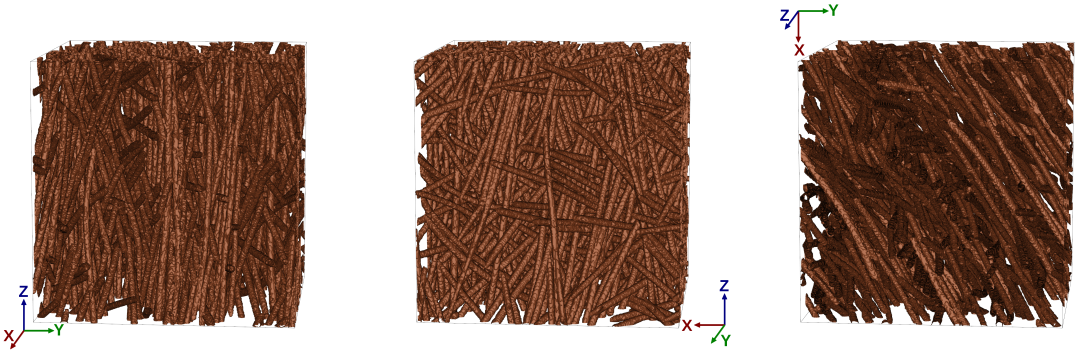

(a) Binary image - view side X. (b) Binary image - view side Y. (c) Binary image - view side Z.

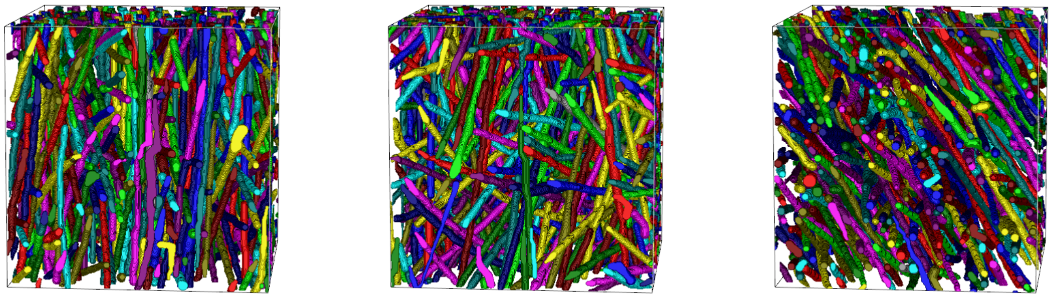

(d) Separated fibers - view side X. (e) Separated fibers - view side Y. (f) Separated fibers - view side Z.

Figure 8.6.: Surface label renderings of the single separated fibers versus surface renderings of the original binary image.

In the following, we will study the radius and orientation distributions of the reconstructed fiber system. Optimally, this will equal the distribution estimated from the original sample. Figure 8.7 shows the length-weighted radius distribution from the separated fibers. We recall that the length-weighted distribution from Figure 8.4 had a mean radius of 5.34 pixels with a deviation of 0.95 pixels. The mean radius from the reconstructed fiber system differs only by 0.1 pixels, which is negligible. The decrease of the deviation to 0.59 is not surprising, as the radius in the separated fibers is only measured at the sphere centers, thus less estimates are taken into account and furthermore, the distorted estimates at the boundaries or the crossing regions do not participate. The normal distribution $\mathcal{N}(5.44, 0.59)$ fits well to the empirical radius distribution as shown in Figure 8.7.

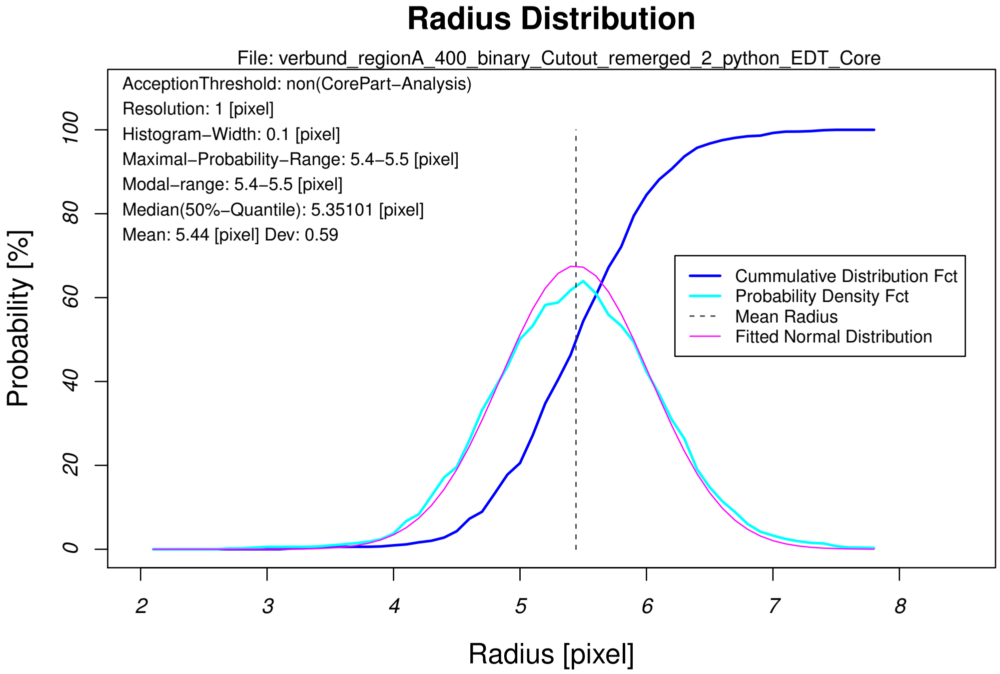

Figure 8.7.: Length-weighted radius distribution of the reconstructed fiber system.

In this case, length-weighted means that all radii assigned to a sphere are taken into account. In the case of number-weighting, every fiber contributes once with its mean radius. In the case of volume-weighting, we discretize the local radius in a radius map from the separated fiber system with the same size as the original image. The distribution is then composed of the estimate from all foreground pixels. Figure 8.8 shows a comparison between the number-, length-, and volume-weighted radius distribution with the fitted normal distribution. We observe again that the volume-weighted distribution is distorted towards larger values, whereas the number-weighted version has a higher deviation. We base our estimation on the length-weighted distribution as it has a higher amount of trials compared to the number-weighted version, and might therefore give a better approximation of the actual radius distribution.

Figure 8.9 shows the length-weighted orientation distribution on the unit sphere. We observe a similar structure as for the analysis of the binary image itself. The difference to Figure 8.5 lies again in the lower deviation of the distributions, thus the preferred orientation has a more concentrated circle

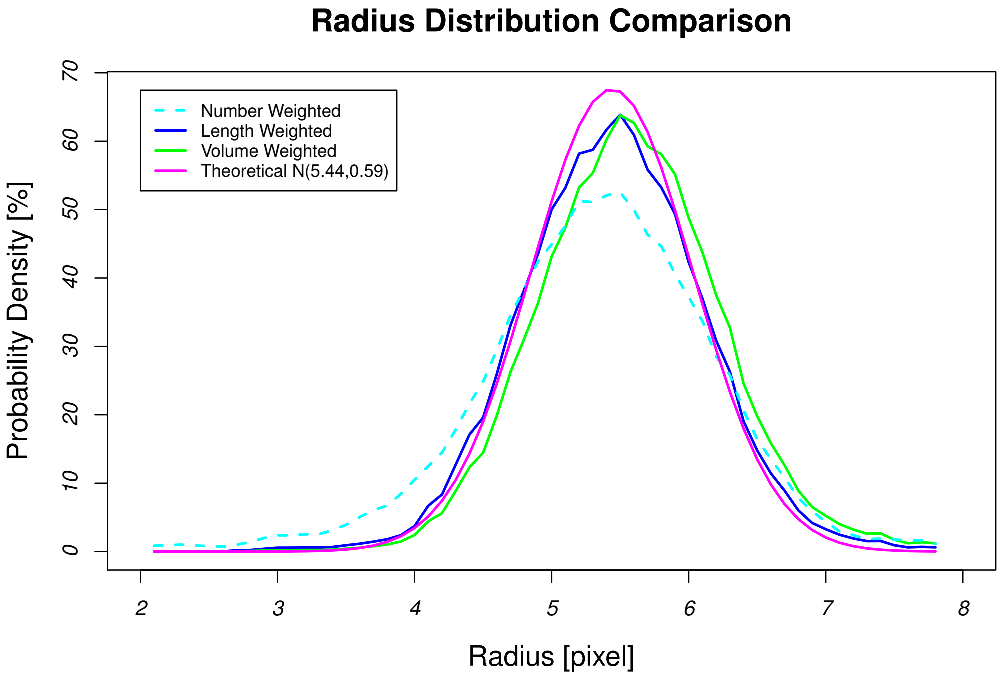

Figure 8.8.: Comparison between the number-, length-, and volume-weighted radius distribution with the fitted normal distribution.

on the z axis and the girdle is more well-defined and thus better visible.

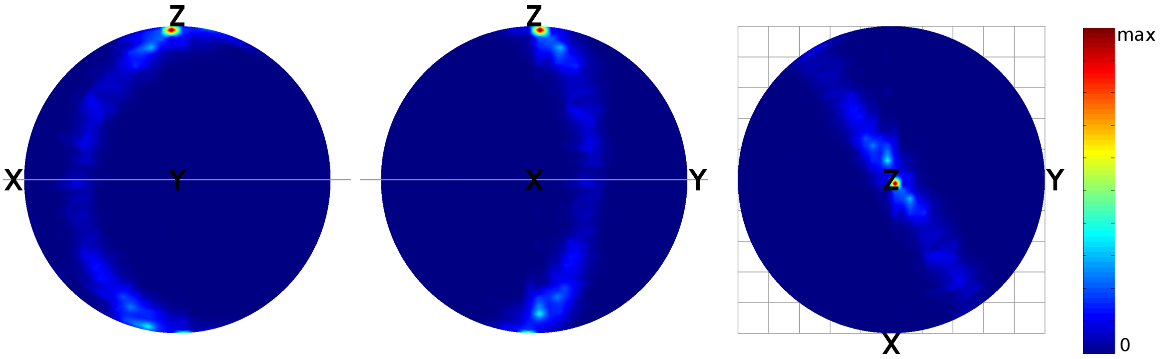

Figure 8.9.: Length weighted orientation distribution of the separated fiber system on the unit sphere.

With the knowledge of the separated fibers, we can now estimate the distribution by classifying the fibers in two sets: the preferred z axis and the girdle distribution. In a first step, we estimate the two parameters β_z, β_g from the complete set of orientations:

$$\Omega = \{\mu_{j,i} \mid 1 \leq j \leq n, 1 \leq i \leq l_j\}. \tag{8.2}$$

Iteratively, we will now classify the orientations in the z preferred and the girdle orientation and estimate the parameters β_z, β_g as well as the preferred orientation μ_z and the girdle normal μ_g, respectively from the separated classes. The orientations are classified according to the higher probability from the β distribution:

$$\Omega_z = \{\mu \in \Omega \mid P_\beta(\mu|\mu_z, \beta_z) > P_\beta(\mu|\mu_g, \beta_g)\} \quad \text{and} \quad \Omega_g = \Omega \setminus \Omega_z. \tag{8.3}$$

After 6 iterations, the classification and parameter estimation has stabilized with the final mixed β distribution:

$$P_{\beta\text{-mixed}}(\mu) = q_z P_\beta(\mu|\mu_z, \beta_z) + q_g P_\beta(\mu|\mu_g, \beta_g) \tag{8.4}$$

$$\text{with} \quad q_z = 0.3933, \quad \mu_z = (0.075406, -0.006289, -0.997133)^T, \quad \beta_z = 0.1141 \tag{8.5}$$

$$\text{and} \quad q_g = 0.6067, \quad \mu_g = (-0.526086, 0.849232, -0.045140)^T, \quad \beta_g = 10.06. \tag{8.6}$$

Figure 8.10 shows the visualization of the mixed β orientation distribution on the unit sphere.

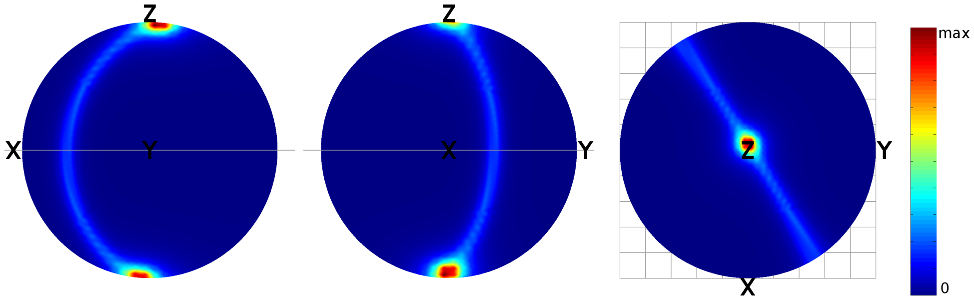

Figure 8.10.: Orientation distribution of the mixed β distribution presented in Equation 8.4.

Furthermore, we estimate the mean fiber length as 340 pixels according to the estimator given in Section 6.6 (page 109). The mean fiber length is surely underestimated as we observed that the fiber tracking was not always successful in reconstructing the fiber with its full length. The curvature parameters were estimated as described in Section 6.6 (page 110) with $\kappa_1 = 30.1612$ and $\kappa_2 = 109.077$.

8.4. Stochastic Modeling

The parameters for the stochastic modeling according to the real microstructure are extracted from the previously described reconstructed fiber system as presented in Table 8.1.

Parameters	Symbol	Value	Description
Volume Fraction	V_V	0.1501	measured from the binarized image
Radius Distribution	P_R	$\mathcal{N}(5.44, 0.59)$	fitted normal distribution
Mean Length	$\hat{L}$	340	from separated fibers (surely underestimated)
Kappa1 Estimate	$\hat{\kappa_1}$	40	adapted to the outcome of the fiber packing
Kappa2 Estimate	$\hat{\kappa_2}$	120	adapted to the outcome of the fiber packing

Table 8.1.: Parameter for the stochastic model estimated from the reconstructed fiber system.

The curvature parameters are slightly higher than the estimated ones, as in general they decrease during the fiber packing process. To avoid other fibers, we allow a certain deviation in the bending of the fibers, which increases the bending and thus decreases the reliability parameters κ_1 and κ_2. The chosen values presented in Table 8.1 are adapted, such that the realization have curvature estimations close to the real microstructure. It keeps in the perspectives to study the change of curvature during the fiber packing process.

Additionally to the force-biased fiber packing (presented in Chapter 6), we will consider a Boolean cylinder model with the same characteristic exempt from the curvature. To study the influence of the microstructure on the physical behavior of the material, we are slightly changing the parameters for the orientation distribution and the bending. For the orientation distribution, we use single and mixed β orientation distributions. The single β orientation distributions varies from z preferred orientations ($\beta = 0.05$) over the isotropic distribution ($\beta = 1$) to a planar or girdle preference ($\beta = 30$). For the mixed β orientation distributions (see Equation 8.4), we vary the parameter q_z ($q_g = 1 - q_z$), which concerns the percentage of influence of the two β distributions. The set of characteristics is shown in Table 8.2. For each configuration, we create 10 realizations in a cubic window of 400 pixels side length and periodic boundary conditions. The changes of the curvature controlling parameters listed in the right hand table are applied to the fiber packing only.

Single β Distributions

Description	β
Z-pref. (β=0.05)	0.05
Z-pref. (β=0.08)	0.08
Z-pref. (β=0.1141)	0.1141
Z-pref. (β=0.15)	0.15
Z-pref. (β=0.30)	0.3
Isotropic (β=1)	1
Planar (β=5)	5
Planar (β=7.5)	7.5
Planar (β=10.06)	10.06
Planar (β=15)	15
Planar (β=30)	30

Mixed Distributions

Description	q_z
Mixed (q=0.2)	0.2
Mixed	0.3933
Mixed (q=0.5)	0.5
Mixed (q=0.8)	0.8

Changes in Curvature

Description	κ_1	κ_2
Mixed (k1=10)	10	120
Mixed (k1=10, k2=80)	10	80
Mixed (k1=10, k2=300)	10	300
Mixed (k1=1)	1	120
Mixed (k1=1, k2=80)	1	80
Mixed (k1=1, k2=300)	1	300
Mixed (k1=40, k2=300)	40	300
Mixed (k1=40, k2=80)	40	80
Mixed (k1=80, k2=80)	80	80
Mixed (k1=80, k2=130)	80	130
Mixed (k1=80, k2=300)	80	300

Table 8.2.: Set of changed characteristics for the stochastic models.

The variety of orientation distributions is shown in Figure 8.11 and Figure 8.12 shows realizations of the according distributions.

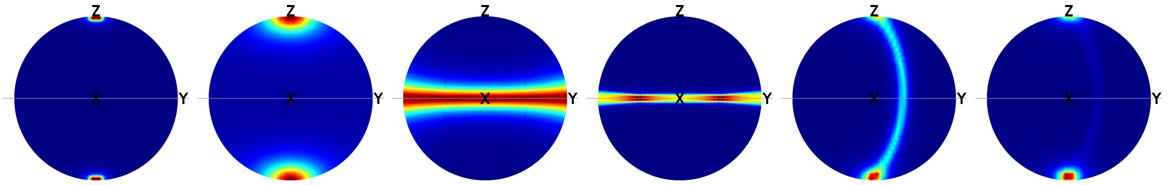

Figure 8.11.: Variety of orientation distributions. From left: Z-pref. ($\beta = 0.05$), Z-pref. ($\beta = 0.3$), Planar ($\beta = 5$), Planar ($\beta = 30$), Mixed ($q = 0.2$), Mixed ($q = 0.8$).

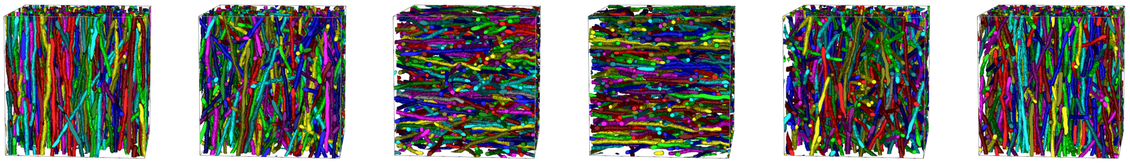

Figure 8.12.: Realizations with varying orientation distributions. From left: Z-pref. ($\beta = 0.05$), Z-pref. ($\beta = 0.3$), Planar ($\beta = 5$), Planar ($\beta = 30$), Mixed ($q = 0.2$), Mixed ($q = 0.8$).

Figure 8.13 shows a comparison of the real material to realizations of the two stochastic models. We observe that the orientation distribution seems to be realistic, whereas the bending in the realizations seems to be too high, as a result of an overestimation on the reconstructed single fibers.

8.5. Physical Simulations

In this section, preliminary results for the quasi static (mechanical and thermal) responses of the various realizations and the original microstructure are shown. The computation is based on a binary discretization of the structure and the initial physical properties for the separated components, as shown in Table 8.3. The effective properties of the different microstructures is determined by a homogenization approach using the FFT method (see Chapter 7). Furthermore, we compare the results to the theoretical bounds of Hashin-Shtrikman, Reuss-Voigt, and Wiener and we compute the size of the representative volume element (RVE) for a cubic, elongated or flat window.

	Young's Modulus	Poisson's Ratio	Bulk Modulus	Shear Modulus	Thermal Conductivity
	E [MPa]	ν	K [MPa]	G [MPa]	k [W/mK]
PA6 Glass Fibers	72000	0.22	42857	29508	1
Polymer Matrix	2002	0.39	3033	720	0.2

Table 8.3.: Characteristics of P6 glass fibers and polymer matrix (see Oumarou *et al.* (2011)).

8.5.1. Verification of the Symmetry Cases

In this section, we compute the fully reconstructed stiffness matrix for the different cases of symmetry. Optimally the matrices fulfill the symmetries described in Section 7.1. In the most restrictive case of isotropy, we expect a matrix with two independent values C_{11} and C_{44} on the first and second halves of the diagonal as explained in Section 7.1.1. The non-diagonal entries of the first quarter equal $C_{11} - C_{44}$, whereas the remaining non-diagonal entries vanish. For an arbitrary realization of the isotropic orientation distribution, we achieve the following stiffness matrix:

$$C_{\text{isotropic}} = \begin{pmatrix} 6391.44 & 3394.00 & 3365.64 & -28.85 & 46.35 & -26.38 \\ 3399.60 & 6502.43 & 3436.42 & -105.23 & -3.08 & -55.95 \\ 3378.52 & 3445.55 & 6394.85 & -121.69 & 28.27 & -12.45 \\ -60.56 & -216.24 & -243.37 & 3118.67 & -26.98 & -14.06 \\ 95.22 & -9.02 & 57.00 & -27.72 & 3053.90 & -79.30 \\ -56.45 & -114.16 & -24.90 & -14.06 & -76.42 & 3072.67 \end{pmatrix}. \tag{8.7}$$

Non-diagonal values do not overrun 250, which is negligible compared to the high values on the diagonal. The diagonal values match the equality conditions of two values and the mean of non-diagonal values in the first quarter is 3403.29, which is close to the difference of the means for C_{11} and C_{44}: 3347.83. Thus, we confirm the symmetry case for the simulated isotropic material.

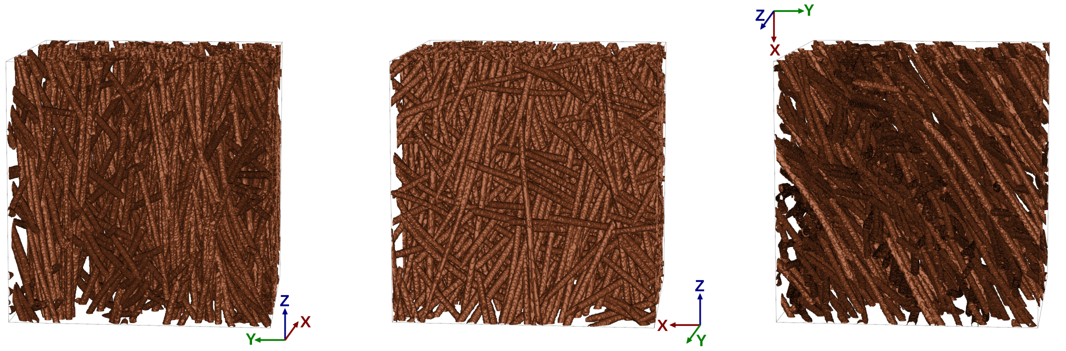

(a) Binary image - view side -X. (b) Binary image - view side Y. (c) Binary image - view side Z.

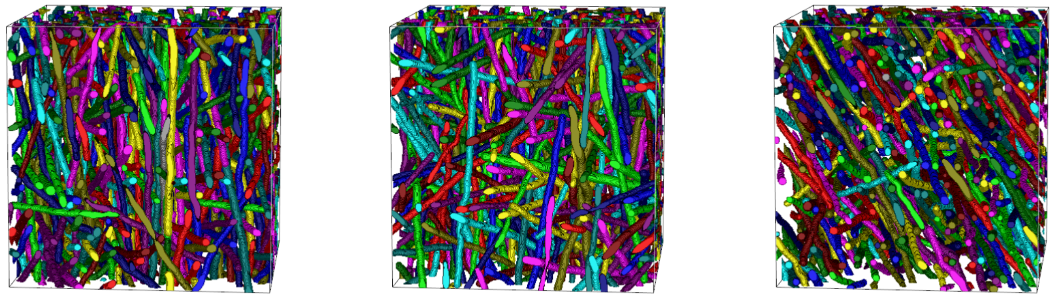

(d) Fiber packing - view side -X. (e) Fiber packing - view side Y. (f) Fiber packing - view side Z.

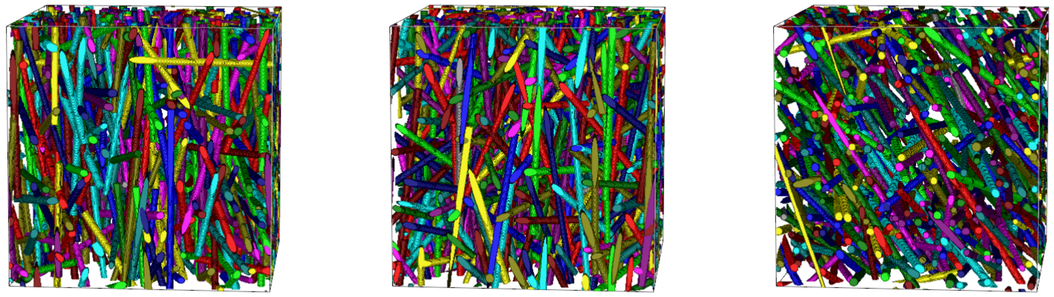

(g) Boolean cylinders - view side -X. (h) Boolean cylinders - view side Y. (i) Boolean cylinders - view side Z.

Figure 8.13.: Surface rendering of the binary image of the real material versus the labeled separated fibers in the realizations of the bent fiber packing and the Boolean cylinders.

The second case of transverse isotropy is slightly more complex as shown in Equation 7.9, which we recall here:

$$C_{rs} = \begin{pmatrix} C_{11} & C_{12} & C_{13} & 0 & 0 & 0 \\ C_{12} & C_{11} & C_{13} & 0 & 0 & 0 \\ C_{13} & C_{13} & C_{33} & 0 & 0 & 0 \\ 0 & 0 & 0 & C_{44} & 0 & 0 \\ 0 & 0 & 0 & 0 & C_{44} & 0 \\ 0 & 0 & 0 & 0 & 0 & C_{11}-C_{12} \end{pmatrix}.$$

This structure is supposed for the case of z preferred or girdle orientation distribution. The corresponding stiffness matrices for arbitrary realizations are

$$C_{z\text{-preferred}} = \begin{pmatrix} 5179.43 & 2982.40 & 3141.73 & 1.74 & -1.74 & -1.91 \\ 3016.38 & 5031.73 & 3051.98 & -1.56 & -15.69 & -3.59 \\ 3090.30 & 3047.32 & 11227.94 & 0.84 & 31.92 & 2.49 \\ 3.77 & -3.22 & 0.46 & 2344.22 & 1.90 & -30.44 \\ -5.24 & -31.39 & 69.54 & 1.58 & 2466.12 & 3.94 \\ -0.91 & -7.18 & 4.13 & -31.88 & 3.94 & 2061.38 \end{pmatrix} \tag{8.8}$$

and

$$C_{\text{girdle}} = \begin{pmatrix} 7799.50 & 3780.97 & 2972.98 & -0.92 & 6.37 & 12.02 \\ 3780.97 & 7554.32 & 2975.42 & -13.65 & 2.03 & 37.79 \\ 2972.63 & 2974.84 & 5078.91 & -7.09 & -3.53 & 1.22 \\ -1.44 & -28.11 & -14.18 & 2169.46 & 5.12 & -1.06 \\ 13.37 & 3.39 & -7.06 & 5.12 & 2181.00 & 5.45 \\ 23.42 & 75.01 & 1.81 & -0.62 & 5.40 & 3820.53 \end{pmatrix}. \tag{8.9}$$

The highest value, that is supposed to vanish, is 75 which is comparatively small. The symmetry in x and y directions is given. It remains to verify the equality of the lower right value to $C_{11} - C_{12}$. The stiffness matrix for the z preferred orientations yields $C_{11} - C_{12} = 2197.03$ versus 2061.38 and for the girdle orientation, it yields $C_{11} - C_{12} = 4018.53$ versus 3820.53. Both constraints are acceptable. Thus, we confirm the transverse isotropy for the simulated material with single β distributions.

In the case of orthotropic microstructure, it suffices to verify the vanishing values in the upper right and lower left quarter of the matrix as well as the diagonal form of the lower right quarter. We verify the stiffness matrix of an arbitrary realization of the type “Mixed“

$$C_{\text{mixed}} = \begin{pmatrix} 6066.10 & 3348.66 & 3404.30 & 1.66 & -25.59 & 524.42 \\ 3360.65 & 5405.84 & 3210.74 & 35.35 & 8.05 & 228.07 \\ 3404.30 & 3202.34 & 8538.99 & 139.00 & -128.68 & 191.09 \\ 3.33 & 66.74 & 277.99 & 2652.07 & 403.67 & 6.86 \\ -51.19 & 15.67 & -257.37 & 403.67 & 3081.05 & 13.26 \\ 1026.54 & 430.45 & 373.77 & 6.29 & 12.84 & 2823.16 \end{pmatrix} \tag{8.10}$$

and the stiffness matrix of the original microstructure

$$C_{\text{orig}} = \begin{pmatrix} 5933.17 & 3283.14 & 3541.18 & 4.87 & -55.50 & 445.01 \\ 3283.14 & 5326.58 & 3210.82 & 28.35 & 26.48 & 190.44 \\ 3509.92 & 3197.54 & 8994.90 & 59.21 & -186.21 & 320.97 \\ 7.66 & 53.62 & 121.16 & 2733.97 & 697.23 & 35.24 \\ -107.38 & 48.60 & -372.41 & 683.03 & 3376.96 & 5.86 \\ 859.89 & 366.84 & 655.95 & 35.24 & 6.89 & 2709.74 \end{pmatrix}. \tag{8.11}$$

The highest value, supposed to vanish, is 1026.54. In this case, we cannot argue any more that the value is comparatively small. However, as there are only few outliers in the part supposed to vanish, we still assume an orthotropic material. The physical responses will be treated as approximations of the accurate effective properties.

8.5.2. Results for the Mechanical and Thermal Responses

Figures 8.14 - 8.18 show the mechanical and thermal responses for all types of realizations, for the original and reconstructed microstructure as well as the bounds adapted to the different cases of symmetry. Table 8.4 presents the bounds for the mechanical and thermal properties. Note that the bounds for the transverse isotropy only yields for properties in directions orthogonal to the fiber arrangement, which are in the case of z preferred directions: $E_x, E_y, G_{xy}, k_x, k_y$ and for the girdle distribution: E_z, k_z. All other properties are bounded by the general Reuss-Voigt or Wiener bounds. Furthermore, the bounds for the Poisson's ratio yield only for the isotropic case.

Description & Symmetry Case	Bulk Modulus	Shear Modulus	Young's Modulus	Poisson's Ratio	Thermal Conductivity
	K [MPa]	G [MPa]	E [MPa]	ν	k [W/mK]
Hashin-Shtrikman 3D	3663.70	986.28	2715.19	0.1680	0.2563
Isotropic Case	6354.24	3124.36	8053.16	0.4262	0.2917
Hashin-Shtrikman 2D	3629.60	923.36	2553.55		0.2444
Transverse Isotropy	5961.24	2228.37	5944.42		0.2766
Reuss-Voigt / Wiener	3524.60	843.59	2343.79		0.2273
Orthotropic Case	9006.90	5038.35	12739.60		0.3200

Table 8.4.: Bounds for mechanical and thermal properties for a glass-polymer ratio of 15%.

The results of the Young's modulus shown in Figure 8.14 are quite intuitive. The material is reinforced in the direction of the fibers, as the fibers are highly stiff, the stiffness of the composite is high in the preferred direction of the fibers. For a planar orientation distribution the Young's modulus is also higher in the planar directions, but not as much as in the case of one preferred direction. This effect is due to the lower amount of fibers reinforcing a certain direction. If stiffness of the material is required in a certain arrangement, the material needs to be oriented correctly.

The boolean model of cylinders has on average a slightly higher stiffness than the corresponding model with bending fibers. This is expected, as both characteristics (straight fibers and connected fiber system) can charge more energy. Still, it is not a realistic model as in practice glass fibers can not penetrate each other. For the bent fiber packing, on the other hand, we observe that the properties of the real microstructure and the corresponding model ("Mixed") are nearly equal, which confirms that we successfully rebuilt the structure of the real material with our stochastic model.

The results of the Poisson's ratio (Figure 8.15) are known to be between 0.05 and 0.5 for composite materials, highly dependent on the directions. We can confirm this observation by responses reaching from 0.12 to 0.51 for the same sample, but different sample rotations. The values for different rotations vary extremely for a parallel fiber system. The values differ less for a planar orientation distribution and also the higher fiber curvature decreases the difference.

The shear modulus (Figure 8.16) is especially high in the planar directions of a girdle orientation. This effect is comprehensible as the stiff fibers in the planar direction directly oppose to the applied strain. The mixed distributions have a nearly equilibrated intermediate behavior. The values for G_{zx} are slightly higher, because the zx plane is closest to the plane in which the girdle orientation distribution is concentrated. As also experienced in Oumarou *et al.* (2011), the shear modulus is close to the lower Hashin-Shtrikman bound for z preferred materials.

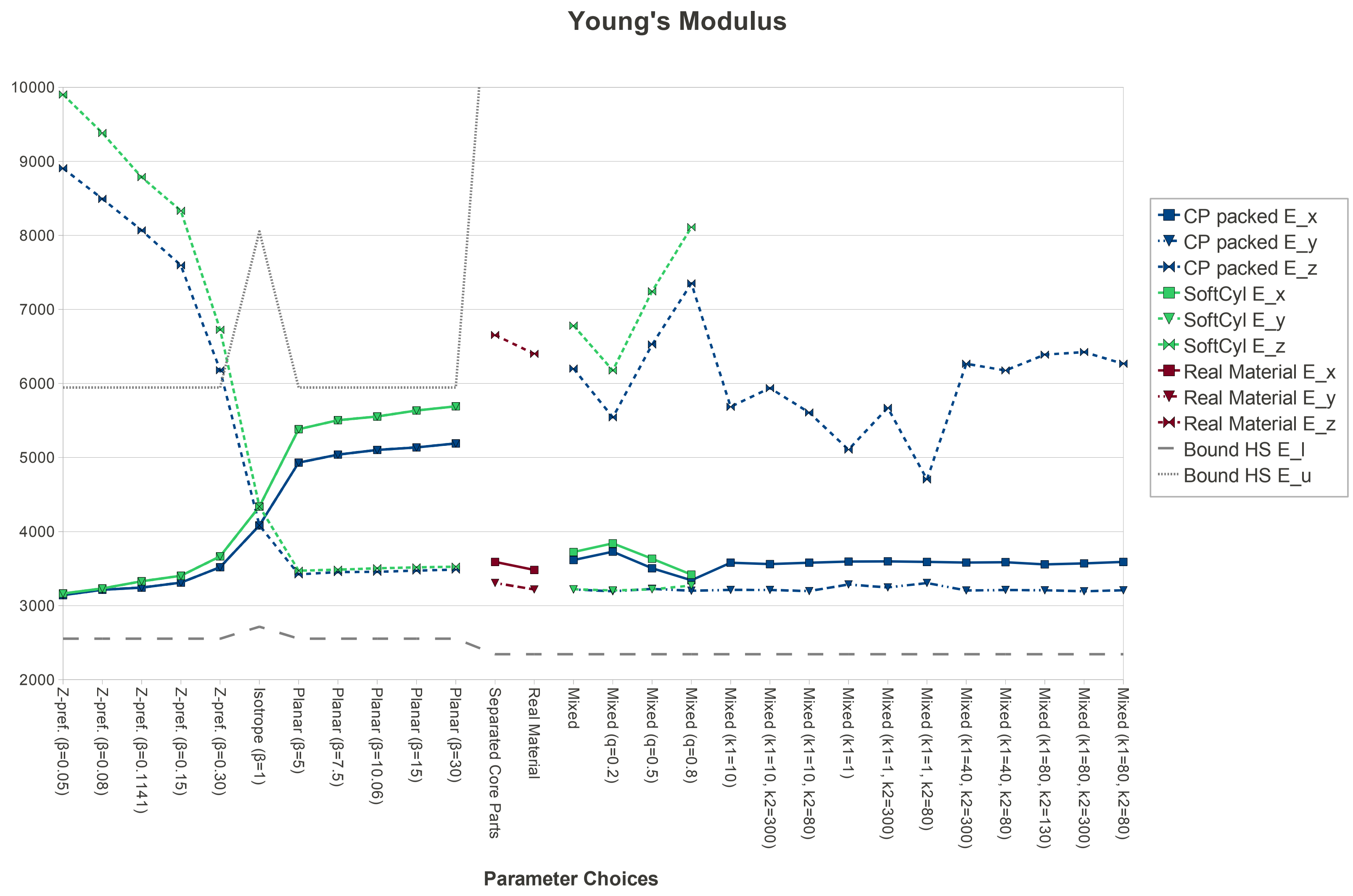

Figure 8.14.: Response of physical simulations for the Young's modulus (given in MPa).

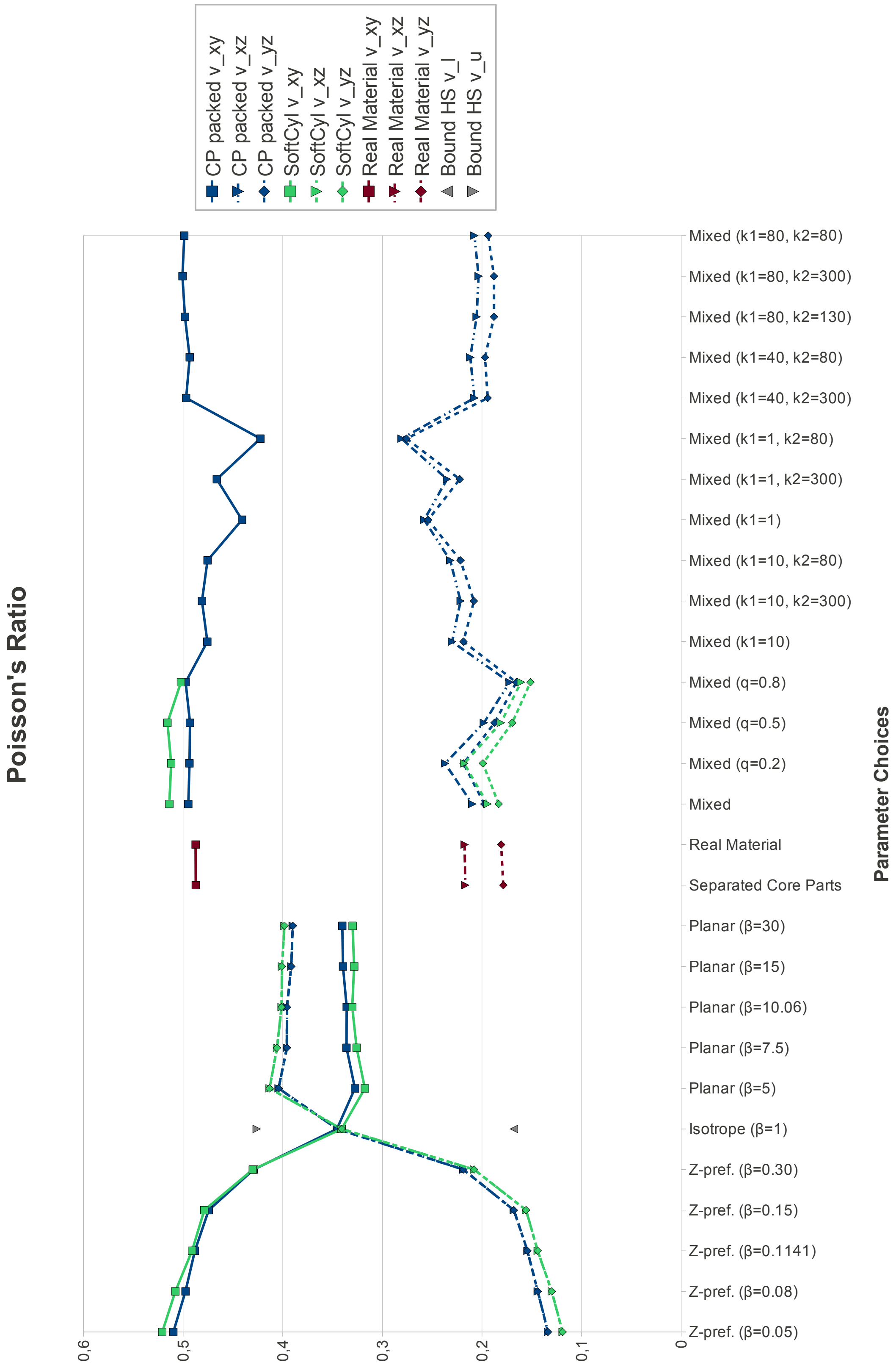

Figure 8.15.: Response of physical simulations for the Poisson's ratio.

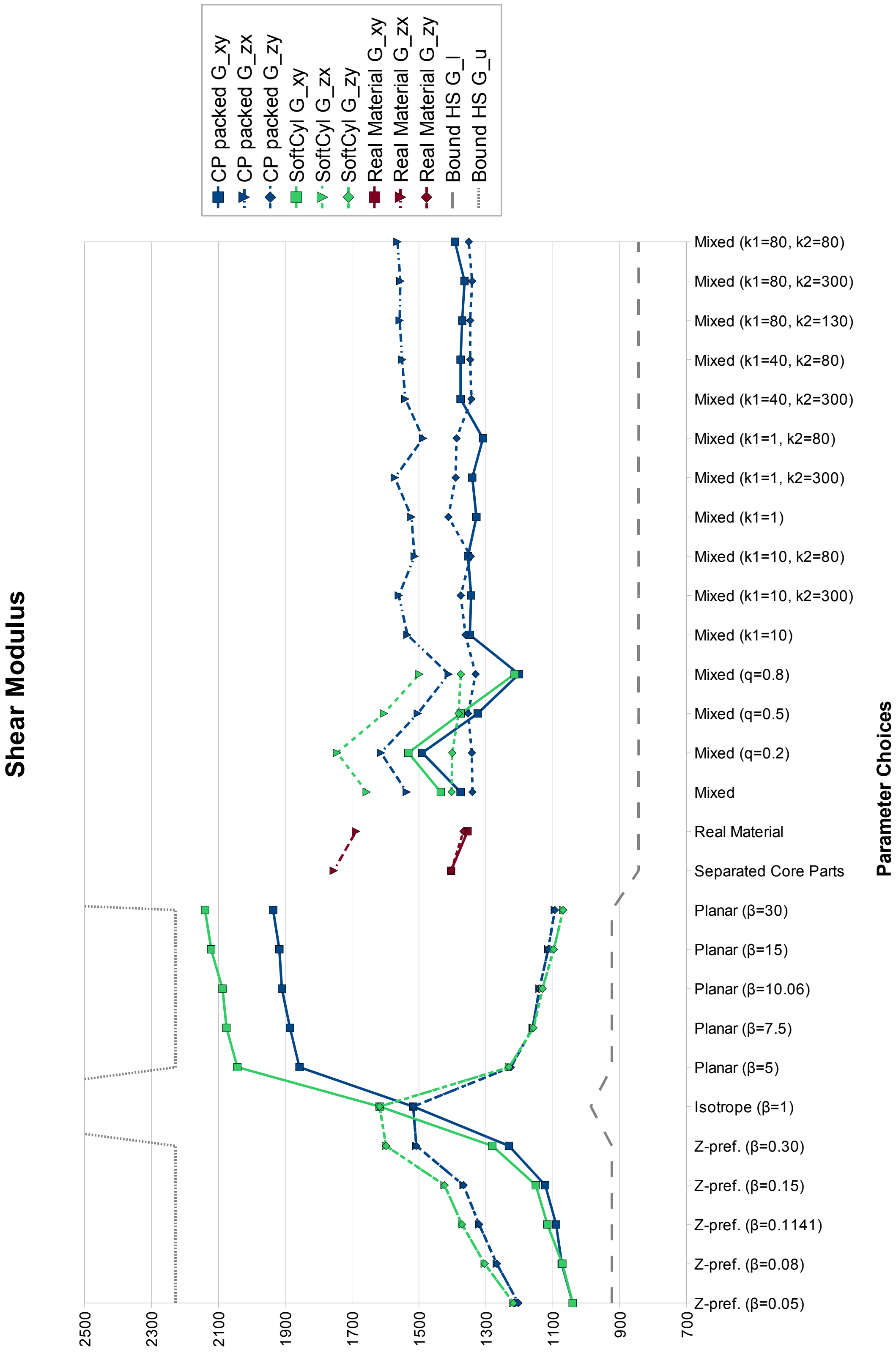

Figure 8.16.: Response of physical simulations for the shear modulus (given in MPa).

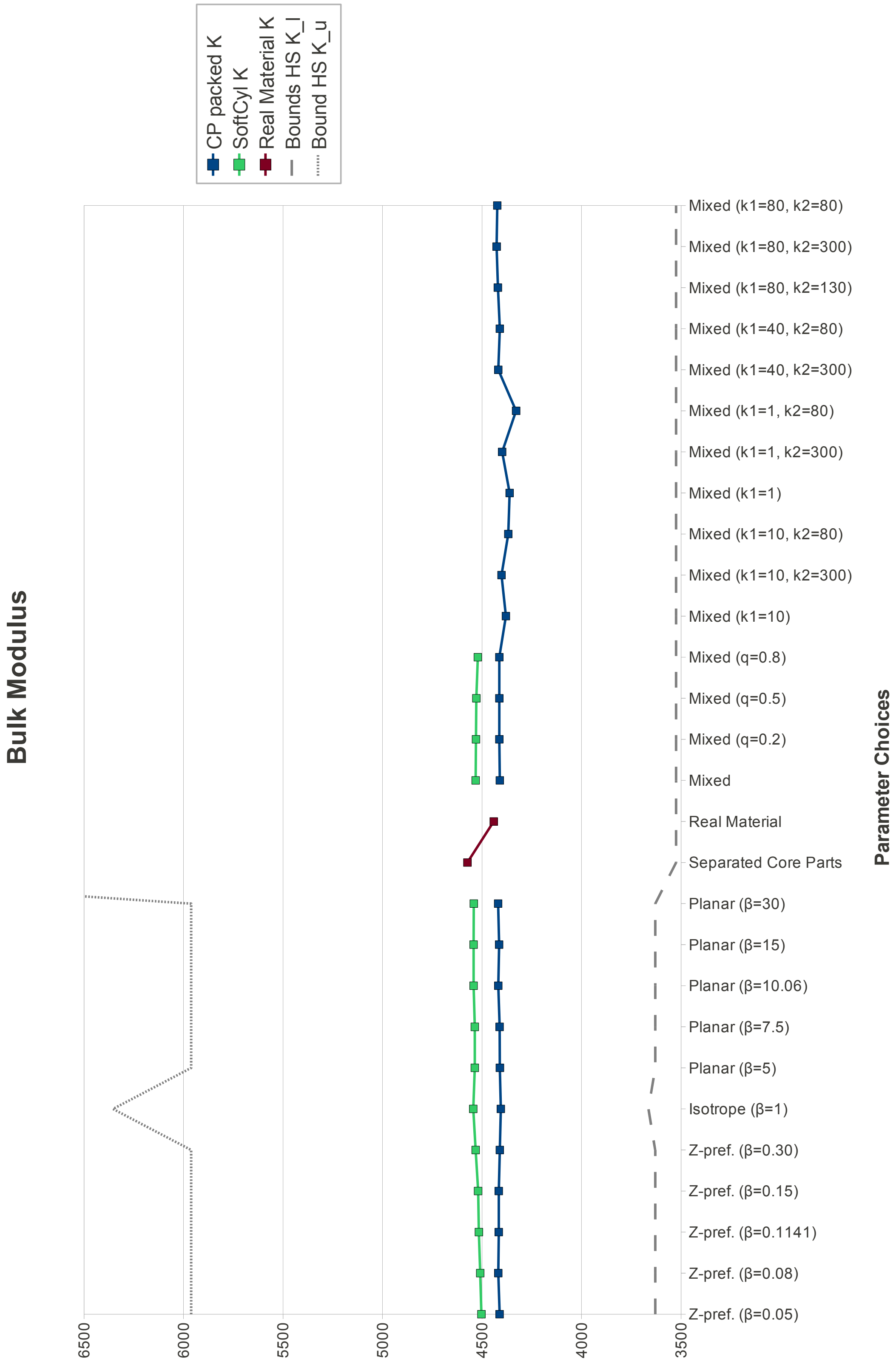

Figure 8.17.: Response of physical simulations for the bulk modulus (given in MPa).

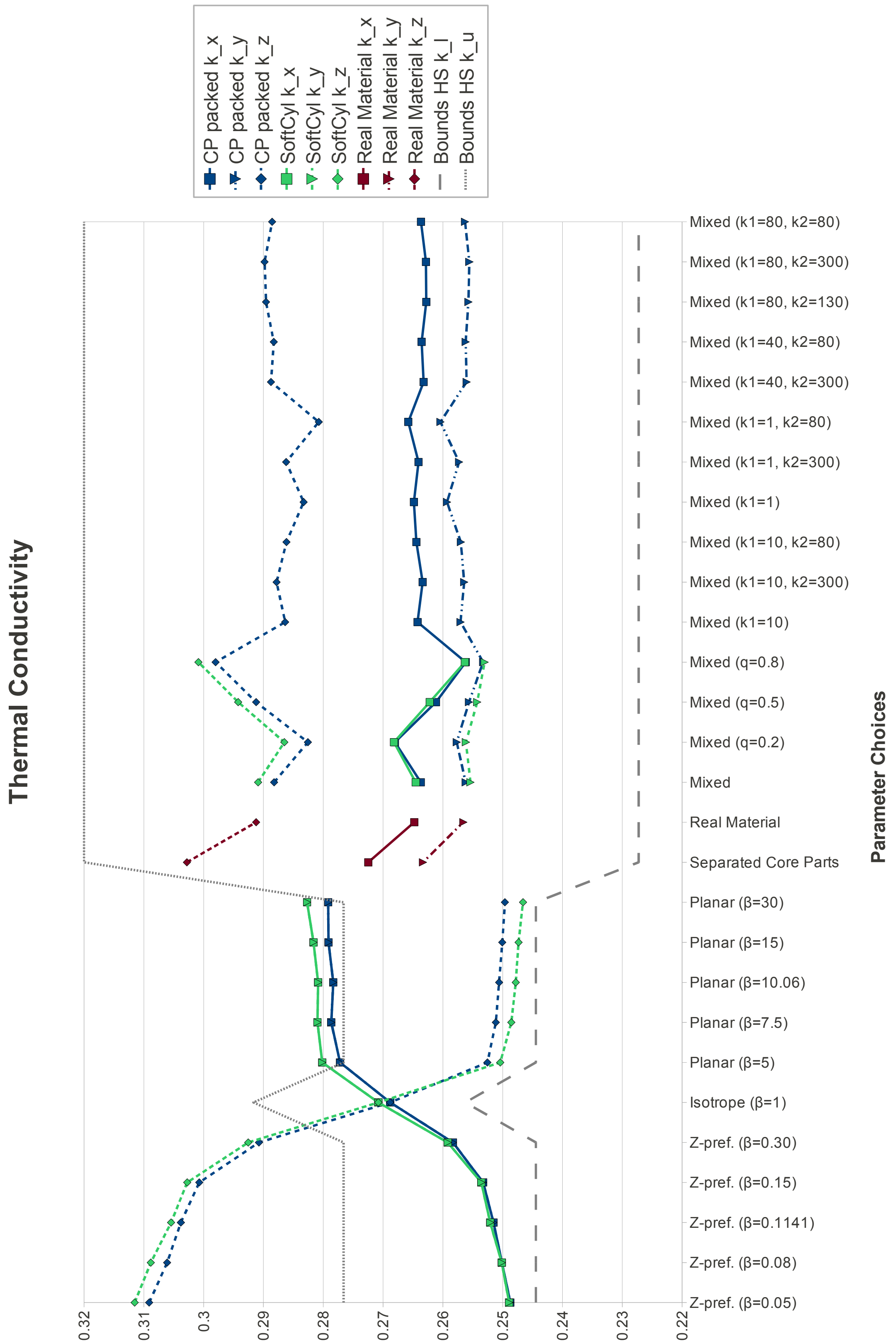

Figure 8.18.: Response of physical simulations for the thermal conductivity (given in W/mK).

The bulk modulus in Figure 8.17 is the response to uniform pressure on the material. As we do not consider different directions of this property, it is not surprising that the bulk modulus does not vary much for different orientation distributions. The response value is mainly dependent on the volume fraction, which is constant in all models. The responses for the boolean model are slightly higher as the fiber system is interconnected and therefore more resistant to the applied strain. The bulk modulus is close to the lower bound for all type of materials.

The thermal conductivity (Figure 8.18) is high along the fiber directions as the very long fibers conduct heat through the material. If we think of the enclosure of boats or airplanes, fibers are usually in a planar configuration, which supports the thermal isolation between interior and exterior. As also experienced in Oumarou *et al.* (2011), the thermal conductivity is close to the lower Hashin-Shtrikman bound for z preferred materials.

We emphasize once more, that the estimated physical properties of the real microstructure and the ones of our stochastic model (”Mixed“) are nearly equal for all physical and thermal responses, which confirms that we successfully rebuilt the structure of the real material.

In this section, we showed various physical responses to mechanical strain and thermal differences. The optimization of the material depends highly on its application and will certainly vary in different situations. This section mirrors preliminary results. More detailed studies and the adaption of the material to its use cases remain in the perspectives.

8.5.3. Calculation of the Representative Volume Element

As presented in Section 7.5, we calculate the RVE for several characteristics for fiber systems with three kinds of orientation distributions: z preferred ($\beta = 0.05$), isotropic ($\beta = 1$), and planar ($\beta = 30$). This study is based on realizations of our stochastic model in cubic images with a volume of 600^3 pixels, model parameters as described in Table 8.1, and periodic boundary conditions. We calculate the variance of a characteristic for non overlapping subwindows to the mean characteristic of the complete volume. We also observe the influence of the height-width ratio on the RVE by taking into account three subwindow shapes: the standard cubic shape (multiples of $(1, 1, 1)^T$), a shape elongated in z direction (multiples of $(1, 1, 10)^T$, and a plate shape in the xy plane (multiples of $(10, 10, 1)^T$.

First of all, we study the accuracy of the RVE calculations. We calculate first the variance of a characteristic in subwindows to the the mean characteristic of the complete volume. The principal idea is then to fit a straight line to the curve of the variance versus the volume of the subwindows (on a logarithmic scale for both axes). Naturally, the first and the last points do not match the straight line. The first ones, because the subwindow is too small and the last ones, because the amount of subwindows is too low. The freedom to choose the points, which contribute to the line fitting, poses the problem of varying values for the RVE. Figure 8.19 shows the curve of variance, where three different straight lines are fitted according to different intervals for the points of interest. Even if the straight lines do not seem to differ a lot on the logarithmic scale, the calculation of the RVE differs from 381^3 to 482^3, which represents twice the volume. In homogeneous, isotropic materials the calculation is more stable as the value of α is known to be equal to 1. For isotropic infinite fibers and for the characteristic of the volume fraction, α is known to be equal to 2/3 (Jeulin, 2011). In our case, which is a stochastic orientation distribution, the value of α may be somewhere in between. This vague constraint is fulfilled for all three fitted lines as well as the constraint $V \gg A_3$, for all points taken into account in the line fitting. Still, their estimations of the RVE differ a lot. This effect can be explained by the relatively small observation window of 600^3 pixels in one realization.

With a larger window or several realizations, the calculation of the RVE might be more stable.

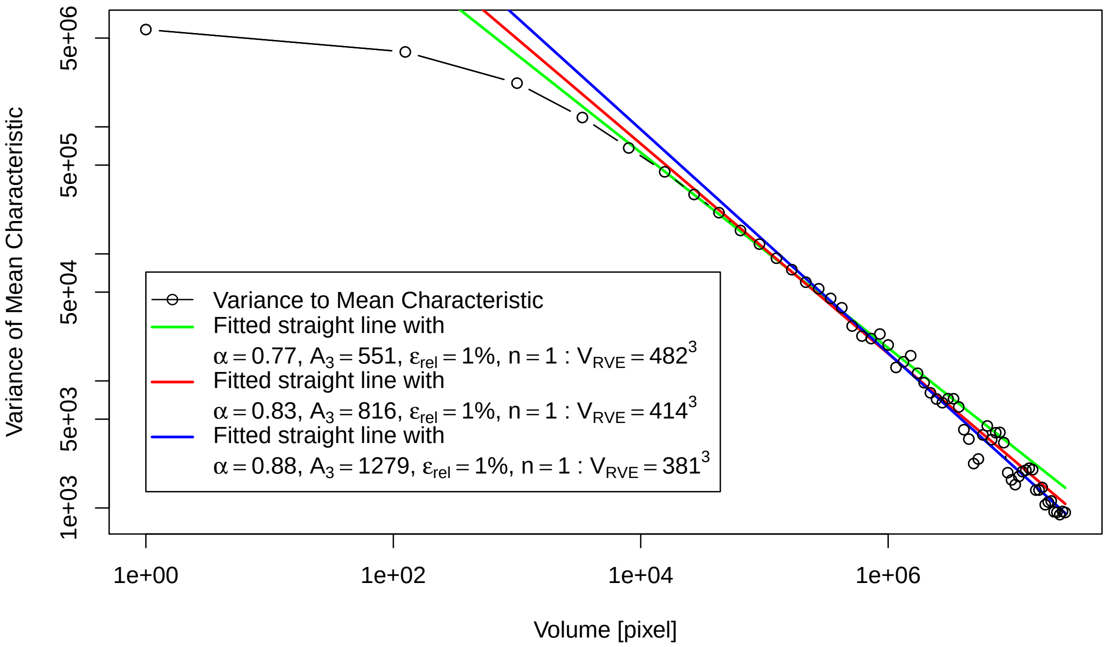

Figure 8.19.: Example of the inaccuracy of the RVE calculation on the bulk modulus and a z preferred orientation distribution ($\beta = 0.05$).

In our experiments, we chose the starting limit for the points of interest by a minimal volume for the subwindow V_s and the end limit by a maximal amount of subwindows m_e. The values for the limits are varying with the shape of the subwindows. We adapted these limits empirically to the curves dependent on the subwindow shape. For cubic shape, we choose $V_s = 10\,000$ and $m_e = 10$, for long shape $V_s = 20\,000$ and $m_e = 120$, and for plate shape $V_s = 10\,000$ and $m_e = 15$.

In Table 8.5, the results for several characteristics and the three realizations are presented. The values for the RVE given in the table are the multiples of the basic shapes of the subwindows. Furthermore, Figures 8.20 - 8.25 show some of the curves with the line fitting. The results state that our experiments based on ten realizations of each 400^3 pixels are sufficient large with a relative error between 0.29% and 1.86%. Furthermore, we observe that for a fiber system with a preferred direction it is sufficient to compute the physical behavior on a flat window with a height of at most 71 pixels. In the literature, nearly parallel fiber system are often approximated by computations on 2D images of spheres assuming infinite parallel fibers. If we consider only such 2D cuts of the microstructure, the deviation to the z axis is not taken into account. Still, the physical simulations on our realizations have shown the influence on the deviation parameter β from the preferred orientation. Knowing that flat shape are preferred for parallel fibers, one could assume that for planar oriented fibers a elongated shape would be preferable. On the right part of Table 8.5 and in Figures 8.24 and 8.25, we observe that not only the fiber orientation has an influence on the preferred window shape but also the direction of the characteristic of interest. The thermal conductivity in z direction can be better approximated in flat window shapes, whereas the thermal conductivity in x or y direction is more accurate in elongated window shapes. For isotropic oriented fibers, the shape of the subwindows has less importance. Remaining differences in the shape preference can be explained by local alignments.

		Z Preferred ($\beta = 0.05$)					Isotropic ($\beta = 1$)				Planar ($\beta = 30$)				
		V_V	K	G_zp	k_p	k_z	V_V	K	G	k	V_V	K	G_{zp}	k_p	k_z
CUBIC	$V_{\text{RVE}}(\epsilon_{\text{rel}} = 1\%, n = 1)$	1886	414	832	371	689	1123	477	938	430	1616	509	672	801	438
	$V_{\text{RVE}}(\epsilon_{\text{rel}} = 1\%, n = 10)$	688	164	326	138	258	466	177	375	173	617	189	249	274	153
	$\epsilon_{\text{rel}}(V = 400^3, n = 10)$ [%]	1.86	0.33	0.78	0.29	0.6	1.22	0.39	0.92	0.35	1.68	0.42	0.58	0.67	0.35
	α	0.76	0.83	0.82	0.77	0.78	0.87	0.77	0.84	0.84	0.8	0.77	0.77	0.71	0.73
	A_3	616	816	1086	827	686	1046	559	1031	1031	801	698	687	580	701
LONG	$V_{\text{RVE}}(\epsilon_{\text{rel}} = 1\%, n = 1)$	771	260	478	158	393	628	207	574	172	1270	312	379	354	301
	$V_{\text{RVE}}(\epsilon_{\text{rel}} = 1\%, n = 10)$	316	105	175	66	156	239	75	199	65	394	94	122	107	91
	α	0.86	0.84	0.76	0.88	0.83	0.8	0.76	0.73	0.79	0.66	0.64	0.68	0.64	0.64
	A_3	2699	2526	790	2315	2833	468	359	287	337	141	128	185	109	445
PLATE	$V_{\text{RVE}}(\epsilon_{\text{rel}} = 1\%, n = 1)$	178	53	109	58	64	239	87	134	116	513	154	84	509	48
	$V_{\text{RVE}}(\epsilon_{\text{rel}} = 1\%, n = 10)$	71	20	42	21	26	94	32	55	41	177	50	33	124	18
	α	0.83	0.8	0.8	0.76	0.85	0.82	0.76	0.87	0.74	0.72	0.68	0.83	0.54	0.77
	A_3	205	118	168	241	160	422	286	491	420	503	333	336	191	185
RVE Ratio	$V_{\text{RVE}}^{\text{long}}/V_{\text{RVE}}^{\text{cubic}}(\epsilon_{\text{rel}} = 1\%)$	0.68	2.48	1.90	0.77	1.86	1.75	0.82	2.29	0.64	4.85	2.30	1.79	0.86	3.25
	$V_{\text{RVE}}^{\text{plate}}/V_{\text{RVE}}^{\text{cubic}}(\epsilon_{\text{rel}} = 1\%)$	0.08	0.21	0.22	0.38	0.08	0.96	0.61	0.29	1.96	3.20	2.77	0.20	25.66	0.13
	$V_{\text{RVE}}^{\text{long}}/V_{\text{RVE}}^{\text{cubic}}(\epsilon_{\text{rel}} = 5\%)$	1.12	2.59	1.39	1.30	2.38	1.27	0.77	1.29	0.50	2.07	0.99	1.03	0.53	1.75
	$V_{\text{RVE}}^{\text{plate}}/V_{\text{RVE}}^{\text{cubic}}(\epsilon_{\text{rel}} = 5\%)$	0.12	0.18	0.20	0.36	0.11	0.77	0.57	0.33	1.17	2.05	1.59	0.26	6.16	0.17

Table 8.5.: Calculation of the representative volume element (RVE) from partial division of a 600^3 cubic image. We consider three shapes for the subvolumes: cubic shape [multiples of $(1,1,1)^T$], long shape elongated in z direction [multiples of $(1,1,10)^T$] and flat plates in the xy plane [multiples of $(10,10,1)^T$]. The values for the RVE given in the table are the multiples of the shape elements (e.g. if the value in the table is 50 for a long shape, the $V_{\text{RVE}} = V[50 \cdot (1,1,10)^T] = 50 \cdot 50 \cdot 500 = 1\,250\,000$). Notations: n denotes the number of realizations and ϵ_{rel} the relative error.

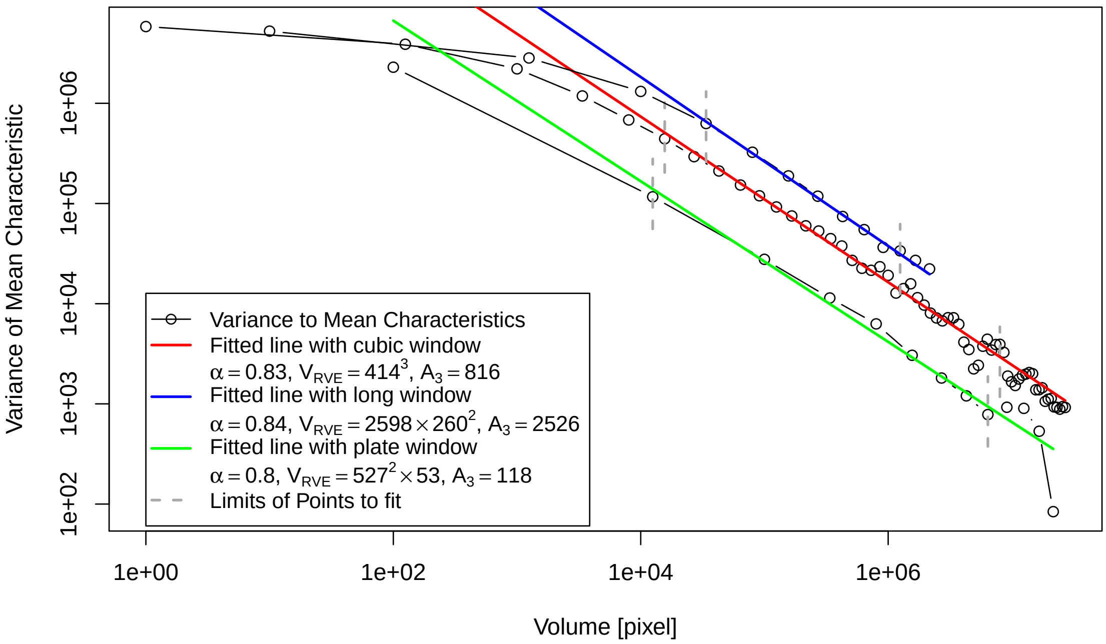

Figure 8.20.: RVE calculation for the bulk modulus and a fiber packing with a z preferred orientation distribution ($\beta = 0.05$).

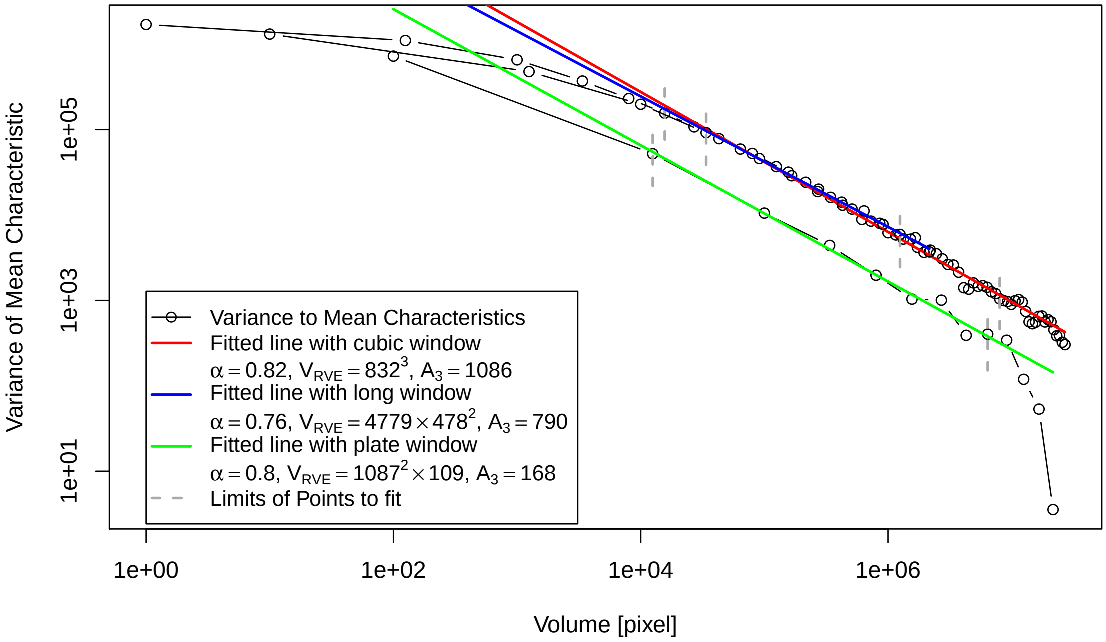

Figure 8.21.: RVE calculation for the shear modulus G_{zp} and a fiber packing with a z preferred orientation distribution ($\beta = 0.05$).

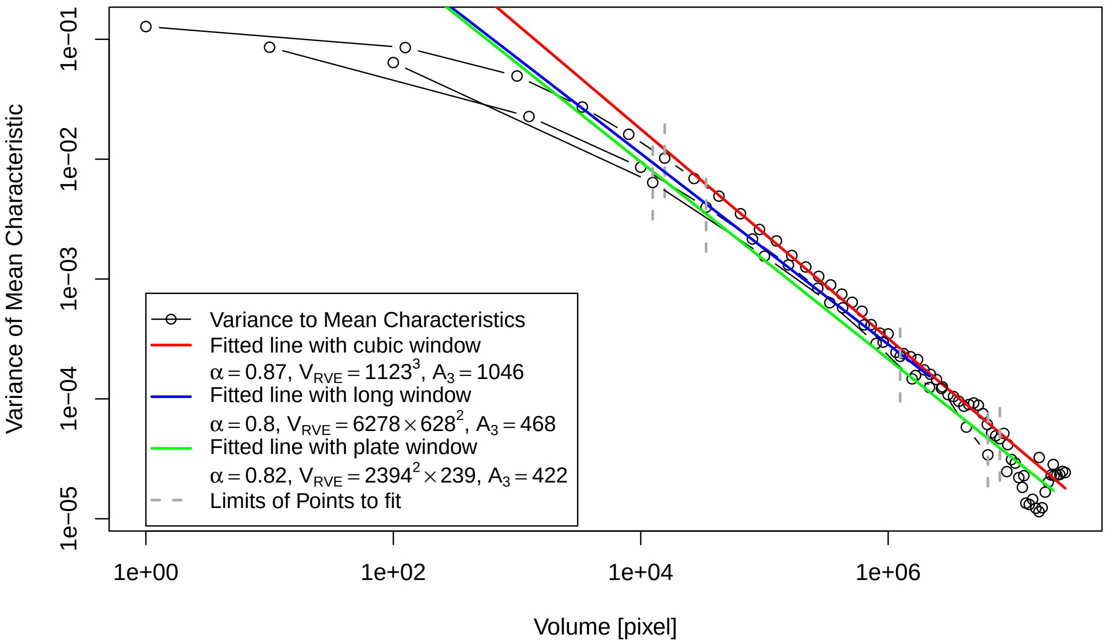

Figure 8.22.: RVE calculation for the volume fraction and a fiber packing with an isotropic orientation distribution ($\beta = 1$).

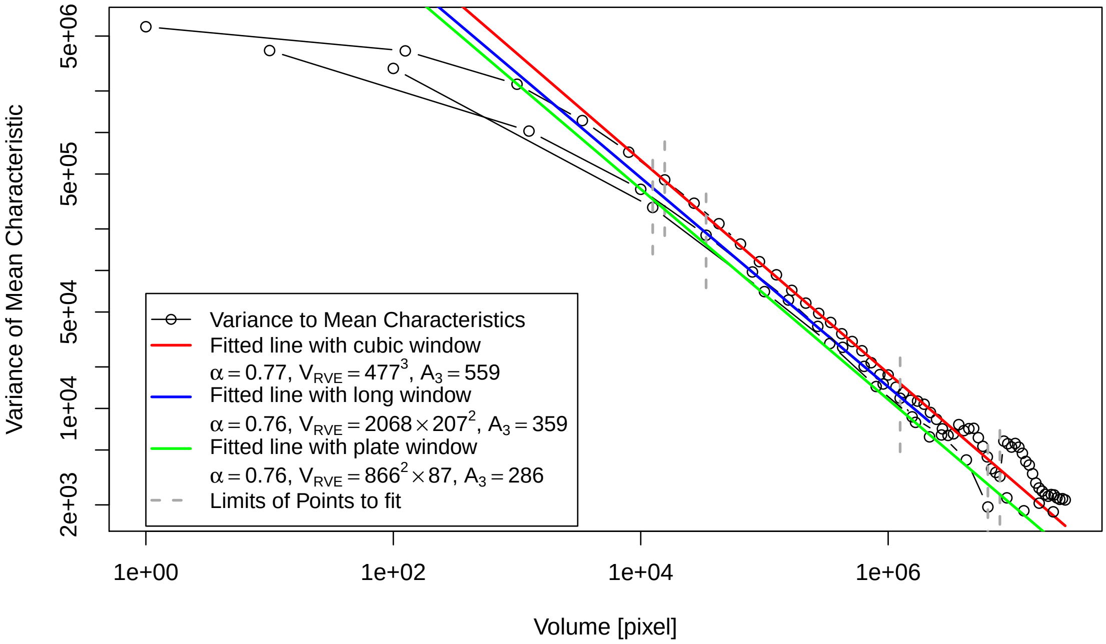

Figure 8.23.: RVE calculation for the bulk modulus and a fiber packing with an isotropic orientation distribution ($\beta = 1$).

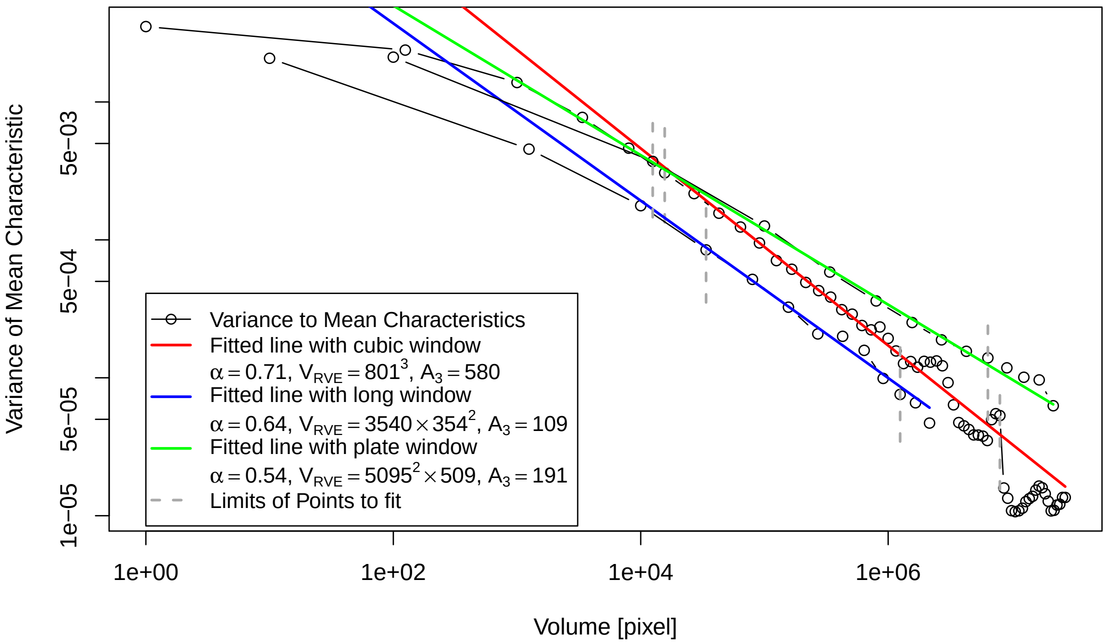

Figure 8.24.: RVE calculation for the thermal conductivity in planar direction and a fiber packing with a planar orientation distribution ($\beta = 30$).

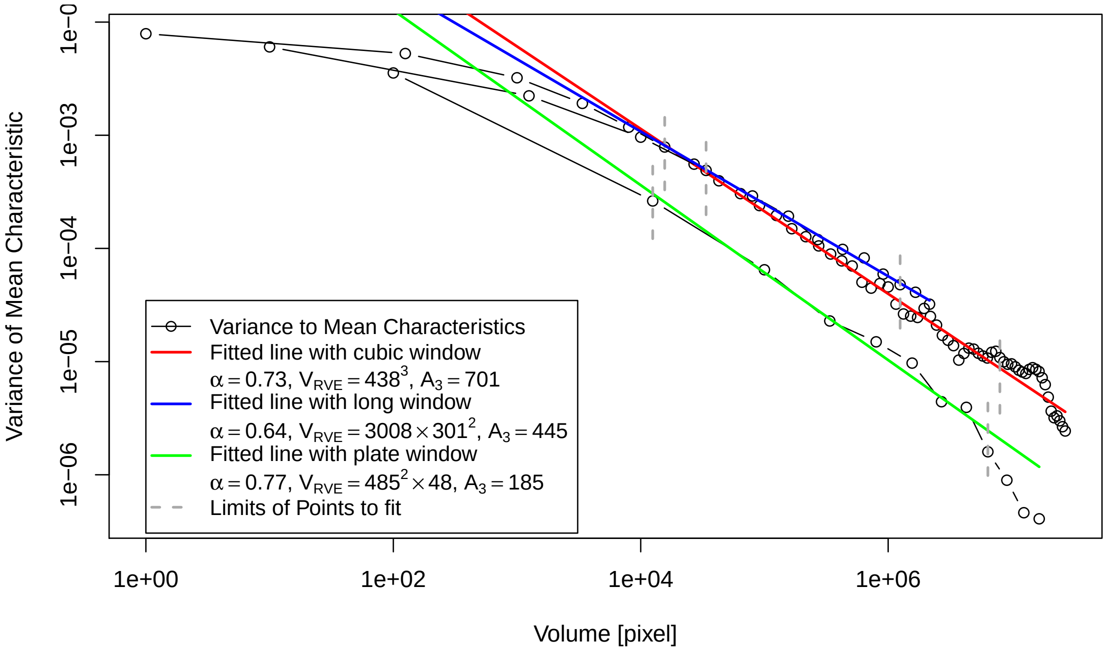

Figure 8.25.: RVE calculation for the thermal conductivity in z direction and a fiber packing with a planar orientation distribution ($\beta = 30$).

Taking into account the various orientation distributions of our fiber system and the different oriented effective properties, we can conclude that the cubic window shape is the adequate choice for our experiments.

In order to check the dimensions of our results, we compare them to Oumarou *et al.* (2011), where the RVE is computed for a 2D section of a parallel fiber system. For fibers with a mean diameter of 16 µm the RVE is determined as a surface with 1311 µm sidelength, for $n = 100$ realizations and a relative error of 1%. Adapted to our realizations with a fiber radius of 5.44 pixels, the pixel sampling would be 1.47 µm/pixel. We can compare this to our calculations for z preferred fibers and a plate window shape. If we flatten the volume to 1 pixel thickness, it can be interpreted as a 2D section. This conversion of our plate RVE results in a 2D section with 1687 µm sidelength. As the fibers in our stochastic model are not completely parallel nor straight, it is reasonable that the RVE is slightly higher than in Oumarou *et al.* (2011).

8.6. Conclusion

In this chapter, we showed the application of the overall chain of virtual material design to a real data set, starting from local radius and orientation analysis, over single fiber separation, parameter estimation, stochastic modeling, to the simulation of physical properties.

Both analyses, from the binary image and the separated fiber system, agree in the radius and orientation distribution, which confirm the single fiber separation. From the reconstructed fiber system, more characteristics as the fiber curvature and the mixed β distribution can be estimated. The estimation of fiber lengths needs to be improved, which also necessitates an improvement in the fiber tracking, as it happens that fibers are split up in parts.

The stochastic model yield the possibility to vary some characteristics of the fiber system and thus to create virtual materials that can be evaluated in the simulation of the physical properties. We observed a high influence of the fiber arrangement to the mechanical and thermal responses, whereas the curvature of the fibers has much less influence. Furthermore, we observe the influence of overlap and fiber bending in comparison to the Boolean cylinders. In general, the effective properties of the rebuilt fiber packing confirm that the microstructure of the real material was reconstructed successfully.

Dependent on the use case of the material, the material can be optimized by changing the parameters respectively. The computation of the representative volume element confirmed that our experiments with 10 trials of size 400^3 have a high accuracy. Still, the computation of the RVE seems to lack on accuracy, which may be improved by a larger observation window. In perspective, it might be interesting to study the influence of other characteristics of the fiber systems as e.g. the aspect ratio, local alignment or layers of different orientation distributions.

Chapter 9.

9 Conclusion and Perspectives

The main motivation of this work is the virtual material design, which is dedicated to optimize the physical properties of a material by adapting its microstructure. This concept includes various steps of image processing, starting with a detailed analysis of the material's microstructure on 3D micro tomography images, fitting a realistic stochastic model, and finally evaluating the physical properties of the virtual materials by numerical simulations. In order to attain our goal, we developed numerous novel methods in the field of local fiber quantification, single fiber separation, stochastic models, and parameter estimation. Furthermore, we studied lateral subjects such as the visualization and evaluation of local characteristics, including regular tessellations of the surface of the unit sphere, color mapping of 3D orientations, and computation of the orientation covariance.

With the approaches developed and presented in this work, the overall process of virtual material design can be applied to all fibrous materials, fulfilling the following constraints: solid fibers with a nearly spherical cross section and an image resolution that samples the fiber radius with at least 2 pixels. A full case study is performed on a sample of glass fiber reinforced material, which confirms the quality of our approaches.

In the following, we summarize the contributions and perspectives of this thesis.

9.1. Contributions

This section contains a summary of all novel methods, developed in the scope of this thesis, that are contributions to the state-of-the-art of research linked to the analysis and optimization of the microstructure of fibrous materials.

Image Analysis for Fiber Quantification. One of the main contributions of this work is the local analysis of fiber radius and orientation. Our method combines a sparse chord length transform with the theory of inertia moments and axis, yielding the advantages of both methods. In contrast to other methods proposed in the literature, our approach of orientation analysis can treat various fiber thicknesses, and moreover computes the fiber radius. Additionally, we gain high precision from the main inertia axis. The approach is also highly efficient in terms of computational complexity. Furthermore, we optimized the results by an orientation correction and an adaptive smoothing weighted by the ratio of local inertia moments. In order to apply the analysis directly to gray value images, we developed and evaluated numerous approaches to compute the directional distance transform on gray value images.

We discussed in detail the difference between number-, length- and volume-weighted distributions, and their theoretical equality in specific cases. Furthermore, we developed a method to tessellate the sphere surface in regular regions. In contrast to existing approaches, for this method the amount of regions can be easily modified (within $6n^2, n \in \mathbb{N}$) and any arbitrary orientation can be directly assigned to a region.

In order to segment single fibers, we developed an approach based on probability maps. For each pixel, we compute the probability that it belongs to a fiber core in a region without overlapping fibers. By tracking high probabilities, we reconstruct parts of the fiber cores, which are conditionally reconnected over crossing regions in a second step. The definition of the probability maps opens the wide possibilities of morphological operations by adapting the structuring elements locally.

Stochastic Modeling and Physical Simulations. The most remarkable development of this thesis consists in the development of a stochastic model for hardcore systems of bent fibers, represented as sphere chains. In order to create random fibers with a controllable level of bending, we combined a random walk with the multivariate von Mises-Fisher orientation distribution, generalized to the multi dimensional space. The created model of overlapping bent fibers is turned into a hardcore system by applying forces to the sphere centers. The force-biased approach is based on earlier models developed for sphere packing, with inspiration of molecular modeling for the definition of the forces. Two kinds of forces are applied, one to remove the overlap and one to keep the fiber structure reasonable in terms of distance and angle between neighbor spheres. Additionally, a placing strategy can accelerate the packing process by choosing an initial configuration with low overlap.

The model fitting requires estimation of the model parameters. Most estimations are straight forward from a system of separated fibers, except the orientation distributions. We developed a novel accurate estimator for the κ parameter in the von Mises-Fisher distribution and an approximation of the curvature parameters, derived from the multivariate von Mises-Fisher distribution.

Further in the field of orientation distribution, there is a lack of multi-functional distributions with parameters that can be easily estimated. By multi-functional distribution, we refer to the β distribution that can concentrate on an arbitrary orientation or on an arbitrary plane. Unfortunately, the parameter β can only be numerically approximated. We propose a modification of the von Mises-Fisher distribution, being able to realize similar distributions with the parameter κ, that can be estimated easily.

Furthermore, we enrich the statistics of fiber systems with the orientation covariance. This second order characteristic can reveal local and global alignment of the fiber system without the need to separate single fibers. It also showed some potential in achieving an estimator for the fiber curvature directly from the local orientation maps.

In the field of physical simulation, we did not add novel algorithms, but give a summary of the theory of effective properties and its characteristics in application to random fiber systems. The overall process was then applied to a glass fiber reinforced composite and discussed in detail.

9.2. Perspectives

The development of novel methods answers some questions, but raises always more new perspectives. This section contains a summary of the various perspectives that arose during the work of this thesis.

Image Analysis for Fiber Quantification. Concerning the local orientation analysis, it might be interesting to study the combination of other orientation information (as e.g. the oriented Gaussian filters) with the inertia moments. This modified approach would lose the advantage of being independent of the fiber radius, but gain robustness in noisy images. An adequate application would be fiber reinforced materials with constant fiber radius, where the resolution is in general low or the contrast between fibers and matrix is low. The Gaussian orientation space alone yields good results, but needs several hours of computation time. The combination with inertia moments, has the potential to decrease the computation time to a minute range, while increasing the precision of the results.

The methods operating directly on the gray value image depend on one or more parameters. With some experience, these parameters can be empirically adapted with respect to the resulting classification map. With further studies, it might be possible to choose the parameters from the local contrasts in the gray value image.

The accuracy of the orientation analysis was studied in detail, whereas the accuracy of the fiber radius especially on gray value images remains to be verified. This should be performed in a first step on synthetic images reconstructing the output of CT or REM imaging. In a second step, the analysis should be compared to the actual fiber radius known from the fabrication process. One should be aware that there remain several sources of errors, such as imaging artifacts, the effect of partial volumes, size dependent gray values, the accuracy of the image resolution given from the CT software, and maybe chemical reactions during the fabrication process.

In the field of visualization of the local orientation maps, we suggest a 3D color mapping for few orientations of interest projected on the surface rendering. A general color mapping fulfilling the constraint of injectivity remains to be developed.

The single fiber separation yields also several possibilities of improvement. The probability maps can be modified to be applied directly on gray value images. The use of the sum of erosions with increasing size of the structuring element is a reasonable candidate for this task. Furthermore, the tracking of fibers can be improved with a more complex propagation algorithm. The existing approach depends on a limit of acceptable probabilities. This limit is in practice rather difficult to choose and has a large influence in the quality of the segmentation. This point can be improved by an iterative approach, starting with a high limit and decreasing the limit in each iteration.

Stochastic Modeling and Physical Simulations. During the packing process of our stochastic model, fibers are displaced to fit in a non overlapping configuration. It turned out that these displacements change the fiber orientation slightly. Thus, highly restricted orientation distributions cannot be realized. This point can be improved by adding forces that maintain the original orientation of the fibers. Furthermore, the relation between the initial and the final curvature during the packing process needs to be studied. Regarding the parameter estimators, properties of the estimators remain to be verified, such as unbiasedness and robustness.

Concerning the orientation covariance, there remains a whole field of research in interpreting this characteristic, to optimize the efficiency of the computation and to estimate curvature parameters directly from the orientation covariance.

A

Appendix A.

Calculation of Theoretical Inertia Moments

In this chapter, we proof the equations 3.16, 3.17 and 3.18 of the theoretical inertia moments and main inertia axis in 2D. The theoretical description of the problem is given as follows:

$$\theta_i = \frac{i\pi}{4}, \quad d(vs_i) = \frac{r}{|\sin(\theta_i - \theta)|}, \quad P_i = \begin{pmatrix} d(vs_i)\cos\theta_i \\ d(vs_i)\sin\theta_i \end{pmatrix}, \quad M_{pq} = \sum_{i=0}^{7} (P_{i,x})^p (P_{i,y})^q \tag{A.1}$$

and the resolution of inertia moments $\lambda_{1,2}$ and the main inertia axis with angle θ':

$$\lambda_{1,2} = \frac{M_{20} + M_{02} \pm \sqrt{4M_{11}^2 + (M_{20} - M_{02})^2}}{16} \tag{A.2}$$

$$\tan(2\theta') = \frac{2M_{11}}{M_{20} - M_{02}} \tag{A.3}$$

Statement: To show are the following equations:

$$\lambda_1 = r^2 \left(\frac{2 + \sqrt{3\cos^2(4\theta) + 1}}{\sin^2(4\theta)} \right) \tag{A.4}$$

$$\lambda_2 = r^2 f(\theta) \qquad \text{with} \quad f(\theta) = \begin{cases} \left(\frac{2+\sqrt{3\cos^2(4\theta)+1}}{\sin^2(4\theta)} \right) & , \sin^2(4\theta) \neq 0 \\ \frac{3}{4} & , \text{otherwise} \end{cases} \tag{A.5}$$

$$\tan(2\theta') = \tan^3(2\theta). \tag{A.6}$$

Proof. Standard trigonometrical formula will be used in a slight modification. From the equation $[\cos(2\alpha) = 2\cos^2\alpha - 1 = 1 - 2\sin^2\alpha]$ we can conclude the following useful modifications:

$$\sin^2\alpha = \frac{1}{2} - \frac{1}{2}\cos(2\alpha) \tag{A.7}$$

$$\cos^2\alpha = \frac{1}{2} + \frac{1}{2}\cos(2\alpha). \tag{A.8}$$

Periodicity of the sine and cosine functions yield the following formula:

$$\sin(\alpha + \pi/2) = \cos\alpha \tag{A.9}$$

$$\cos(\alpha + \pi/2) = -\sin\alpha \tag{A.10}$$

$$\sin(\alpha + \pi) = -\sin\alpha. \tag{A.11}$$

From the symmetrical ordering of the sampled directions θ_i, we know that $\theta_{i+4} = \theta_i + \pi$. This implies

$$\sin^2(\theta_{i+4} - \theta) = \sin^2(\theta_i + \pi - \theta) = \sin^2(\theta_i - \theta) \tag{A.12}$$

$$\sin(\theta_{i+4})\cos(\theta_{i+4}) = \sin(\theta_i)\cos(\theta_i). \tag{A.13}$$

With this ways of simplification, we resolve first the second order moments M_{11}, M_{20} and M_{02}:

$$
\begin{aligned}
M_{11} &= \sum_{i=0}^{7} P_{i,x}P_{i,y} = \sum_{i=0}^{7} d^2(vs_i)\sin(\theta_i)\cos(\theta_i) = \sum_{i=0}^{7} \frac{r^2}{\sin^2(\theta_i-\theta)}\sin(\theta_i)\cos(\theta_i)\\
&= 2\sum_{i=0}^{3} \frac{r^2}{\sin^2(\theta_i-\theta)}\sin(\theta_i)\cos(\theta_i) \quad \text{(with symmetry from A.12 and A.13)}\\
&= 2r^2\sum_{i=0}^{3} \frac{\sin(\theta_i)\cos(\theta_i)}{\sin^2(\theta_i-\theta)}\\
&= 2r^2\left(\underbrace{\frac{\sin(0)\cos(0)}{\sin^2(-\theta)}}_{=0} + \frac{\sin(\pi/4)\cos(\pi/4)}{\sin^2(\pi/4-\theta)} + \underbrace{\frac{\sin(\pi/2)\cos(\pi/2)}{\sin^2(\pi/2-\theta)}}_{=0} + \frac{\sin(3\pi/4)\cos(3\pi/4)}{\sin^2(3\pi/4-\theta)}\right)\\
&= 2r^2\left(\frac{1/2}{\sin^2(\pi/4-\theta)} - \frac{1/2}{\sin^2(3\pi/4-\theta)}\right)\\
&= r^2\left(\frac{1}{\sin^2(\pi/4-\theta)} - \frac{1}{\sin^2(3\pi/4-\theta)}\right)\\
&= r^2\left(\frac{1}{\sin^2(\pi/4-\theta)} - \frac{1}{\cos^2(\pi/4-\theta)}\right) \quad \text{(with A.9)}\\
&= r^2\left(\frac{1}{\frac{1}{2}-\frac{1}{2}\cos(\pi/2-2\theta)} - \frac{1}{\frac{1}{2}+\frac{1}{2}\cos(\pi/2-2\theta)}\right) \quad \text{(with A.7)}\\
&= r^2\left(\frac{\frac{1}{2}+\frac{1}{2}\cos(\pi/2-2\theta)-\frac{1}{2}+\frac{1}{2}\cos(\pi/2-2\theta)}{\frac{1}{4}-\frac{1}{4}\cos^2(\pi/2-2\theta)}\right)\\
&= 4r^2\left(\frac{\cos(\pi/2-2\theta)}{\sin^2(\pi/2-2\theta)}\right) = 4r^2\left(\frac{\sin(2\theta)}{\cos^2(2\theta)}\right)
\end{aligned}
$$

$$
\begin{aligned}
M_{20} &= \sum_{i=0}^{7} P_{i,x}P_{i,y} = \sum_{i=0}^{7} d^2(vs_i)\cos^2(\theta_i)\\
&= 2\sum_{i=0}^{3} \frac{r^2}{\sin^2(\theta_i-\theta)}\cos^2(\theta_i) \quad \text{(with symmetry from A.12 and A.13)}\\
&= 2r^2\left(\frac{\cos^2(0)}{\sin^2(-\theta)} + \frac{\cos^2(\pi/4)}{\sin^2(\pi/4-\theta)} + \underbrace{\frac{\cos^2(\pi/2)}{\sin^2(\pi/2-\theta)}}_{=0} + \frac{\cos^2(3\pi/4)}{\sin^2(3\pi/4-\theta)}\right)\\
&= 2r^2\left(\frac{1}{\sin^2(-\theta)} + \frac{1/2}{\sin^2(\pi/4-\theta)} + \frac{1/2}{\sin^2(3\pi/4-\theta)}\right)\\
&= r^2\left(\frac{2}{\sin^2(-\theta)} + \frac{1}{\sin^2(\pi/4-\theta)} + \frac{1}{\sin^2(3\pi/4-\theta)}\right)\\
&= r^2\left(\frac{2}{\sin^2(-\theta)} + \frac{\frac{1}{2}+\frac{1}{2}\cos(\pi/2-2\theta)+\frac{1}{2}-\frac{1}{2}\cos(\pi/2-2\theta)}{\frac{1}{4}-\frac{1}{4}\cos^2(\pi/2-2\theta)}\right)\\
&= r^2\left(\frac{2}{\sin^2(\theta)} + \frac{4}{\sin^2(\pi/2-2\theta)}\right) = r^2\left(\frac{2}{\sin^2(\theta)} + \frac{4}{\cos^2(2\theta)}\right)
\end{aligned}
$$

$$
\begin{aligned}
M_{02} &= \sum_{i=0}^{7} P_{i,x}P_{i,y} = \sum_{i=0}^{7} d^2(vs_i)\sin^2(\theta_i) = 2\sum_{i=0}^{3}\frac{r^2}{\sin^2(\theta_i-\theta)}\sin^2(\theta_i)\\
&= 2r^2\left(\underbrace{\frac{\sin^2(0)}{\sin^2(-\theta)}}_{=0}+\frac{\sin^2(\pi/4)}{\sin^2(\pi/4-\theta)}+\frac{\sin^2(\pi/2)}{\sin^2(\pi/2-\theta)}+\frac{\sin^2(3\pi/4)}{\sin^2(3\pi/4-\theta)}\right)\\
&= 2r^2\left(\frac{1/2}{\sin^2(\pi/4-\theta)}+\frac{1}{\sin^2(\pi/2-\theta)}+\frac{1/2}{\sin^2(3\pi/4-\theta)}\right)\\
&= r^2\left(\frac{1}{\sin^2(\pi/4-\theta)}+\frac{2}{\sin^2(\pi/2-\theta)}+\frac{1}{\sin^2(3\pi/4-\theta)}\right)\\
&= r^2\left(\frac{2}{\sin^2(\pi/2-\theta)}+\frac{4}{\sin^2(\pi/2-2\theta)}\right) = r^2\left(\frac{2}{\cos^2(\theta)}+\frac{4}{\cos^2(2\theta)}\right)
\end{aligned}
$$

To apply this knowledge to the eigenvalues $\lambda_{1,2}$ and the main inertia axis θ', we first simplify the equations $M_{20}+M_{02}$, $M_{20}-M_{02}$ and $(M_{11})^2$:

$$
\begin{aligned}
M_{20}+M_{02} &= r^2\left(\frac{2}{\sin^2(\theta)}+\frac{4}{\cos^2(2\theta)}\right)+r^2\left(\frac{2}{\cos^2(\theta)}+\frac{4}{\cos^2(2\theta)}\right)\\
&= r^2\left(\frac{2}{\sin^2(\theta)\cos^2(\theta)}+\frac{8}{\cos^2(2\theta)}\right)\\
&= r^2\left(\frac{8}{\sin^2(2\theta)}+\frac{8}{\cos^2(2\theta)}\right) = r^2\left(\frac{32}{\sin^2(4\theta)}\right)
\end{aligned}
$$

$$
\begin{aligned}
M_{20}-M_{02} &= r^2\left(\frac{2}{\sin^2(\theta)}+\frac{4}{\cos^2(2\theta)}\right)-r^2\left(\frac{2}{\cos^2(\theta)}+\frac{4}{\cos^2(2\theta)}\right)\\
&= r^2\left(\frac{2}{\sin^2(\theta)}-\frac{2}{\cos^2(\theta)}\right) = r^2\left(\frac{8\cos(2\theta)}{\sin^2(2\theta)}\right)
\end{aligned}
$$

$$
(M_{11})^2 = 16r^4\left(\frac{\sin(2\theta)}{\cos^2(2\theta)}\right)^2 = 16r^4\left(\frac{\sin^2(2\theta)}{\cos^4(2\theta)}\right)
$$

We include this information in the equations A.2 and A.3:

$$\begin{aligned}
\lambda_{1,2} &= \frac{M_{20} + M_{02} \pm \sqrt{4M_{11}^2 + (M_{20} - M_{02})^2}}{16} \\
&= \frac{r^2\left(\frac{32}{\sin^2(4\theta)}\right) \pm \sqrt{64r^4\left(\frac{\sin^2(2\theta)}{\cos^4(2\theta)}\right) + (r^2\left(\frac{8\cos(2\theta)}{\sin^2(2\theta)}\right))^2}}{16} \\
&= r^2\left(\frac{2}{\sin^2(4\theta)} \pm \frac{1}{2}\sqrt{\frac{\sin^2(2\theta)}{\cos^4(2\theta)} + \frac{\cos^2(2\theta)}{\sin^4(2\theta)}}\right) \\
&= r^2\left(\frac{2}{\sin^2(4\theta)} \pm \frac{\sqrt{\sin^6(2\theta) + \cos^6(2\theta)}}{2\cos^2(2\theta)\sin^2(2\theta)}\right) \\
&= r^2\left(\frac{2}{\sin^2(4\theta)} \pm \frac{\sqrt{\frac{1}{8}((1 - cos(4\theta))^3 + (1 + cos(4\theta))^3)}}{2\cos^2(2\theta)\sin^2(2\theta)}\right) \\
&= r^2\left(\frac{2}{\sin^2(4\theta)} \pm \frac{\sqrt{1 + 3\cos^2(4\theta)}}{4\cos^2(2\theta)\sin^2(2\theta)}\right) \\
&= r^2\left(\frac{2}{\sin^2(4\theta)} \pm \frac{\sqrt{1 + 3\cos^2(4\theta)}}{\sin^2(4\theta)}\right) = r^2\left(\frac{2 \pm \sqrt{1 + 3\cos^2(4\theta)}}{\sin^2(4\theta)}\right)
\end{aligned}$$

This partly proves the statement for the second order moments. If θ is a multiple of $\pi/4$ the divisor $\sin^2(4\theta)$ tends to zero. For λ_1 and $\theta = n\pi/4, n \in \mathbb{N}$, the dividend $2 + \sqrt{1 + 3\cos^2(4\theta)}$ equals 4, therefore λ_1 diverges to infinity. Whereas for λ_2, the dividend $2 - \sqrt{1 + 3\cos^2(4\theta)}$ vanishes equally and we can compute the limit with the rule of L'Hospital applied twice:

$$\begin{aligned}
\lim_{(\theta \to n\pi/4)} \frac{\lambda_2}{r^2} &= \lim_{(\theta \to n\pi/4)} \frac{2 - \sqrt{1 + 3\cos^2(4\theta)}}{\sin^2(4\theta)} \overset{\text{L'H}}{=} \lim_{(\theta \to n\pi/4)} \frac{12\frac{\cos(4\theta)\sin(4\theta)}{\sqrt{1+3\cos^2(4\theta)}}}{8\sin(4\theta)\cos(4\theta)} \\
&= \lim_{(\theta \to n\pi/4)} \frac{3}{2\sqrt{1 + 3\cos^2(4\theta)}} = \frac{3}{4}.
\end{aligned}$$

As both limits of dividend and divisor exist, the rule of L'Hospital holds and λ_2 converges to $\frac{3}{4}r^2$ for $\theta \to n\pi/4$. It remains to show the equation of the main inertia axis θ':

$$\tan(2\theta') = \frac{2M_{11}}{M_{20} - M_{02}} = \frac{8r^2\left(\frac{\sin(2\theta)}{\cos^2(2\theta)}\right)}{r^2\left(\frac{8\cos(2\theta)}{\sin^2(2\theta)}\right)} = \frac{\sin^3(2\theta)}{\cos^3(2\theta)} = \tan^3(2\theta)$$

□

B

Appendix B.

Publications

B.1. Articles - Journals and Conference Proceedings

H. Altendorf and D. Jeulin (Jun. 2009). *3D Directional Mathematical Morphology for Analysis of Fiber Orientations.* Proceedings of **10th European Congress of Stereology and Image Analysis**, published digitally. URL: `http://www.mat.unimi.it/OCS/index.php/ECS/ecs10/paper/view/36`.

H. Altendorf and D. Jeulin (Nov. 2009). *3D Directional Mathematical Morphology for Analysis of Fiber Orientations.* **Image Analysis and Stereology**, 28/3, pages: 143 – 153. URL: `http://www.ias-iss.org/ojs/IAS/article/view/857`.

H. Altendorf and D. Jeulin (Aug. 2009). *Fiber Separation from Local Orientation and Probability Maps.* Proceedings of **9th International Symposium, ISMM 2009, Groningen** Book of Extended Abstract, pages: 33 – 36. University of Groningen, M.H.F. Wilkinson and J.B.T.M. Roerdink (Eds.).

H. Altendorf, S. Didas and T. Batt (Dec. 2010). *Automatische Bestimmung von Faserradienverteilungen.* Proceedings of **Forum Bildverarbeitung 2010**, pages: 59 – 70. KIT Scientific Publisher. URL: `uvka.ubka.uni-karlsruhe.de/shop/download/1000020266`.

H. Altendorf and D. Jeulin (Apr. 2011). *Random-Walk-Based Stochastic Modeling of Three-Dimensional Fiber Systems.* **Phys. Rev. E**, 83, 041804. Submitted oct 2010. URL: `http://pre.aps.org/abstract/PRE/v83/i4/e041804`.

H. Altendorf and D. Jeulin (Jul. 2011). *Stochastic Modeling of a Glass Fiber Reinforced Polymer.* **Lecture Notes in Computer Science**, Volume 6671, Mathematical Morphology and Its Applications to Image and Signal Processing, pages: 439 – 450. URL: `http://www.springerlink.com/content/2113478360418154/fulltext.pdf`.

H. Altendorf and D. Jeulin (Oct. 2011). *3D Modeling of Dense Packings of Bended Fibers.* Proceedings of **13th International Congress for Stereology**.

H. Altendorf, E. Decencière, D. Jeulin, P. D. S. Peixoto, A. Deniset-Besseau, E. Angelini, G. Mosser and M.-C. Schanne-Klein (submitted Jun. 2011). *Imaging and 3D Morphological Analysis of Collagen Fibrils.* Submitted to **Journal of Microscopy**.

B.2. Presentations and Conferences

3d Carnot Workshop Presentation (english) at *2nd International Fraunhofer Workshop "3d Imaging, Analysis, Modeling and Simulation of Macroscopic Properties"* 04.-05.11.08 Kaiserslautern, Germany. Title: "Morphological Analysis of 3d Random Fiber Networks" (30 min).

Fiber Seminar Presentation (french) at *Seminaire de fibres* 27.11.08 Fontainebleau, France. Title: "Morphologie Mathématique 3D Directionelle pour l'Analyse des Réseaux de Fibre" (30 min).

MiPoM Poster at *Workshop on Models and Images for Porous Media* 12.-16.01.09 Paris, France. Title: "Characterization and Modeling of Microstructures Using Volume Images".

ESRF Seminar Presentation (english) at *ESRF Seminar, Invitation of Alexander Rack* 16.01.09 ESRF Grenoble, France. Title: "Mathematical Morphology for Analysis of Fiber Networks" (60 min).

ISS 2009 Presentation (french) at *32ème journée ISS France* 05.02.09 Paris, France. Title: "Morphologie Mathématique 3D Directionelle pour l'Analyse des Réseaux de Fibre" (15 min).

QIA Presentation (german) at *15. Workshop on Quantitative Image Analysis* 08.05.09 Bissersheim, Germany. Title: "Lokale Vermessung von Fasersystemen: Aktuelle Entwicklungen und offene Fragestellungen an der Schnittstelle zur Modellierung".

ECS 10 Presentation + Paper of 6 pages for *ECS 10 - The 10th European Congress of Stereology and Image Analysis* 22.-26.06.09 Milan, Italy: "3D Directional Mathematical Morphology for Analysis of Fiber Orientations".

1st Year Oral Presentation + Report for *1st year orals* 29.06.09 in Fontainebleau, France.

ISMM Poster and extended abstract for *International Symposium on Mathematical Morphology 2009* 24.-27.08.09 Groningen, Netherlands: "Fiber separation from local orientation and probability maps".

ICIP 2009 Conference Participation at *IEEE International Conference on Image Processing* 07.-10.11.09 Cairo, Egypt.

MIA 2009 Conference Participation at *Mathematics and Image Analysis 2009* 14.-16.12.09 Paris, France.

ISS 2010 Presentation (french) at *33ème journée ISS France* 04.02.10 Paris, France. Title: "Morphological Analysis of Random Fiber Networks with Thresholded Quasi Distance" (15 min).

WIP 2010 Presentation at *Workshop Image Processing – Trends and Applications* 11.-12.03.10 Kaiserslautern, Germany. Title: "3D Directional Mathematical Morphology for Analysis of Fiber Orientations" (25 min).

WMM Conference Participation at *Workshop Morphologie Mathématique – 70ème Anniversaire Jean Serra* 01.04.10 Paris, France.

W3D 2010 Presentation at *3rd International Workshop: 3D Imaging, Analysis, Modeling and Simulation of Macroscopic Properties* 20.-21.04.10 Fontainebleau, France. Title: "Modeling Fiber Systems using Random Walks" (30 min).

ECCM IV Presentation at *2010 European Congress on Computational Mechanics: Solids, Structures and Coupled Problems in Engineering* 17.-21.05.10 Paris, France. Title: "Modeling Fiber Systems using Random Walks" (30 min).

IWAP Presentation at *5th International Workshop on Applied Probability* 05.-08.07.10 Madrid, Spain. Title: "Modeling Fiber Reinforced Polymers" (30 min).

ECMI Presentation at *16th European Conference on Mathematics for Industry* 26.-30.07.10 Wupperthal, Germany. Title: "Modeling Fiber Systems using Random Walks" (30 min).

Composite 2010 Presentation at *23rd International Workshop Research in Mechanics of Composites* 29.-30.11.10 Bad Herrenalb, Germany. Title: "3D Characterization of Fibre-Reinforced Composites" (30 min).

BV-Forum Poster at *Bildverarbeitungs-Forum 2010* 02.-03.12.10 Regensburg, Germany. Title: "Automatische Bestimmung von Faserradienverteilungen" (presented by Stephan Didas).

ISS 2011 Presentation (french) at *34ème journée ISS France* 03.02.11 Paris, France. Title: "3D Modeling of Dense Packings of Bended Fibers" (15 min).

CMM-ITWM Presentation at *Research Workshop franco-allemand* 21.-23.03.11 Fontainebleau, France. Title: "Stochastic Modeling of a Glass Fiber Reinforced Polymer" (30 min).

ENS Cachan Invited Presentation at *Seminaire CMLA-ENS Cachan* 28.04.11 Cachan, France. Title: "Morphological Analysis and Stochastic Modeling of Random Fiber Networks" (45 min).

ISMM 2011 Poster at *International Symposium on Mathematical Morphology 2011* 06.-08.07.11 Intra, Italy. Title: "Stochastic Modeling of a Glass Fiber Reinforced Polymer".

ICS 13 Presentation at *13th International Congress for Stereology* 19.-23.10.11 Beijing, China. Title: "3d Modeling of Dense Packings of Bended Fibers" (presented by Dominique Jeulin).

3DMM Presentation at *3D Microstructure Meeting* 02.-04.11.11 Saarbrücken, Germany. Title: "Application of Virtual Material Design on a Glass Fiber Reinforced Polymer".

C

Appendix C.

Curriculum Vitae

Professional Experiences

2008 - 2011	PhD Thesis in Applied Mathematics and participation in industrial projects (Mines ParisTech, Fontainebleau, France – Fraunhofer ITWM Institute for Industrial Mathematics, Kaiserslautern, Germany)
2007 - 2008	ProSAT (project studies in advanced technologies) – Fraunhofer ITWM Kaiserslautern
2006	Internship at Fraunhofer ITWM Kaiserslautern
2004 - 2006	Tutor for the lectures “Advanced Mathematics” and “Algorithms and Data Structures” at University of Mannheim, Germany
2002 - 2004	Scientific assistant at the University of Mannheim.

Education

2011	PhD in Applied Mathematics (Mines ParisTech, Fontainebleau, France – University of Kaiserslautern, Germany)
2007	Master Degree in Mathematics (University of Mannheim and Fraunhofer ITWM, Kaiserslautern, Germany)
2006	Master Degree in Computer Science (University of Mannheim, Germany)
2001	High School Diploma in Worms, Germany. Specialties Mathematics, Physics and English.

Skills

Languages:	German (native tongue), English (fluent), French (fluent), Spanish (basics)
Programming:	C++, Java, R, Shell Scripting, Python, Matlab, SQL, Latex

Bibliography

Aboudi, J. (1991). *Mechanics of Composite materials - A unified Micromechanical Approach*. Elsevier Science.

Ahlborn, D. T. M., Peuse, M. E. J. & Misson, M. D. L. (2008). Ultra-high-performance-concrete for michigan bridges material performance – phase i. Tech. Rep. RC-1525, Center for Structural Durability, Michigan Tech Transportation Institute.

Altendorf, H. (2007). *Consistent Pairs of Adjacency Systems in 3D Image Analysis (Konsistente Paare von Nachbarschafts-Systemen für die 3D Bildanalyse)*. Diploma thesis, University of Mannheim, Fraunhofer ITWM.

Altendorf, H., Decencière, E., Jeulin, D., Peixoto, P. D. S., Deniset-Besseau, A., Angelini, E., Mosser, G. & Schanne-Klein, M.-C. (2011). Imaging and 3d morphological analysis of collagen fibrils. Submitted to Journal of Microscopy.

Altendorf, H., Didas, S. & Batt, T. (2010). Automatische Bestimmung von Faserradienverteilungen. In *Forum Bildverarbeitung 2010*, 59–70. KIT Scientific Publisher.

Altendorf, H. & Jeulin, D. (2009a). 3d directional mathematical morphology for analysis of fiber orientations. *Image Analysis and Stereology*, **28**, 143–153.

Altendorf, H. & Jeulin, D. (2009b). Fiber separation from local orientation and probability maps. In *Abstract book of the 9th Int. Symp on Math. Morph. (ISMM'2009)*, edited by M. Wilkinson & J. Roerdink, 33–36. University of Groningen, The Netherlands.

Altendorf, H. & Jeulin, D. (2011a). Random-walk-based stochastic modeling of three-dimensional fiber systems. *Phys. Rev. E*, **83**, 041804. Submitted oct 2010.

Altendorf, H. & Jeulin, D. (2011b). Stochastic modeling of a glass fiber reinforced polymer. *Lecture Notes in Computer Science*, **6671**, 439–450.

Association Française de Génie Civil (2002). Ultra high performance fibre-reinforced concretes—interim recommendations.

Axelsson, M. (2009). *Image Analysis for Volumetric Characterisation of Microstructure*. Ph.D. thesis, Swedish University of Agricultural Sciences at Uppsala.

Bache-Wiig, J. & Henden, P. C. (2005). *Individual fiber segmentation of three-dimensional microtomogram of paper materials*. master thesis, Norwegian University of Science and Technology.

Bakhadyrov, I. & Jafari, M. (1999). Inertia tensor as a way of feature vector definition for one-dimensional signatures. 904–909.

Banerjee, A., Dhillon, I. S., Ghosh, J. & Sra, S. (2005). Clustering on the unit hypersphere using von Mises-Fisher distributions. *J. Mach. Learn. Res.*, **6**, 1345–1382.

Banhart, J. (2008). *Advanced Tomographic Methods in Materials Research and Engineering*. Oxford University Press.

Barbero, E. (2007). *Finite Element Analysis of Composite Materials*. Crc Pr Inc.

Bayan, C., Levitt, J. M., Miller, E., Kaplan, D. & Georgakoudi, I. (2009). Fully automated, quantitative, noninvasive assessment of collagen fiber content and organization in thick collagen gels. *J. Appl. Phys.*, **105**, 102042.

Berhan, L. & Sastry, A. M. (2007a). Modeling percolation in high-aspect-ratio fiber systems. i. soft-core versus hard-core models. *Phys. Rev. E*, **75**, 041120.

Berhan, L. & Sastry, A. M. (2007b). Modeling percolation in high-aspect-ratio fiber systems. ii. the effect of waviness on the percolation onset. *Phys. Rev. E*, **75**, 041121.

Beucher, S. (2007). Numerical residues. *Image and Vision Computing*, **25**, 405 – 415. Presented at International Symposium on Mathematical Morphology 2005.

Bezrukov, A., Bargieł, M. & Stoyan, D. (2002). Statistical analysis of simulated random packings of spheres. *Part. Part. Systems Char.*, **19**, 111–118.

Bezrukov, A. & Stoyan, D. (2006). Simulation and statistical analysis of random packings of ellipsoids. *Particle & Particle Systems Characterization*, **23**, 388 – 398.

Bigun, J. & Granlund, G. H. (1987). Optimal orientation detection of linear symmetry. 433–438.

Bornert, M., Bretheau, T. & Gilormini, P. (2001). *Homogénéisation en mécanique des matériaux 1*. HERMES Science Europe Ltd.

Bowles, R. D., Williams, R. M., Zipfel, W. R. & Bonassar, L. J. (2010). Self-assembly of aligned tissue-engineered annulus fibrosus and intervertebral disc composite via collagen gel contraction. *Tissue Eng A*, **16**, 1339–1348.

Campagnola, P. J., Millard, A. C., Terasaki, M., Hoppe, P. E., Malone, C. J. & Mohler, W. (2002). Three-dimensional high-resolution second-harmonic generation imaging of endogenous structural proteins in biological tissues. *Biophys. J.*, **82**, 493–508.

Carson, J. K., Lovatt, S. J., Tanner, D. J. & Cleland, A. C. (2005). Thermal conductivity bounds for isotropic, porous materials. *International Journal of Heat and Mass Transfer*, **48**, 2150–2158.

Catté, F., Lions, P.-L., Morel, J.-M. & Coll, T. (1992). Image selective smoothing and edge detection by nonlinear diffusion. *SIAM Journal on Numerical Analysis*, **29**, 182–193.

Chan, F. K. & O'Neill, I. (1975). Feasibility study of a quadrilateralized spherical cube earth data base. Tech. Rep. 2-75 (CSC), Computer Sciences Corporation, EPRF, Monterey, California. Prepared for the Environmental Prediction Research Facility.

Chin, W.-K., Liu, H.-T. & Lee, Y.-D. (1988). Effects of fiber length and orientation distribution on the elastic modulus of short fiber reinforced thermoplastics. *Polymer Composites*, **9**, 27–35.

Cinacchi, G. & Gaetani, L. D. (2008). Phase behavior of wormlike rods. *Physical Review E*, **77**.

Coelho, D., Thovert, J.-F. & Adler, P. (1997). Geometrical and transport properties of random packings of spheres and aspherical particles. *Physical Review E*, **55**, 1959–1978.

Decker, L., Jeulin, D. & Tovena, I. (1998). 3d morphological analysis of the connectivity of a porous media. *Acta Stereologica*, **17**, 107–112.

Department of Polymer Science at University of Southern Mississippi (2005). Carbon fiber information. published electronically at `http://www.pslc.ws/mactest/carfib.htm`.

Duda, R. O. & Hart, P. E. (1973). *Pattern Classification and Scene Analysis*. John Wiley & Sons Inc.

East Coast Fibreglass Supplies (2010). Guide to glass reinforced plastics. online.

Elsner, A., Wagner, A., Aste, T., Hermann, H. & Stoyan, D. (2009). Specific surface area and volume fraction of the cherry-pit model with packed pits. *The Journal of Physical Chemistry B*, **113**, 7780–7784. PMID: 19425581.

Eyre, D. & Milton, G. (1999). A fast numerical scheme for computing the response of composites using grid refinement. *Eur. Phys. J. AP*, **6**.

Fabrizio, J. & Marcotegui, B. (2006). Text segmentation in natural scene using toggle-mapping. Tech. rep., University Paris 06 and Mines ParisTech, France.

Fabrizio, J., Marcotegui, B. & Cord, M. (2009). Text segmentation in natural scenes using toggle-mapping. In *Proc. 16th IEEE International Conference on Image Processing*, 2373–2376. IEEE Signal Processing Society, Cairo, Egypt.

Faessel, M., Delisée, C., Boss, F. & Castera, P. (2005). 3d modelling of random cellulosic fibrous networks based on x-ray tomography and image analysis. *Composites science and technology*, **65**, 1931–1940.

Favier, V., Dendievel, R., Canova, G., Cavaille, J. & Gilormini, P. (1997). Simulation and modeling of three-dimensional percolating structures: Case of a latex matrix reinforced by a network of cellulose fibers. *Acta Materialia*, **45**, 1557–1565.

Feder, J. (1980). Random sequential adsorption. *Journal of Theoretical Biology*, **87**, 237 – 254.

Fisher, N. (1996). *Statistical analysis of circular data*. Cambridge Univ Pr.

Fisher, N. I., Embleton, B. J. J. & Lewis, T. (1993). *Statistical analysis of spherical data*. Cambridge University Press, Cambridge [England]; Oakleigh [Vic.], [rev. ed.] ed.

Fisher, R. A. (1953). Dispersion on a sphere. *Proceedings of the Royal Society of London, Series A*, **217**, 295–305.

Fliege, J. & Maier, U. (1996). A two-stage approach for computing cubature formulae for the sphere. In *Mathematik 139T, Universitat Dortmund, Fachbereich Mathematik, Universitat Dortmund, 44221*.

Frangi, A., Niessen, W., Vincken, K. & Viergever, M. (1998). Multiscale vessel enhancement filtering. 130–137.

Fu, S.-Y. & Lauke, B. (1996). Effects of fiber length and fiber orientation distributions on the tensile strength of short-fiber-reinforced polymers. *Composites Science and Technology*, **56**, 1179 – 1190.

Gobeaux, F., Belamie, E., Mosser, G., Davidson, P., Panine, P. & Giraud-Guille, M.-M. (2007). Cooperative ordering of collagen triple helices in the dense state. *Langmuir*, **23**, 6411–6417.

Gobeaux, F., Mosser, G., Anglo, A., Panine, P., Davidson, P., Giraud-Guille, M.-M. & Belamie, E. (2008). Fibrillogenesis in dense collagen solutions: a physicochemical study. *J. Mol. Biol.*, **376**, 1509–1522.

Górski, K. M., Hivon, E., Banday, A. J., Wandelt, B. D., Hansen, F. K., Reinecke, M. & Bartelmann, M. (2005). HEALPix: A Framework for High-Resolution Discretization and Fast Analysis of Data Distributed on the Sphere. *The Astrophysical Journal*, **622**, 759–771.

Granlund, G. H. & Knutsson, H. (1995). *Signal Processing for Computer Vision*. Kluwer Academic Publishers.

Grewenig, S., Weickert, J. & Bruhn, A. (2010). From box filtering to fast explicit diffusion. In *DAGM-Symposium'10*, 533–542.

Gross, D. & Seelig, T. (2011). *Bruchmechanik - Mit Einführung in die Mikromechanik*. Springer.

Hardin, R. H., Sloane, N. J. A. & Smith, W. D. (1994). Tables of spherical codes with icosahedral symmetry. published electronically at `http://www.research.att.com/~njas/icosahedral.codes/`.

Hardin, R. H., Sloane, N. J. A. & Smith, W. D. (2000). A library of good packings, coverings and maximal volume arrangements of points on the sphere in 3 dimensions having icosahedral symmetry. Tech. rep., AT&T Shannon Lab, USA.

Hashin, Z. & Shtrikman, S. (1962). A variational approach to the theory of the effective magnetic permeability of muliphase materials. *Journal of Applied Physics*, **33**, 3125–3131.

Hine, P. J., Davidson, N., Duckett, R. A. & Ward, I. M. (1995). Measuring the fibre orientation and modelling the elastic properties of injection-moulded long-glass-fibre-reinforced nylon. *Composites Science and Technology*, **53**, 125 – 131. Mesostructures and Mesomechanics in Fibre Composites.

Hinrichsen, E. L., Feder, J. & Jøssang, T. (1990). Random packing of disks in two dimensions. *Phys. Rev. A*, **41**, 4199–4209.

Hu, M.-K. (1962). Visual pattern recognition by moment invariants. *Information Theory, IRE Transactions on*, **8**, 179 –187.

Iijima, T. (1962). Basic theory on normalization of pattern (in case of typical one-dimensional pattern). *Bulletin of the Electrotechnical Laboratory*, **26**, 368–388. (In Japanese).

International, F. (1968). The new steel - carbon-fibre-reinforced plastics: the materials that may revolutionise aircraft design. *Flight International*, 669–670.

Jain, L. & Wetherhold, R. (1992). Effect of fiber orientation on the fracture toughness of brittle matrix composites. *Acta Metallurgica et Materialia*, **40**, 1135 – 1143.

Jeulin, D. (2008). Physics and mechanics of random media. Lecture Notes. MINES ParisTech.

Jeulin, D. (2011). Variance scaling of Boolean random varieties. In preparation.

Jeulin, D. & Moreaud, M. (2008a). Segmentation of 2d and 3d textures from estimates of the local orientation. *Image Analysis and Stereology*, **27**, 183–192.

Jeulin, D. & Moreaud, M. (2008b). Statistical representative volume element for predicting the dielectric permittivity of random media. In *Proceedings of CMDS 11*, 429–436. Les Presses de l'École des Mines de Paris.

Jupp, P. & Mardia, K. (1989). A unified view of the theory of directional statistics, 1975-1988. *International Statistical Review/Revue Internationale de Statistique*, **57**, 261–294.

Kanit, T., Forest, S., Galliet, I., Mounoury, V. & Jeulin, D. (2003). Determination of the size of the representative volume element for random composites : statistical and numerical approach. *International Journal of Solids and Structures*, **40**, 3647–3679.

Kanit, T., N'Guyen, F., Forest, S., Jeulin, D., Reed, M. & Singleton, S. (2006). Apparent and effective physical properties of heterogeneous materials: Representativity of samples of two materials from food industry. *Comput. Methods Appl. Mech. Engrg.*, **195**, 3960–3982.

Karayiannis, N. C. & Laso, M. (2008). Monte Carlo scheme for generation and relaxation of dense and nearly jammed random structures of freely jointed hard-sphere chains. *Macromolecules*, **41**, 1537 – 1551.

Karkkainen, S., Nyblom, J., Miettinen, A., Turpeinen, T. & Pötschke, P. (2008). A stochastic shape model for fibres with an application to carbon nanotubes.

Kroner, E. (1972). *Statistical Continuum Mechanics*. Springer-Verlag, Wien.

Laso, M., Karayiannis, N. C., Foteinopoulou, K., Mansfield, M. L. & Kröger, M. (2009). Random packing of model polymers: local structure, topological hindrance and universal scaling. *Soft Matter*, **5**, 1762–1770.

Lemons, R. A. & Quate, C. F. (1974). Acoustic microscope–scanning version. *Appl. Phys. Lett.*, **24**, 163–165.

Mandel, J. (1966). *Cours de Mécanique des Milieux Continus*. GauthiersVillars.

Mardia, K., Jupp, P. & Corporation, E. (2000). *Directional statistics*. Wiley Chichester.

Markov, K. Z. & Zvyatkov, K. D. (1995). Functional series and Hashin-Shtrikman type bounds on the effective conductivity of random media. *European Journal of Applied Mathematics*, **6**, 611–629.

Matheron, G. (1975). *Random sets and integral geometry*. Wiley series in probability and mathematical statistics. Probability and mathematical statistics. Wiley.

Matteini, P., Ratto, F., Rossi, F., Cicchi, R., Stringari, C., Kapsokalyvas, D., Pavone, F. S. & Pini, R. (2009). Photothermally-induced disordered patterns of corneal collagen revealed by shg imaging. *Opt. Express*, **17**, 4868–4878.

Mayer, R. M. (1993). *Design with reinforced plastics*. Springer.

McCartin, B. J. (2007). On concentration and inertia ellipsoids. *Applied Mathematical Sciences*, **1**, 1–11.

Meyer, F. (1979). Iterative image transformations for an automatic screening of cervical smears. *Journal of Histochemistry and Cytochemistry*, **27**, 128–135.

Meyer, F. (1986). Automatic screening of cytological scpecimens. *Computer Vision, Graphics, and Image Processing*, **35**, 356–369.

Michel, J.-C., Moulinec, H. & Suquet, P. (2001). A computational scheme for linear and non-linear composites with arbitrary phase contrast. *Int. J. Numer. Meth. Engng.*.

Mościński, J. & Bargieł, M. (1989). The force-biased algorithm for the irregular close packing of equal hard spheres. *Molecular Simulation*, **3**, 201–212.

Moulinec, H. & Suquet, P. (1994). A fast numerical method for computing the linear and nonlinear properties of composites. *C. R. Acad. Sci. Paris, Sér. II*, **318**, 1417–1423.

Moulinec, H. & Suquet, P. (1998). A numerical method for computing the overall response of nonlinear composites with complex microstructure. *Comput. Methods Appl. Mech. Engrg.*, **157**.

Moulinec, H. & Suquet, P. (2003). Comparison of FFT-based methods for computing the response of composites with highly contrasted mechanical properties. *Phys. B*, **338**.

Mura, T. (1987). *Micromechanics of defects in solids*. Martinus Nijhoff Publishers.

Nawy, E. G. (2001). *Fundamentals of high-performance concrete (2 ed.)*. John Wiley and Sons.

Nemat-Nasser, S. & Hori, M. (1998). *Micromechanics: Overall Properties of Heterogeneous Materials*. North-Holland Series in Applied Mathematics and Mechanics.

Ohser, J. & Schladitz, K. (2009). *3d Images of Materials Structures – Processing and Analysis*. Wiley VCH, Weinheim.

O'Neill, I. & Laubscher, R. E. (1976). Extended studies of a quadrilateralized spherical cube earth data base. Tech. Rep. 3-76 (CSC), Computer Sciences Corporation, NEPRF, Monterey, California. Prepared for the Naval Environmental Prediction Research Facility.

Osher, S. & Rudin, L. I. (1990). Feature-oriented image enhancement using shock filters. *SIAM Journal on Numerical Analysis*, **27**, 919–940.

Oumarou, M., Jeulin, D. & Renard, J. (2011). Etude numérique et statistique du comportement d'un composite thermoplastique. *Revue des composites et des matériaux avancés*, **21**, 221–254.

Pan, Y., Iorga, L. & Pelegri, A. A. (2008). Numerical generation of a random chopped fiber composite rve and its elastic properties. *Composites Science and Technology*, **68**, 2792–2798.

Parzen, E. (1962). On estimation of a probability density function and mode. *The Annals of Mathematical Statistics*, **33**, 1065–1076.

Patt, F. (1993). Sphere cube. published online.

Pena, A.-M., Fabre, A., Débarre, D., Marchal-Somme, J., Crestani, B., Martin, J.-L., Beaurepaire, E. & Schanne-Klein, M.-C. (2007). Three-dimensional investigation and scoring of extracellular matrix remodeling during lung fibrosis using multiphoton microscopy. *Microsc. Res. Tech.*, **70**, 162–170.

Pena, A.-M., Fagot, D., Olive, C., Michelet, J.-F., Galey, J.-B., Leroy, F., Beaurepaire, E., Martin, J.-L., Colonna, A. & Schanne-Klein, M.-C. (2010). Multiphoton microscopy of engineered dermal substitutes: assessment of 3d collagen matrix remodeling induced by fibroblasts contraction. *J. Biomed. Opt.*, **in press**.

Perona, P. & Malik, J. (1990). Scale space and edge detection using anisotropic diffusion. *IEEE Transactions on Pattern Analysis and Machine Intelligence*, **12**, 629–639.

Peter Wall, L. (1997). A comparison of homogenization, Hashin-Shtrikman bounds and the Halpin-Tsai equations. *Applications of Mathematics*, **42**, 245–257.

Peters, D. M. (1968). *Design Engineering (UK).*

Peyrega, C., Jeulin, D., Delisée, C. & Malvestio, J. (2009). 3d morphological modelling of a random fibrous network. *Image Analysis and Stereology*, **18**, 129–141.

Provatas, N., Haataja, M., Asikainen, J., Majaniemi, S., Alava, M. & Ala-Nissila, T. (2000). Fiber deposition models in two and three spatial dimensions. *Colloids and Surfaces A: Physicochemical and Engineering Aspects*, **165**, 209–229.

Rack, A. (2006). *Untersuchung komplexer Materialsysteme mittels Synchrotron-Tomographie und 3D-Bildanalyse Investigations on complex material systems by synchrotron tomography and 3D image analysis*. Ph.D. thesis, Technischen Universität Berlin.

Rack, A., Zabler, S., Müller, B. R., Riesemeier, H., Weidemann, G., Lange, A., Goebbels, J., Hentschel, M. & Görner, W. (2008). High resolution synchrotron-based radiography and tomography using hard x-rays at the bamline (bessy ii). *Nuclear Instruments and Methods in Physics Research A*, **586**, 327–344.

Raub, C. B., Unruh, J., Suresh, V., Krasieva, T., Lindmo, T., Gratton, E., Tromberg, B. J. & George, S. C. (2008). Image correlation spectroscopy of multiphoton images correlates with collagen mechanical properties. *Biophys. J.*, **94**, 2361.

Reuze, P., Coatrieux, J., Luo, L. & Dillenseger, J. (1993). A 3d moment based approach for blood vessel detection and quantification in mra. *Technol. Health Care 1*, 181–188.

Rikvold, P. A. & Stell, G. (1985). Porosity and specific surface for interpenetrable-sphere models of two-phase random media. *The Journal of Chemical Physics*, **82**, 1014–1020.

Robb, K., Wirjadi, O. & Schladitz, K. (2007). Fiber orientation estimation from 3D image data: Practical algorithms, visualization, and interpretation. 320–325.

Rosenfeld, A. & Pfaltz, J. L. (1966). Sequential operations in digital picture processing. *J. ACM*, **13**, 471–494.

Salembier, P. & Serra, J. (1995). Flat zones filtering, connected operators, and filters by reconstruction. *IEEE Transactions on Image Processing*, **4**, 1153–1160.

Sandau, K. & Ohser, J. (2007). The chord length transform and the segmentation of crossing fibres. *J. Microscopy*, **226**, 43–53.

Schladitz, K., Peters, S., Reinel-Bitzer, D., Wiegmann, A. & Ohser, J. (2006). Design of acoustic trim based on geometric modeling and flow simulation for non-woven. *Computational Materials Science*, **38**, 56–66.

Schmauder, S. & Mishnaevsky, L. (2008). *Micromechanics and Nanosimulation of Metals and Composites*. Springer.

Schuler, F., Sych, T. & Schnell, J. (2007). Analyse der faserorientierung in betonen mit hilfe der computer-tomographie. Forschungsvorhaben dbv 273 (antrag 07/07), Fraunhofer ITWM and Technical University of Kaiserslautern.

Schulgasser, K. (1985). Fibre orientation in machine-made paper. *Journal of Materials Science*, **20**, 859–866.

Serra, J. (1982). *Image analysis and mathematical morphology*. Academic Press, London.

Serra, J. (1989). Toggle mappings. In *From pixels to features*, edited by J. C. Simon, 61–72. North-Holland, Elsevier.

Spiller, E. (1980). Recent developments towards high resolution x-ray imaging. *Nuclear Instruments and Methods*, **177**, 187–192.

Stock, S. R. (2008). *MicroComputed Tomography: Methodology and Applications*. CRC Press.

Stoyan, D., Kendall, W. S. & Mecke, J. (1987). *Stochastic Geometry and Its Applications*. Wiley in Chichester [W. Sussex], New York.

Stoyan, D. & Stoyan, H. (1992). *Fractals, Random Shapes and Point Fields: Methods of Geometric Statistics*. Akademie-Verlag, Berlin.

Strupler, M., Hernest, M., Fligny, C., Martin, J.-L., Tharaux, P.-L. & Schanne-Klein, M.-C. (2008). Second harmonic microscopy to quantify renal interstitial fibrosis and arterial remodeling. *J. Biomed. Optics*, **13**, 054 041.

Strupler, M., Pena, A.-M., Hernest, M., Tharaux, P.-L., Martin, J.-L., Beaurepaire, E. & Schanne-Klein, M.-C. (2007). Second harmonic imaging and scoring of collagen in fibrotic tissues. *Opt. Express*, **15**, 4054–4065.

Sun, W. X., Chang, S., Tai, D. C. S., Tan, N., Xiao, G. F., Tang, H. H. & Yu, H. (2008). Nonlinear optical microscopy: use of second harmonic generation and two-photon microscopy for automated quantitative liver fibrosis studies. *J. Biomed. Optics*, **13**, 064010.

Talbot, H., Lee, T., Jeulin, D., Hanton, D. & Hobbs, L. W. (2000). Image analysis of insulation mineral fibres. *Journal of Microscopy*, **200**, 251–268.

Tankyevych, O., Talbot, H. & Dokladal, P. (2008). Curvilinear morpho-hessian filter. 1011–1014.

Torquato, S. (1991). Random heterogeneous media: microstructure and improved bounds on effective properties. *Applied Mechanics Reviews*, **44**, 37–76.

Torquato, S. (2002). *Random Heterogeneous Materials: Microstructure and Macroscopic Properties*. Springer-Verlag, New York. Interdisciplinary Applied Mathematics Series.

Trias, D., Costa, J., Turon, A. & Hurtado, J. (2006). Determination of the critical size of a statistical representative volume element (srve) for carbon reinforced polymers. *Acta materialia*, **54**, 3471–3484.

Vincent, L. (1993). Morphological gray scale reconstruction in image analysis: Applications and efficient algorithms. **2**, 176–201.

Walther, T., Terzic, K., Donath, T., Meine, H., Beckmann, F. & Thoemen, H. (2006). Microstructural analysis of lignocellulosic fiber networks. In *Developments in X-Ray Tomography V*, edited by U. Bonse, vol. 6318. Society of Photo-Optical Instrumentation Engineers (SPIE).

Watson, G. S. (1965). Equatorial distributions on a sphere. *Biometrika*, **52**, 193–201.

Weickert, J. (1998). *Anisotropic Diffusion in Image Processing*. B. G. Teubner, Stuttgart.

Weickert, J., Ishikawa, S. & Imiya, A. (1999). Linear scale-space has first been proposed in Japan. *Journal of Mathematical Imaging and Vision*, **10**, 237–252.

Weickert, J., ter Haar Romeny, B. M. & Viergever, M. A. (1998). Efficient and reliable schemes for nonlinear diffusion filtering. *IEEE Transactions on Image Processing*, **7**, 398–410.

White, R. A. & Stemwedel, S. W. (1992). The quadrilateralized spherical cube and quad-tree for all sky data. *Astronomical Data Analysis Software and Systems I, A.S.P. Conference Series*, **25**.

Widom, B. (1966). Random sequential addition of hard spheres to a volume. *Journal of Chemical Physics*, **44**.

Williams, S. R. & Philipse, A. P. (2003). Random packings of spheres and spherocylinders simulated by mechanical contraction. *Phys. Rev. E*, **67**, 051301.

Willot, F. & Jeulin, D. (2009). Elastic behavior of composites containing Boolean random sets of inhomogeneities. *International Journal of Engineering Science*, **47**, 313–324.

Wirjadi, O. (2009). *Models and Algorithms for Image-Based Analysis of Microstructures*. Ph.D. thesis, Technische Universität Kaiserslautern.

Wirjadi, O., Schladitz, K., Rack, A. & Breuel, T. (2009). Applications of anisotropic image filters for computing 2d and 3d-fiber orientations. In *Proc. 10th European Conference of ISS*, vol. 4, 107–112.

Witkin, A. P. (1983). Scale-space filtering. In *Proc. Eighth International Joint Conference on Artificial Intelligence*, vol. 2, 945–951. Karlsruhe, Germany.

Zipfel, W. R., Williams, R., Christie, R., Nikitin, A., Hyman, B. & Webb, W. (2003a). Live tissue intrinsic emission microscopy using multiphoton-excited native fluorescence and second harmonic generation. *Proc. Natl. Acad. Sci. USA*, **100**, 7075–7080.

Zipfel, W. R., Williams, R. & Webb, W. (2003b). Nonlinear magic: multiphoton microscopy in the biosciences. *Nature Biotech.*, **21**, 1369–1377.

Zohdi, T. & Wriggers, P. (2008). *An introduction to computational micromechanics*. Springer.